1 OF 2

N85-26668 UNCLAS

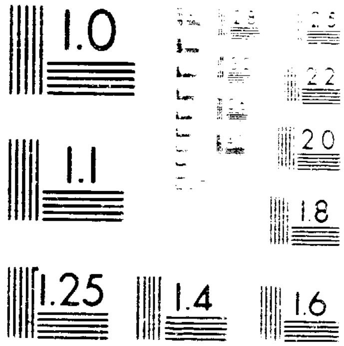

MICROCOPY RESOLUTION TEST CHART
NATIONAL BUREAU OF STANDARDS
STANDARD REFERENCE MATERIAL 1010a
(ANSI and ISO TEST CHART No. 2)

NASA-CR-174849

DEVELOPMENT OF A ROTOR WAKE/VORTEX MODEL

VOLUME I - FINAL REPORT

By
R.K. Majjigi
P.R. Gliebe

General Electric Aircraft Engine Business Group
Advanced Technology Programs Department
Cincinnati, Ohio 45215

Contract NAS3-23681

Prepared For
National Aeronautics and Space Administration
Lewis Research Center
21000 Brookpark Road
Cleveland, Ohio 44135

(NASA-CR-174849) DEVELOPMENT OF A ROTOR WAKE-VORTEX MODEL, VOLUME 1 Final Technical Report (General Electric Co.) 171 p HC A08/MF A01 CSCL 01A
N85-26668
Unclas
G3/02 21232

NASA STI FACILITY
ACCESS DEPT.

National Aeronautics and
Space Administration

ACKNOWLEDGEMENTS

This work was supported by the National Aeronautics and Space Administration through the Contract NAS3-23681, with Len Homyak of NASA Lewis as the Program Manager. The authors would like to thank Len Homyak and John Groeneweg for supplying the rotor wake data on Rotor 67 and the JT15D fan rotor for the data-theory comparison and also for the various technical discussions.

We would like to thank Prof. B. Lakshminarayana of the Pennsylvania State University, who performed rotor wake momentum integral analysis as a consultant for this program. We would also like to thank Dr. C. Hah of General Electric Corporate Research and Development for the analytical correlation of turbulent wake decay he performed and for his technical assistance during this program.

The authors would like to express their sincere thanks to Ron Coffin for his help in developing the computer graphics software which was extensively used during the execution of this program.

TABLE OF CONTENTS

TABLE OF CONTENTS (Concluded)

LIST OF ILLUSTRATIONS

LIST OF ILLUSTRATIONS (Continued)

LIST OF ILLUSTRATIONS (Continued)

LIST OF ILLUSTRATIONS (Continued)

LIST OF ILLUSTRATIONS (Continued)

LIST OF ILLUSTRATIONS (Concluded)

LIST OF TABLES

1.0 INTRODUCTION

Noise generated by fan and compressor stages is a complex spectrum of tone and broadband sources produced by several source mechanisms. One major source of fan noise is the interaction of the nonuniform, unsteady rotor exit flow field with the downstream stator vanes. Rotor exit flow nonuniformities and unsteadiness produce fluctuations in flow velocity and flow angle into the stator, thereby generating unsteady fluctuating lift forces on the stator vanes. These rotor exit flow nonuniformities and unsteadinesses are produced by the viscous wakes shed from the rotor blade trailing edges and by the secondary flow vortices formed in the rotor blade passages.

The combined effects of blade wake and hub and tip vortex formations result in a rather complex rotor exit velocity field, seen by the downstream stator vanes as a time-varying, periodic gust excitation with a complex waveform. The resulting vane row unsteady lift exhibits a spectrum containing tones at integral multiples of rotor blade passing frequency (BPF), as well as some broadband response, thought to be associated with the random unsteadiness and turbulence produced in the blade wakes and end wall (hub and tip) regions of the rotor exit flow. The resultant noise spectrum is directly related to the vane unsteady lift spectrum through the coupling of the unsteady lift energy to acoustic modes in the fan duct.

It is thus clear that the vane row unsteady lift response and the resulting noise spectrum is directly linked to the character (spatial and time variations) of the combined wake/vortex flow field of the rotor. In order to be able to adequately predict this rotor/stator interaction and noise spectrum, a realistic model of a rotor exit wake/vortex flow field is required.

The major objective of the program summarized in this report was to establish and verify a rotor wake and vortex model for specific application to fan and compressor rotor-stator interaction noise generation. The model could also be used to evaluate stator vane forced vibration excitations. A primary requirement for this model was that it be, in its final computer code form, compact and computationally rapid so that it could easily be adapted as a subprogram or subroutine to a larger fan noise prediction computer program.

The approach selected for development of the rotor wake and vortex model was to analyze existing rotor exit flow wake and vortex data and evolve an empirical or semiempirical correlation. This correlation was to be guided by parallel analytical studies aimed at identifying the appropriate similarity parameters in order to cast the correlation into a "universal" or general form. The specific approach taken was to develop the empirical correlations of rotor wake and vortex properties (such as wake centerline velocity defect, wake semiwidth, etc.) in a rotor-fixed (rotating) reference frame, then mathematically transform these results into a stationary, stator-fixed reference frame.

The present program comprises two major tasks. The first task consists of developing a mathematical model and the associated computer program to predict viscous wakes and secondary flow vortex velocity fields downstream of a rotating blade row. This task includes a literature search and a compilation and evaluation of existing rotor wake data for use in the model development. Semiempirical models of the rotor wake mean flow and turbulence intensity characteristics have been developed using the data compiled from the literature survey, and a parallel analytical model of the viscous wake has been developed to help guide the progress of the semiempirical model. A simplified analytical model of rotor exit secondary vortex formation and downstream development has also been incorporated into the rotor wake and vortex model. The resulting model is tailored to predict the stator vane upwash velocity spectrum, and is linked to the steady aerodynamic characteristics of the fan rotor.

The second task consists of evaluating the prediction procedure developed in Task I, through parametric studies to assess the behavior of the model when key parameters are varied and through comparisons to existing sets of relevant data. Task II concludes with an identification of those aspects of the wake and vortex model requiring further development. Specific experimental and/or analytical programs to improve the model are recommended.

The following sections describe and summarize the details of the rotor wake and vortex model development and the results of the studies carried out using the model. A description of the computer program and user's manual is published under a separate cover entitled "Development of a Rotor Wake/Vortex Model, Volume II, User's Manual For Computer Program," (NASA CR-174850).

2.0 LITERATURE SURVEY AND DATA SCREENING

In order to locate sources of rotor wake and vortex data suitable for the development of an empirical model, three computerized literature searches were performed:

1. General Electric in-house literature search system
2. NASA/RECON search system
3. DoD/DTOC search system

Abstracts from all three searches were reviewed for relevant wake and vortex information. A summary of relevant literature, References 1 through 9, and the type and quantity of data available from each reference, with categories for test configuration type, facility type, flow/tip-speed range, instrumentation type, and measured flow parameters, are presented in Table I. (This table is not complete in all respects because information is lacking in the published literature). References 2, 3, and 4 contained an exhaustive amount of mean and turbulent rotor wake data at various spanwise and axial stations, which were extensively employed in the development of the empirical rotor wake relationships for wake centerline defect, semiwake width, turbulent velocities, and wake tangential profiles. The geometric and aerodynamic information regarding the test vehicles in References 2, 3, and 4 was sufficiently detailed that the data presented in them could be renormalized as needed for this program and correlated appropriately. Detailed information was also available for Rotor 55 (Reference 6); however, since it was intended to be one of the test cases for evaluating the developed rotor wake and vortex model, these data were not used in the development of the empirical rotor wake model.

ORIGINAL PAGE IS
OF POOR QUALITY

Table I. Summary of Rotor Wake Reports.

						Geometric Parameters				
Ref No	Authors	Experimental Vehicle/Model	Measurement Scheme	IGV Yes/No	Free/ Forced Vortex	No. of Rotor Blades	No. of Stator Vanes	R/S Spacing	Tip Dia. (Inches)	Hub Tip Ratio
1.	Maglíozzi, Hanson, Johnson, and Metzger	Single Stage Subsonic Tip Speed Fan	Hot Wire Probe Dynamic Total pr. Probe Stationary Ref. Frame	No		12 NACA 65-Series	7	1.85C	18	0.5
2.	Reynolds and Lakshminarayana	Single Stage Subsonic Tip Speed Fan	Tri-axial Hot Wire Probe Both in Rotor and Stationary Ref. Frame. Static pr. Probe in Rotating Frame.	No	Free Vortex	12 No Camber; British C-1 Profile	No Stator Vanes		21.5	0.44
3.	Ravindranath and Lakshminarayana	Single Stage Subsonic Tip Speed Fan	Tri-axial Hot Wire Probe in Rotor Ref. Frame. Static and Stagnation pr. Probe in Rotor Ref. Frame	Yes 41 Blades		21 Circular Camber, NACA 65-010	25	3.0 (at Tip)	36.7	0.5
4.	Lakshminarayana, Govindan, and Reynolds	Single Stage Subsonic Tip Speed Fan	Single 3 Sensor Hot Wire Probe, Stationary ref. Frame. RN at V_t = 163 fps is 4.2 x 10^5 RN at V_t = 94 fps is 2.4 x 10^5 at Midspan Chord Length	No		9 Camber	No Stator		21.3	0.44
5.	Dring, Joslyn, and Hardin	UTRC's Large Scale Rotating Rig	Single 5 Probe Sensor in Rotating Ref. Frame RN = 5 x 10^5	No	Free Vortex	28 Circular Camber, NACA 65-Series	25		60	0.8
6	Shaw and Balombin	NASA Lewis Anechoic, W.T.	Stationary Cross Film Anemometer	No		15	25	0.54C 1.23C 1.77C	20	0.46
7	Koc, DeRuyck, and Hirsch	VonKarman Inst. Brussels, Belgium	Single Slanted Hot Wire in Rotating Ref. Frame	Yes 33 Blades		25 Camber, NACA 65-(A10)06	No Stator		27.6	0.71
8.	Fleeter, Jay, and Bennett	DDA Single Stage Subsonic Tip Speed Fan	Single Hot Wire Probe in Stationary Ref. Frame	No		42 NACA 65-Series	40 NACA 65-Series	0.24C 0.43C	48.01	0.8
9.	Larguier and Desievers	ONERA Single Stage Rotor	Single Hot Wire Probe in Rotating Ref. Frame	No		20 Conic Section	No Stator		19.69	0.67

Notes

RN = Reynolds Number
V_t = Tip speed, fps
R/S = Rotor/Stator
AR = Aspect Ratio (Span/Chord)
C_D = Drag Coefficient
X = Axial Distance

ORIGINAL PAGE IS
OF POOR QUALITY

Table I. Summary of Rotor Wake Reports (Concluded).

Performance Parameters									Wake Parameters					
Rotor Solidity	Tip Chord (Inches)	AR	V_t (fps)	Incidence Angles, °	Pr	Rotor Inlet Axial Velocity (fps)	Rel. Exit Angle β, °	C_D Info Yes/No	No. of Axial Stations	No. of Span Stations	Mean Velocity Components	Turbulent Velocity Components	Limit X/C Value
0.78			775		1.18		58	No	1	10	Axial and Tangential		1.85C
0.68	6	1	95	0 ,5 10 ,15		5υ	45	Yes	9 (Rotating 9 (Stationary	2 (Rotating 6 (Stationary	3 Comp.	3 Comp.	1.717C
1.28	6.07	1.51	168			89	16	No	6	7	3 Comp.	3 Comp.	0.688C
	6 (Const)	1.00	163 and 94	3 3				No	10	10	3 Comp.	3 Comp.	1.331C
	3.03 Mid-span	1.00	134	4 Loadings			15.5 at Tip	No	4		2 Comp. (No Tangential comp.)	No	1.1C
	3.53	1.77	700		1.2	435		No	3	4	2 Comp. (Streamwise and Upwash)	2 Comp.	1.77C
1.018 at Tip	3.53	1.13						No	1	2	2 Comp.	No	0.34C
1.435	4.589	1.05	184	5 Loadings	1.0125 at Design		42.41	No	3	1 (Mid-span)		No	0.43C
	1.81	1.79	258	1			≈35	No	4	3	Streamwise & Tangential Only	No	4.67C

3.0 EMPIRICAL PREDICTION MODEL FOR ROTOR WAKE AND VORTEX

The measured stator upwash velocity spectrum exhibits tonal and broadband chacteristics. The tonal character of the spectrum can be ascribed to the fluctuating lift due to the periodic incidence of the rotor wake and vortex flow on the stator. The broadband character of the upwash velocity spectrum can be ascribed to the impingement of the turbulence of the rotor exit flow on the stator. The quasi-three-dimensional model of the rotor exit flow field, detailed in this section, employs a streamline-by-streamline approach. It predicts the development of the rotor blade wake and secondary flow phenomena behind the rotor blade row. This in turn yields the stator incident gust and the corresponding tonal content of the stator upwash velocity spectrum, which has a direct bearing on the rotor/stator interaction noise level. An axisymmetric turbulence velocity spectrum model, described briefly in this section, predicts the broadband portion of the stator upwash velocity spectrum.

This section briefly describes the methodology developed to predict the following:

1. The viscous wake mean flow properties; namely, the streamwise variation of the wake centerline velocity defect, the semiwake width, and the tangential wake profile

2. The viscous wake turbulence properties; namely, the streamwise variation of the peak turbulence velocities, and their tangential distribution

3. The secondary flow resulting from tip and hub vortices

4. The stator upwash gust harmonic spectrum and the axisymmetric turbulent velocity spectrum

Volume II of this report, "User's Manual for Computer Program" (NASA CR-174850), gives a detailed description of the evolved computer program, a listing of the program, definitions of input/output parameters, and a sample input/output case.

3.1 VISCOUS WAKE MODEL

For the development of the empirical correlations of the wake center line velocity defect, semiwake width, and turbulent velocities, the extensive data reported in References 2 and 3 were employed. The semiwake width (δ) is defined as the width of the wake at which the velocity defect equals one-half the wake centerline velocity defect (see Figure 1).

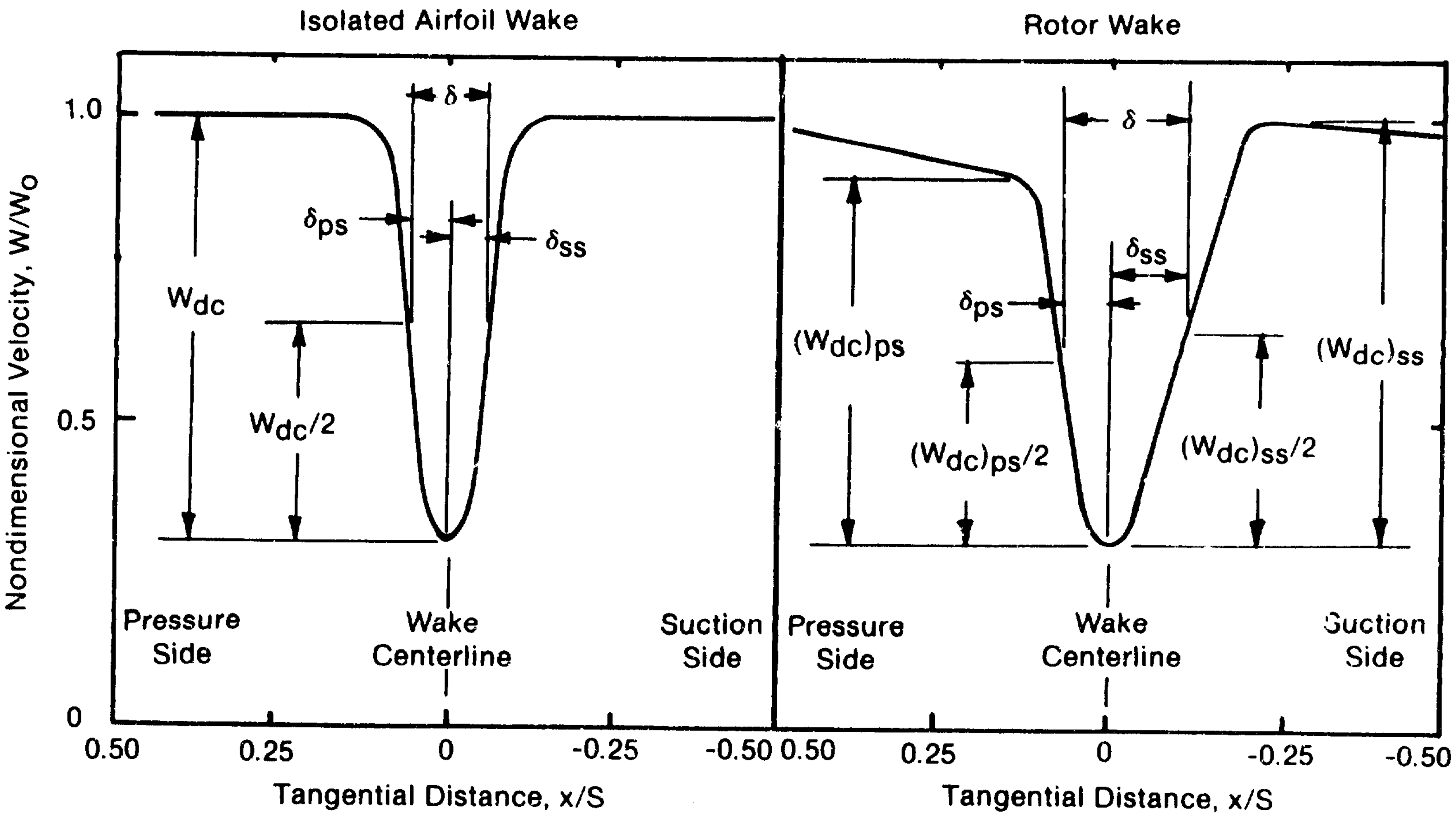

Figure 1. Definition of Wake Velocity Defects and Wake Widths for Isolated Airfoil Wake and Rotor Wake.

3.1.1 Correlation of the Mean Flow Properties

Empirical correlations employed in References 2 and 3 use different expressions for "near-wake" and "far-wake" regions. Regions with streamwise distance/rotor aerodynamic chord (s/c) less than 0.5 have been designated as "near-wake" while those with s/c greater than 0.5 have been designated as "far-wake" regions.

An alternative form of correlation for both the wake centerline velocity defect and semiwake width using linear rational functions was developed during the course of this study. The correlations developed are of the following type:

$$y = \frac{ax + b}{cx + 1} \tag{1}$$

where a, b, and c are empirically determined constants, and y could be

$$\frac{W_{dc}}{W_o} \text{ or } \frac{\delta}{S} \text{ or } \frac{\delta}{c} \text{ and } x = s/c$$

Linear rational functions of the type shown in Equation 1 are essentially infinite series and are ideally suited for monotonically varying data such as wake centerline velocity defect and semiwake width. The advantage of the correlations using linear rational functions over the correlations developed in References 2 and 3 is that only one expression is needed to correlate over the entire region of interest, and it is not necessary to provide a criterion to identify "near-wake" and "far-wake" regions.

The wake decay characteristics of five rotors [see Reynolds(2) Ravindranath(3), Dring(5), Fleeter(8), Larguier(9)], have been studied. These data generally indicate that the higher loadings give larger wake velocity defects. In References 2 and 3, local section drag coefficient, C_D, has been used as a correlating parameter for wake velocity defect and semiwake width for rotors with different loadings. As in the classical similarity solution for a wake behind a two-dimensional isolated body(10), the wake velocity defect and semiwake width for rotor wakes have been proposed to be proportional to $\sqrt{C_D}$ in References 2 and 3. In Reference 2 correlations with $C_D^{1/4}$ were also attempted. The data of References 2 and 3 indicate that the wake velocity defect and the semiwake width for rotors have a weaker dependence on C_D than those of the isolated body. Also, in the case of a rotor, as a result of the merging of the wakes from the adjacent blades, there is an upper limit to the semiwake width of S/2, where S is the blade spacing, irrespective of C_D.

The correlation for the semiwake width (δ) has been developed with both blade spacing (S) and rotor aerodynamic chord (c) as the normalizing dimension since for rotors with low solidity, rotor aerodynamic chord is probably the appropriate characteristic dimension, whereas for rotors with high solidity, blade spacing is probably the appropriate characteristic dimension.

Empirical correlations with different positive fractional of exponents of C_D in the x-coordinate [such as (s/c) $C_D^{1/4}$] and different negative exponents of C_D in the y-coordinate [such as $(\delta/c)/\sqrt{C_D}$] were developed for the data of References 2 and 3, and were compared on the basis of normalized standard deviation, defined as (standard deviation/maximum y-coordinate) x 100. The criterion for the selection of the empirical correlation form was the minimum value of the normalized standard deviation.

Figures 2, 3, and 4 show the curve fits obtained with linear rational functions for (δ/S) versus (s/c), (δ/S) $1/\sqrt{C_D}$ versus (s/c), and δ/S versus (s/c)$C_D^{1/8}$, respectively.

In the case of Figure 2, C_D is not included in the correlation at all. The standard deviation of the curvefit is 0.023375, and the maximum value of the y-coordinate equals 0.4165, yielding a normalized standard deviation of 5.61%. In the case of Figure 3 the C_D exponent is in the y-coordinate. This is the way the wake correlations were developed in References 2 and 3. The $\sqrt{C_D}$ factor was based on the wake analysis of two-dimensional isolated bodies (Reference 10). Now the standard deviation of the curvefit is 0.530131 and the maximum value of the y-coordinate is 3.9836. This yields a normalized standard deviation of 13.36%. In the case of Figure 4, the C_D exponent is in the x-coordinate. The curvefit yields a standard deviation of 0.020405 and the maximum value of the y-coordinate equals 0.4165 (as in Figure 2). This yields a normalized standard deviation of 4.9%. When comparing Figures 2, 3, and 4, it can be noted that the correlation shown in Figure 4 fits the data much better than that shown in Figures 2 and 3.

Figures 5, 6, and 7 show the curve fits obtained with linear rational functions for (δ/c) versus (s/c), (δ/c) $1/\sqrt{C_D}$ versus (s/c), and δ/c versus (s/c) $C_D^{1/8}$, respectively.

As in the case of Figures 2 through 4, the correlation shown in Figure 7 fits the data much better than that shown in Figures 5 and 6. The normalized standard deviation error for Figure 5 is 6.22%. For Figure 6 it is 14.81%, and for Figure 7, 5.69%.

Figure 8 shows the influence of C_D exponent on normalized standard deviation for (δ/c) and (δ/S). One notes that the minimum normalized standard deviation occurs if (δ/S) and (δ/c) are correlated with (s/c) $C_D^{1/8}$. Also, the linear rational function correlations of (δ/S) $1/\sqrt{C_D}$ and (δ/c) $1/\sqrt{C_D}$ with (s/c) yield large errors. For the case of (δ/S) or (δ/c) correlated with (δ/c) $C_D^{1/8}$, at large values of (s/c), the rational function correlation for (δ/c) and (δ/S) will approach a constant value, independent of C_D. This study thus indicates that the semiwake width for rotors depends weakly on C_D. The equations developed for the semiwake width are

ORIGINAL PAGE IS
OF POOR QUALITY

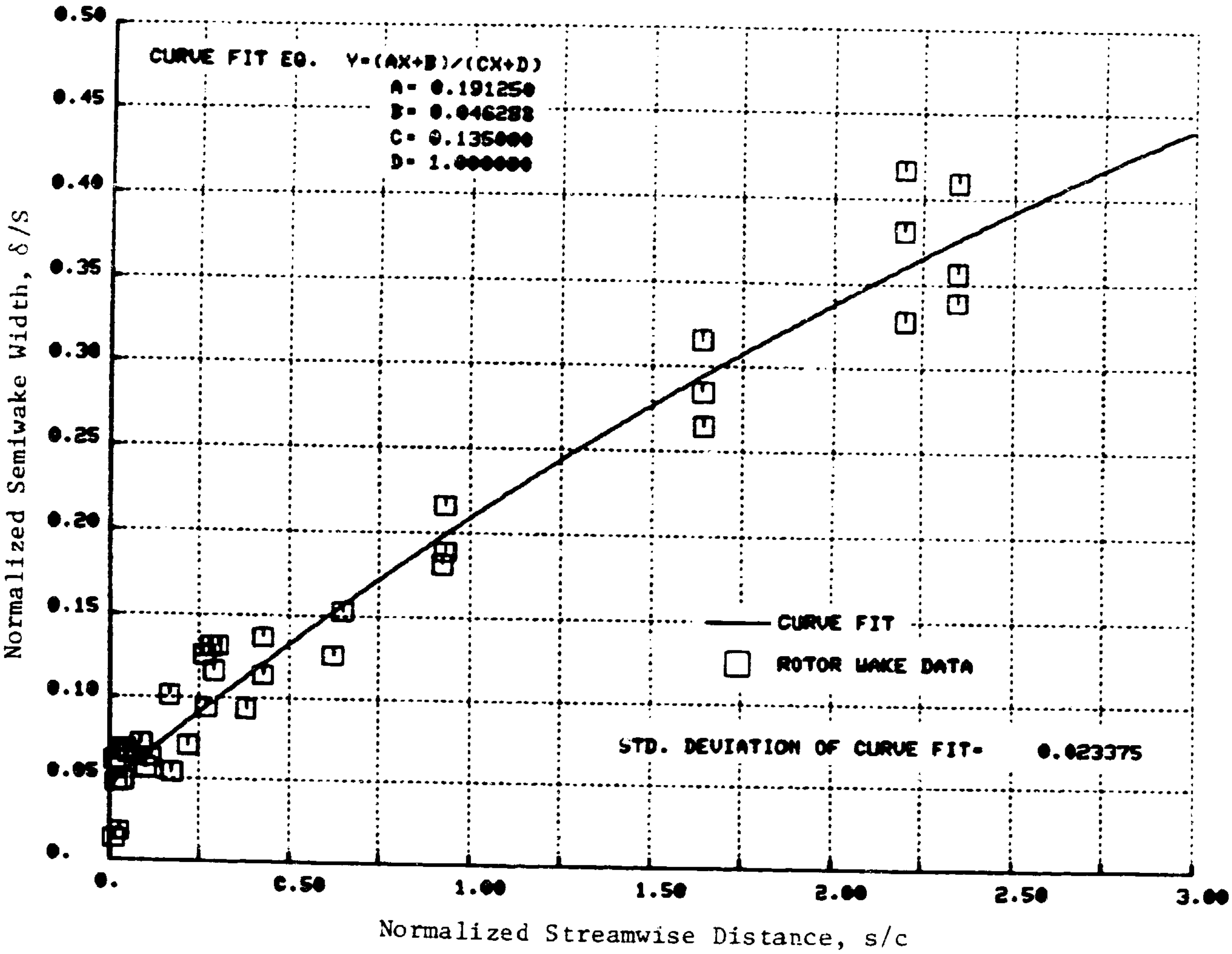

Figure 2. Correlation of δ/S with s/c for Midspan Data of Reynolds (Reference 2) and Ravindranath (Reference 3) Rotors.

ORIG
OF PO

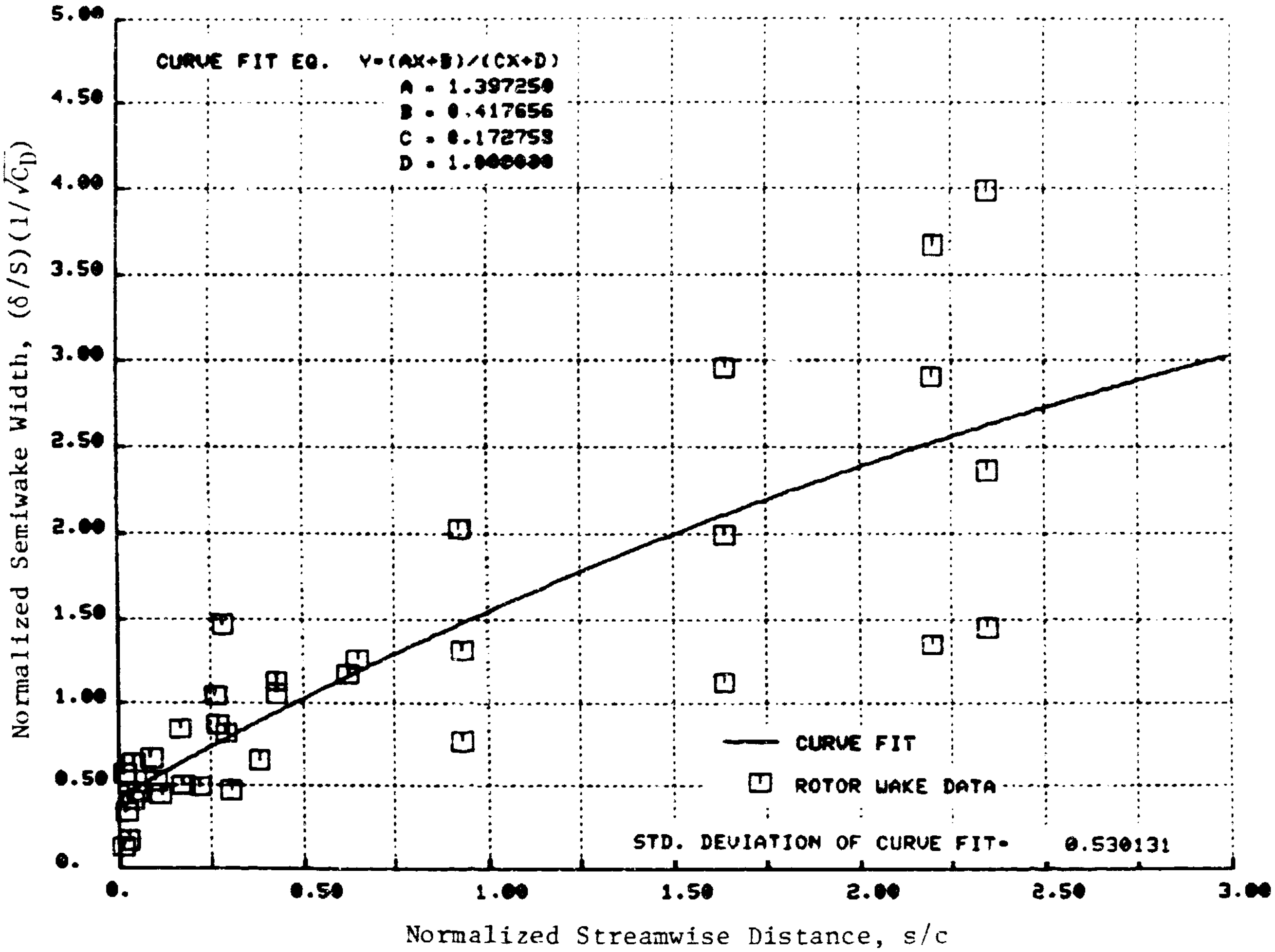

Figure 3. Correlation of $(\delta/S)(1/\sqrt{C_D})$ with s/c for Midspan Data of Reynolds (Reference 2) and Ravindranath (Reference 3) Rotors.

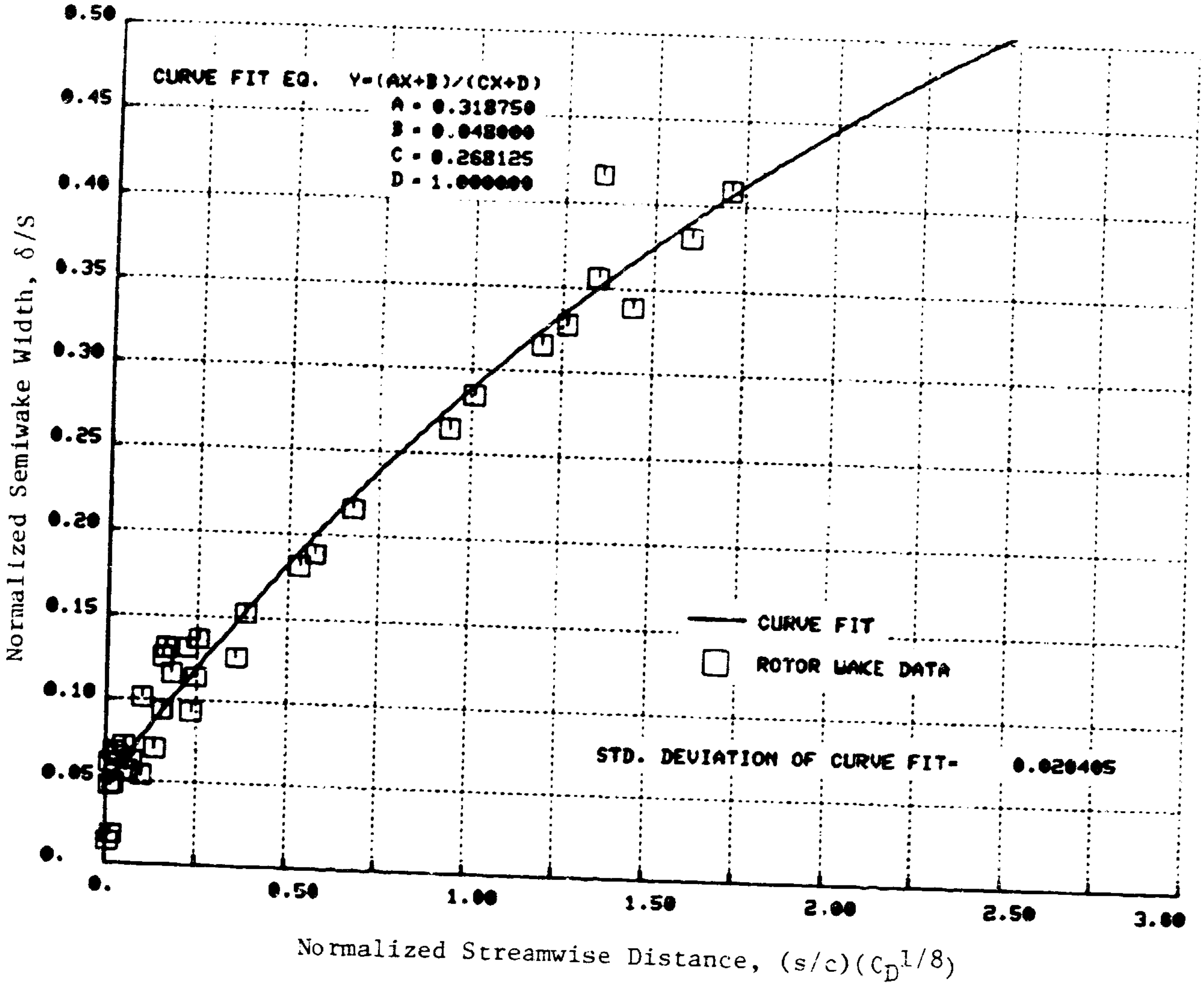

Figure 4. Correlation of δ/S with $(s/c)(C_D{}^{1/8})$ for Midspan Data of Reynolds (Reference 2) and Ravindranath (Reference 3) Rotors.

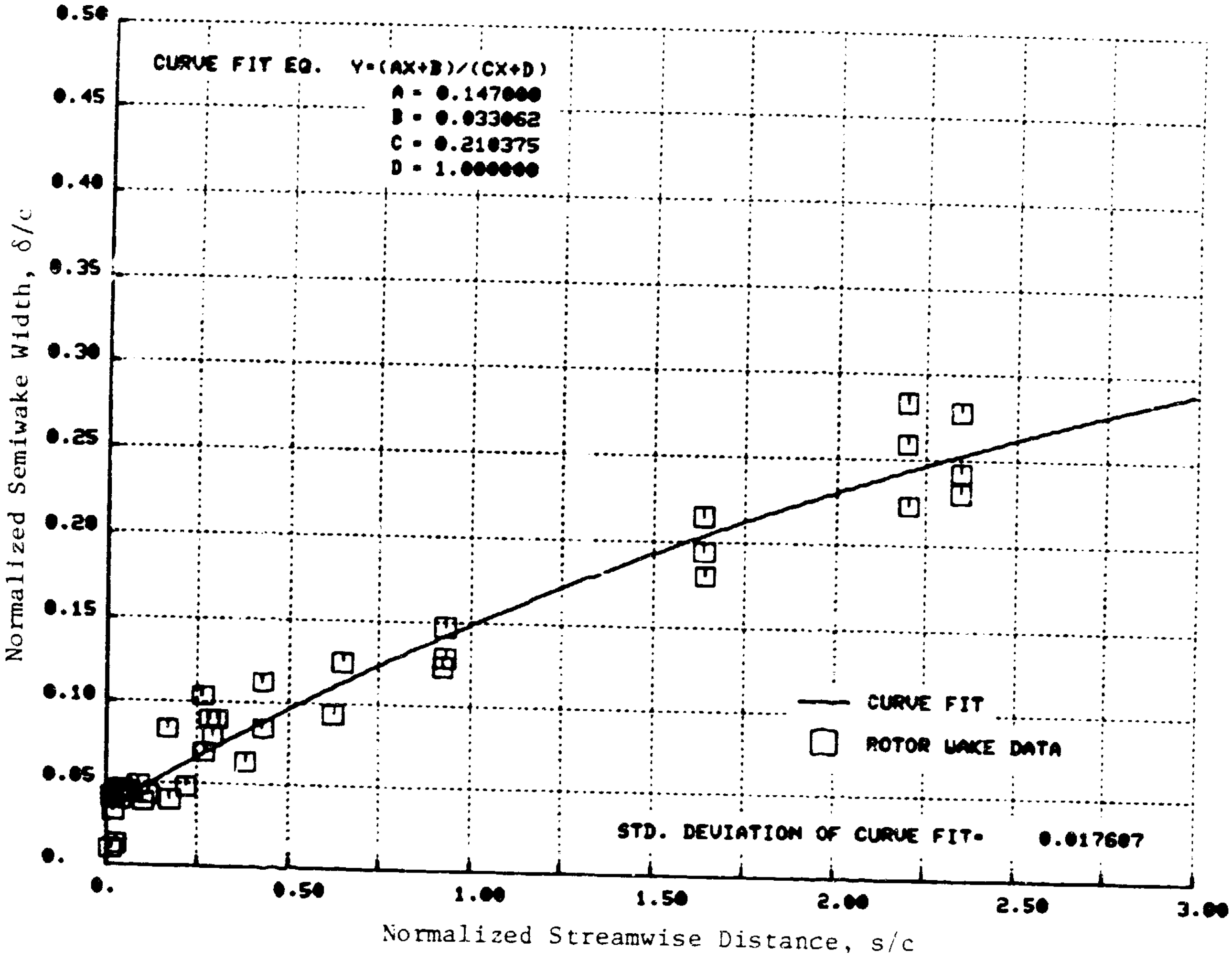

Figure 5. Correlation of δ/c with s/c for Midspan Data of Reynolds (Reference 2) and Ravindranath (Reference 3) Rotors.

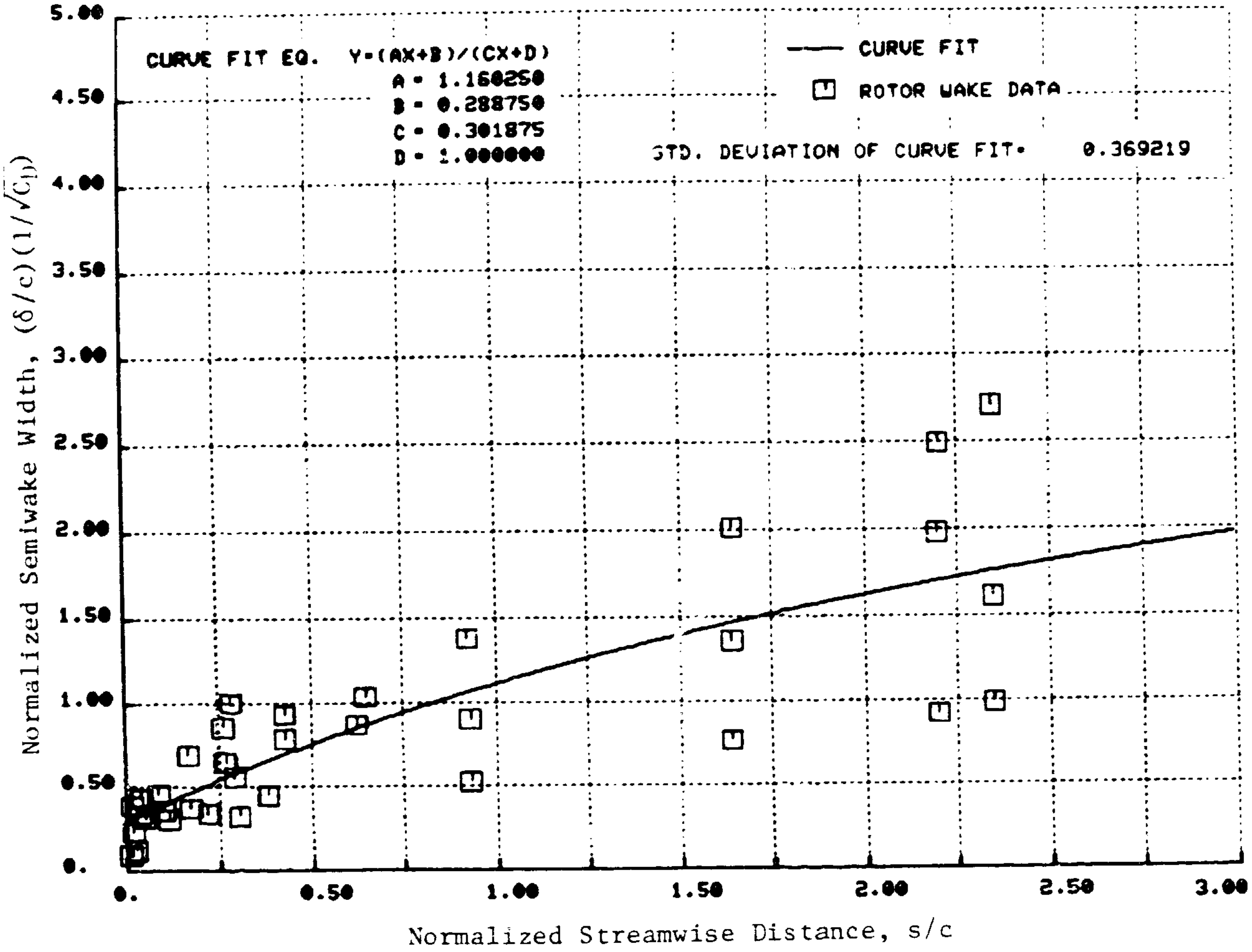

Figure 6. Correlation of $(\delta/c)(1/\sqrt{C_D})$ with s/c for Midspan Data of Reynolds (Reference 2) and Ravindranath (Reference 3) Rotors.

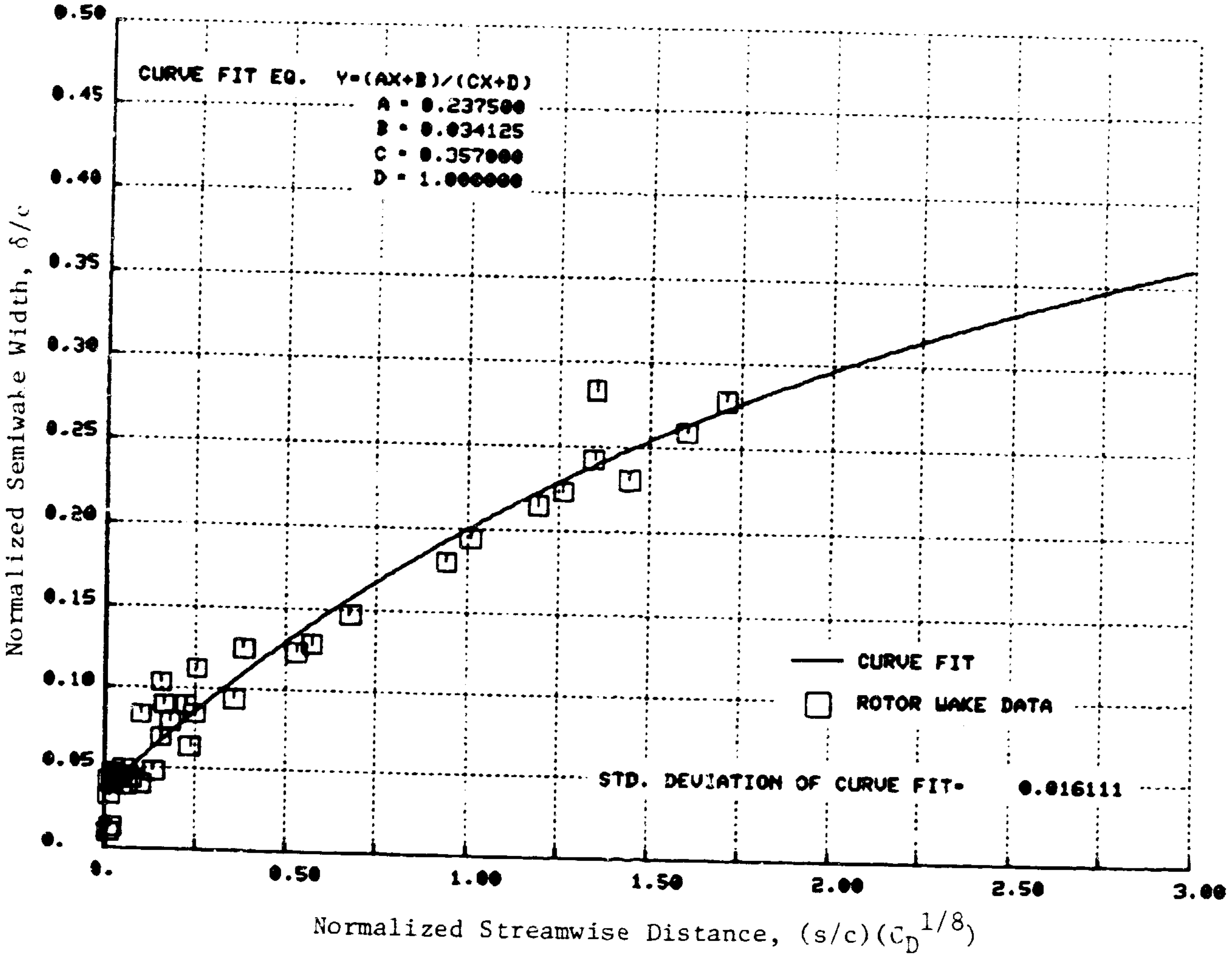

Figure 7. Correlation of δ/c with $(s/c)(C_D^{1/8})$ for Midspan Data of Reynolds (Reference 2) and Ravindranath (Reference 3) Rotors.

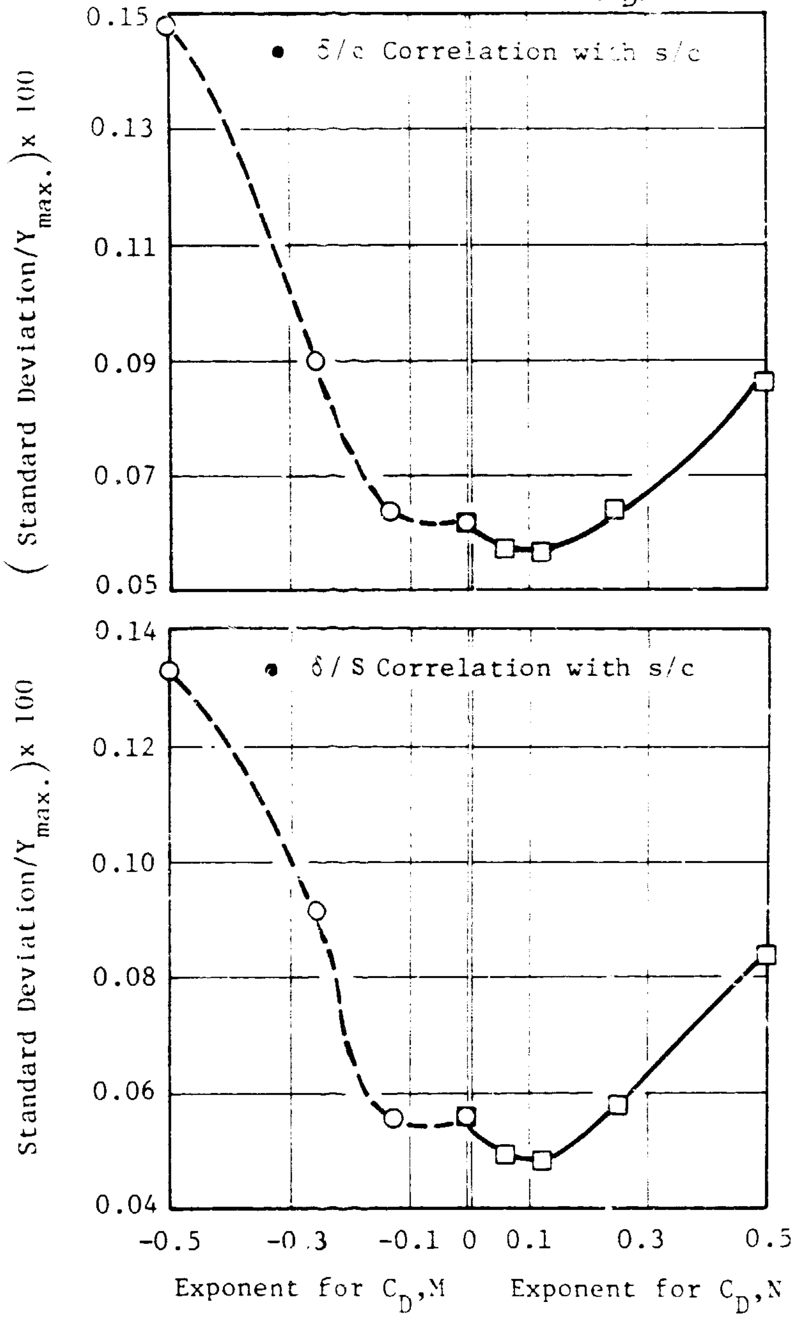

Note: Positive Exponent, N for C_D Refers to $(s/c)(C_D^N)$

Negative Exponent, M for C_D Refers to $(\delta/c)(C_D^M)$ and $(\delta/S)(C_D^M)$

Figure 8. Influence of C_D Exponent on Normalized Standard Deviation for the Semiwake Width Correlation.

$$(\delta/S) = \frac{0.31875\ (s/c)\ C_D^{1/8} + 0.048}{0.268125\ (s/c)\ C_D^{1/8} + 1.0} \tag{2}$$

and

$$(\delta/c) = \frac{0.2375\ (s/c)\ C_D^{1/8} + 0.034125}{0.357\ (s/c)\ C_D^{1/8} + 1.0} \tag{3}$$

where

δ = Semiwake width
c = Rotor aerodynamic chord
S = Blade to blade spacing
s = Streamwise distance from rotor trailing edge
C_D = Section drag coefficient

Since this rotor wake model is essentially aimed at predicting wake characteristics of turbofan rotors whose solidity is normally high ($\sigma_r \geq 1$), Equation 2 is included in the computer program. An upper limit of 0.5 is prescribed for (δ/S), as $(\delta/S) = 0.5$ signifies merging of wakes from adjacent rotor blades.

Similar attempts to correlate the wake centerline defect using different fractional powers of C_D were made. Figures 9, 10, and 11 show the curvefits obtained using linear rational functions for (W_{dc}/W_o) versus (s/c), $(W_{dc}/W_o)\ 1/\sqrt{C_D}$ versus (s/c), and $(W_{dc}/W_o)\left(1/C_D^{1/4}\right)$ versus (s/c), respectively.

The normalized standard deviation error for Figures 9, 10, and 11 are 11.28%, 11.00%, and 10.80% respectively. Figure 12 shows the influence of C_D exponent on normalized standard deviation, showing that the correlation of $(W_{dc}/W_o)\left(1/C_D^{1/4}\right)$ with (s/c) yields the minimum normalized standard deviation. Note, however, that the variation in normalized standard deviation for various C_D exponents is much smaller than for the semiwake width correlations (see Figure 8). The correlation yielding the minimum normalized standard deviation is given by:

$$\left(\frac{W_{dc}}{W_o}\right)\left(\frac{1}{C_D^{1/4}}\right) = \frac{0.3675\ (s/c) + 1.95}{7.65\ (s/c) + 1.0} \tag{4}$$

where

W_{dc} = Wake centerline defect of the total relative velocity

and

W_o = Free-stream total relative velocity.

ORIGINAL PAGE IS
OF POOR QUALITY

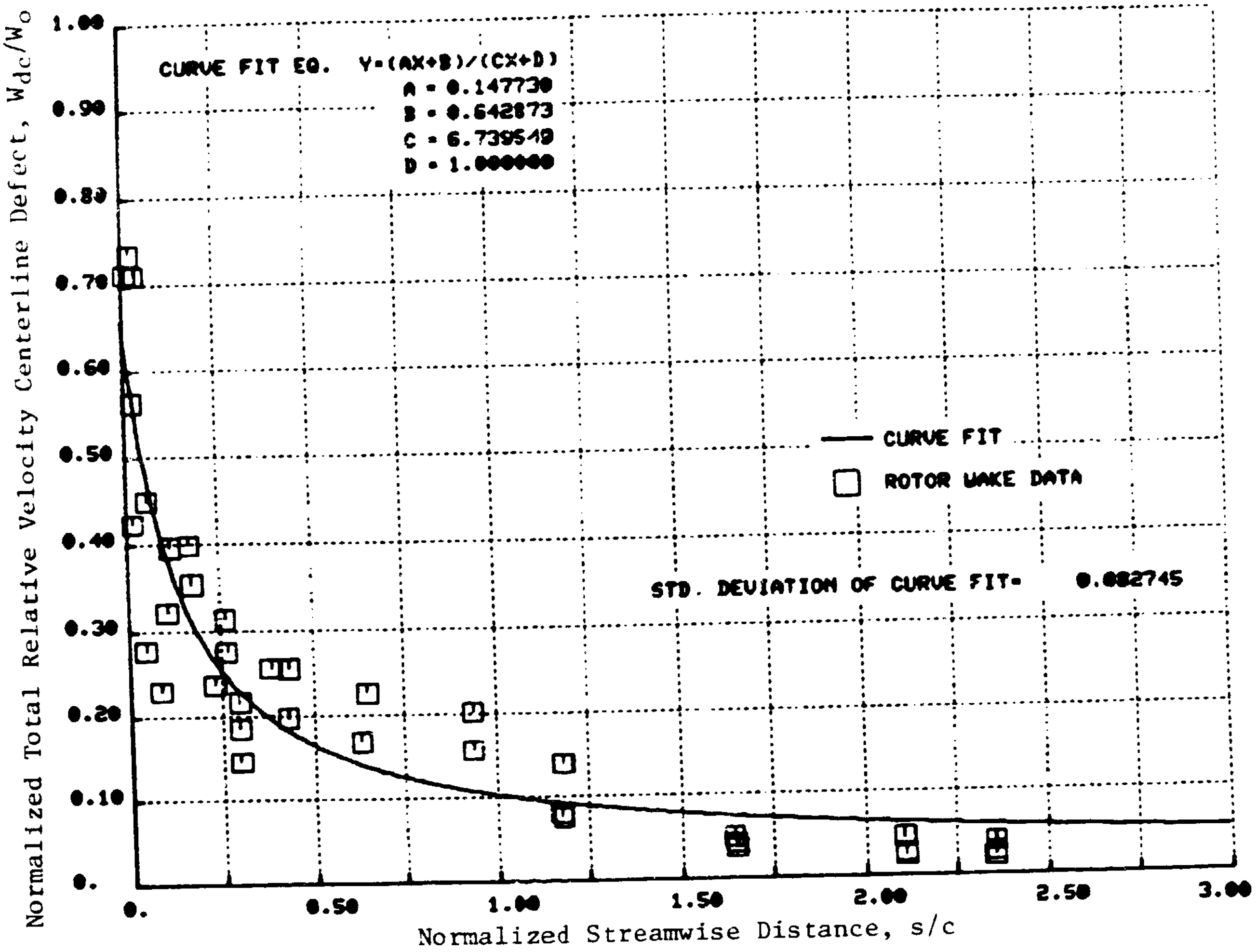

Figure 9. Correlation of W_{dc}/W_o with s/c for Midspan Data of Reynolds (Reference 2) and Ravindranath (Reference 3) Rotors.

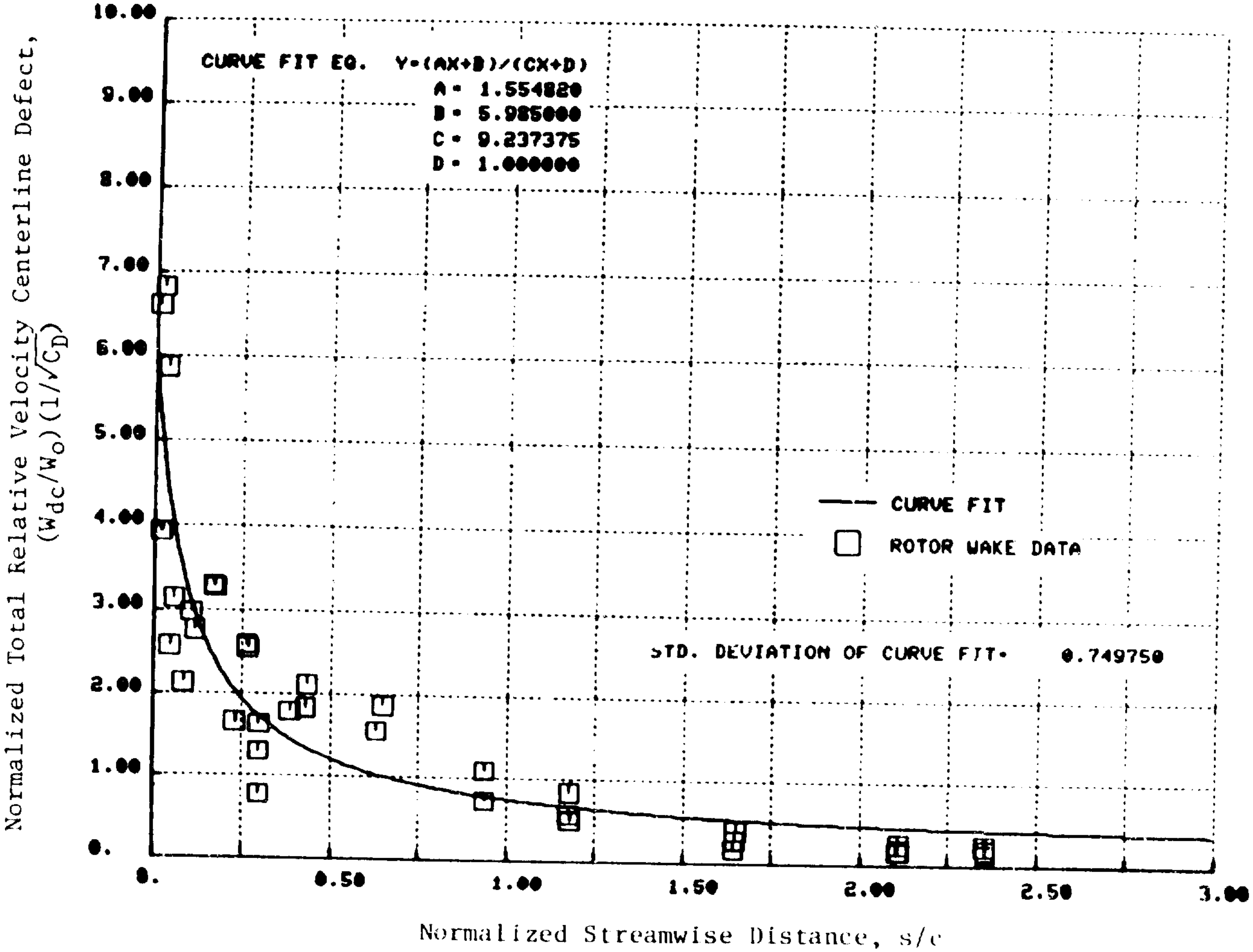

Figure 10. Correlation of $(W_{dc}/W_o)(1/\sqrt{C_D})$ with s/c for Midspan Data of Reynolds (Reference 2) and Ravindranath (Reference 3) Rotors.

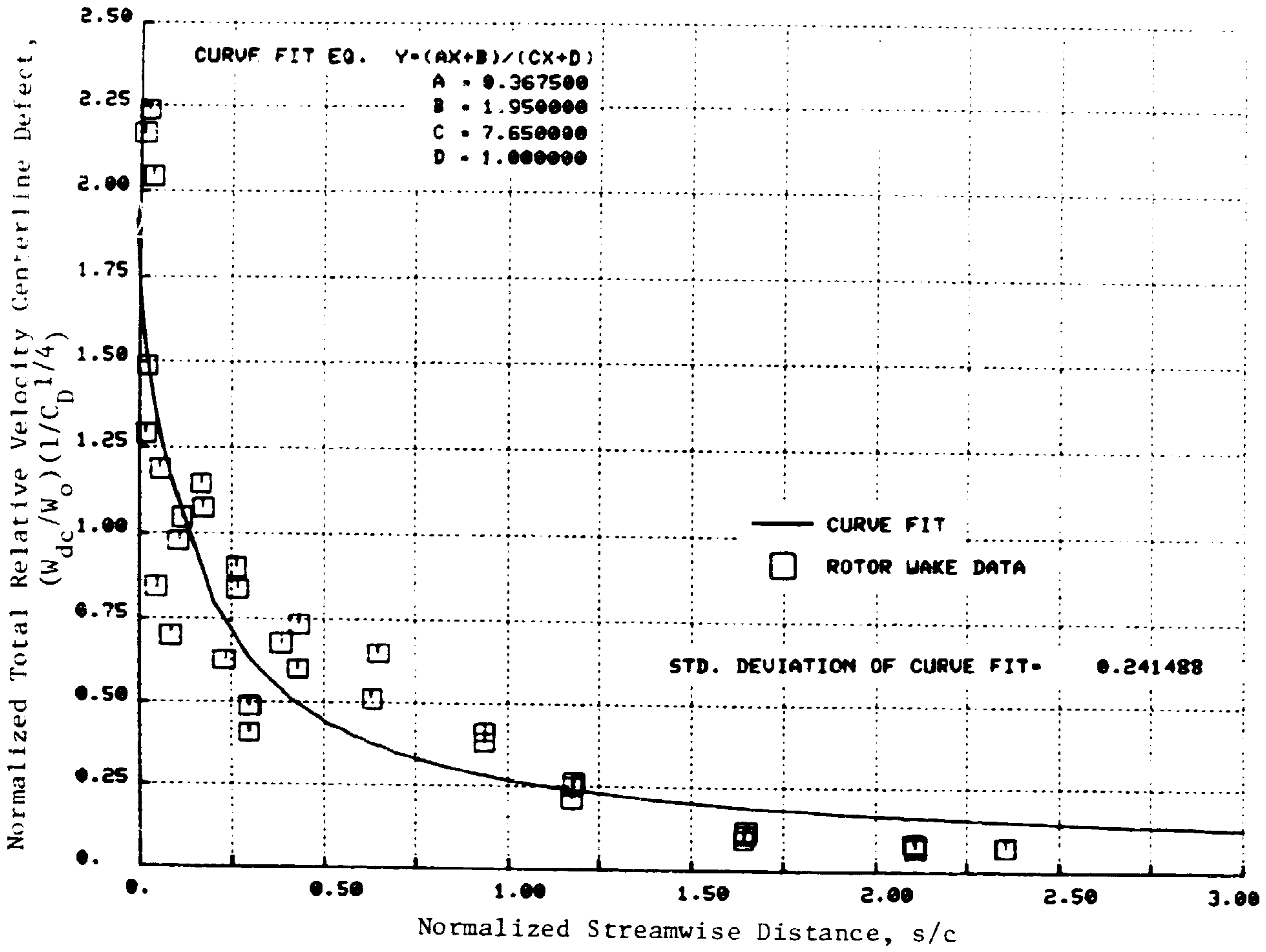

Figure 11. Correlation of $(W_{dc}/W_o)(1/C_D{}^{1/4})$ with s/c for Midspan Data of Reynolds (Reference 2) and Ravindranath (Reference 3) Rotors.

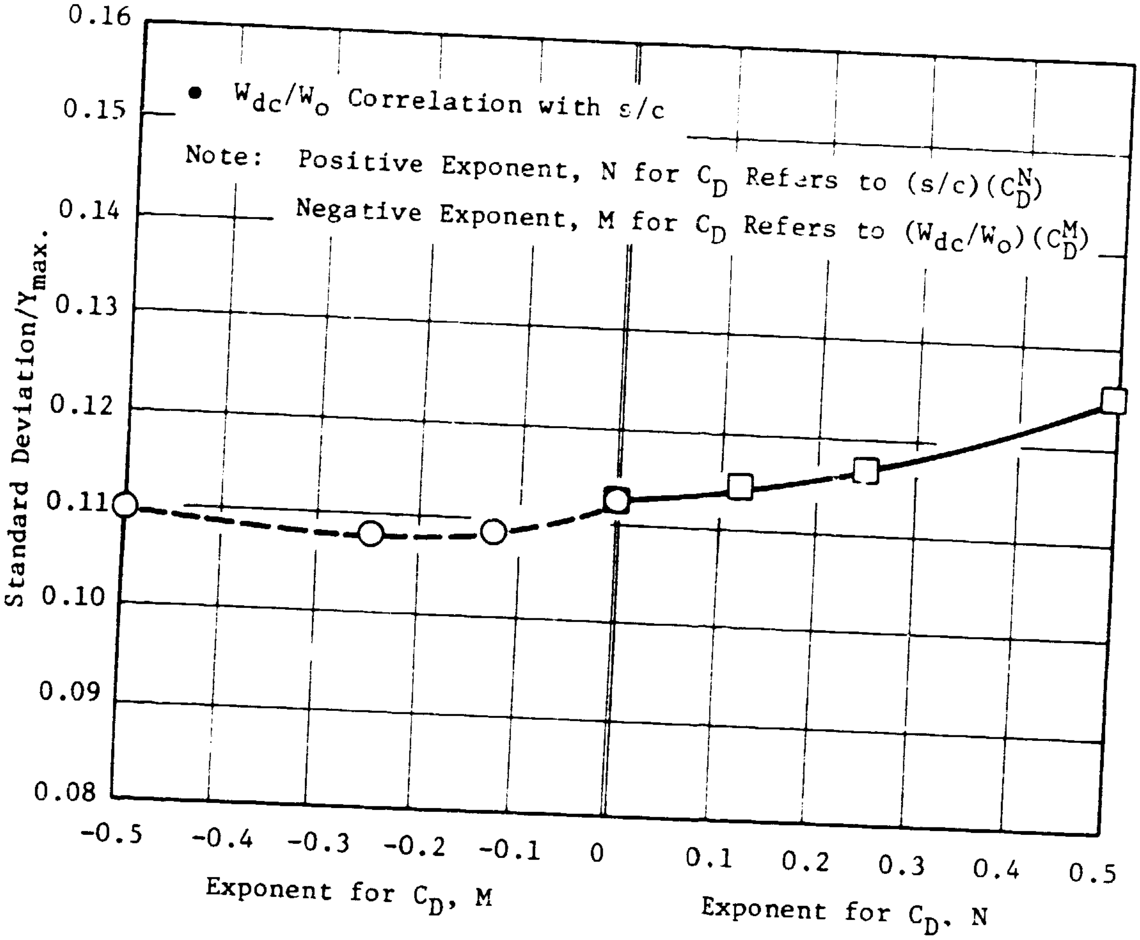

Figure 12. Influence of C_D Exponent on Normalized Standard Deviation for Total Velocity Defect Correlation.

Thus, the velocity defect for rotor wakes is also seen to depend weakly on C_D compared to the velocity defect of wakes of isolated bodies.

The rotor loading manifests itself in terms of different free stream velocities and unequal wake widths on the pressure and suction sides of the rotor blade row (see Figure 1 for a conceptual illustration). References 2 and 3 attempted to study the influence of rotor loading on rotor wakes in terms of the unequal wake widths on the pressure and suction sides of the rotor blade row. Figure 13 shows the variation of the rotor wake asymmetry (in terms of the difference in the wake widths on the pressure and suction sides normalized by the total semiwake width) and the semiwake width with streamwise distance for the data of Reference 3 at four rotor blade incidence angles. Similarly, Figure 14 shows the streamwise variation of the rotor wake asymmetry and the semiwake width for the data of Reference 2. Note that at some streamwise locations the suction side wake width is larger than the pressure side and at some other streamwise locations the pressure side wake width is larger. However, the extent of asymmetry in the wake widths decreases as the streamwise distance increases. This indicates that the difference in the free stream velocity on the pressure and suction side of the rotor blade row may be a more easily discernible effect of rotor loading on wake asymmetry than the distribution of unequal wake widths on either side of the rotor blade.

The (δ/S) dependence on (s/c) in Figures 13 and 14 seems to show different trends. In Figure 13, one is limited to (s/c) values of ≈ 0.6 wherein the near-wake effects are predominant, while in Figure 14, both near- and far-wake effects are evident. However, (δ/S) values at comparable (s/c) locations are about the same.

The wake model developed incorporates a constant inviscid velocity gradient from the suction to the pressure side (see Figure 15). A constant inviscid velocity gradient in the absence of wake represents a linear variation of the velocity from the suction to the pressure side. This, when coupled with the wake model, simulates wake asymmetry on the pressure and suction sides, and the effect of rotor wake asymmetry on the stator gust description can be studied. In principle, the inviscid velocity gradient can be related to the rotor loading. As the rotor loading becomes greater, so does the difference between the free stream velocities on the suction and pressure sides, thereby increasing the inviscid velocity gradient.

Unfortunately an empirical relationship between the rotor loading and the inviscid velocity gradient could not be developed in this program because applicable data were lacking. However, certain parametric studies were conducted (see Subsection 5.2.6) to enable a study of the influence of rotor wake asymmetry. This was accomplished by ascribing a specific value to the inviscid velocity gradient and studying the influence on the stator gust description. In the absence of any other specific information, the streamwise decay of the inviscid velocity gradient is modeled to be the same as that of the wake centerline defect.

Next, using both a Gaussian distribution function and a hyperbolic secant function, the tangential distribution of the velocity defect of rotor wakes

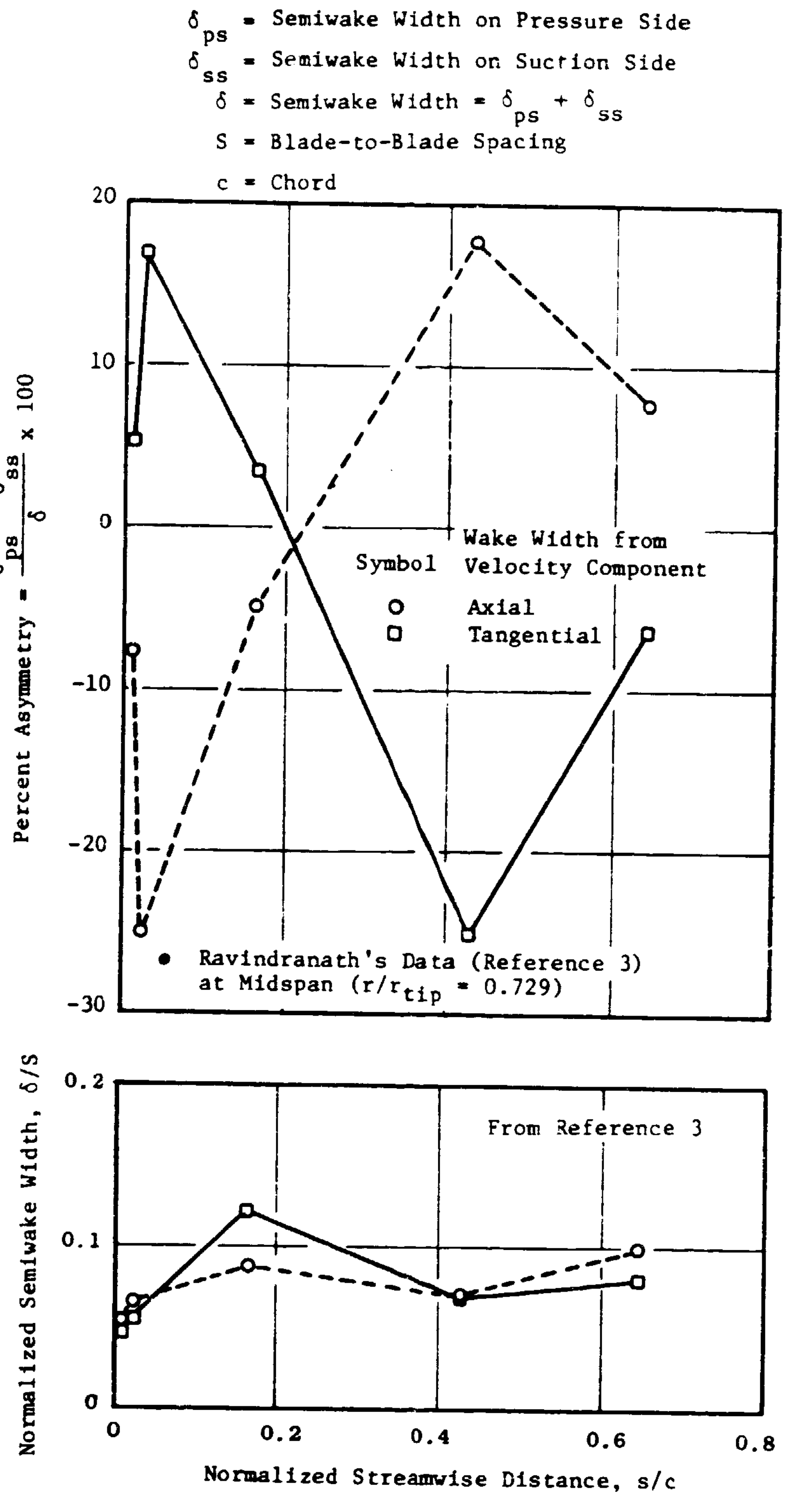

Figure 13. Rotor Wake Asymmetry and Semiwake Width Variation with Streamwise Distance.

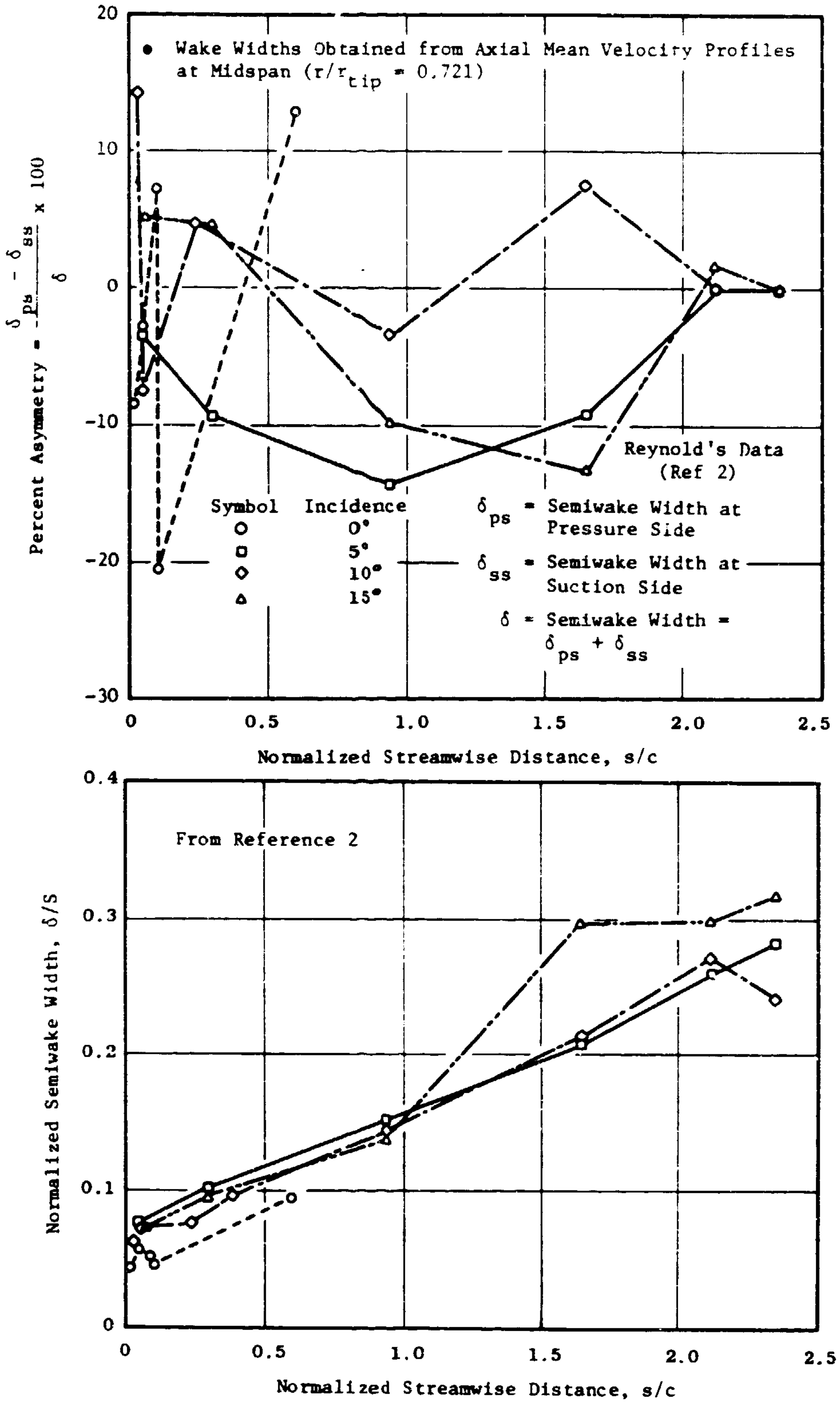

Figure 14. Rotor Wake Asymmetry and Semiwake Width Variation with Streamwise Distance.

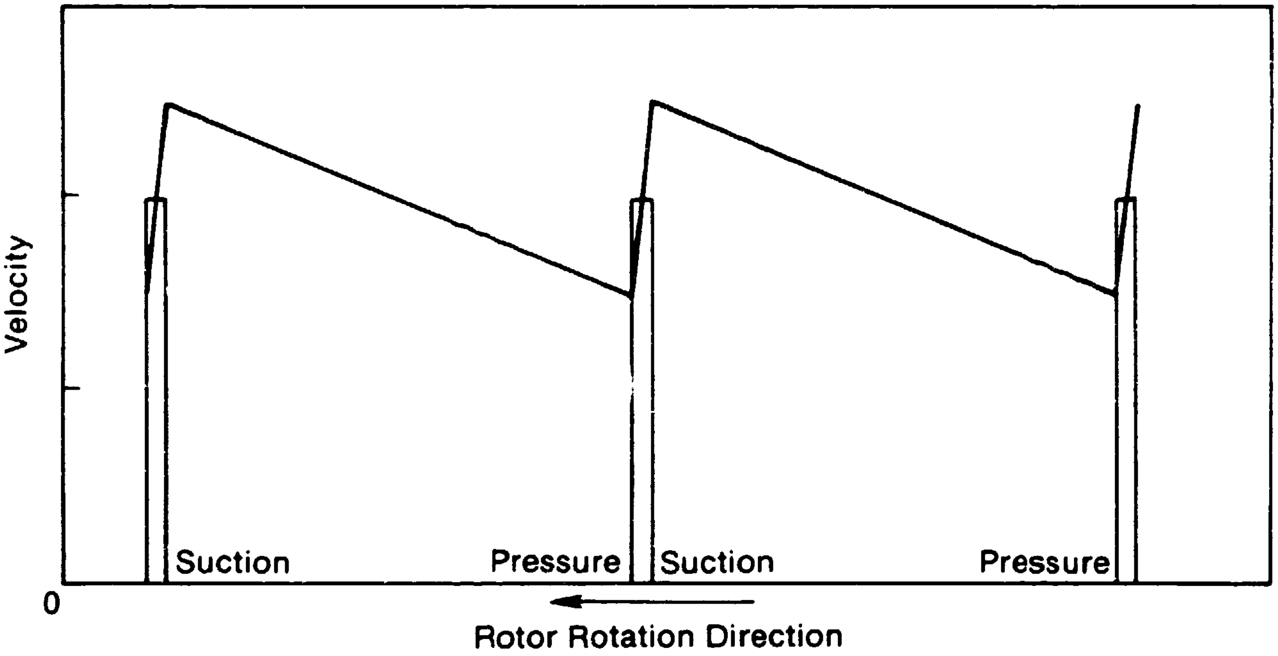

a. Free Stream Velocity Variation Without Wake Defect

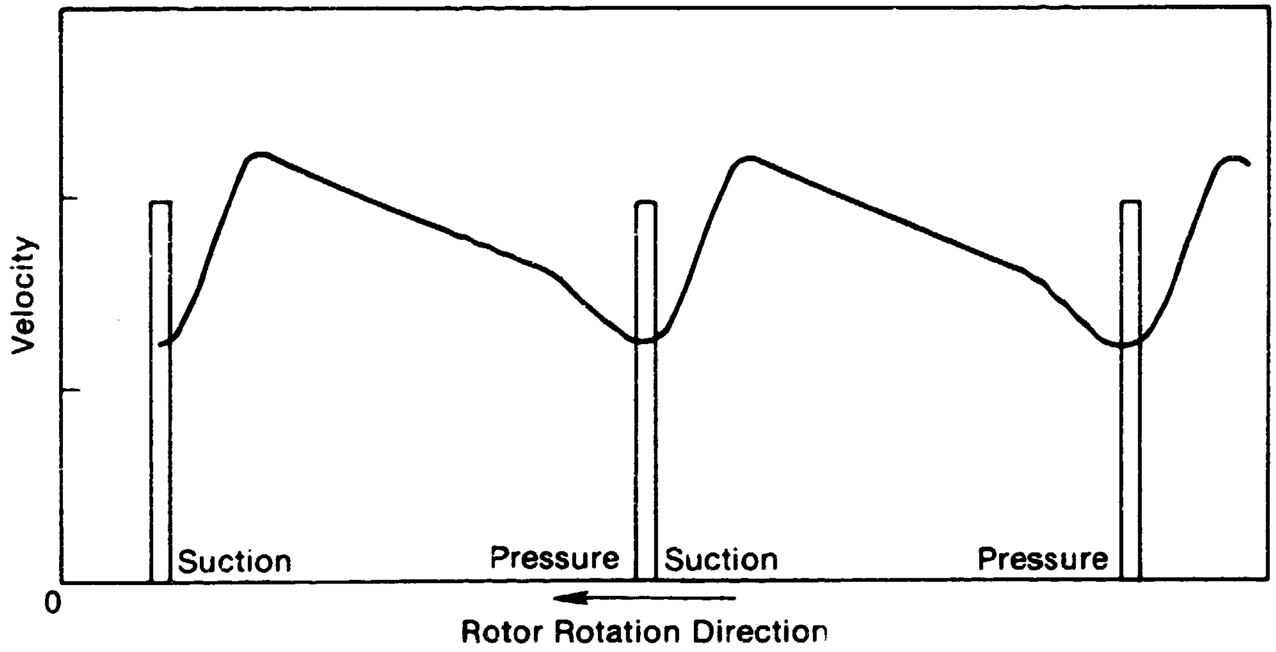

b. Free Stream Velocity Variation With Wake Defect

Figure 15. Schematic of the Effect of a Constant Inviscid Velocity Gradient on the Tangential Distribution of the Free Stream Velocity With and Without Wake Defect.

was correlated. To make a comparative evaluation of the Gaussian distribution function and the hyperbolic secant function, the tangential distribution of the wake defect of axial and tangential velocity components, reported in References 2 and 3 at various operating conditions, was digitized and stored as a data base.

Figure 16 shows the correlation of the tangential distribution of the normalized axial velocity component wake defect data with the Gaussian distribution function, and Figure 17 shows the correlation of the same data with the hyperbolic secant function. The Gaussian distribution function is given by:

$$\frac{u_d}{u_{dc}} = e^{-\ln 2 \times \eta^2} \tag{5}$$

where

u_d = Axial component of the wake defect at y tangential distance away from the wake centerline

u_{dc} = Axial component of the centerline wake defect

η = Normalized tangential distance = $x/(\sigma/2)$

The hyperbolic secant function is given by

$$\frac{u_d}{u_{dc}} = \text{sech}\ (a\eta) \tag{6}$$

where $a = \cosh^{-1}(2) = 1.3169579$

Figure 18 shows the correlation of the tangential distribution of the normalized tangential velocity component wake defect data with the Gaussian distribution function, and Figure 19 shows the correlation of the same data with the hyperbolic secant function.

Note that the standard deviation of the curve fit for the Gaussian function is slightly higher than that obtained with the hyperbolic secant function for the tangential velocity component of the wake defect (see Figures 18 and 19), while the reverse is true for the axial velocity component. Therefore, both tangential wake profile correlations are equally applicable for describing the tangential distribution of the wake defect.

3.1.2 Correlation of the Turbulent Flow Properties

The motive for correlating the rotor wake turbulent velocities is to develop a turbulent velocity spectrum prediction model. The turbulence data reported in References 2 and 3 are in terms of the decay of the peak axial,

ORIGINAL PAGE IS
OF POOR QUALITY

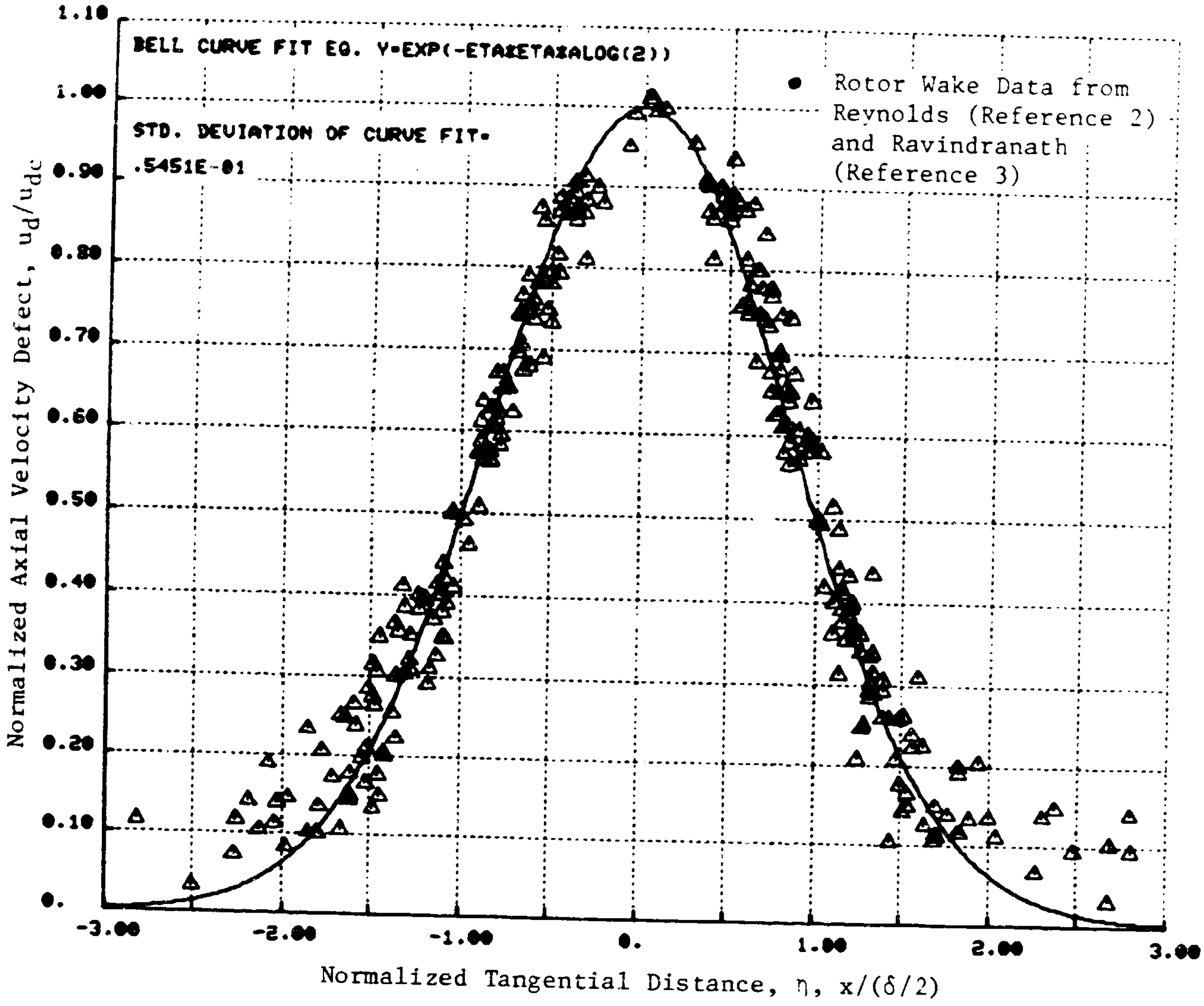

Figure 16. Tangential Distribution of Normalized Axial Velocity Component Wake Defect Correlated with the Gaussian Distribution Function.

ORIGINAL PAGE IS
OF POOR QUALITY

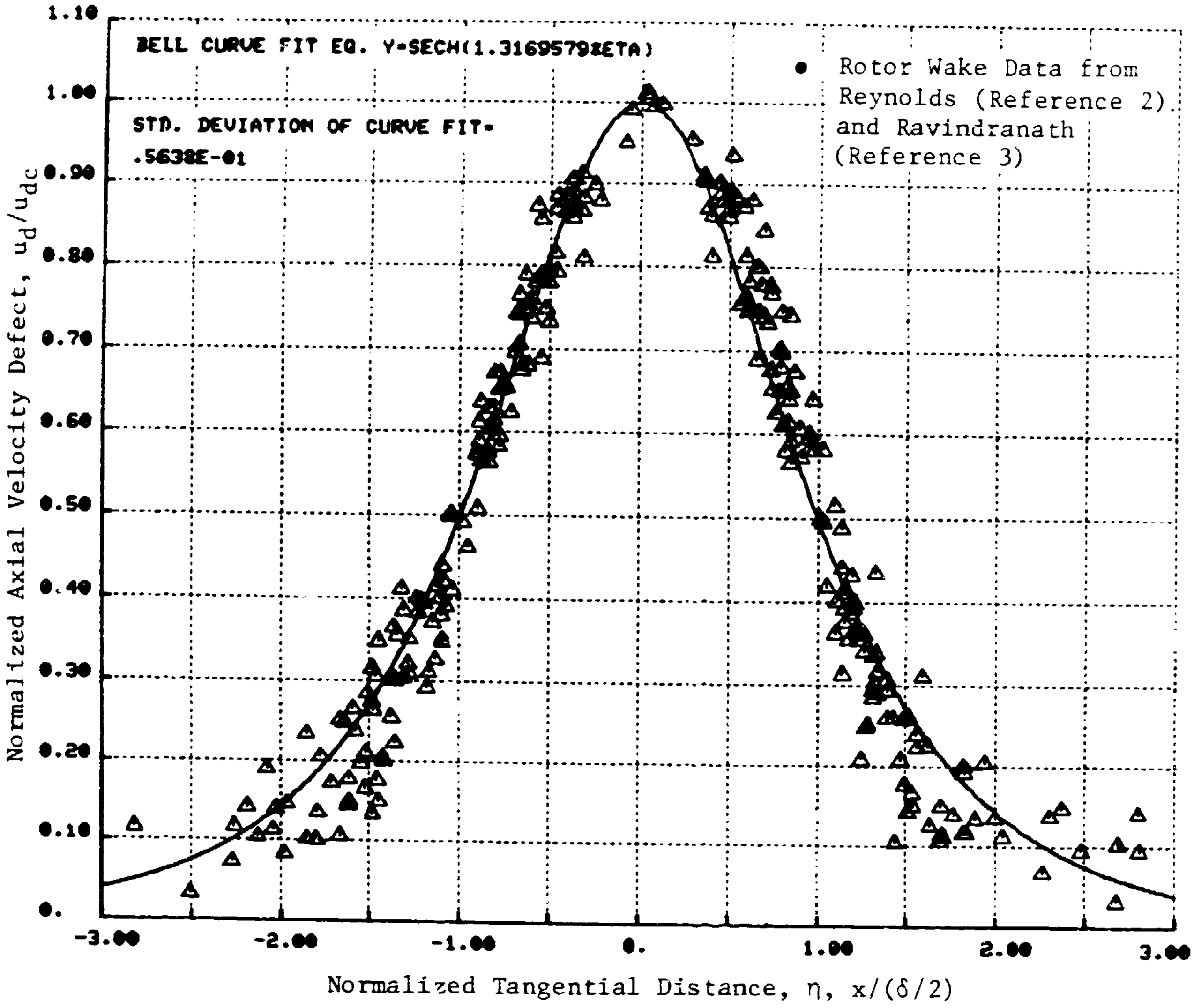

Figure 17. Tangential Distribution of Normalized Axial Velocity Component Wake Defect Correlated with the Hyperbolic Secant Function

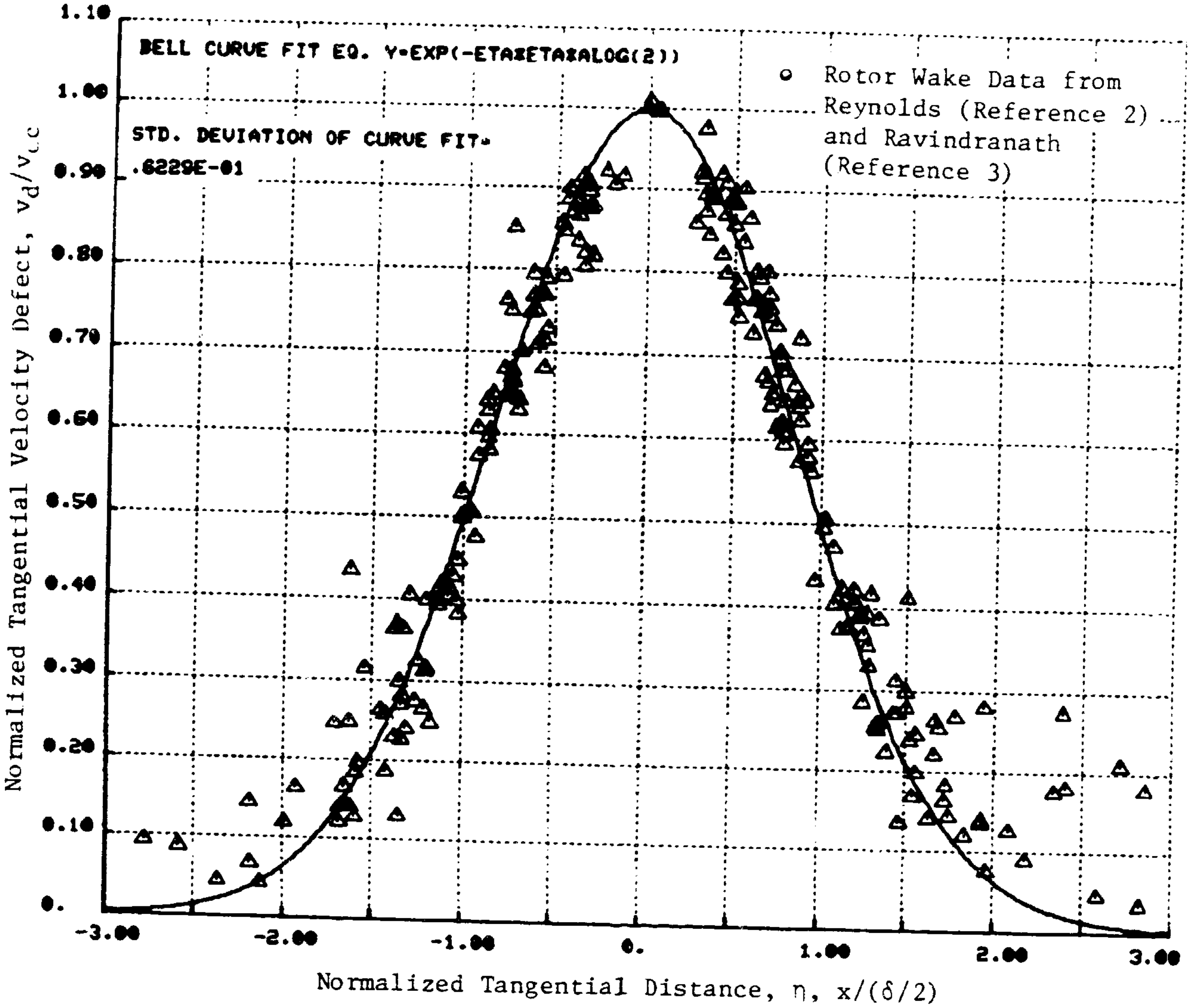

Figure 18. Tangential Distribution of Normalized Tangential Velocity Component Wake Defect Correlated with Gaussian Distribution Function.

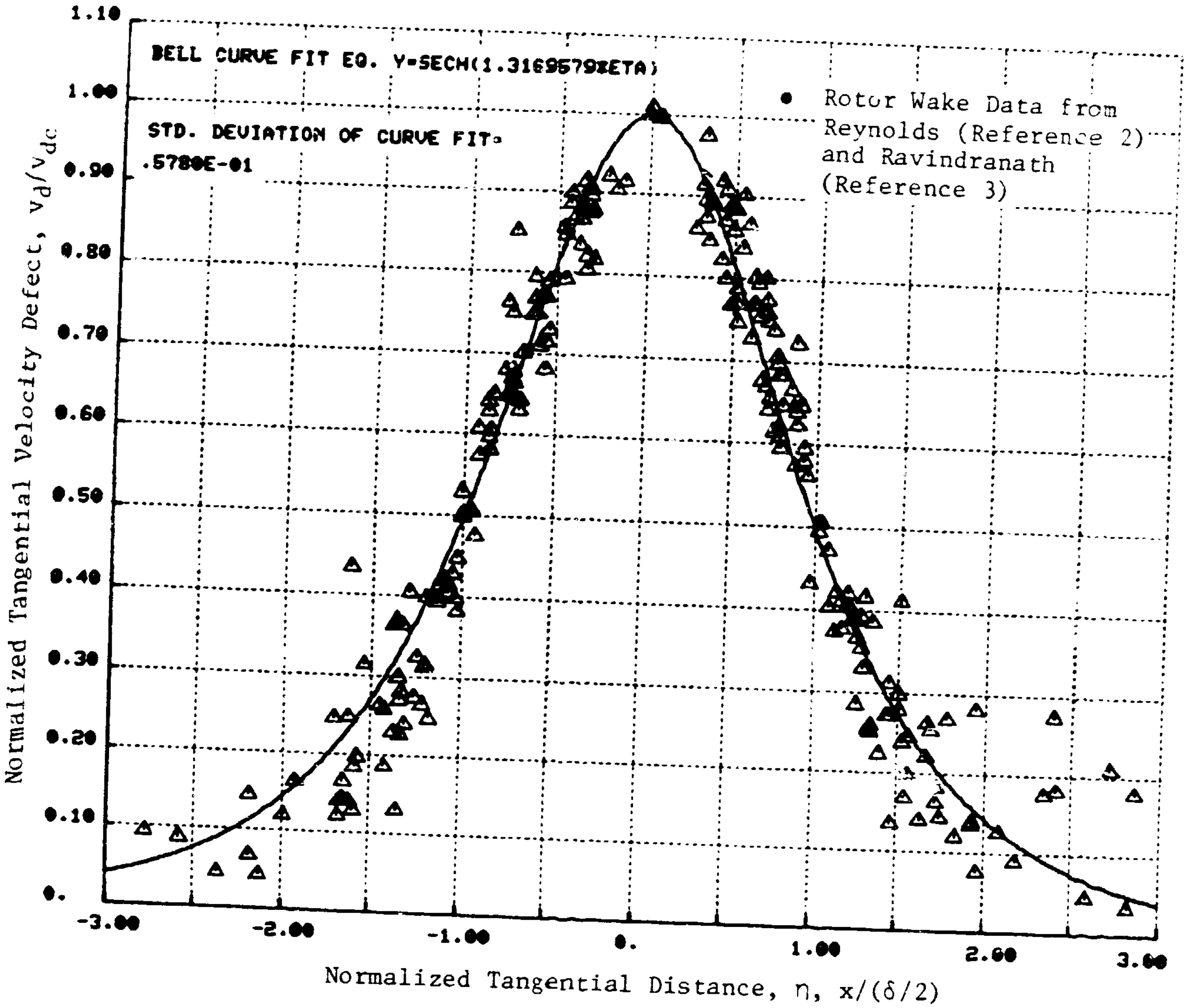

Figure 19. Tangential Distribution of Normalized Tangential Velocity Component Wake Defect Correlated with the Hyperbolic Secant Function.

tangential, and radial turbulent intensities (turbulent velocity/local mean flow velocity). The peak turbulent intensities have been measured at the wake centerline where the mean flow velocity is the lowest. The turbulent velocity spectrum prediction model (to be discussed in Subsection 3.3.2) requires turbulent velocities and not turbulent intensities as input, so the turbulent velocity data of References 2 and 3 were renormalized with respect to a constant free stream velocity (velocity outside the wake region). For example, for axial turbulent velocity, u',

$$\begin{aligned} \frac{u'}{W_o} &= \frac{u'}{W_c} \times \frac{W_c}{W_o} \\ &= \frac{u'}{W_c} \times \left(\frac{W_o - W_{dc}}{W_o}\right) \qquad (7) \\ &= \frac{u'}{W_c} \times \left[1 - \frac{W_{dc}}{W_o}\right] \end{aligned}$$

where,

u' = Axial turbulent velocity at wake centerline

W_c = Total relative velocity at wake centerline

The first term on the right-hand side of Equation 7 is the axial turbulent intensity reported in References 2 and 3. By using the correlation for the streamwise decay of the wake centerline velocity defect (see Equation 4) and the reported data on wake centerline turbulent intensity decay in the streamwise direction (References 2 and 3), the variation of the axial, tangential, and radial turbulent velocities normalized by the free stream total relative velocity at the wake centerline in the streamwise direction was obtained. Examination of the renormalized turbulent velocity data (see Figure 20) reveals that the axial and tangential turbulent velocity values are about the same, whereas the radial turbulent velocity values are higher. Thus, the axial and tangential turbulent velocities are correlated with one expression and the radial turbulent velocity is correlated with another expression.

Linear rational function correlations were developed for the turbulent velocities, as in the case of wake centerline velocity defect data (see Subsection 3.1.1), with different positive powers of C_D in the x-coordinate [for example, $(s/c)C_D^{1.5}$] and different negative powers of C_D in the y-coordinate [for example, $(w'/W_o)(1/C_D^{0.5})$]. These correlations were compared on the basis of normalized standard deviation, defined as (standard deviation/maximum y-coordinate) x 100. Figure 21 shows the influence of the C_D exponent on the normalized standard deviation for the combined axial and tangential turbulent velocity correlation and Figure 22 shows the influence of the C_D exponent on

OF POOR QUALITY

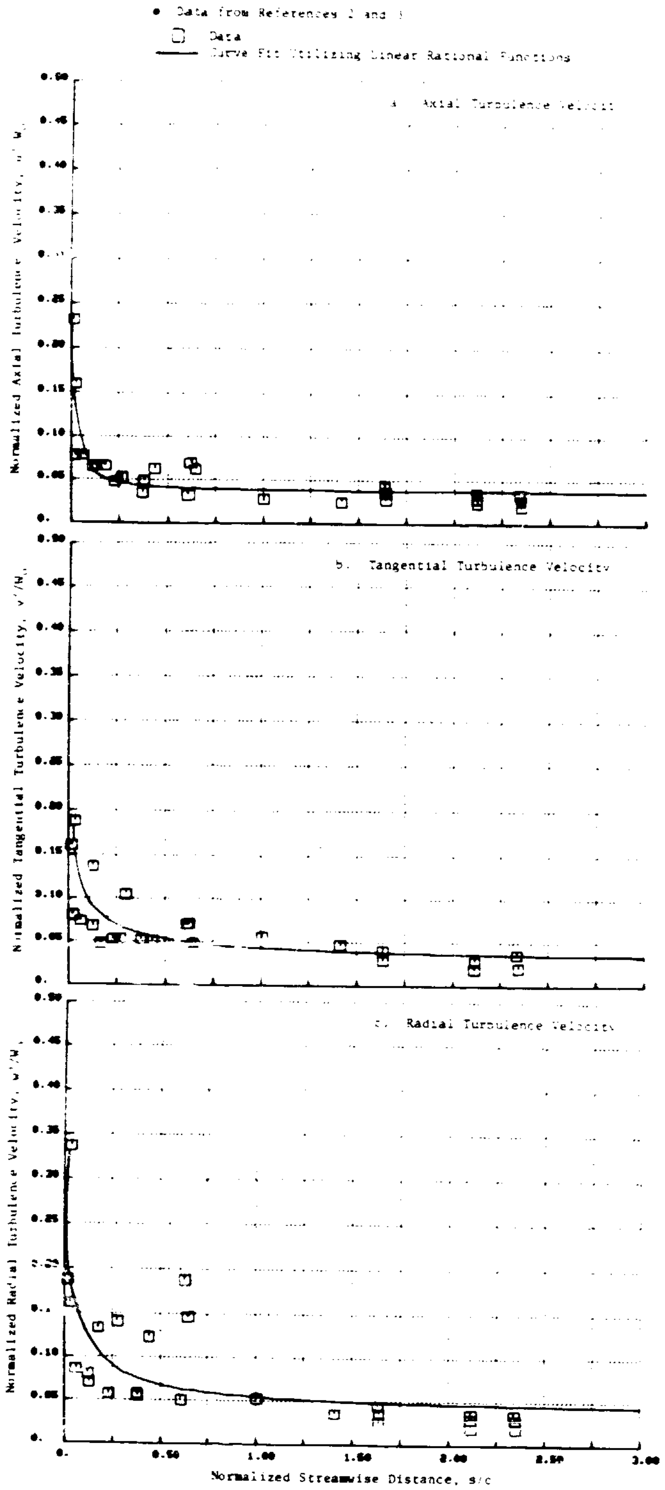

Figure 20. Streamwise Variation of the Measured Axial, Tangential and Radial Turbulent Velocities Normalized by the Freestream Total Relative Velocity.

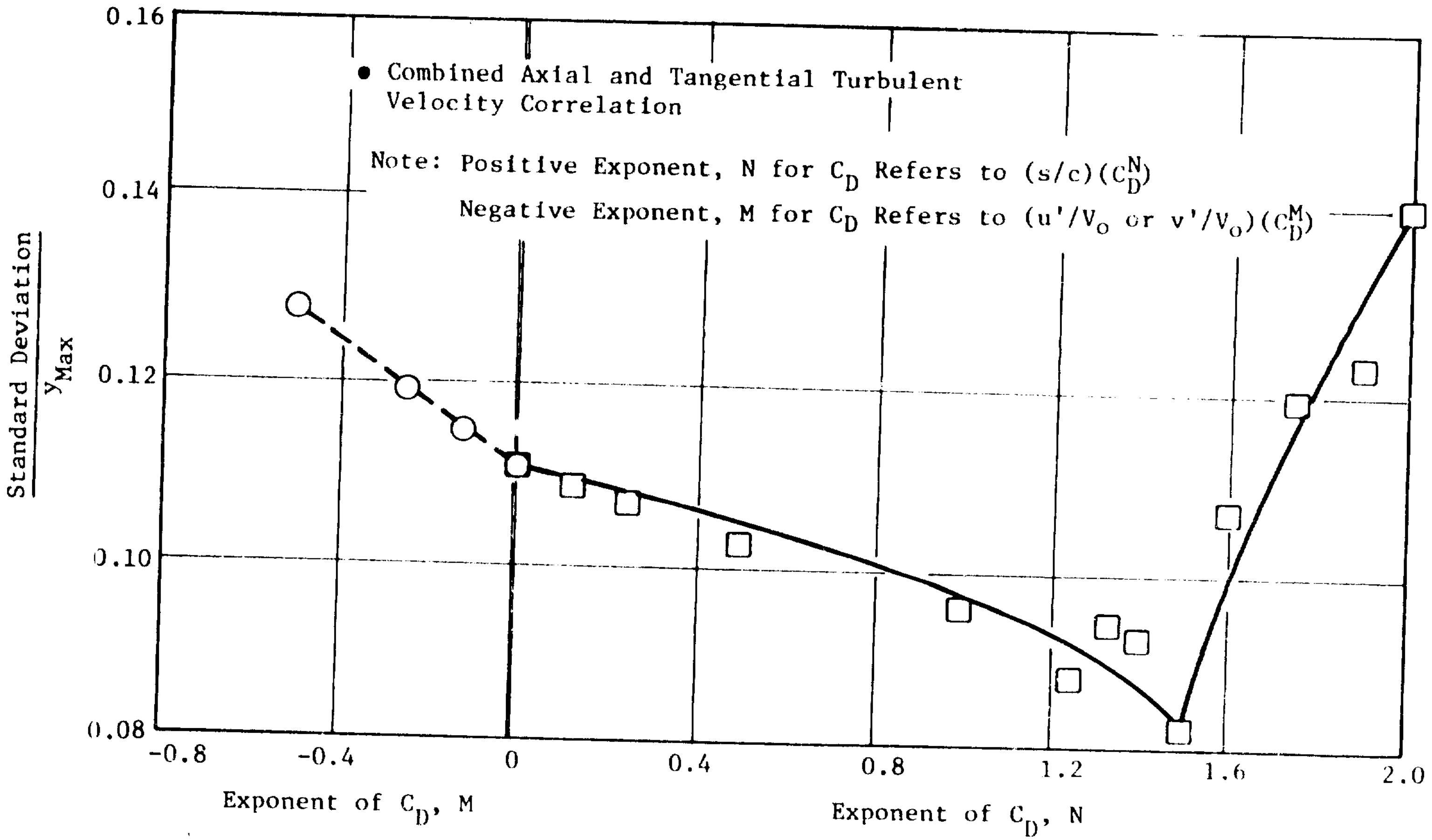

Figure 21. Influence of C_D Exponent on Normalized Standard Deviation for Combined Axial and Tangential Turbulent Velocity Correlation.

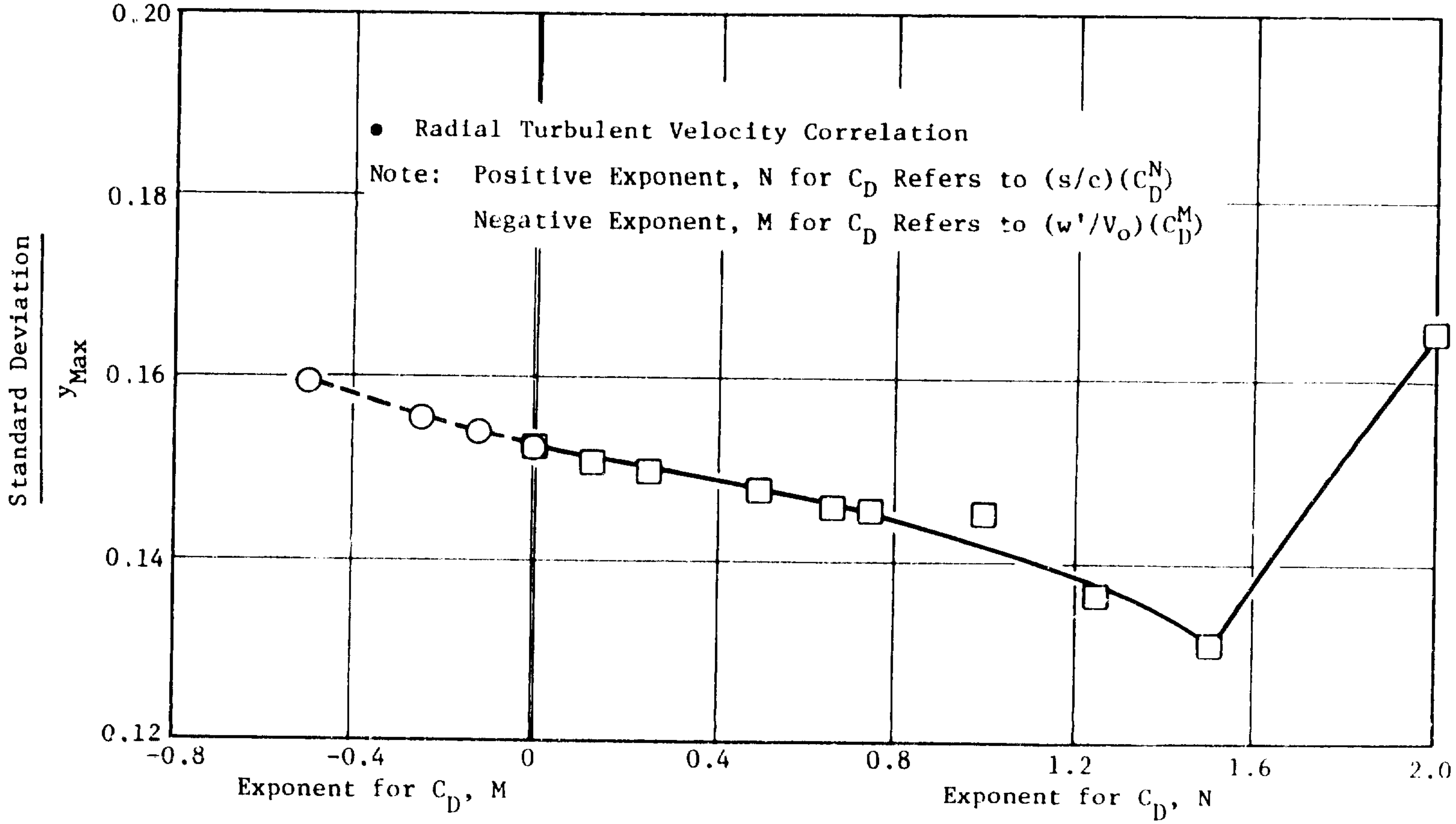

Figure 22. Influence of C_D Exponent on Normalized Standard Deviation for Radial Turbulent Velocity Correlation.

the normalized standard deviation for the radial turbulent velocity correlation. The minumum normalized standard deviation occurs when (u'/W_o), (v'/W_o), and (w'/W_o) are correlated with $(s/c)C_D^{1.5}$. The linear rational function correlation corresponding to the minimum normalized standard deviation for (u'/W_o) or (v'/W_o) is given by

$$\begin{matrix}(u'/W_o)\\ \text{or}\\ (v'/W_o)\end{matrix} = \frac{425.0 * s/c * C_D^{1.5} + 0.18}{12500 * s/c * C_D^{1.5} + 1.0} \qquad (8)$$

Figure 23 shows the good collapse of the axial and tangential turbulent velocity data for the above correlation. The linear rational function correlation corresponding to the minimum normalized standard deviation for (w'/W_o) is given by:

$$\frac{w'}{W_o} = \frac{345.0 * s/c * C_D^{1.5} + 0.264}{8625.0 * s/c * C_D^{1.5} + 1.0} \qquad (9)$$

Figure 24 shows the good collapse of the radial turbulent velocity data for the above correlation.

The extent of anisotropy of the turbulent velocity scales in the rotor wake can be estimated by comparing the radial turbulent velocity variation in the streamwise direction to that of either axial or tangential turbulent velocity variation using Equations 8 and 9. Figure 25 shows the streamwise variation of the ratio of radial turbulent velocity to either axial or tangential turbulent velocity. The anisotropy is high near the rotor trailing edge and decreases as the streamwise distance from the rotor trailing edge increases. However, even at large streamwise distance from the rotor trailing edge, a residual anisotropy exists.

The tangential distribution of the normalized turbulent velocity is significantly different from that of the turbulent intensity, since the normalized turbulent velocity is obtained by dividing the turbulent velocity by the constant free stream velocity, whereas the turbulent intensity is obtained by dividing the turbulent velocity by the local velocity. Reynolds (Reference 2) and Ravindranath (Reference 3) have shown that the axial, tangential, and radial turbulent intensity components normalized suitably (see below) exhibit a Gaussian tangential distribution. For example, consider the tangential distribution of the axial turbulent intensity. Reynolds and Ravindranath showed that:

$$\frac{\tau_x - \tau_{x,o}}{(\tau_x)_c - \tau_{x,o}} = e^{-\ln 2\eta^2} \qquad (10)$$

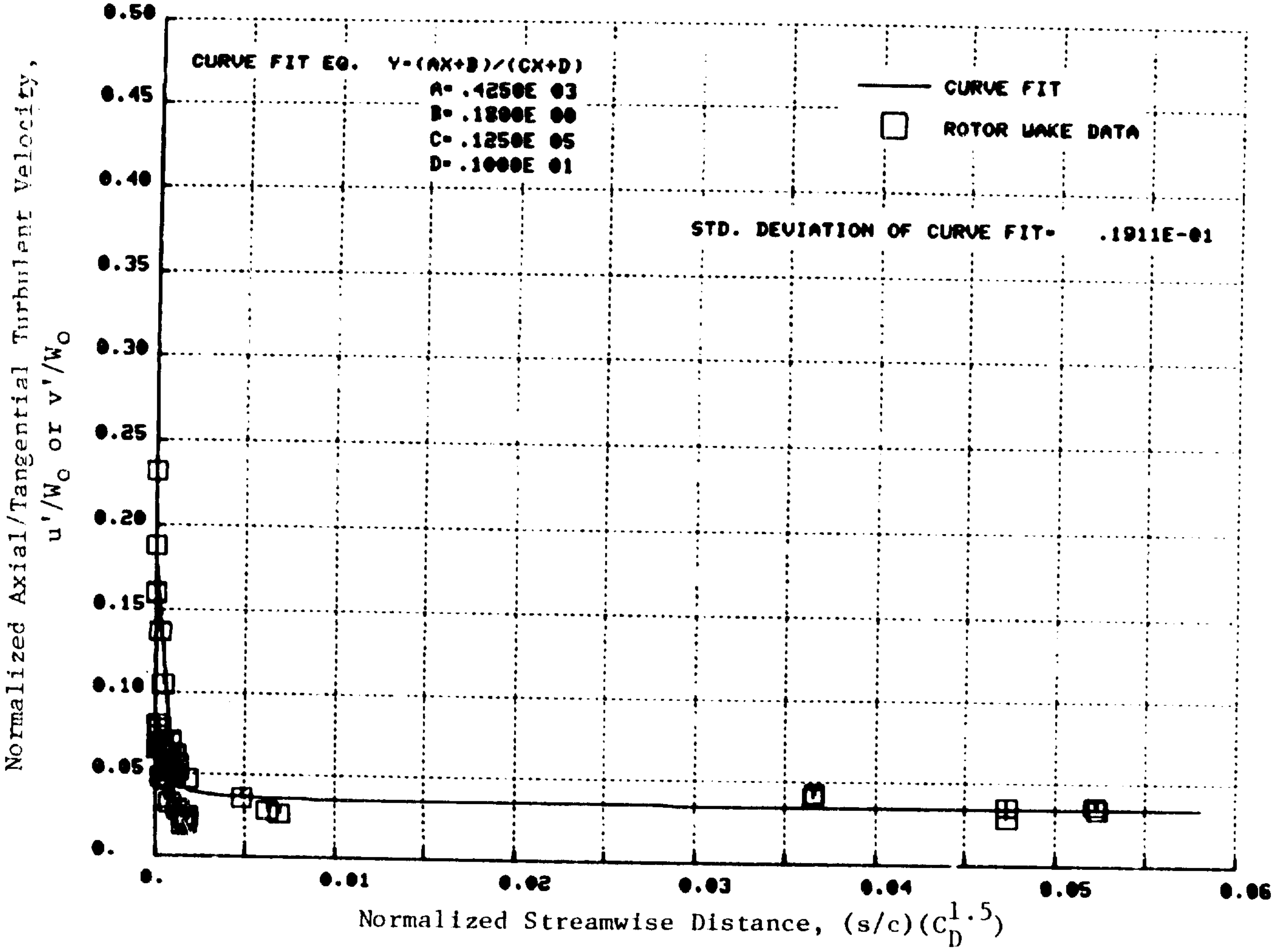

Figure 23. Correlation for Normalized Axial or Tangential Turbulent Velocities for Midspan Location for Reynolds (Reference 2) and Ravindranath (Reference 3) Rotor Wake Data.

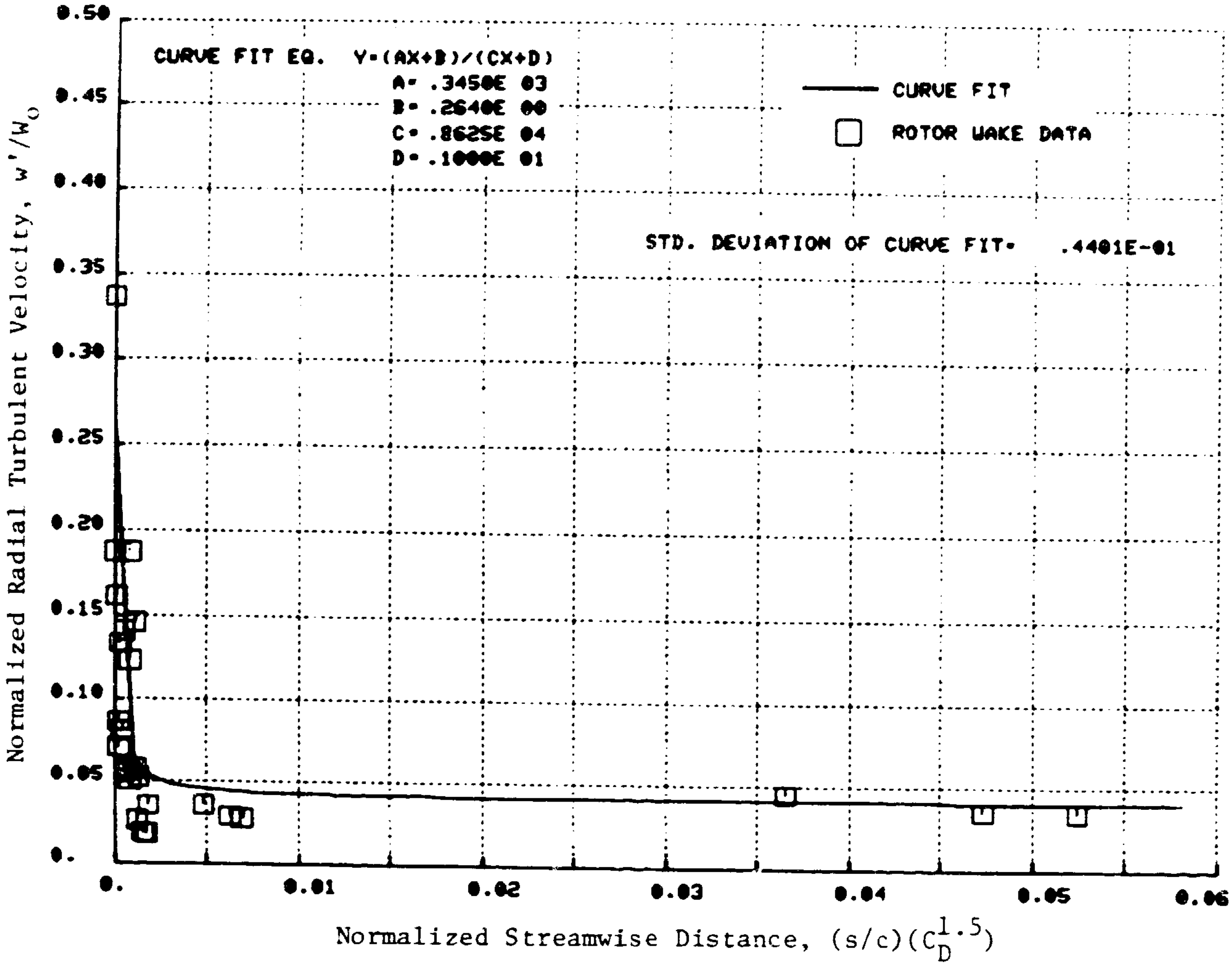

Figure 24. Correlation for Normalized Radial Turbulent Velocity for Midspan Location for Reynolds (Reference 2) and Ravindranath (Reference 3) Rotor Wake Data.

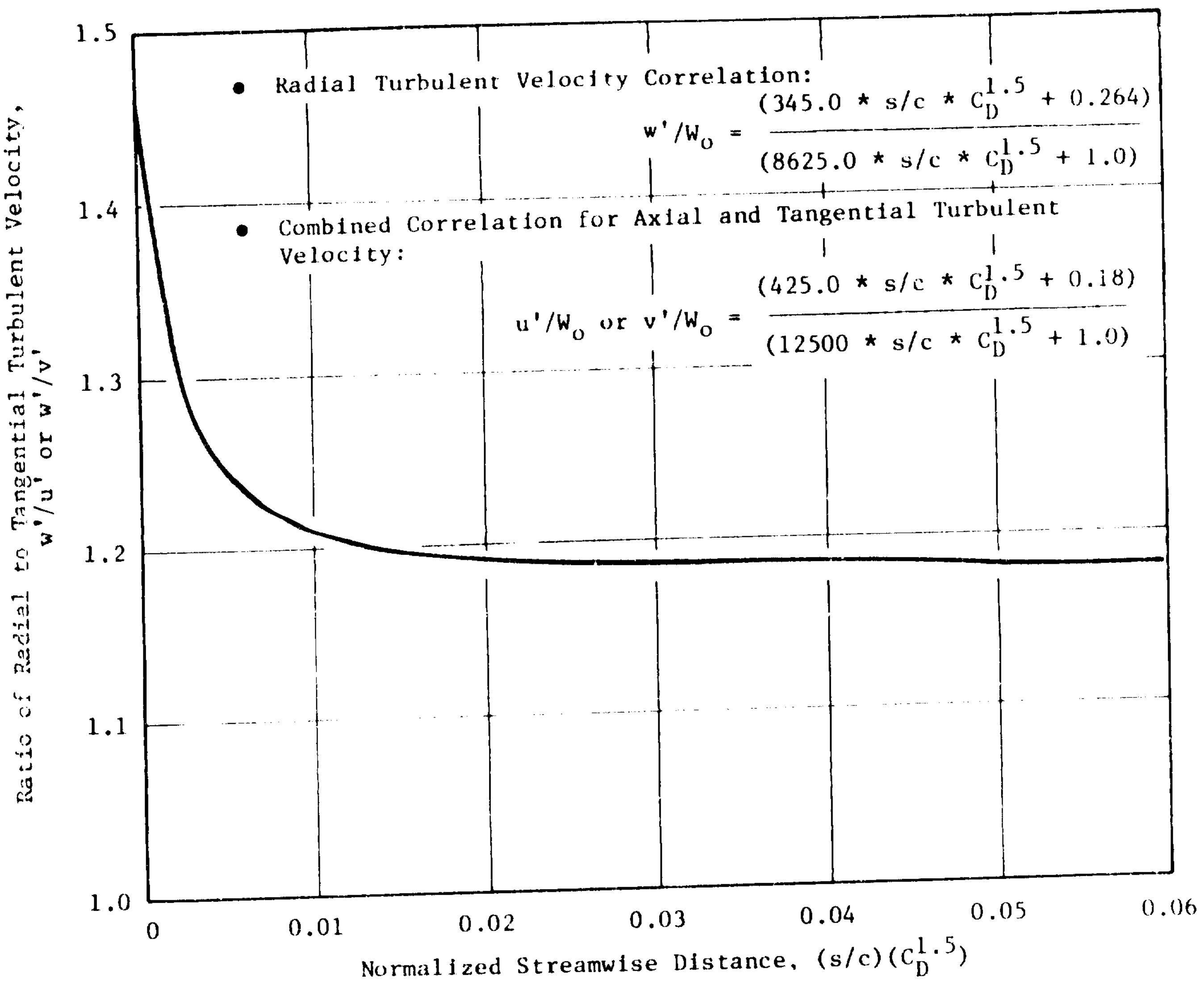

Figure 25. Streamwise Variation of Anisotropy of the Rotor Wake Turbulence Velocities as Predicted by the Correlations for Radial, Axial and Tangential Turbulent Velocities.

where

τ_x = Axial turbulent intensity at the tangential distance x from the wake centerline

$\tau_{x,o}$ = Axial turbulent intensity in the free stream

$(\tau_x)_c$ = Axial turbulent intensity at the wake centerline

and

$\eta = x/(\delta/2)$

x = Tangential distance from the wake centerline.

By definition of the turbulent intensity,

$$\tau_x = \frac{u'(x)}{W(x)} \tag{11a}$$

$$\tau_{x,o} = \frac{u'|x \to \infty}{W_o} \tag{11b}$$

and

$$\tau_{x,c} = \frac{u'|x=o}{W_c} \tag{11c}$$

where

u'(x) is the turbulent velocity at x distance from the wake centerline,

W(x) is the local mean flow relative velocity at x distance from the wake centerline,

W_c is the mean flow relative velocity at the wake centerline.

The data indicate that the free stream turbulence given by Equation 11b is about 0.04 (see References 2 and 3). Substituting Equation 11 into Equation 10 and solving for u'(x)/W(x), one obtains:

$$\frac{u'(x)}{W(x)} = e^{-\ln 2\eta^2}\left[\frac{u'|x=0}{W_c} - 0.04\right] + 0.04 \tag{12}$$

Consider,

$$\frac{u'|x=0}{W_c} = \frac{u'|x=0}{W_o - W_{dc}} = \frac{u'|x=0}{W_o} \times \frac{1}{\left[1 - \frac{W_{dc}}{W_o}\right]} \tag{13}$$

where W_{dc} is the velocity defect at the wake centerline. Also, consider the left-hand side of Equation 12,

$$\frac{u'(x)}{W(x)} = \frac{u'(x)}{W_o} * \frac{W_o}{W(x)} \tag{14}$$

Substituting Equations 13 and 14 into Equation 12 and solving for $u'(x)/W_o$, yields

$$\frac{u'(x)}{W_o} = \frac{W(x)}{W_o}\left[e^{-\ln 2\eta^2}\left\{\frac{u'|x=0}{W_o}\quad\frac{1}{1-\frac{W_{dc}}{W_o}} - 0.04\right\} + 0.04\right] \tag{15}$$

Let us look at $\frac{W(x)}{W_o}$:

$$\frac{W(x)}{W_o} = \frac{W_o - W_d(x)}{W_o} = 1 - \frac{W_d(x)}{W_o} = 1 - \frac{W_d(x)}{W_{dc}}\ \frac{W_{dc}}{W_o} \tag{16}$$

where $W_{d(x)}$ is the wake defect at a tangential distance x from the wake centerline.

The wake defect tangential distribution $W_d(x)/W_{dc}$ has been shown to correlate well with the Gaussian distribution function (References 2 and 3), that is,

$$\frac{W_{d(x)}}{W_{dc}} = e^{-\ln 2\eta^2} \tag{17}$$

Substituting Equations 16 and 17 into Equation 15, one gets

$$\frac{u'(x)}{W_o} = \left[1 - \frac{W_{dc}}{W_o}\ e^{-\ln 2\eta^2}\right] \times \left[e^{-\ln 2\eta^2}\left\{\frac{u'|x=0}{W_o} \times \frac{1}{\left(1-\frac{W_{dc}}{W_o}\right)} - 0.04\right\} + 0.04\right] \tag{18}$$

We have developed linear rational function correlations for W_{dc}/W_o (see Equation 4) and $\frac{u'|x=0}{W_o}$ (see Equation 8). Denoting $W_{dc}/W_o = f$ and $\frac{u'|x=0}{W_o} = g$ and simplifying, we obtain from Equation 18

$$\frac{u'(x)}{W_o} = e^{-\ln 2\eta^2}\left[\frac{g}{1-f} - 0.04 - 0.04\ f\right]$$

$$- f\ e^{-\ln 4\eta^2}\left[\frac{g}{1-f} - 0.04\right]$$

$$+ 0.04 \qquad (19)$$

The limiting forms of Equation 19 are:

a. In the free stream,

$$\lim_{x\to\infty} \frac{u'(x)}{W_o} = \lim_{\eta\to\infty} [\text{right-hand side of Equation 19}] = 0.04 \qquad (20a)$$

b. At the wake centerline,

$$\left.\frac{u'(x)}{W_o}\right|_{x=0} = g \qquad (20b)$$

Thus, Equation 19 yields the expected values at the wake centerline and in the free stream. To study the tangential distribution of the turbulent velocity, consider a numerical example. Let $s/c = 0.5$ and $C_D = 0.02$. Equation 4 yields

$$\frac{W_{dc}}{W_o} = f = 0.1663$$

Equation 8 yields

$$\frac{u'|x=0}{W_o} = g = 0.0418$$

As indicated by the limiting terms of the normalized turbulent velocity variation in the tangential direction (see Equation 20),

$$0.04 \leq \frac{u'(x)}{W_o} \leq 0.0418.$$

Thus, we see that when the turbulent velocity is normalized by the free stream velocity the tangential distribution is quite flat, whereas when the turbulent velocity is normalized by the local velocity, it exhibits a Gaussian tangential distribution. The numerical example chosen is a typical case. For larger values of (s/c), the tangential profile of the turbulent velocity will be even flatter. Hence, for the empirical model developed, which is intended to predict the rotor wake characteristics for 0.5 to 5.0 chord spacings between the rotor and stator, it is reasonable to assume a flat tangential profile (that is, a homogeneous tangential distribution) for the axial, tangential, and radial turbulent velocities normalized by the free stream velocity.

3.2 SECONDARY FLOW VORTEX MODEL

The existence of secondary flow vortices in and behind a rotor blade passage has been observed in experiments to be dominated by the tip clearance leakage flow vortex formation, as discussed by Johnsen, Reference 11, and Lakshminarayana, Reference 12. Other sources of secondary flow vortex formations are present in rotor blade passages. These include end wall boundary layer secondary flow formations at both hub and tip, as discussed by Adkins and Smith in Reference 13.

A tip clearance secondary flow vortex model was developed at General Electric for use in predicting secondary flow effects on fan tone noise, Reference 14. This model was extended during the course of this study to include a hub vortex model to compute the velocity induced by both hub and tip vortices. The model consists of a forced vortex core and surrounding free vortex for both tip and hub vortices as illustrated in Figure 26. A description of the prediction of the velocity fields created by the tip and hub vortices is given in the following paragraphs.

3.2.1 Tip Vortex Model

The tip vortex model superimposes a row of combined forced/free vortices and an image row opposite the annulus wall to enforce the zero radial velocity at the wall (see Figure 26). The tip vortices are located at a periodic tangential spacing equal to the blade spacing at the tip, S_t. The tangential distance of the center of the vortex core from the projected downstream blade wake centerline is specified by the parameter, b_t. The tangential location of the tip vortex has a significant influence on the stator upwash gust harmonic spectra, as will be shown through parametric studies in Section 5.0. From the experimental data surveyed, it is not possible to pin down a specific value for b_t, since it would vary not only from rotor to rotor, but also for the same rotor at different operating conditions. Hence, one will have to be aware of the sensitivity of the gust harmonic spectra to b_t and excercise a judgment in the selection of b_t. The blade span, tip clearance, and the tip vortex core size are designated by h, τ, and a_t, respectively.

It is assumed that the vortex core contains all the shed vorticity so that the motion outside is irrotational. The radius of the tip vortex core, a_t, is determined from Rain's (Reference 15) analysis of tip leakage flow, which assumes inviscid flow and an idealized blade pressure distribution. Rain's expression to compute the radius of the vortex core at the trailing edge of the rotor blade is

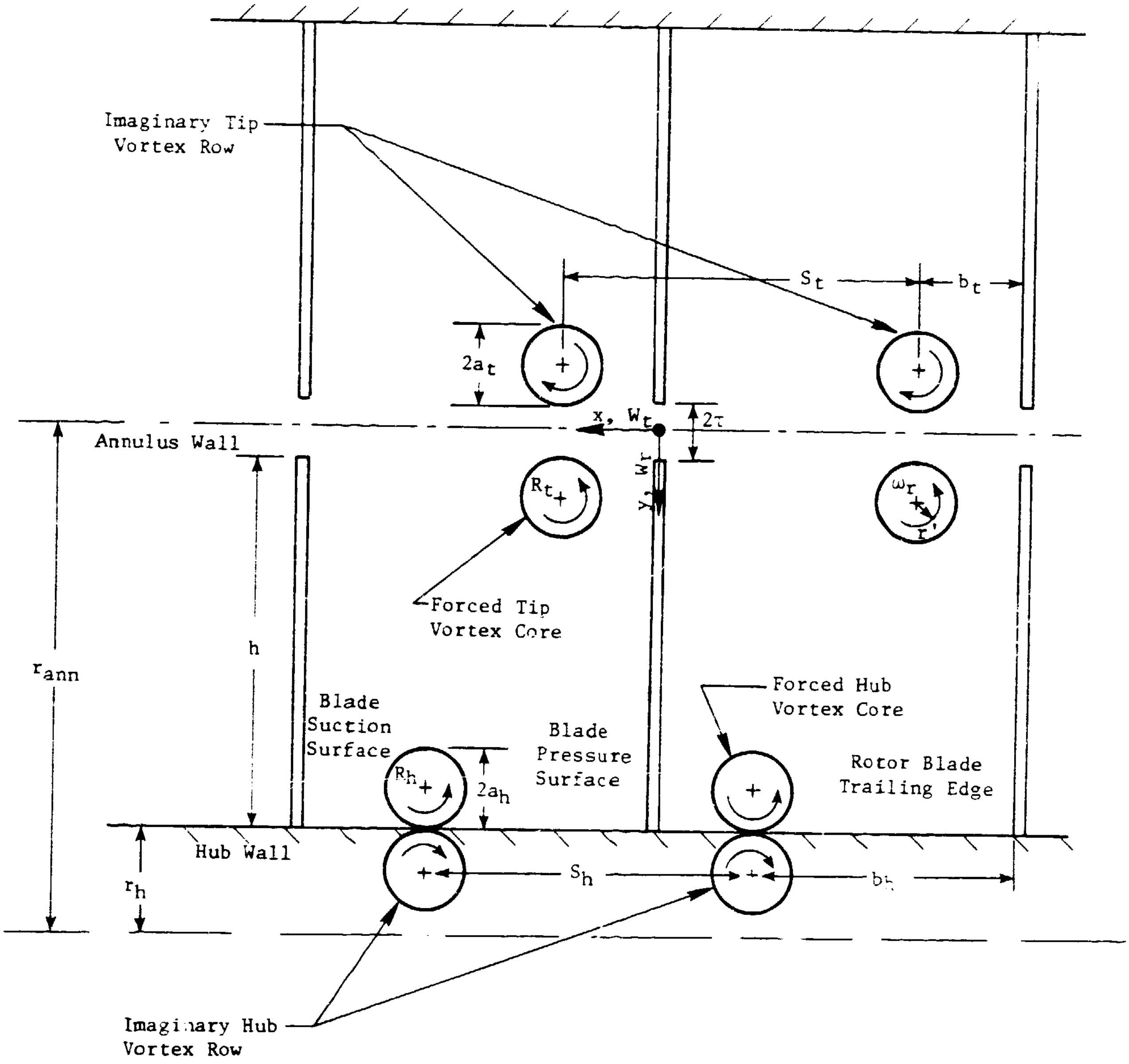

Figure 26. Nature of Tip and Hub Vortex Flow Model.

$$\left.\frac{a_t}{\tau}\right|_{TE} = 0.14\left[\frac{c}{\tau}\,(C_L)^{1/2}_{tip}\right]^{0.85} \qquad (21)$$

where τ is the clearance gap height and $(C_L)_{tip}$ is the lift coefficient at the tip.

The circulation at the tip per unit span is related to $(C_L)_{tip}$ through the following expresion:

$$(\Gamma)_{tip} = \frac{1}{2}\,(C_L)_{tip} \times (W_o)_{tip} \times (c)_{tip} \qquad (22)$$

where $(W_o)_{tip}$ is the free stream velocity and $(c)_{tip}$ is the rotor aerodynamic chord at the tip.

The fraction of the tip circulation lost to the tip vortex $(k)_{tip}$ was determined by Lakshminarayana in Reference 12 from blade pressure measurements at the blade tip of a cascade rig. It can be approximated by

$$(k)_{tip} = 0.23 + 7.45\left(\frac{\tau}{S_t}\right) \text{ for } 0.01 < \frac{\tau}{S_t} < 0.1 \qquad (23)$$

Thus, the amount of circulation in the tip vortex is given by:

$$(\Gamma tip)_{vtx} = (k)_{tip}\,(\Gamma)_{tip} \qquad (24)$$

The spanwise and the tangential (+y and +x directions respectively, see Figure 26) velocities outside the tip vortex core were determined by employing an extension of Lamb's (Reference 16) solution for the induced flow field about two infinite rows of vortices of finite radius as modeled in Figure 26. The resulting expressions for the induced velocities outside the domain R_t follow.

For the tangential velocity $W_t|_{tip}$:

$$W_t|_{tip} = -\frac{(\Gamma tip)_{vtx}}{2\,S_t}\left[\frac{\sinh M_t}{\cosh M_t - \cos p_t} - \frac{\sinh N_t}{\cosh N_t - \cos p_t}\right] \qquad (25)$$

and, for the radial velocity $W_r|_{tip}$:

$$W_r|_{tip} = -\frac{(\Gamma tip)_{vtx}}{2S_t}\left[\frac{\sin p_t}{\cosh M_t - \cos p_t} - \frac{\sin p_t}{\cosh N_t - \cos p_t}\right] \qquad (26)$$

where

$$M_t = \frac{2\pi}{S_t} (y - a_t - \tau) \tag{27}$$

$$N_t = \frac{2\pi}{S_t} (y + a_t + \tau) \tag{28}$$

and

$$P_t = \frac{2\pi}{S_t} (x - b_t) \tag{29}$$

The parameters x and y are coordinates of the unwrapped annulus.

The region within the domain R_t behaves as a forced vortex (solid body of revolution). The domain R_t is given by:

$$(x-b_t)^2 + (y-a_t-\tau)^2 \leq a_t^2 \tag{30}$$

The angular velocity of the tip vortex can be related to the circulation of the tip vortex by:

$$\omega_t = \frac{(\Gamma_{tip})_{vtx}}{2\pi\ a_t^2} \tag{31}$$

For a point P(x,y) within the domain R_t, the tangential component of the velocity induced by the tip vortex is given by:

$$W_t|_{tip} = - \omega_t\ r \sin \alpha \tag{32}$$

and the radial component by

$$W_r|_{tip} = \omega_t\ r \cos \alpha \tag{33}$$

where

$$r = \{(x-b_t)^2 + (y - a_t - \tau)^2\}^{1/2}$$

and

$$\alpha = \tan^{-1}\left[\frac{y - a_t - \tau}{x - b_t}\right] \tag{34}$$

Equations 25 through 34 specify the induced velocity field in a radial plane behind the blade trailing edge due to the presence of the tip vortex core. The radius of the vortex core increases, and the velocity deficiency of the vortex in the streamwise direction W_{dv} decreases as the flow proceeds downstream and the vorticity diffuses outwards. Also, the rotational velocity at any particular radius within the core decreases until, very far downstream, the velocity is negligible and the vortex has completely decayed. The maximum strength of the vortex core and deficit in streamwise velocity is assumed to occur at the rotor blade trailing edge where the flow generation process terminates. The decay of the tip leakage vortex core was modeled after the viscous decay of a steady, three-dimensional, trailing vortex behind the tip of an airfoil investigated by Dosanjh et al. in Reference 17. The various velocity distributions in the vortex measured by Dosanjh were in good agreement with a linearized, axisymmetric, laminar, incompressible, viscous vortex model from Neuman (Reference 18). However, the decay of the velocity and length scales (W_{dv} and a) was found to be approximately eight to ten times faster than predicted by Neuman's analysis which was based on a laminar kinematic viscosity ν. Since the vortex from the tip is turbulent, the vorticity diffusion is stronger than for the purely laminar case. Effectively, the virtual or apparent kinematic viscosity ν_t is likely to be eight to ten times greater than the laminar kinematic viscosity ν. Therefore, in the vortex decay correlations presented below, a constant ν_t/ν is assumed.

At the trailing edge of the rotor blade row, the maximum defect in streamwise velocity W_{dv} of the vortex core is given by Lakshminarayana (Reference 12) as:

$$W_{dv} = \frac{(\omega a_t)^2}{2W_1} \ln\left[\frac{0.75\, cW_m}{\nu_t}\right] \tag{35}$$

where W_1 is the mainstream flow velocity at the rotor inlet and W_m is the mean flow velocity through the blade passage. Also, as the vortex proceeds downstream, the maximum velocity deficit decays as $(1 + s/c)^{-1}$ as shown by Dosanjh et al. in Reference 17, for the case of the decay of a viscous trailing vortex (see note below). The radius of the vortex core was shown by Dosanjh et al. (Reference 17) to increase with downstream distance as $(1 + s/c)^{1/2}$ as given by:

$$\left.\frac{a_t}{\tau}\right|_{(s/c)} = \left.\frac{a_t}{\tau}\right|_{TE}\left(\sqrt{1 + (s/c)}\right) \tag{36}$$

Note: It is assumed that the tip vortex originates at the rotor blade leading edge. Hence, the decay or growth rates associated with tip vortex are functions of (1 + s/c) and not (s/c).

Dosanjh et al. (Reference 17) have also shown the maximum rotational velocity due to the vortex decays with the downstream distance as $(1 + s/c)^{1/2}$ (see note). It is assumed that the streamwise decay of the circulation of the vortex follows that of the maximum rotational velocity. Also, at a given radius from the vortex core, the streamwise velocity deficiency is shown by Dosanjh et al. (Reference 17) to be:

$$W_d(r')/W_{dv} = \exp\left[-\ln 2\,(r'/a_t)^2\right] \qquad (37)$$

where r' is the radial distance from the vortex core.

From the above considerations, the three-dimensional velocity field due to the presence of the tip vortex can be calculated.

3.2.2 Hub Vortex Model

Though the existence of a hub vortex in rotors has been postulated, data presented in References 2, 3, 19, and 20 do not unequivocally confirm the presence of a hub vortex. Ravindranath (Reference 3) reports that the wake behavior near the hub region is considerably influenced by the secondary flow due to hub-wall boundary layer and also radial transport of mass and momentum. The surveyed literature (References 2, 3, 5, 8, 9, 19, and 20 do not have any kind of data which can be used to develop empirical expressions for hub vortex parameters such as vortex strength, vortex radius, etc.). Thus, only the methodology of calculating the velocities induced by a hub vortex is described in this subsection. When experimental data regarding hub vortex parameters become available, the emprirical relations can be firmly established and appropriate calculations of the induced velocities due to hub vortex can be performed.

The mathematical development for computing the tangential and radial velocity components induced by the hub vortex follows a methodology identical to the tip vortex case. The origin and the axes of the coordinate system are still the same as for the tip vortex case. The changes relative to the tip vortex case are as follows (see Figure 26):

Parameter	Tip Vortex	Hub Vortex
Radius of the Vortex	a_t	a_h
y-Coordinate of the Image Plane	0	$r_{ann} - r_n$
y-Coordinate of the Vortex Center	$a_t + \tau$	$r_{ann}-r_n-a_h$
Clearance Between Blade and Tip Wall	τ	0
x-Coordinate of the Vortex Center	b_t	b_h
Tangential Distance Between Two Adjacent Vortices	S_t	S_h
Circulation of the Vortex	$(\Gamma_{tip})_{vtx}$	$(\Gamma_{hub})_{vtx}$

Since the identical coordinate system and sign conventions are applied for both the hub and tip vortices, relations for computing the tangential and radial velocities induced by the hub vortex can be obtained from Equations 25 through 34 (keeping in mind the differences between the hub and tip vortex systems listed in the previous table). Hence, the following expressions for the induced velocities outside the domain R_h result. For the tangential velocity $W_t|_{hub}$:

$$W_t|_{hub} = -\frac{(\Gamma_{hub})_{vtx}}{2\,S_h}\left[\frac{\sin M_h}{\cosh M_h - \cos p_h} - \frac{\sin N_h}{\cosh N_h - \cos p_h}\right] \qquad (38)$$

and, for the radial velocity $W_r|_{hub}$:

$$W_r|_{hub} = -\frac{(\Gamma_{hub})_{vtx}}{2\,S_h}\left[\frac{\sin p_h}{\cosh M_h - \cos p_h} - \frac{\sin p_h}{\cosh N_h - \cos p_h}\right] \qquad (39)$$

where,

$$M_h = \frac{2\pi}{S_h}\left\{y - (r_{ann} - r_h) - (r_{ann} - r_h - a_h)\right\} \qquad (40)$$

$$N_h = \frac{2\pi}{S_h}\left\{y - (r_{ann} - r_h) + (r_{ann} - r_h + a_h)\right\} \qquad (41)$$

and

$$p_h = \frac{2\pi}{S_h}(x - b_h) \qquad (42)$$

As in the case of the tip vortex, the domain R_h behaves as a forced vortex. The domain R_h is given by

$$(x - b_h)^2 + (y - r_{ann} + r_h + a_h)^2 \leq a_h^2 \qquad (43)$$

The angular velocity of the hub vortex is related to the circulation of the hub vortex by

$$\omega_h = \frac{(\Gamma_{hub})_{vtx}}{2\pi\,a_h^2} \qquad (44)$$

For a point P(x,y) within the domain R_h. The tangential component of the velocity induced by the hub vortex is given by

$$W_t|_{hub} = -\omega_h r \sin\alpha \tag{45}$$

and the radial component by

$$W_r|_{hub} = \omega_h r \cos\alpha \tag{46}$$

where

$$r = [(x - b_h)^2 + (y - r_{ann} + r_h + a_h)^2]^{1/2}$$

and

$$\alpha = \tan^{-1}\left\{\frac{y - r_{ann} + r_h + a_h}{x - b_h}\right\} \tag{47}$$

Since empirical expressions for $(\Gamma_{hub})_{vtx}$, a_h and b_h could not be developed due to lack of data on hub vortex, the following pseudorelations are incorporated into the computer program with the goal of checking out the program logic for any compilation and execution errors:

$$\begin{aligned}(\Gamma_{hub})_{vtx} &= 0.2 \times \frac{1}{2}(C_L)_{hub} \times (W_o)_{hub} \times (c)_{hub}\\ a_h &= 0.2\ (c)_{hub}\\ b_h &= 0.5 * S_h\end{aligned} \tag{48}$$

where

$(c)_{hub}$ = Rotor aerodynamic chord at hub
$(C_L)_{hub}$ = Lift coefficient at hub
$(W_o)_{hub}$ = Free stream velocity at hub.

Once better definitions of the preceding parameters become available, the relations (Equation 48) can be replaced in the computer program.

The model used for the streamwise growth of the radius of the vortex core and the viscous decay of the circulation, and the streamwise defect of the tip vortex has been used for the hub vortex case, in the absence of anything better.

The mathematical development for the hub and tip vortices neglects the influence of the annulus wall on the hub vortex and the influence of the hub wall on the tip vortex. Also, since the wake/vortex model employs a streamline-by-streamline approach, only the tangential velocity component induced by the tip and hub vortices is computed.

3.3 SPECTRAL PREDICTION OF THE STATOR UPWASH

Sections 3.1 and 3.2 described the procedure to predict the mean and turbulent velocities of the rotor wake and the mean velocity induced by the hub and tip vortices in a frame of reference rotating with the rotor. This section briefly describes the following:

a. Coordinate transformation of the combined flow field properties of the wake and vortex to a stationary reference frame,

b. Evaluation of the description of upwash gust impinging on the stator and the corresponding evaluation of the gust harmonic spectrum,

c. Evaluation of the turbulent velocity spectrum.

3.3.1 Stator Upwash Gust Harmonic Amplitude Distribution

The streamwise and the tangential velocity components of the rotor wake and the vortex flow in the frame of reference rotating with the rotor are summed algebraically to yield the integrated rotor wake/vortex streamwise and tangential velocity components. Thus, the wake/vortex integrated relative velocity vector is known. Adding the wheel velocity vector to the wake/vortex integrated relative velocity vector yields the absolute velocity vector. Figure 27 shows the velocity triangles in the free stream and at the wake centerline. For simplicity, it is assumed that the relative velocity has only a streamwise component. The perturbation velocity vector ($\bar{V}'$) in the stationary frame of reference is obtained by the vector subtraction of the absolute velocity vector in the free stream ($\bar{V}_o$) from that in the wake ($\bar{V}$). The component of $\bar{V}'$ in the direction of $\bar{V}_o$ is the streamwise perturbation component and the component of $\bar{V}'$ normal to $\bar{V}_o$ is the upwash component. As the wake of one rotor blade passes in front of a stator, the upwash component of the perturbation velocity goes from a zero value (in the free stream) to a maximum (at the wake centerline) and to a zero value, again (in the free stream on the other side of the blade). From two-dimensional nonstationary airfoil theory, the fluctuating lift has been proven to be acting at the 1/4 chord point. Therefore, the stator upwash velocities are evaluated at the 1/4 chord point of the stator. The fluctuating lift on the stator blade is one of the principal sources of the rotor/stator interaction noise. This subsection briefly describes the procedure employed for determining the spectral composition of the upwash component.

Notes

$\overline{W}$: Relative Velocity Vector at Wake Centerline

$\overline{W}_o$: Relative Velocity Vector in the Free Stream

$\overline{U}$: Wheel Speed Vector

$\overline{V}$: Absolute Velocity Vector at Wake Centerline

$\overline{V}_o$: Absolute Velocity in the Free Stream

$\overline{V}'$: Perturbation Velocity Vector

EB: Upwash Component of $\overline{V}'$, V'_n

DE: Streamwise Component of $\overline{V}'$, V'_S

$$\boxed{V'_n = (\overline{W}_o - W) \sin(\beta + \alpha_o)}$$

Vector Relations

- In the Free Stream: $\overline{V}_o = \overline{W}_o + \overline{U}$
- At the Wake Centerline $\overline{V} = \overline{W} + \overline{U}$
- $\overline{V}' = \overline{V} - \overline{V}_o$

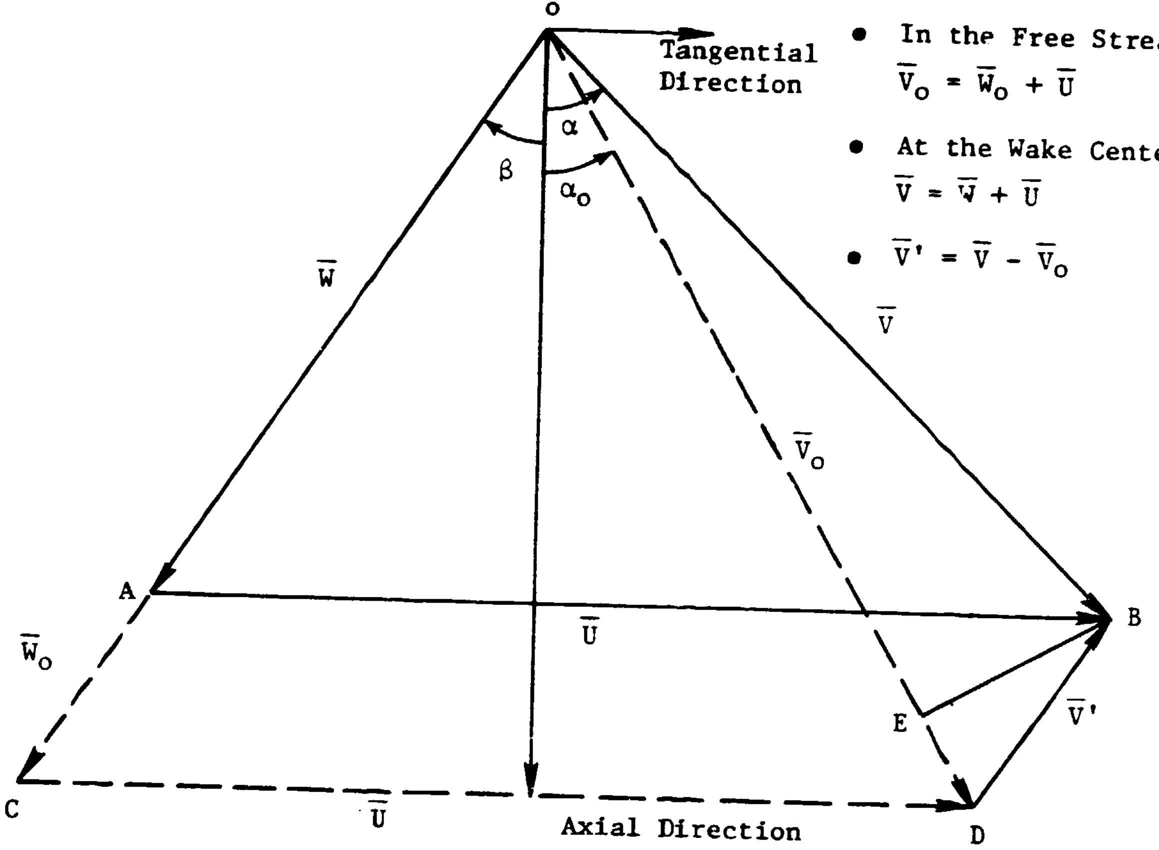

Figure 27. Schematic Velocity Triangles for Rotor Exit Flow in the Free-stream and at the Wake Centerline.

The coordinate transformation yields the tangential distribution of the upwash component $v_N'(y)$ over one blade spacing (S). Since $V_N'(y)$ is periodic over S, it can be represented by a complex Fourier series as follows:

$$V_N'(y) = \sum_{m=-\infty}^{\infty} c_m \, e^{im\pi y/(S/2)} \tag{49}$$

where

$i = \sqrt{-1}$
$c_m = a_m + ib_m$
a_m, b_m are real numbers.

The above representation includes both the sine and cosine terms of the Fourier series. The complex coefficients c_m can be evaluated using the orthogonality property of $e^{im\pi y/(S/2)}$ function and are given by

$$c_m = \frac{1}{S} \int_0^S V_N'(y) \, e^{-im\pi y/(S/2)} \, dy,$$

$$m = -\infty, \ldots .-2, -1, 0, 1, 2, \ldots \infty \tag{50}$$

The zero'th coefficient, c_o, is essentially the average value of the upwash velocity over the blade spacing and as such of no interest in the spectral distribution, since it corresponds to the level at zero frequency. For a real function $V_n'(y)$, $c_{-m} = c_m^*$ where c_m^* is the complex conjugate of c_m. Thus, in determining the gust harmonic amplitude, the coefficients of negative values of m do not contribute any new information. Therefore, the Fourier coefficients corresponding to positive (nonzero) values of m only will be evaluated for this study.

The integral in Equation 50 is evaluated numerically in complex arithmetic by using the Simpson's rule for positive values of m (see Reference 20). The absolute value of c_m and its phase are given, respectively, by

$$\left.\begin{aligned} |c_m| &= (a_m{}^2 + b_m{}^2)^{1/2} \\ &\text{and} \\ \phi_m &= \tan^{-1}\left[\frac{b_m}{a_m}\right] \end{aligned}\right\} \quad m = 1, 2, \ldots \infty \tag{51}$$

Note that $|c_m|$ has units of velocity. A nondimensional decibel value for the coefficients of the Fourier series is defined by:

$$dB_m = 10 \log_{10} \left[\frac{|c_m|^2}{V_{ref}{}^2} \right], \quad m = 1,2 \ldots \infty \tag{52}$$

where V_{ref} is a chosen reference velocity.

While numerically integrating Equation 50 for the case of rotor wake only (without tip or hub vortex), it was noticed that dB_m did not fall monotonically for increasing values of m, as has been experimentally observed, particularly when δ/S approached a value of 0.5. The principal reason for this anomalous spectral behavior is that so far the influence of the wake from the adjacent blades has been neglected (see Figure 28). This is a reasonable assumption when δ/S is small. However, when δ/S approaches 0.5, there is a large wake defect at the midpassage. Figure 28 shows the case which has maximum defect at mid passage. The wake defect profile, whose Fourier components were determined by the above process (that is, neglecting the wake from the adjacent blade), exhibits a sharp corner at $y = 0.5\ S$ (see Figure 28, wake defects for Blade 1 and Blade 2). A sharp corner in the profile excites higher harmonics (Fourier series for a step function). This was circumvented by combining the wake defects from the two adjacent blades. The combined wake defect does not exhibit sharp corner (Figure 28). The upwash spectrum of the combined wakes from the adjacent blades showed a monotonic fall with the harmonic number.

The twist of the rotor blade from hub to tip causes a time/phase lag between the wakes from the hub and tip regions impinging on the stator. The analysis for predicting the phase lag due to the twist of the rotor blades was developed under a previous GE Independent Research and Development (IR&D) project and is included herein, for the sake of completeness.

Let the angle from the rotor blade stacking axis to the trailing edge be $\phi_o(r)$ (see Figure 29a) and let the angle from the blade trailing edge to the stator leading edge along the wake centerline be $\Delta\phi(r,\Delta X)$. It is assumed that the wake centerline "sheet" is fixed in space in a coordinate system fixed to the rotor. The angular displacement of the wake at the 1/4 chord point of the stator relative to the rotor stacking axis is given by:

$$\phi(r,X) = \phi_o(r) + \Delta\phi(r,\Delta X) \tag{53}$$

The hub and tip values are respectively,

$$\begin{aligned} \phi_h(r_h,X_h) &= \phi_o(r_h) + \Delta\phi(r_h,\Delta X_h) \\ \phi_t(r_t,X_t) &= \phi_o(r_t) + \Delta\phi(r_t,\Delta X_t) \end{aligned} \tag{54}$$

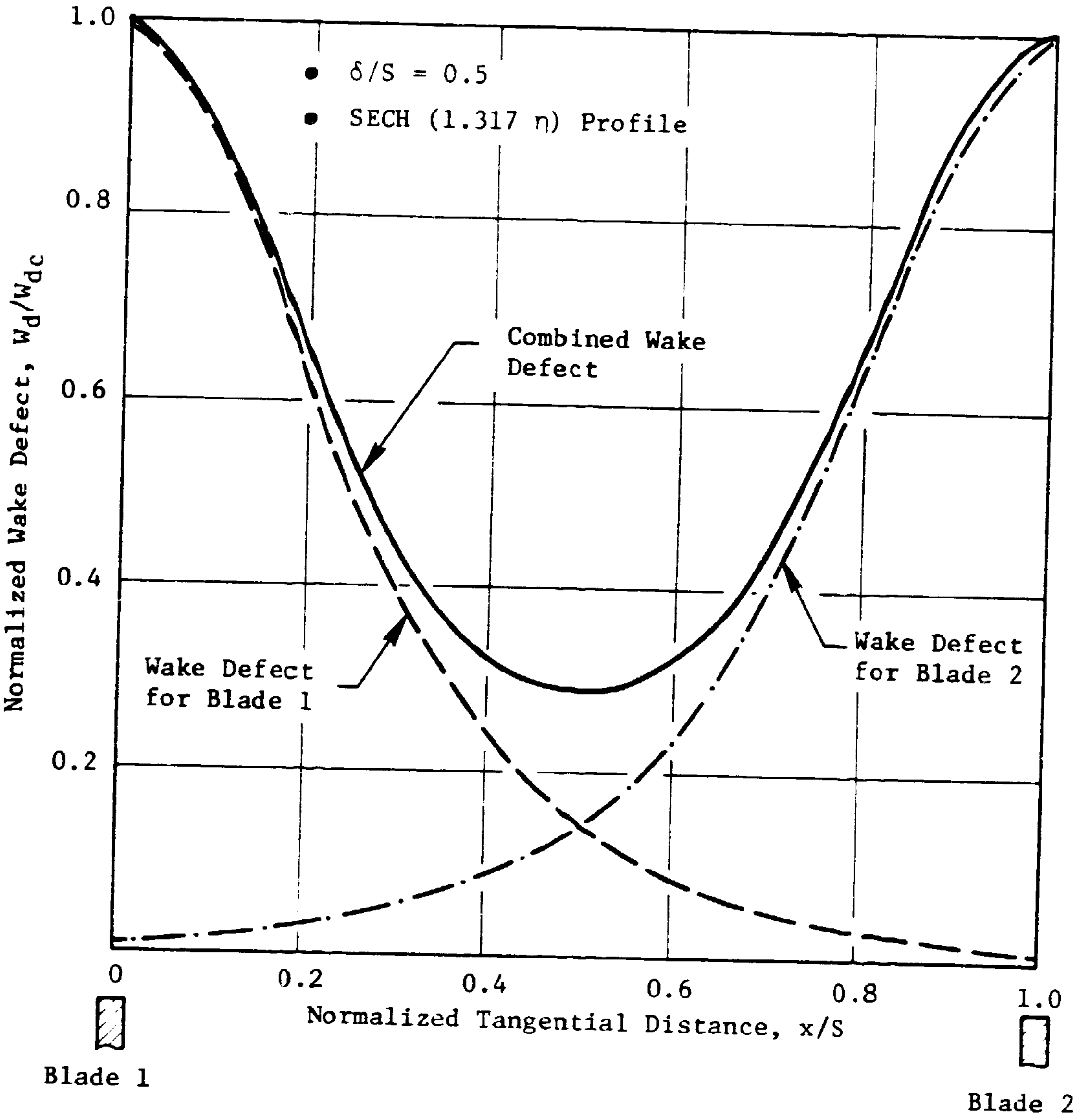

Figure 28. Illustration of Merging of Wakes from Adjacent Blades.

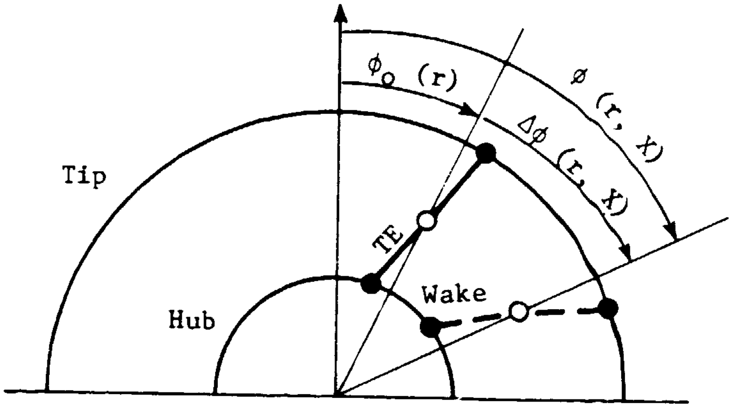

a. End View of Rotor Trailing Edge Line and Rotor Wake Line at Stator 1/4 Chord Point

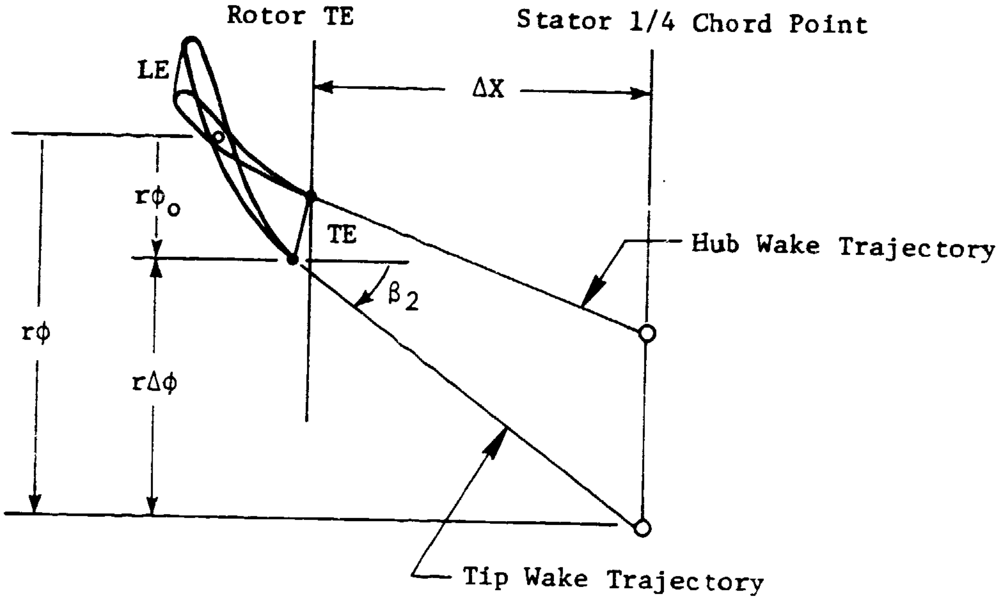

b. Cascade View of Rotor Trailing Edge Line and Rotor Wake Line at Stator 1/4 Chord Point

Figure 29. Geometry for Aerodynamic Phase Lag Computation Due to Twist of Rotor Blade.

Along a cylindrical stream surface, $\Delta\phi$ is given by (see Figure 29):

$$\Delta\phi(r, \Delta X) = \frac{\Delta X}{r} \tan \beta_2 (r) \tag{55}$$

where $\beta_2(r)$ is the rotor relative air angle at the rotor trailing edge. The trailing edge angular displacement ϕ_o is given by:

$$\phi_o (r) = \frac{c(r)}{2r} \sin \gamma_R \tag{56}$$

where c(r) is the rotor aerodynamic chord and γ_R is the rotor stagger angle.

The phase lag for the 1/4 chord point at a given radial location of the stator to "feel" the wake impact relative to the phase at which the same rotor wake impacts the 1/4 chord point at the tip of the stator is then given by

$$\phi(r,X)_{lag} = \phi(r,X) - \phi_t (r_t,X_t) \tag{57}$$

The angular spacing for the rotor is given by

$$\phi_B = \frac{2\pi}{B} \tag{58}$$

where B is the number of rotor blades. A normalized phase lag relative to the tip can be defined as

$$\phi(r,X)_{lag}\Big|_{norm} = \frac{\phi(r,X)_{lag}}{\phi_B} \tag{59}$$

The normalized phase lag at a given radial location is the phase lag relative to tip at that location relative to the rotor angular spacing.

3.3.2 Axisymmetric Turbulent Velocity Spectrum Prediction

The total stator gust upwash spectrum is treated as a superposition of a broadband spectrum determined by the rotor exit turbulence characteristics and a tone harmonic spectrum determined by the rotor exit mean velocity circumferential profiles. This section discusses the broadband component of the spectrum associated with the rotor exit flow turbulence.

In Section 3.1.2, it was shown that, except in the immediate vicinity of the rotor trailing edge, the rms turbulent velocity is spatially uniform in the tangential direction when normalized by free-stream velocity. As a good approximation, it can be modeled as homogeneous turbulence. The mathematical models for turbulence-rotor interaction given in References 21-23 were selected as the starting point for the present turbulence-stator interaction model and associated stator gust upwash broadband spectrum prediction procedure. Only a few samples of turbulent velocity spectrum measurements were uncovered in the Literature Survey (Section 2.0); due to insufficient data, an empirical correlation approach was not possible. A theoretical model approach was therefore selected, and (as will be shown later) the model was verified using the few sample data cases available.

Following Reference 21, a model of convected, homogeneous turbulence is assumed, incident upon a stationary blade row. The turbulence is assumed to be homogeneous, but not (necessarily) isotropic, with two of the three component directions having the same turbulence intensity and integral length scale. A sketch of the flow diagram, blade geometry, and nomenclature is shown in Figure 30, in the $(\bar{x},\bar{y})$-plane or cascade plane. The turbulence is assumed to convect with the mean (free-stream) flow, having axial velocity U and tangential velocity $V_{\bar{y}}$, and flow angle $\alpha_s = \tan^{-1}(V_{\bar{y}}/U)$.

Denoting axial, tangential, and radial directions by $\bar{x}$, $\bar{y}$, and $\bar{z}$, respectively, and fluid-fixed coordinates by $(\bar{x}_o, \bar{y}_o, \bar{z}_o)$, we have that

$$\bar{x}_o = \bar{x} + Ut; \ \bar{y}_o = \bar{y} - V_y t; \ \bar{z}_o = \bar{z}$$

Note that $\bar{x}$ is positive in the upstream direction, $\bar{y}$ is positive in the direction of rotor rotation, and U is positive in the negative $\bar{x}$ direction.

Assuming the turbulence to be statistically stationary in a reference frame moving with the fluid ($\bar{x}_o$, $\bar{y}_o$, $\bar{z}_o$ - coordinates), the turbulent velocities in the three component directions can be expressed as an integral summation of shear waves (see Equation 1 of Reference 21) as follows:

$$(u,v,w) = \int dZ_{u,v,w}(\underline{k}) \exp\left(j\, \underline{k} \cdot \underline{r}_o\right) \tag{60}$$

In terms of stationary coordinates $(\bar{x},\bar{y},\bar{z})$, this becomes

$$(u,v,w) = \int dZ_{u,v,w}(\underline{k}) \exp\{j[\underline{k}\cdot\underline{r} + (Uk_{\bar{x}} - V_{\bar{y}}k_{\bar{y}})t]\} \tag{61}$$

In Equations 60 and 61, (u,v,w) are the $(\bar{x}_o,\bar{y}_o,\bar{z}_o)$ - components of the turbulent velocity, and $dZ_{u,v,w}(\underline{k})$ represents the spectral density functions corresponding to (u,v,w), given by

$$dZ_u(\underline{k}')\, dZ_v(\underline{k}'') = \delta(\underline{k}'-\underline{k}'')\, \Phi_{uv}(\underline{k}')\, d^3\underline{k}'\, d^3\underline{k}'' \tag{62}$$

The component of velocity normal to the stator chord line (see Figure 30) at an angle γ_s relative to the axial $(\bar{x})$ direction is given by

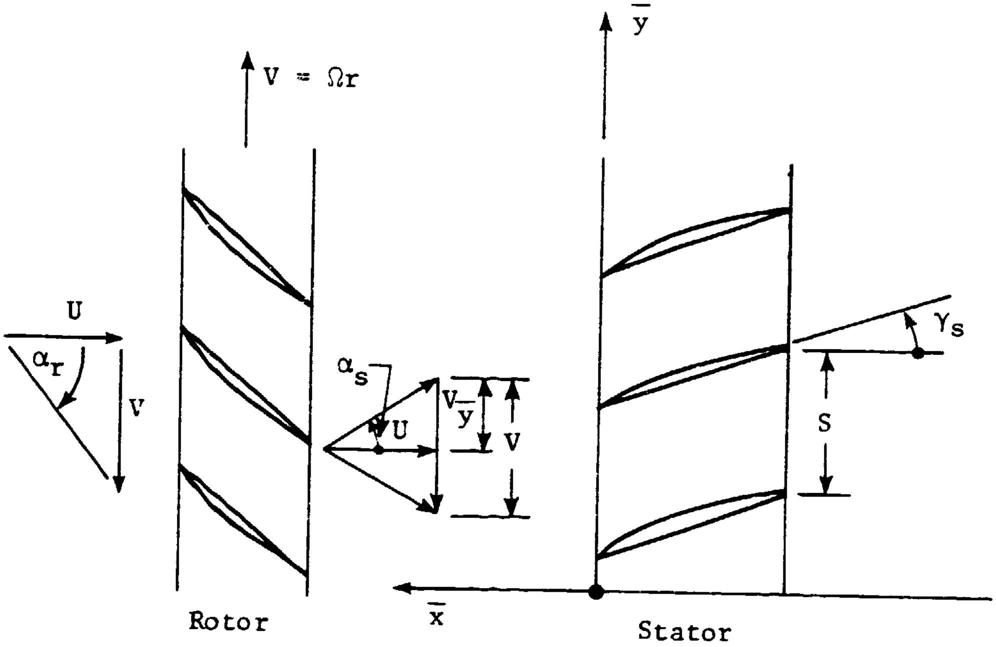

Figure 30. Rotor-Generated Turbulence Incident Upon a Stator.

$$v_n = u \sin \gamma_s + v \cos \gamma_s \tag{63}$$

Thus

$$|v_n|^2 = u^2 \sin^2 \gamma_s + 2\, uv \sin\gamma_s \cos \gamma_s + v^2 \cos^2 \gamma_s \tag{64}$$

The corresponding turbulent velocity spectrum for the velocity normal to the chord line, that is, the upwash or gust velocity spectrum γ_{nn}, is then given by

$$\phi_{nn} = \phi_{uu} \sin^2 \gamma_s + 2\phi_{uv} \sin\gamma_s \cos\gamma_s + \phi_{vv} \cos^2 \gamma_s \tag{65}$$

Reference 21 considered only the case of a flat plate stator (and rotor) at zero incidence and zero stagger. The present analysis treats a staggered stator and extends the turbulence model to the axisymmetric case, one step higher in complexity than the isotropic turbulence model assumed in Reference 21. Equations 61 and 65 become identical to the rotor equations in Reference 21 if V_y is replaced by $-V = -\phi r$, the rotor wheel speed, and γ_s is replaced by $-\Omega_r$, the rotor relative air angle. Any results derived for the case of turbulence incident upon a rotor may therefore be extended to the case of turbulence incident upon a stator by replacing V by $-V_y$ and α_r by $-\gamma_s$ in the appropriate equations. Since References 22 and 23 developed extensions of the rotor problem in Reference 21 to axisymmetric turbulence, we can use those results and transform them directly to the stator problem.

Consider first the case of isotropic turbulence incident upon a rotor blade row. The turbulence spectrum for the gust velocity component normal to the relative free-stream velocity vector is then

$$\phi_{nn} = \phi_{uu} \sin^2 \alpha_r - 2 \sin\phi_r \cos\alpha_r\, \phi_{uv} + \phi_{vv} \cos^2 \alpha_r \tag{66}$$

For isotropic turbulence, the component spectra are given by

$$\phi_{ij} = \frac{E(k)}{4\pi k^2} \left\{ \delta_{ij} - \frac{k_i k_j}{k^2} \right\} \tag{67}$$

where

$$k^2 = k_1^2 + k_2^2 + k_3^2 \tag{68}$$

and

$$E(k) = \frac{8\, k^4\, \bar{u}^2}{\pi L\, (L^{-2} + k^2)^3} \tag{69}$$

Upon combining Equations 66 and 69 by first evaluating Equation 67 for $\phi_{uu} = \phi_{11}$, $\phi_{uv} = \phi_{12}$ and $\phi_{vv} = \phi_{22}$, then substituting the results into Equation 66, the following expression for ϕ_{nn} is obtained:

$$\phi_{nn} = \frac{E(k)}{4\pi k^4} \left[k_1^2 \cos^2\alpha_r + 2k_1 k_2 \sin\alpha_r \cos\alpha_r + k_2^2 \sin^2\alpha_r + k_3^2 \right] \tag{70}$$

Following the format of Reference 21, we need to integrate Equation 70 over spanwise wavenumber $k_3 = k_{\bar{z}}$ (note that axial wavenumber $k_{\bar{x}} = k_1$ and tangential wavenumber $k_{\bar{y}} = k_2$ notation is adopted herein). Integrating ϕ_{nn} (k_1, k_2, k_3) over $-\infty < k_3 < \infty$ gives the gust spectrum $\phi^*_{nn}(k_1, k_2)$ as follows:

$$\phi^*_{nn}\ (k_1, k_2) = \int_{-\infty}^{\infty} \phi_{nn}(k_1, k_2, k_3)\, dk_3 \tag{71}$$

Substituting Equations 69 and 70 into the above, we have

$$\phi^*_{nn} = \int_{-\infty}^{\infty} \frac{2\,\overline{u^2}}{\pi^2 L} \left[\frac{(k_{\bar{x}} \cos\alpha_r + k_{\bar{y}} \sin\alpha_r)^2 + k_{\bar{z}}^2}{(L^{-2} + k_{\bar{x}}^2 + k_{\bar{y}}^2 + k_{\bar{z}}^2)^3} \right] dk_{\bar{z}} \tag{72}$$

In the preceding expressions, L denotes the turbulence integral length scale, and $\overline{u^2}$ denotes the mean-square turbulence velocity.

By employing the substitutions $k_z = A \tan\theta$, where $A^2 = L^{-2} + k_{\bar{x}}^2 + k_{\bar{y}}^2$, Equation 72 can be integrated analytically to yield the following:

$$\phi^*_{nn} = \frac{\overline{u^2}}{4\pi L A^5} \left[3(k_{\bar{x}} \cos\alpha_r + k_{\bar{y}} \sin\alpha_r)^2 + A^2 \right] \tag{73}$$

After rearranging terms, this can be rewritten as follows:

$$\phi^*_{nn} = \frac{\overline{u^2}}{4\pi L}\left[\frac{c_1 k_{\bar{x}}^2 + c_2 k_{\bar{x}} k_{\bar{y}} + c_3 k_{\bar{y}}^2 + L^{-2}}{(L^{-2} + k_{\bar{x}}^2 + k_{\bar{y}}^2)^{5/2}}\right] \tag{74}$$

where

$$c_1 = 1 + 3\cos^2\alpha_r$$
$$c_2 = 6\sin\alpha_r \cos\alpha_r \tag{75}$$
$$c_3 = 1 + 3\sin^2\alpha_r$$

The next step is to integrate ϕ^*_{nn} over circumferential or tangential wavenumber $k_2 = k_{\bar{y}}$. The turbulent velocity spectrum ϕ^*_{nn} is a function of both $k_{\bar{x}}$ and $k_{\bar{y}}$. As is discussed in References 21 and 22, $k_{\bar{x}}$ (axial wavenumber) is related to the spectrum frequency $\bar{\omega}$ through the equation (for rotors)

$$\bar{\omega} = 2\pi n\, V/D - U k_{\bar{x}} \tag{76}$$

The tangential wavenumber corresponds to the spinning mode lobe number associated with discrete-frequency harmonic disturbances. Hence Reference 21 concludes that the integration over $k_{\bar{y}}$, for the purpose of estimating turbulence-rotor interaction noise, need only be over the range of $k_{\bar{y}}$ corresponding to propagating or cut-on modes in the fan duct.

Although the actual turbulence spectrum is the result of turbulence energy contributions over all wavenumbers $k_{\bar{y}}$, it is of interest to evaluate the portion of the tangential wavenumber spectrum that can produce acoustic energy. Therefore, an integration of ϕ^*_{nn} was carried out over finite limits corresponding to the cutoff limits of the duct at the frequencies and duct flow Mach numbers of interest. The integration limits can then be extended to $\pm\infty$ to determine the total turbulence spectral amplitude at frequency $\bar{\omega}$.

Defining $\phi_n(k_{\bar{x}})$ as the turbulence gust velocity spectrum, we need to evaluate

$$\phi_n(k_{\bar{x}}) = \frac{u^2}{4\pi L}\,\Phi(k_{\bar{x}}) \tag{77}$$

where

$$\Phi(k_{\bar{x}}) = \int_a^b \frac{c_1 k_{\bar{x}}^2 + c_2 k_{\bar{x}} k_{\bar{y}} + c_3 k_{\bar{y}}^2 + L^{-2}}{(L^{-2} + k_{\bar{x}}^2 + k_{\bar{y}}^2)^{5/2}} \, dk_{\bar{y}} \qquad (78)$$

and a and b are the lower and upper limits of $k_{\bar{y}}$ corresponding to duct (two-dimensional) cutoff. For a rotor, these limits are given by (see References 21 and 22)

$$\left.\begin{aligned} a &= -\,\chi/\sqrt{1-M_a^2} - 2\pi n/S \\ b &= +\,\chi/\sqrt{1-M_a^2} - 2\pi n/S \end{aligned}\right\} \qquad (79)$$

where

M_a = Axial flow Mach number U/c_o
χ = Frequency wavenumber $\bar{\omega}/c_o$
S = Rotor blade-to-blade spacing (pitch)
n = An integer, $-\infty \leq n \leq \infty$

Note that Reference 21 had an erroneous exponent of 1/2 in the denominator of $\Phi(k_{\bar{x}})$ given by Equation 78. Equation 78 can be integrated analytically. To do this we again introduce the transformation:

$$A^2 = 1 + \bar{k}_{\bar{x}}^{\,2} \quad \text{and} \quad \bar{k}_{\bar{y}} = A \tan\theta$$

where

$$\bar{k}_{\bar{x}} = Lk_{\bar{x}} \quad \text{and} \quad \bar{k}_{\bar{y}} = Lk_{\bar{y}}$$

Then

$$d\bar{k}_{\bar{y}} = A \sec^2\theta \, d\theta$$

and Equation 78 can be written as

$$\Phi(k_{\bar{x}}) = \frac{L^2}{A^4} \int_{\theta_a}^{\theta_b} \Big\{ [1 + k_{\bar{x}}^{\,2}] \cos^3\theta + [c_2 \bar{k}_{\bar{x}} A] \cos^2\theta \sin\theta + [c_3 A^2] \sin^2\theta \cos\theta \Big\} \, d\theta$$

This can be integrated analytically to give the following expression for $\Phi(k_{\bar{x}})$:

$$\begin{aligned}\Phi(k_{\bar{x}}) = \frac{L^2}{3A^4} \Bigg\{ & \left[1 + c_1 \bar{k}_{\bar{x}}^{\,2}\right] \left[(2 + \cos^2\theta_b) \sin\theta_b \right. \\ & \left. - (2 + \cos^2\theta_a) \sin\theta_a\right] \\ & - \left[c_2 \bar{k}_{\bar{x}} A\right] \left[\cos^3\theta_b - \cos^3\theta_a\right] \\ & + \left[c_3 A^2\right] \left[\sin^3\theta_b - \sin^3\theta_a\right] \Bigg\} \end{aligned} \tag{80}$$

where

$$\theta_a = \tan^{-1}(\bar{a}/A) \quad \text{and} \quad \theta_b = \tan^{-1}(\bar{b}/A) \tag{81}$$

and

$$\left.\begin{aligned}\bar{a} &= La = -(L/S)\left(\chi S/\sqrt{1-M_a^2} + 2\pi n\right) \\ \bar{b} &= Lb = +(L/S)\left(\chi S/\sqrt{1-M_a^2} - 2\pi n\right)\end{aligned}\right\} \tag{82}$$

Equations 77 and 80 through 82 define the turbulent velocity upwash spectrum for isotropic turbulence incident upon a rotor. The fraction of upwash energy that produces propagating modes is accounted for by the limits $\bar{a}$ and $\bar{b}$.

Having outlined the methodology to derive the gust upwash turbulent velocity spectrum using the simple case of isotropic turbulence incident upon a rotor, we now consider the case of axisymmetric turbulence incident upon a rotor. From Reference 22, the component three-dimensional wavenumber spectra analogous to Equations 67 through 69 are given by the following equations:

$$\Phi_{11} = (k_2^2 + k_3^2)\, F(k_1,k_2,k_3) \tag{83}$$

$$\Phi_{12} = -k_1 k_2\, F(k_1,k_2,k_3) \tag{84}$$

$$\Phi_{22} = (k_2^2 + k_3^2)\, F(k_1,k_2,k_3) + k_3^2\, G(k_1,k_2,k_3) \tag{85}$$

where F and G are given by

$$F = \frac{2}{\pi 2} \frac{L_a L_t^4 \overline{u_a^2}}{(1 + L_a^2 k_a^2 + L_t^2 k_t^2)^3} \tag{86}$$

$$G = \frac{2}{\pi 2} \frac{L_a L_t^4 \left[2 \overline{u_t^2} - \overline{u_a^2} (1 + L_t^2/L_a^2)\right]}{(1 + L_a^2 k_a^2 + L_t^2 k_t^2)^3} \tag{87}$$

and

$$k_t^2 = k_2^2 + k_3^2 \quad , k_a = k_1 \tag{88}$$

In the above expressions,

$\overline{u_a^2}$ = axial component of turbulence intensity

$\overline{u_t^2}$ = transverse component of turbulence intensity

L_a = axial turblence length scale

L_t = transverse turbulence length scale

It is assumed that the axis of symmetry of the turbulence is in the axial direction, and the turbulence intensities and length scales in the two component directions normal to the axis of symmetry are equal, being denoted by $\overline{u^2}_t$ and L_t, respectively. This allows a specification of radial turbulence intensity and length scale different from axial turbulence intensity and length scale.

We next substitute Equations 83 - 88 into Equation 66 and the result into Equation 71. Carrying out the algebra and subsequent integral evaluations as was done for the isotropic turbulence case, we get the following expression for ϕ^*_{nn}:

$$\phi^*_{nn} = \frac{L_a L_t \overline{u_a^2}}{4\pi A^5} \left\{ c_1 L_a^2 k_1^2 + E + c_2 L_t k_2 L_a k_1 + c_3 L_t^2 k_2^2 \right\} \tag{89}$$

where:

$$\begin{aligned}
A &= 1 + L_a^2 k_1^2 + L_t^2 k_2^2 \\
c_1 &= E + 3\,(L_t/L_a)^2 \cos^2\alpha_r \\
c_2 &= 6\,(L_t/L_a) \sin\alpha_r \cos\alpha_r \\
c_3 &= E + 3 \sin^2\alpha_r \\
E &= \sin^2\alpha_r + \varepsilon \cos^2\alpha_r \\
\varepsilon &= 2\,\overline{u_t^2}/\overline{u_a^2} - (L_t/L_a)^2
\end{aligned} \tag{90}$$

For isotropic turbulence, $\overline{u_a^2} = \overline{u_t^2}$ and $L_t = L_a$, so that $\varepsilon = 1$ and $E = 1$. Thus expression 90 reduces to previously derived formulae for isotropic turbulence. Note that L_t/L_a appears in combination with $\cos\alpha_r$ in the above expressions for c_1, c_2, and c_3. The turbulence axisymmetry manifests itself in the two parameters E and $(L_t/L_a)\cos\alpha_r$.

Again, defining $\phi_n(k_1)$ as in Equations 77 and 78, we obtain the following expressions for the total turbulence spectrum function $\Phi(k_{\bar{x}})$

$$\Phi(k_{\bar{x}}) = L_a^2 \int_{\bar{a}}^{\bar{b}} \frac{E + c_1\bar{k}_1^{\,2} + c_2\bar{k}_1\bar{k}_2 + c_3\bar{k}_2^{\,2}}{(1 + \bar{k}_1^{\,2} + \bar{k}_2^{\,2})^{5/2}}\, d\bar{k}_2 \tag{91}$$

where $\bar{k}_1 = L_a k_1$ and $\bar{k}_2 = L_t k_2$. Equation 91 has the same form as the isotropic formulation 78, except that the term in the numerator $1 + c_1\bar{k}_1^{\,2}$ is replaced by $E + c_1\bar{k}_1^{\,2}$. The integral evaluation has the same form with the same term modification. We therefore have the following closed-form expression for the axisymmetric turbulence incident upwash gust spectrum of a rotor:

$$\begin{aligned}
\Phi(k_1) = \frac{L_a^2}{3(1+\bar{k}_1^{\,2})^2} \Bigg\{ &\left[E + c_1\bar{k}_1^{\,2}\right]\Big[(2+\cos^2\theta_b)\sin\theta_b \\
&- (2+\cos^2\theta_a)\sin\theta_a\Big] - \left[c_2\bar{k}_1(1+\bar{k}_1^{\,2})^{1/2}\right] \\
&\left[\cos^3\theta_b - \cos^3\theta_a\right] + \left[c_3\,(1+\bar{k}_1^{\,2})\right]\left[\sin^3\theta_b - \sin^3\theta_a\right] \Bigg\}
\end{aligned} \tag{92}$$

where

$$\theta_b = \tan^{-1}\left(\bar{b}/\sqrt{1 + \bar{k}_1^{\,2}}\right)$$

$$\theta_a = \tan^{-1}\left(\bar{a}/\sqrt{1 + \bar{k}_1^{\,2}}\right) \qquad (93)$$

and

$$\bar{a} = L_t a, \quad \bar{b} = L_t b.$$

It was previously shown that the stator inflow turbulence spectrum Φ^*_{nn} can be derived from the rotor inflow turbulence spectrum by replacing α_r by $-\gamma_s$. Equations 92 and 93 can thus be applied to stator inflow turbulence with c_1, c_2, and c_3 replaced by the following:

$$\begin{aligned}
c_1 &= E + 3\,(L_t/L_a)^2 \cos^2\gamma_s \\
c_2 &= -6\,(L_t/L_a)\,\sin\gamma_s \cos\gamma_s \\
c_3 &= E + 3\,\sin^2\gamma_s \\
E &= \sin^2\gamma_s + \epsilon\,\cos^2\gamma_s
\end{aligned} \qquad (94)$$

The stator axisymmetric upwash turbulence spectrum is then given by:

$$\Phi_n(k_1) = \frac{\overline{u_a^2}}{4\pi L_a}\,\Phi(k_1) \qquad (95)$$

where $\Phi(k_1)$ is given by Equations 92, 93, and 94. The limits a and b given by Equation 79 or 82 are simpler for a stator because the integer n results from a summation over blade-passing frequency harmonic numbers, and only the n=0 term applies for homogeneous turbulence incident upon a stator blade row. Thus, a = -b, and this allows simplification of Equation 92 to the following form:

$$\Phi(k_1) = \frac{2\,L_a^2}{3(1 + \bar{k}_1^{\,2})^2}\left\{\left[E + c_1\bar{k}_1^{\,2}\right]\left[(2 + \cos^2\theta_b)\,\sin\theta_b\right] + \left[c_3(1 + \bar{k}_1^{\,2})\right]\left[\sin^3\theta_b\right]\right\} \qquad (96)$$

Equations 93 through 96 completely describe the stator incident turbulence upwash spectrum, and require as input u_a^2, u_t^2, L_a, and L_t. This formulation is used in the computer program.

4.0 ANALYTICAL WAKE MODEL STUDIES

Two analytical wake model studies were conducted during the course of this research program to complement the empirical wake model study described in Section 3.1. They were:

1. Analytical Correlation of Turbulent Wake Decay by Dr. C. Hah of General Electric.
2. Rotor Wake Momentum Integral Analysis by Prof. B. Lakshminarayana of the Pennsylvania State University.

A brief description of these studies is given in the following sections.

4.1 ANALYTICAL CORRELATION OF TURBULENT WAKE DECAY

The objective of this study was to provide a physically sound formulation for the development of a semiempirical model for the decay of mean velocity and turbulence intensity downstream of a turbofan rotor. As the primary application of the program is for predicting noise and unsteady vane forces due to rotor-stator interaction, the analysis is focused on the moderately near and far wake region (0.5 to 5.0 chord lengths downstream of the trailing edge of the blade).

4.1.1 Mean Velocity Decay Formulation

The evolution of turbulent wake behind a turbofan is governed by various length and velocity scales. Depending on the dominant scales, the entire wake field can be divided into several regions (very near, near, and far wake). Because of these distinctly different scales, one universal correlation for the entire wake field may not be feasible. In the following, a formulation is developed that is valid in the moderately near and far wake regions (approximately 0.5 to 5 chord lengths downstream of the trailing edge.)

The Far Wake - Far downstream of the trailing edge, the effects of loading, rotation, curvature, etc. on the wake evolution disappear and a similarity solution based on slow evolution can be derived. In this region, the difference between free stream velocity (W_o) and local velocity (W) is smaller than free stream velocity.

$$W_d = W_o - W << W_o \qquad (97)$$

With the above assumption, the governing momentum conservation equation in the streamwise direction can be simplified to the following (Reference 10):

$$-W_o \frac{\partial W_d}{\partial S} = \frac{1}{\rho} \frac{\partial \tau_t}{\partial n} \qquad (98)$$

where ρ is density and τ_t is turbulent shear stress. In the far wake region, simple mixing length theory can be used and the decrease of W_d is assumed to be a power function of s. Also, the mixing length is assumed to be proportional to the wake width, which is the spacing of the cascade (S) in the far wake. Then, the wake defect (W_d) should decrease in proportion to s^{-1} (See Reference 10).

Schlichting, using the above assumptions (Reference 10), obtained the following analytical distribution of velocity behind a row of cylinders:

$$W_d = \frac{W_o}{8\pi^3} \left(\frac{S}{L}\right)^2 \frac{S}{s} \cos\left(\frac{2\pi n}{S}\right) \tag{99}$$

where L is mixing length and the experimentally obtained value of L is

$$\frac{L}{S} = 0.103 \text{ for } \frac{c}{S} = 0.125 \text{ (c = Chord)}$$

For the turbofan wake, Equation (99) should be approximately valid in the far wake where the effects of blade loading, machine rotation, and other operating parameters disappear. Note, however, that Equation (99) gives only a single harmonic amplitude for the spectrum of the wake waveform, which does not agree with the experimental evidence.

<u>The Near Wake</u> - To extend the above analysis to the moderately near wake region, the following general form of mean velocity decay was assumed:

$$\frac{W_{dc}}{W_o} = A + \frac{B}{s+D} \tag{100}$$

where W_{dc} is the maximum wake defect and D represents different scale effects in the near wake and possible shift of origin of the wake. A can be used as another parameter for the wake shift (such as Mach number effect). However, A is dropped for the present derivation.

The formulation (100) should be correct at far downstream, where the effect of D should disappear. In the far downstream, the dominant parameter is the solidity of the cascade (c/S), and the following form is proposed for B:

$$B = A_1 \left(\frac{S}{c}\right)^3 \tag{101}$$

The effect of loading, machine rotation, blade geometry, etc., should be included in D. The following simple form is assumed for the current study:

$$D = A_2 C_D \frac{1}{2} s^{-p} \tag{102}$$

where C_D is blade drag coefficient and $p>1$.

Combining Equations (100), (101), and (102) yields:

$$\frac{W_{dc}}{W_o} = \frac{A_1 \, (S/c)^3}{s + A_2 \, C_D^{\frac{1}{2}} \, s^{-p}} \tag{103}$$

The formulation (103) can be reduced to the same form as the exact solution for the far wake given by Equation (99), and the coefficients A_2 and p for the near wake effect, along with A_1, can be optimized with data. It should be noted, however, that Equation (103) yields $W_{dc} = 0$ in the limit as $s \rightarrow 0$, which is physically unrealistic. Thus, selecting A_1 and A_2 to give a satisfactory data match may prove difficult.

4.1.2 Turbulence Intensity Decay Formulation

For the general correlation of the turbulence quantities, a far wake solution is first derived. Then the formulation is generalized for the moderately near wake region.

To evaluate proper length scales for the decay of turbulence quantities at far wake, the following two scales are defined:

L_s = the scale of change in the streamline direction

L_n = the scale of change in the normal direction.

then

$$\frac{\partial U}{\partial n} = O\left(\frac{W_{dc}}{L_n}\right) \tag{104}$$

$$\frac{\partial U}{\partial s} = O\left(\frac{W_{dc}}{L_s}\right)$$

and

$$-\overline{uv} = O(\mu^2), \quad \overline{u^2} = O(\mu^2), \quad \overline{v^2} = O(\mu^2)$$

where μ is turbulence velocity scale, u and v are fluctuating velocity components, and O( ) indicates the order of magnitude.

From the continuity equation, an order-of-magnitude analysis yields the following:

$$V = O\left(W_{dc} \; \frac{L_n}{L_s}\right) \tag{105}$$

Using the order analysis of (104) and (105), the cross-stream momentum equation in the far wake can be simplified as follows (see Reference 24):

$$\frac{\partial \overline{v^2}}{\partial n} = -\frac{1}{\rho}\frac{\partial P}{\partial n} \tag{106}$$

Integration of Equation (106) yields

$$\frac{P}{\rho} + \overline{v^2} = \frac{P_o}{\rho} \tag{107}$$

The streamwise momentum equation in the far wake can be written,

$$U\frac{\partial U}{\partial s} + V\frac{\partial U}{\partial n} = -\frac{1}{\rho}\frac{\partial P}{\partial s} - \frac{\partial}{\partial s}\overline{u^2} - \frac{\partial}{\partial n}\overline{uv} + \nu\left(\frac{\partial^2 U}{\partial s^2} + \frac{\partial^2 U}{\partial n^2}\right) \tag{108}$$

Combining (107) and (108)

$$U\frac{\partial U}{\partial s} + V\frac{\partial v}{\partial n} + \frac{\partial}{\partial s}\left(\overline{u^2} - \overline{v^2}\right) + \frac{\partial}{\partial n}\left(\overline{uv}\right) = \nu\left(\frac{\partial^2 U}{\partial s^2} + \frac{\partial^2 U}{\partial n^2}\right) \tag{109}$$

The orders of the magnitude of the terms in Equation (109) are estimated with Equations (104) and (105). For the high Reynolds number and in the far wake,

$$\frac{UL}{\nu} \to \infty \text{ and } \frac{L_n}{L_s} \to 0$$

Then the first and the fourth terms remain large and should balance each other. The order of magnitude of these terms is:

$$U\frac{\partial U}{\partial s} = U^2\frac{W_{dc}}{L_s} = \left(\frac{W_o}{\mu}\cdot\frac{U}{\mu}\cdot\frac{L_n}{L_s}\right)\frac{\mu^2}{L_n} \tag{110}$$

and

$$\frac{\partial}{\partial n}\left(\overline{uv}\right) = -\frac{\mu^2}{L_n} \tag{111}$$

Therefore

$$\frac{W_o}{\mu}\cdot\frac{W_{dc}}{\mu}\cdot\frac{L_n}{L_s} = 0\ (L_n) \tag{112}$$

In the far wake,

$$\frac{\mu}{W_o} = O\left(\frac{L_n}{L_s}\right) \tag{113}$$

Therefore,

$$\frac{\mu}{W_{dc}} = O\ (L_n) \tag{114}$$

The derived Equation (114) indicates that turbulence intensities are of the same order as the velocity defect. The decay of turbulence intensities should also be proportional to the s^{-1}, as the mean velocity decay.

Based on the above assumptions and order-of-magnitude argument, the following generalized correlation is proposed for the decay of the turbulence quantities:

$$\frac{\left(\overline{u_i^2}\right)_m}{W_o} = \frac{T_1 \times (S/c)^3}{s + T_2\ C_D\ \frac{1}{2}\ s^{-T_3}} \tag{115}$$

where T_1, T_2, T_3, should be determined from the experimental data.

In the near wake, the turbulence structure is highly anisotropic, but becomes isotropic in the far wake. Therefore, different values of T_2 and T_3 are suggested for different intensity components. Various effects on the local structure of turbulence (loading, Mach number, rotation, etc.) can also be explicitly included in T_2.

The correlation method used in Section 3.1 is based on the following correlation function:

$$y = \frac{ax + b}{cx + d} \tag{116}$$

The above equation can be rewritten as follows:

$$y = A' + \frac{b'}{x+c'} \tag{117}$$

Equation (116), which is used for mean velocity and turbulence quantities, shows various features similar to Equations (103) and (115), and actually represents various experimental data very well. However, Equation (116) has one shortcoming in that the mean velocity and turbulence quantities do not decay properly far downstream in the limit as $s \to \infty$. Over the range of data correlations, however, the formulation works quite well.

Equations (103) and (115) are based on the analytical solution at far downstream and the effect of blade spacing is explicitly included, although the dependency is somewhat arbitrary. By optimizing the coefficients of the correlations, these formulations can be successfully used both in the moderately near and far wake regions. Any additional effects on the decay of the wake can be systematically included in the formulation. However, Equations (103) and (115), have the wrong behavior in the limit as s → 0 (near wake), and this would more likely pose a problem in establishing satisfactory data correlations than would the s → ∞ behavior (y → constant instead of zero) of Equation (116). It was therefore decided to use Equation (116).

4.2 ROTOR WAKE MOMENTUM INTEGRAL ANALYSIS

An analysis of a rotor wake was carried out using the momentum integral technique. Two momentum integral equations on each side of the wake provided the necessary closure equations to predict wake defect as a function of downstream distance. Professor B. Lakshminarayana of Pennsylvania State University performed this analysis as a consultant to this program.

4.2.1 Introduction

The wake from a compressor or fan rotor blade is three-dimensional and turbulent with substantial radial component. The wake profile and the decay depend on various blade and flow parameters such as solidity, stagger angle, blade loading, Reynolds number, Mach number, inlet turbulence, etc. All of the earlier analyses available for the rotor wake are based on simplifying assumptions. Raj and Lakshminarayana (Reference 25) assumed that velocity profiles are similar and linearized the equations (assuming that the velocity defect is small compared to the freestream velocity) to derive analytical expressions for the decay of the streamwise and radial velocities. Their expressions are given by

$$\frac{W}{U_e} = \frac{u_c}{U_e} \left\{ \frac{-8(A+\phi)\nu_\tau^2 + U_e^2(BS\cos\lambda)^2}{4B\Omega\sin\lambda(s^2\cos^2\lambda)\nu_\tau} \right\} \cdot A_2\cos\left\{ \left[\frac{A+\phi}{B}\right]^{1/2}\eta \right\}$$

where A and B are given by

$$A = B^2R_s^2 \text{ and } (A + \phi)/B = \pi^2/4$$

and $\frac{u_c}{U_e} = \exp\left[-\frac{BU_eS\cos\lambda}{2\nu_\tau}\left(\frac{s}{S\cos\lambda}\right)\right]$

where u_c and U_e are streamwise velocity defect at the centerline and freestream velocity (streamwise), respectively. W is the local radial velocity and ϕ is a rotation parameter given by

$$\phi = \frac{\Omega^2S^2}{U_e^2}\{\sin^2\lambda\cos^2\lambda\}.$$

All other notations are explained in the nomenclature (Section 8.0).

Lakshminarayana (Reference 26) later used the momentum integral approach and the linearized equations to predict the decay of the axial, tangential, and radial velocity components, and they showed good agreement with measured trends in a low-speed fan rotor. The analysis is restricted to free vortex flow. This analysis was extended by Reynolds and Lakshminarayana (Reference 2) to other types of rotors.

Recently, Kool and Hirsh (Reference 27) used the Pennsylvania State data to include the effect of streamwise pressure gradients in the decay of the rotor wake. Their correlation agreed well with the Pennsylvania State data on the rotor wake characteristics.

Hah and Lakshminarayana (Reference 28) developed a computer program to solve the exact equations of motion in three dimensions, employing a Reynolds stress model. This is an elliptic formulation with initial conditions (at the trailing edge) derived from the experimental data. They also provided an expression for the near-wake characteristics for two-dimensional wakes.

The present analysis is a new formulation and the analysis is valid for near wake as well as the far wake. The defect in velocities could be large in this formulation. The analysis and equations are presented in this report; results from the analysis will be evaluated at a later date.

4.2.2 Momentum Integral Analysis

The most suitable coordinate system for the analysis of the rotor wake is the s, n, r system shown in Figure 31. The streamwise coordinate aligned with the external streamline is given by s, n is the principal normal, and r is the radial direction. The corresponding velocities are u, v, and w, respectively. The analysis given below is valid for an asymmetric and incompressible rotor wake, even through its extension to include the compressibility effect is fairly straightforward. The profile in the n direction is assumed to be Gaussian in the momentum integral formulation.

The equations of motion in the coordinate system shown in Figure 31 are given in Reference 29.

Radial Momentum Equation:

$$W \frac{\partial W}{\partial r} + V \frac{\partial W}{\partial n} + U \frac{\partial W}{\partial s} + 2\Omega V\cos\lambda + 2\Omega U\sin\lambda - \frac{U^2}{r} \sin^2\lambda - \frac{V^2}{r} \cos^2\lambda$$

$$= - \frac{1}{\rho} \frac{\partial p^*}{\partial r} \quad \frac{\partial}{\partial n} (\tau_{rn}) \tag{118}$$

where

$$p^* = p - \frac{\rho\Omega^2 r^2}{2} .$$

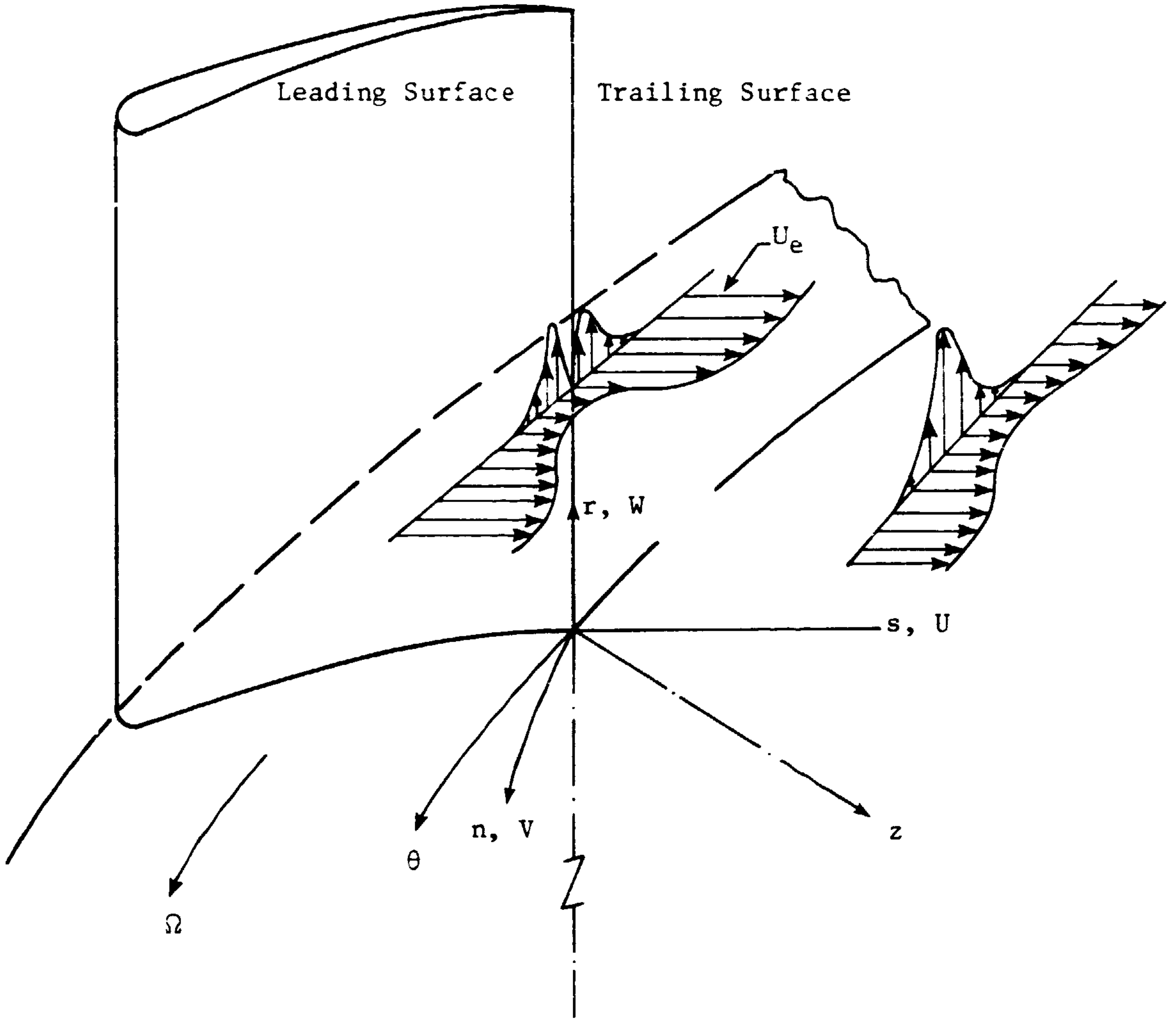

Figure 31. Characteristics of Rotor Wake and Notations Used.

The turbulence normal stresses are neglected in this equation. If the pressure gradient in the n direction is assumed to be very small (boundary layer approximation), the following approximation can be made;

$$\frac{1}{\rho}\frac{\partial p_e}{\partial r} = \frac{1}{\rho}\frac{\partial p}{\partial r} = -2\Omega U_e \sin\lambda + \frac{U_e^2}{r}\sin^2\lambda .$$

Hence, Equation (118) reduces to

$$W\frac{\partial W}{\partial r} + V\frac{\partial W}{\partial n} + U\frac{\partial W}{\partial s} - 2\Omega(U_e - U)\sin\lambda + \frac{U_e^2 - U^2}{r}\sin^2\lambda = \frac{\partial}{\partial n}(\tau_{rn}) \qquad (119)$$

where τ_{rn} is the turbulent shear stress in the radial direction.

Streamwise Momentum Equation:

If the streamwise pressure gradient ($\partial p/\partial s$) is neglected, the streamwise momentum equation reduces to (Reference 29).

$$U\frac{\partial U}{\partial s} + V\frac{\partial U}{\partial n} + W\frac{\partial U}{\partial r} - 2\Omega W\sin\lambda + \frac{UW}{r}\sin^2\lambda = \frac{1}{\rho}\frac{\partial \tau_{sn}}{\partial n} \qquad (120)$$

Continuity Equation:

$$\frac{\partial U}{\partial s} + \frac{\partial V}{\partial n} + \frac{\partial W}{\partial r} + \frac{W}{r} = 0 \qquad (121)$$

The momentum integral equations for a three-dimensional blade boundary layer on a turbomachinery rotor were derived in Reference 30. Even though the procedure for the wake is similar, there are major differences between the two in evaluating the integration from the wake center to the wake edge. The integration is carried out from the wake center to the edge of the wake on the suction side, and a similar integration is carried out from the wake center to the edge on the pressure side.

The essential differences between the momentum integral analysis for a boundary layer and a wake can be illustrated for two-dimensional flows (Reference 31). Let s and n be streamwise and normal directions, with W = 0 and $\partial/\partial r = 0$. The continuity equation then reduces to

$$\frac{\partial V}{\partial n} = -\frac{\partial U}{\partial s} \qquad (122)$$

$$V = -\int_0^n \frac{\partial U}{\partial s}\, dn + C. \qquad (123)$$

The velocity V is not zero at the wake centerline, so

$$V = - \int \frac{\partial U}{\partial s}\, dn + V_c \tag{124}$$

The appearance of V_c on the right side is the essential new element in the momentum integral analysis for a wake. Using the standard procedure (Reference 32), the following momentum integral equation can be derived for two-dimensional viscous flows:

$$\frac{d\theta_1}{ds} = \theta_1 \frac{H + 2}{U_e} \frac{dU_e}{dx} = \frac{V_c}{U_e} \left(\frac{U_e - U_c}{U_e} \right)$$

where θ_1 is the momentum thickness, H is the shape factor, and U_c is velocity at the centerline.

4.2.3 Momentum Integral Analysis for the Rotor Wake

Following a procedure similar to the two-dimensional flow described above, the momentum integral equations for 3D flows can be derived by integrating Equations (119) and (120) in the normal (n) direction. The velocity V in these equations is derived from the continuity Equation (121),

$$V = - \int_0^n \left(\frac{\partial U}{\partial s} + \frac{\partial W}{\partial r} + \frac{W}{r} \right) dn + V_c \tag{125}$$

and substituted in Equations (119) and (120) before integrating. For the sake of brevity the detailed derivation is not given here, but is similar to the 3D boundary layer momentum integral derivation given by Mager (Reference 33). The additional terms appearing in the wake equations arise because of nonzero values of V_c in Equation (125). The momentum integral equations governing the wake on each side of the wake center is given by:

$$\begin{aligned} &\frac{\partial \theta_{11}}{\partial s} + \frac{2}{Ue} \frac{\partial U_e}{\partial s} \theta_{11} + \frac{\partial \theta_{12}}{\partial r} + \frac{2}{U_e} \frac{\partial U_e}{\partial r} \theta_{12} + \frac{1}{U_e} \frac{\partial U_e}{\partial s} \delta_1 + \frac{1}{U_e} \frac{\partial U_e}{\partial r} \delta_2 \\ &\quad + \frac{\sin^2\lambda}{r} (\theta_{12} + \theta_{21}) - 2 \frac{\delta_2 \Omega \sin\lambda}{U_e} = \frac{V_c}{U_e} \left(\frac{U_e - U_c}{U_e} \right) \end{aligned} \tag{126}$$

and

$$\begin{aligned} &\frac{\partial \theta_{21}}{\partial s} + \frac{2}{U} \frac{\partial U_e}{\partial s} \theta_{21} + \frac{\partial \theta_{22}}{\partial r} + \frac{2}{U} \frac{\partial U_e}{\partial r} \theta_{22} + \frac{\sin^2\lambda}{r} (\theta_{22} - \theta_{11} - \delta_1) \\ &\quad + 2\delta_1 \frac{\Omega \sin\lambda}{U_e} = \frac{V_c}{U_e} \left(\frac{W_e - W_c}{U_e} \right) \end{aligned} \tag{127}$$

where

$$\theta_{11} = \int_{o}^{\delta} \frac{U}{U_e}\left(1 - \frac{U}{U_e}\right) dn \tag{128}$$

$$\theta_{12} = \int_{o}^{\delta} \frac{W}{U_e}\left(1 - \frac{U}{U_e}\right) dn \tag{129}$$

$$\theta_{21} = - \int_{o}^{\delta} \left(\frac{UW}{U^2{}_e}\right) dn \tag{130}$$

$$\theta_{22} = - \int_{o}^{\delta} \left(\frac{W}{U_e}\right)^2 dn \tag{131}$$

$$\delta_1 = \int_{o}^{\delta} \left(1 - \frac{U}{U_e}\right) dn, \quad \delta_2 = - \int_{o}^{\delta} \frac{W}{U_e} dn \tag{132}$$

where δ is the distance beyond the wake edge.

There are two such equations [Equation (126) and (127) for each side], and there are nine unknowns, θ_{11}, θ_{12}, θ_{21}, θ_{22}, δ_1, δ_2, V_c, U_c, W_c on each side (total of fifteen knowns, as V_c, U_c, W_c are the same for both sides of the wake). Hence, some simplifying assumptions have to made made in order to couple various thicknesses in the equations. Such an assumption can be made in selecting the velocity profiles U(n) and W(n). It has been well-established in low speed tests in References 2 and 3 that velocity profiles are similar for both the streamwise and the radial velocity. The similarity profiles are given by

$$\frac{U}{U_e} = 1 - u_c \exp\left(-0.693\ \eta^2\right) \tag{133}$$

$$\frac{W}{U_e} = \frac{W_c}{U} \exp\left(-0.693\ \eta^2\right) \tag{134}$$

where

$$\eta = \frac{n}{L_p}, \text{ or } \frac{n}{L_s}$$

L_p, L_s = wake width at half the depth on the pressure and suction surfaces of the wake, respectively.

Substituting Equation (133) and (134) in (128) through (132), the thicknesses can be expressed in terms of velocity defects. For example,

$$\theta_{11} = L \int_0^\infty [1 - u_c \exp(-0.693\ \eta^2)][u_c \exp(-0.693\ \eta^2)]\ d\eta$$

$$= L \frac{u_c}{U_e} \left[1.06 - 0.7530 \frac{u_c}{U_e} \right] \tag{135}$$

since

$$\int_0^\infty e^{-a^2 x^2}\ dx = \frac{\sqrt{\pi}}{2a}$$

Similarly,

$$\theta_{12} = 0.7530\ L \frac{W_c}{U_e} \frac{u_c}{U_e} \tag{136}$$

$$\theta_{21} = -L \left[\frac{W_c}{U_e} 1.06 - \frac{u_c}{U_e} \frac{W_c}{U_e} 0.7530 \right] \tag{137}$$

$$\theta_{22} = - \frac{L W_c{}^2}{U_e^2} [0.7530] \tag{138}$$

$$\delta_1 = L \frac{u_c}{U_e} 1.06 \tag{139}$$

$$\delta_2 = -L \frac{W_c}{U_e} 1.06 \tag{140}$$

Substituting Equations (135) through (140) in Equations (126) and (127), we get

<u>s momentum</u>:

$$\frac{\partial F}{\partial s} + \frac{2}{U_e}\left(\frac{\partial U_e}{\partial s}\right) F + \frac{\partial}{\partial r}\left(0.71\ G \frac{W_c}{U_e}\right) + \frac{2}{U_e}\frac{\partial U_e}{\partial r}\left(0.71\ G \frac{W_c}{U_e}\right) + \frac{1}{U_e} G \frac{\partial U_e}{\partial s}$$

$$- \frac{H}{U_e}\frac{\partial U_e}{\partial r} + \frac{\sin^2\lambda}{r}\left(0.71\ G - F \frac{U_e}{u_c}\right)\frac{W_c}{U} + \frac{2H\Omega \sin\lambda}{U_e} \tag{141}$$

$$= \frac{V_c}{U_e}\left(\frac{U_e - U_c}{U_e}\right)$$

r momentum:

$$\frac{\partial}{\partial s}\left(-F\,\frac{W_c}{u_c}\right) + \frac{2}{U_e}\,\frac{\partial U_e}{\partial s}\left(-F\,\frac{W_c}{u_c}\right) + \frac{\partial}{\partial r}\left(-0.71\,H\,\frac{W_c}{U_e}\right) + \frac{2}{U_e}\,\frac{\partial U_e}{\partial r}\left(-0.71\,H\,\frac{W_c}{U_e}\right)$$

$$+ \frac{\sin^{2\lambda}}{r}\left(-0.71\,H\,\frac{W_c}{U_e} - F - G\right) + 2\,G\,\frac{\Omega \sin\lambda}{U_e} = \frac{V_c}{U_e}\left(\frac{W_e - W_c}{U_e}\right) \qquad (142)$$

where

$$F = \frac{Lu_c}{U_e}\left[1.06 - 0.7530\,\frac{u_c}{U_e}\right] \qquad (143)$$

$$G = 1.06\,L\,\frac{u_c}{U_e} \qquad (144)$$

$$H = 1.06\,L\,\frac{W_c}{U_e} \qquad (145)$$

Each side of the wake has two equations: Equations (141) and (142), for a total of five unknowns; L_p, L_s, u_c, W_c, and V_c. The velocity U_e (s,n) is either prescribed or derived from an inviscid analysis.

An additional closure equation is needed to complete the set of equations for predicting the variation of V_c, u_c, W_c, L_p, and L_s with distance. Constieux and Aupoix (Reference 31) employ Head's entrainment equation. Head related the growth of a turbulent boundary layer to the amount of fluid the boundary layer entrains from the irrotational flow around it (see Reference 34), to yield an auxillary equation which came to be known as the Head's entrainment equation. In the case of a wake at sufficient downstream distances, the entrainment was shown to be proportional to the velocity defect at the wake center line (Reference 34). By definition, the mass flow rate within a boundary layer of thickness δ is directly proportional to $(\delta-\delta_1)$, where δ_1 is the displacement thickness. Hence, the streamwise variation of the mass flow rate within a boundary layer (in other words, entrainment) is represented by the streamwise derivative of $(\delta-\delta_1)$. Coustieux and Aupoix have developed the three dimensional formulation of the Head's entrainment equation which is given by:

$$\frac{1}{U_e}\,\frac{\partial}{\partial s}\left[U_e\,(\delta-\delta_1)\right] - \frac{\partial \delta_2}{\partial r} = C_E + \frac{V_c}{U_e} \qquad (146)$$

where C_E = Head's entrainment factor.

4.2.4 Calculation Procedure

On the pressure side, there are two equations governing the rotor wake flow (Equations (141) and (142) with L_p in place of L). There are also two equations on the suction side (Equations (141) and (142) with L_s in place of L). These equations, along with Head's entrainment equation (146), can be solved simultaneously to derive the values of the wake width $(L_s + L_p)$, velocity defect (u_c), radial velocity at the wake center (W_c), and the wake trajectory (V_c) as a function of the downstream distance. These equations can be programmed to predict the wake properties. During the initial calculation, the terms $\partial U_e/\partial s$ can be neglected. It may be possible to correct for the change in U_e through a blockage coefficient derived from the wake width and profile. The programming and calculations were not carried out during the present study due to a lack of time and resources. The analysis does, however, offer promise of the ability to predict rotor wake structure, accounting for many more influential parameters with much less empiricism than the current correlation approach (Section 3.1). It is strongly recommended that this effort be pursued as a follow-on study to the current program.

5.0 MODEL EVALUATION

The empirical rotor wake/vortex model developed in Section 3.0 was evaluated through data-theory comparisons for three rotors (Rotor 55, JT15D fan rotor, and Rotor 67) and various parametric studies. Table II lists certain key geometric and aerodynamic parameters for Rotor 55, JT15D fan rotor, Rotor 67, and various parametric studies. Section 5.1 deals with the data-theory comparisons, and Section 5.2 deals with the parametric studies.

5.1 DATA-THEORY COMPARISONS

The data-theory comparisons are performed for rotors which were not part of the data base used to develop the empirical wake relationships, so that this set of data-theory comparisons constitutes an independent validation of the empirical model. The inviscid velocity gradient, WTIV (see Figure 15), has been set equal to zero for all the data-theory comparisons. Subsection 5.1.1 describes the data theory comparisons for Rotor 55; Subsection 5.1.2 addresses the same for JT15D fan rotor; and Subsection 5.1.3 deals with Rotor 67.

5.1.1 Rotor 55 Data-Theory Comparisons

The rotor wake and stator upwash harmonic data for Rotor 55 were obtained from References 19 and 6 for three rotor speeds. The geometric data and aerodynamic data at the three rotor speeds were obtained from Reference 35. The section drag coefficients at the required span locations were computed from the measured profile loss coefficients, reported in Reference 35.

Figure 32 compares the predicted and measured axial variation of centerline wake defect (W_{dc}/W_0) and semiwake width (δ/S) at 30% span from tip for 80% and 115% design rpm's. The data at 80% design rpm were taken with and without the tunnel velocity. The data at 115% design rpm were taken with a tunnel velocity of 41.1 m/s. The wake defect predictions at 80% design rpm agree reasonably well with the data. The theory overpredicts the semiwake width for the 80% design rpm case. Both the predictions and data indicate that the influence of the tip speed at constant loading (that is, for operation along the fan operating line) on the wake characteristics is negligible. The agreement between the data and predictions for the semiwake width at 115% design rpm is very reasonable.

Figure 33 shows the comparison of the measured and predicted gust harmonic amplitude and broadband turbulence spectra at 30% span from tip for the 80% design rpm case. The levels of the data are adjusted so that the prediction and the data for the BPF level of the gust harmonic amplitude agree. The measured broadband level is adjusted by the same ΔdB and compared to the prediction. The measured and predicted gust harmonic spectra show similar trends (monotonically falling with increasing frequency) for this spanwise location, which is close to midspan location where effects of the tip vortex are not

Table II. Key Geometric and Aerodynamic Parameters for Rotor 55, JT15D Fan, and Rotor 67.

Parameter	Rotor-55	JT15D Fan Rotor	Rotor-67(1)
Diameter, Inches	20.00	21.00	19.54
Number of Rotor Blades	15	28	22
Number of Stator Vanes	25(2)	66	34
Hub-Tip Ratio	0.460	0.434	0.477
Tip Clearance, Inch	0.0315	0.0236	0.0157
Design rpm	8020	15800	16043
Tip Speed at Design rpm, fps	700	1448	1407
Rotor Solidity at Tip	0.896	1.34	1.327
Rotor Solidity at Midspan	0.998	1.53	1.772
Rotor Solidity at Hub	1.186	---	2.879
Camber at Tip, °	22.65	N.A.(3)	11.41
Camber at Midspan, °	39.54	N.A.(3)	17.57
Camber at Hub, °	45.22	N.A.(3)	54.12
Aerodynamic Chord at Tip, Inches	3.651	3.086	3.655
Aerodynamic Chord at Pitch, Inches	3.033	2.536	3.646
Aerodynamic Chord at Hub, Inches	2.412	---	3.720
Drag Coefficient, C_D at Tip(4)	0.107	0.075	0.034
C_D at Pitch(4)	0.038	0.031	0.012
C_D at Hub(4)	0.128	---	0.102

Table II. Key Geometric and Aerodynamic Parameters for Rotor 55, JT15D Fan Rotor, and Rotor 67 (Concluded).

Parameter	Rotor 55	JT15D Fan Rotor	Rotor 67(1)
Work Coefficient, W_θ at Tip(4)	0.486	0.314	0.382
W_θ at Pitch(4)	0.688	0.371	0.509
W_θ at Hub(4)	1.098	---	1.095
Rotor Outlet Relative Flow Angle, β_2 at Tip °(4)	40.2	63.1	60.6
β_2 at Pitch, °(4)	19.1	52.4	41.8
β_2 at Hub, °(4)	-4.9	---	-6.7

Notes

1. Rotor 67 is a two-stage rotor. The parameters tabulated here correspond to the first stage.

2. A 25-vane stator was employed in the wake study of Reference 19 and an 11-vane stator was employed in the aerodynamic performance study of Reference 35.

3. N.A. - Not available.

4. Quoted Aerodynamic Performance for Rotor 55 is at 80% design rpm;

   Quoted Aerodynamic Performance for JT15D fan rotor is at 66% design rpm;

   Quoted Aerodynamic Performance for Rotor 67 is at 100% design rpm.

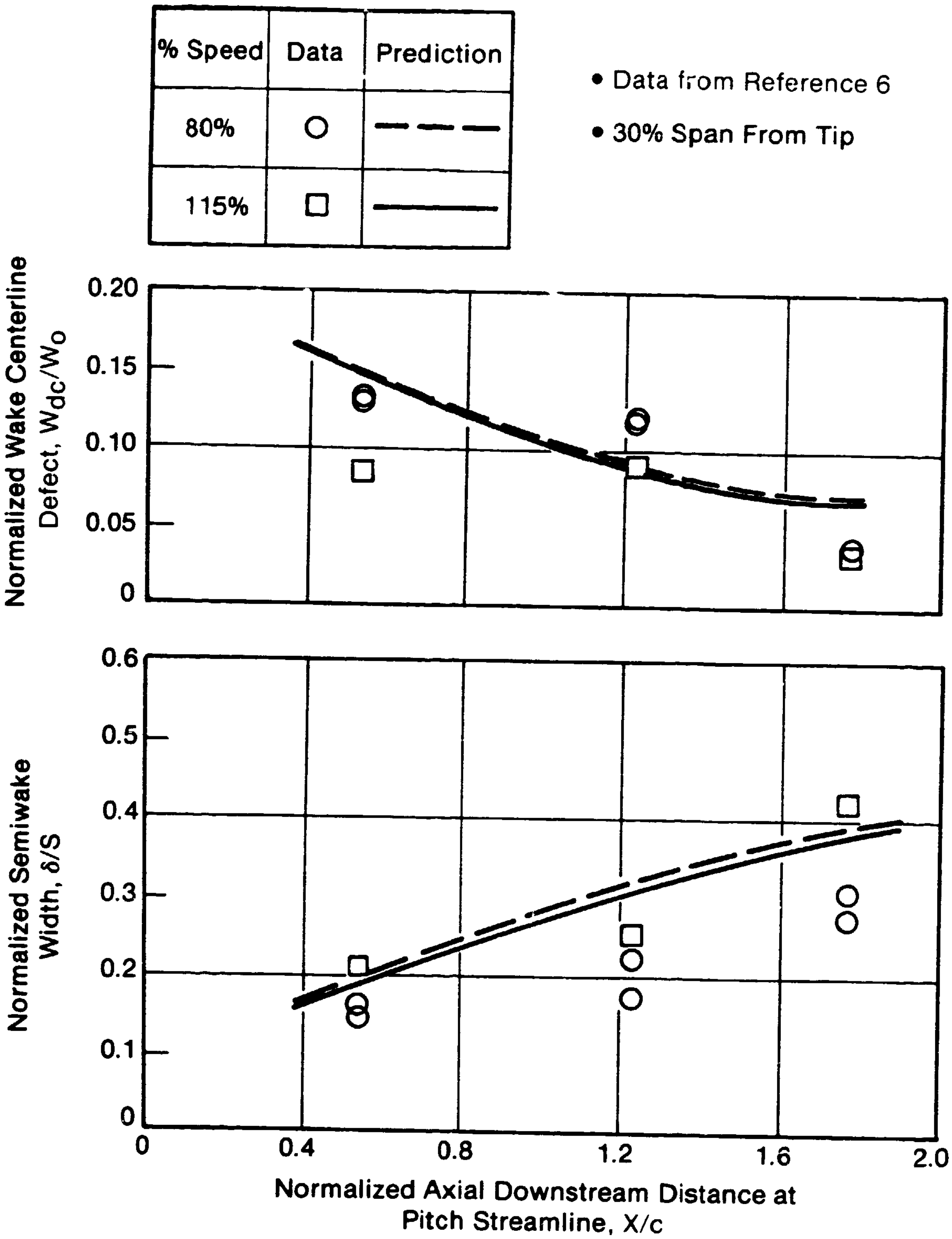

Figure 32. Comparison of Predicted and Measured Axial Variation of Wake Defect and Semiwake Width at Two Speeds for Rotor 55.

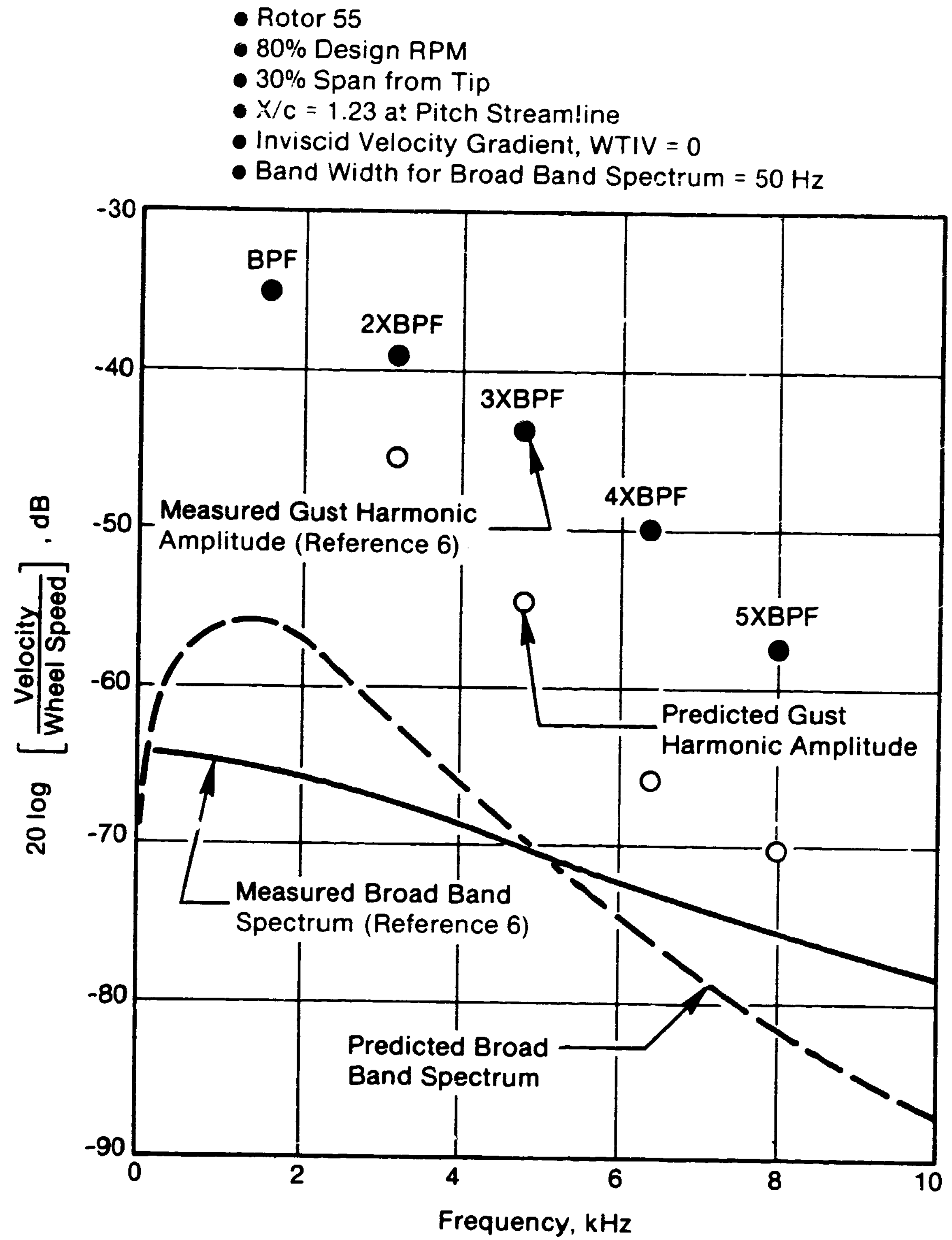

- Rotor 55
- 80% Design RPM
- 30% Span from Tip
- X/c = 1.23 at Pitch Streamline
- Inviscid Velocity Gradient, WTIV = 0
- Band Width for Broad Band Spectrum = 50 Hz

Figure 33. Comparison of Measured and Predicted Gust Harmonic Amplitude and Broadband Turbulence Spectra.

significant. The predicted gust harmonic spectrum shows steeper fall with frequency than the measurement, since the predicted semiwake width is larger than the measured semiwake width. As semiwake width increases, the wake profile over a blade-to-blade spacing resembles a sinusoidal function with a period equal to the blade-to-blade spacing. Hence, the contribution of higher harmonics to the spectrum decreases sharply and the BPF dominates the spectrum. The band width for the broadband data and predictions is 50 Hz. The predicted broadband spectrum shows a steeper fall with frequency above 1.5 kHz compared to the data. However, they do show comparable trends. Keep in mind though, that the measured broadband data show a significant amount of scatter, and the best estimate of the random data was made for this comparison.

Figures 34 and 35 compare the predicted and measured gust harmonic amplitude and broadband turbulence spectra at two spanwise locations (10% span from tip and 50% span from tip) for the 96% design rpm case. The agreement between the measured and predicted gust harmonic amplitude levels and the broadband spectra for the 10% span location from the tip is good. This spanwise location is influenced by the tip vortex. The tangential location of the tip vortex for this computation was selected to be $b_t/S = 0.42$. The agreement between the data and predictions for the broadband turbulence spectra is also good. For the case of 50% span location from the tip (see Figure 35), the data show that the even multiples of BPF show higher levels than the odd multiples (for example, 2xBPF level is higher than BPF, 4xBPF level is higher than 3xBPF). This is a typical trend if there are two defects within one blade-to-blade spacing, as would be the case when a strong tip vortex exists in that region. However, at this spanwise location, which is sufficiently far from the tip region, one would anticipate negligible influence of the tip vortex. The predictions indicate a monotonic fall-off with increase in harmonic number, since the prediction model is based on the rationale described above. At present this behavior of the measured gust harmonic spectra is not understood. The predicted and measured broadband levels show reasonable agreement.

Figures 36 and 37 compare the predicted and measured gust harmonic amplitude spectra at three axial spacings for the 80% design rpm case at two spanwise locations (10% and 30% span from tip). The tangential location of the tip vortex is chosen to be $b_t/S = 0.42$, as before. For the case of 10% span from tip, both the data and theory predict the 2xBPF levels to be higher than BPF levels at all three axial spacings (Figure 36). As described earlier, such a trend occurs whenever a tip vortex is dominant. Both the data and theory indicate that the influence of the tip vortex is considerable, even at the farthest axial spacing ($X/c = 1.77$ at the pitch streamline). The trends predicted by the theory are quite representative of the data. Figure 37 compares the predictions and measurement of the gust harmonic spectra for the 80% design rpm case at a typical midspan location (30% span from tip). Note the monotonic fall-off of the harmonic content at the midspan location, showing that influence of tip vortex at the midspan location at all axial spacings is negligible. At smaller axial spacings, the semiwake width is smaller. The wake shape resembles a delta function when the semiwake width goes to zero. In such a case, the Fourier coefficients of higher harmonics do not fall off rapidly. This situation is observed at $X/c = 0.54$. As the wake spreads out at larger spacings, the fall-off rate of the harmonics increases. The trends

2 OF 2

N85 26668 UNCLAS

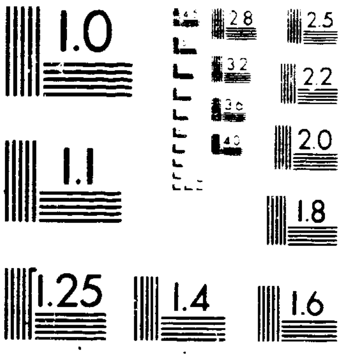

MICROCOPY RESOLUTION TEST CHART
NATIONAL BUREAU OF STANDARDS
STANDARD REFERENCE MATERIAL 1010a
ANSI and ISO TEST CHART No. 2

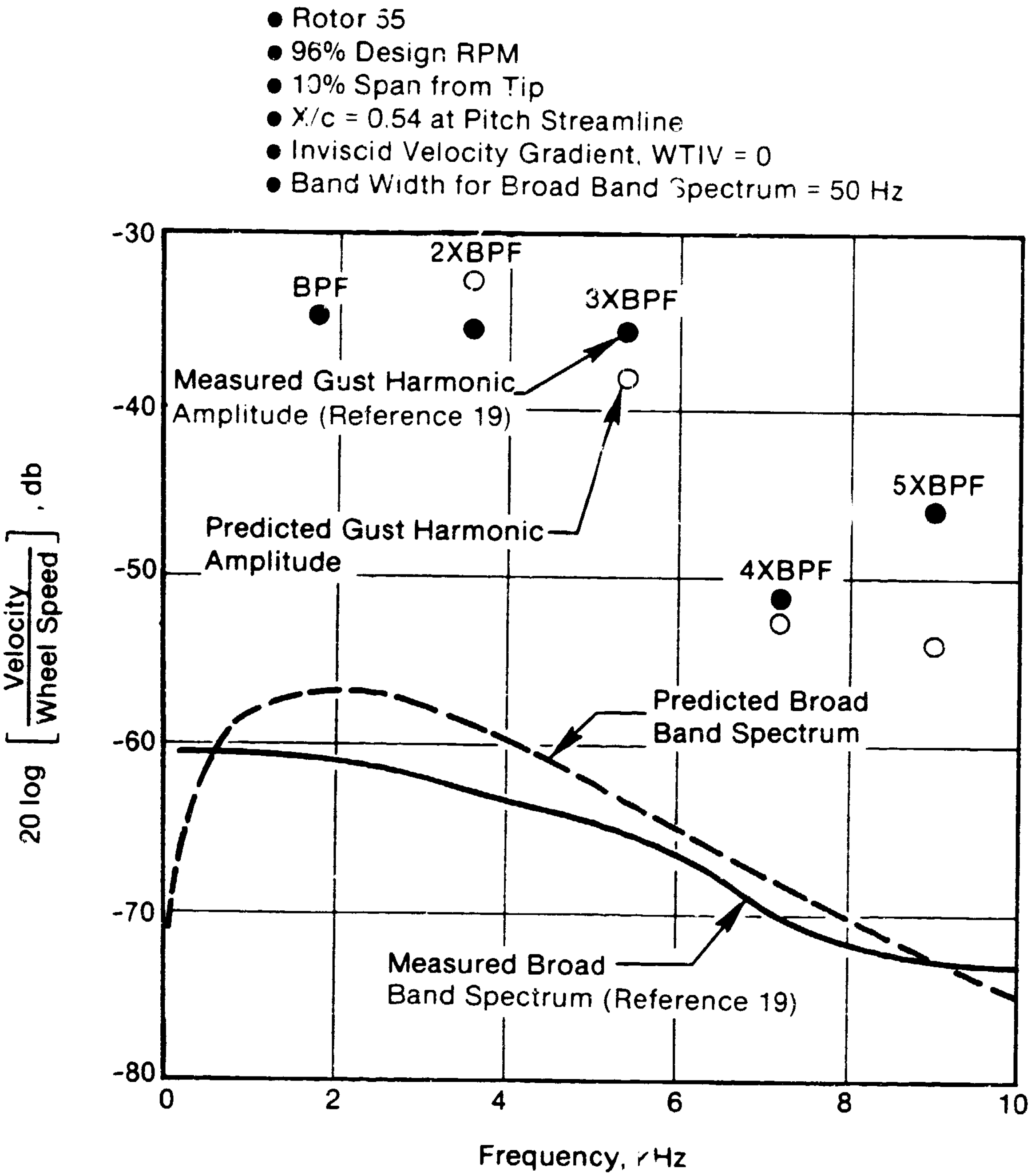

Figure 34. Comparison of Measured and Predicted Gust Harmonic Amplitude and Broadband Turbulence Spectra.

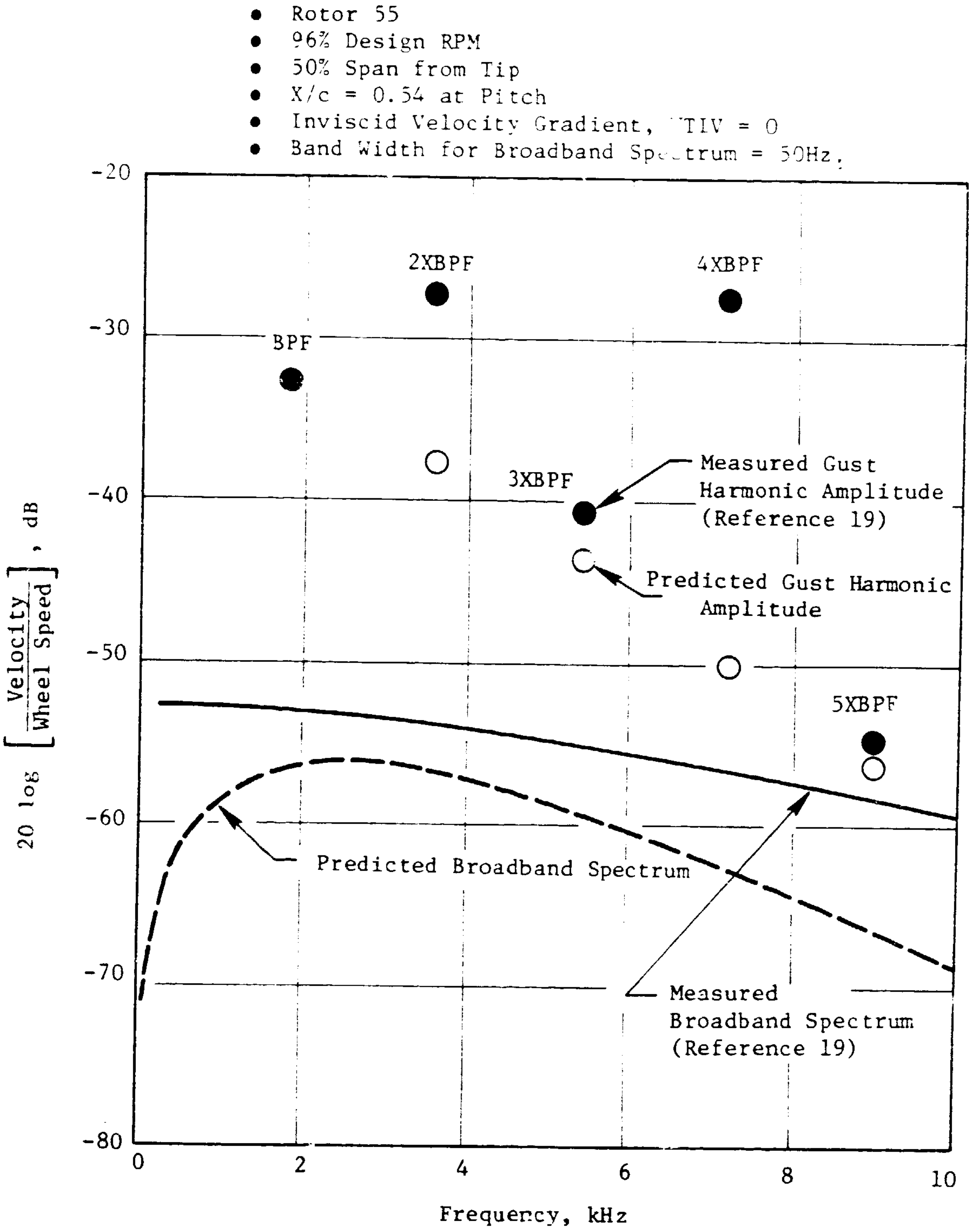

Figure 35. Comparison of Measured and Predicted Gust Harmonic Amplitude and Broadband Turbulence Spectra.

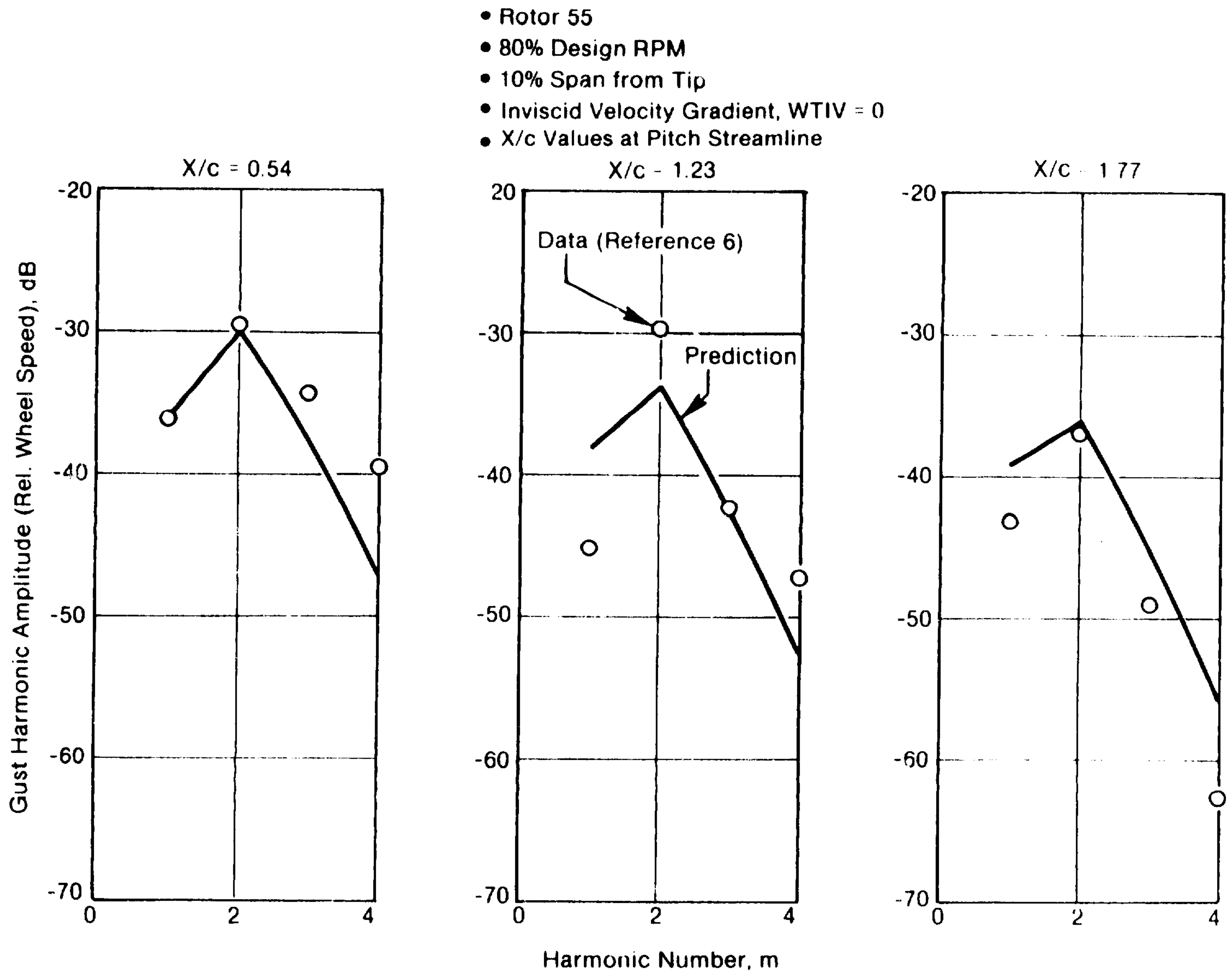

Figure 36. Comparison of Measured and Predicted Gust Harmonic Amplitude Spectrum at Three Rotor/Stator Spacings.

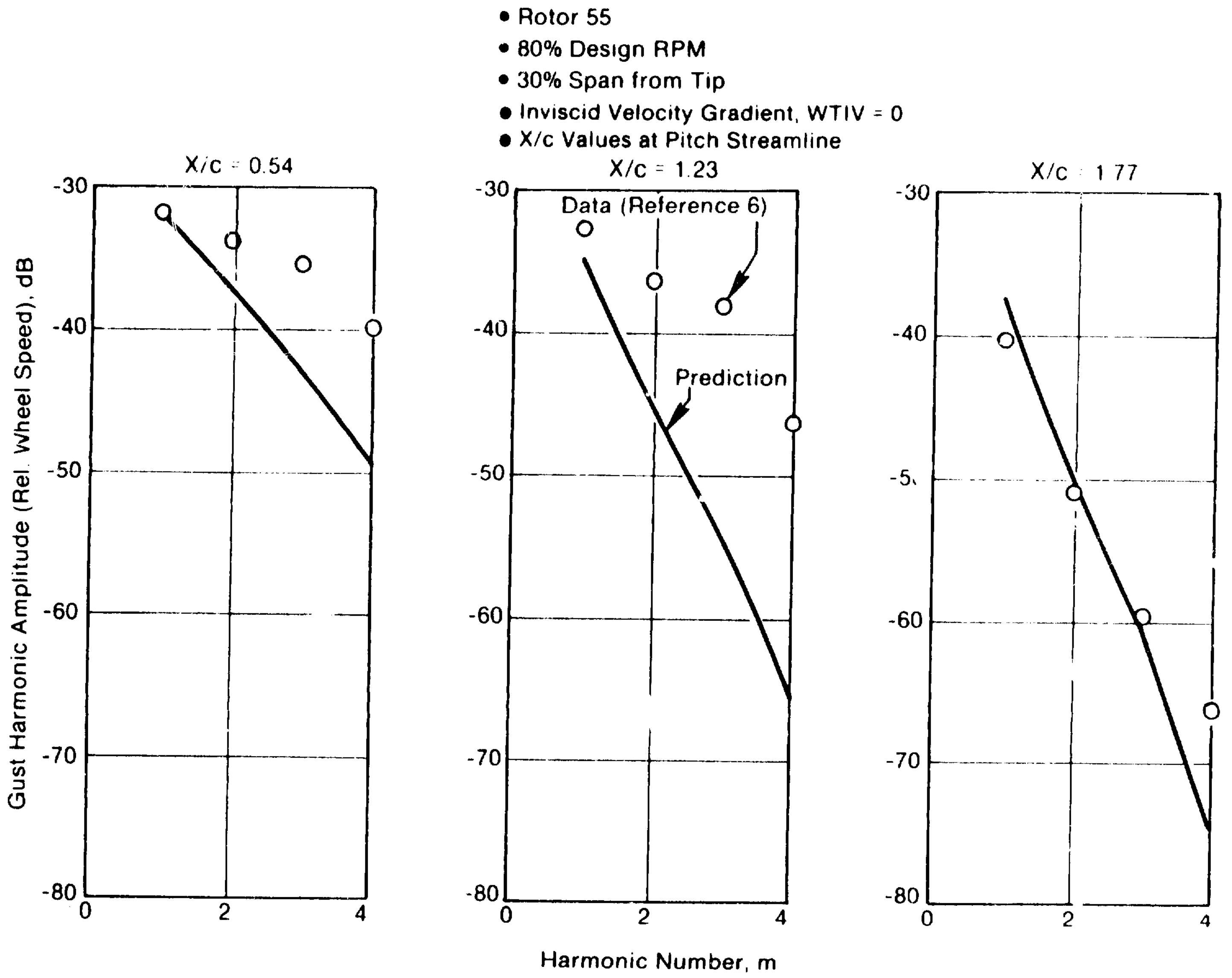

Figure 37. Comparison of Measured and Predicted Gust Harmonic Amplitude Spectrum at Three Rotor/Stator Spacings.

predicted agree well with the data. The maximum deviation in data and prediction is seen for $X/c = 1.23$. The measured semiwake width at this location is smaller than the predicted semiwake width (see Figure 32). Thus, the predictions at $X/c = 1.23$ show a steeper fall-off rate for higher harmonics than do the data.

Figures 38 and 39 are similar comparisons of the data and predictions of the gust harmonic amplitude for the 115% design rpm case at two span locations. The data at 10% span from the tip indicate that a strong tip vortex (Figure 38) is absent. Hence, the predictions for this case do not include any tip vortex. Note that the agreement between the theory and predictions is good at $X/c = 0.54$ and 1.23. The predictions at $X/c = 1.77$ show a similar fall-off rate as the data, except for the 4xBPF tone. Figure 39 compares the data and predictions at 30% span from the tip location. The agreement is quite good at $X/c = 0.54$ and 1.7, and the fall-off rate of data and predictions agree with each other at $X/c = 1.23$.

In summary, the empirical rotor wake and vortex model is seen to predict very well the observed trends both in the gust harmonic speeds and the turbulence spectra for Rotor 55.

5.1.2 JT15D Fan Rotor Data-Theory Comparisons

The relevant data for JT15D fan rotor data-theory comparisons were taken from Reference 36. The wake upwash component was measured at four spanwise stations on the bypass stator and the gust harmonic data at four speeds (43%, 54%, 61%, and 66% design rpms) were supplied for the data-theory comparisons (Reference 36). Figure 40 compares the spanwise distribution of certain key geometric and aerodynamic parameters relevant to rotor wake studies for Rotor 55 and for the JT15D fan rotor. The aerodynamic data for Rotor 55 are for the 80% design rpm case, and the aerodynamic data for JT15D fan rotor are for the 66% design rpm case. The section drag coefficients for Rotor 55 were computed from the measured profile loss coefficients. The section drag coefficients for the JT15D fan rotor were computed from the profile loss coefficient, which in turn has been correlated with the diffusion factor for NACA 65-(A_{10})-series and double-circular-arc blades (Reference 11). The axial spacing for Rotor 55 corresponds to the case when X/c at the pitch streamline equals 0.54 (Note the high rotor solidity and the large rotor exit relative flow angle of the JT15D fan rotor compared to those of Rotor 55).

The rotor wake and vortex computations were performed with the tip vortex tangential location of $b_t/S = 0.45$. The gust harmonic amplitudes are computed using a 10 fps velocity as a reference velocity so that a one-to-one comparison to the data could be made. Figure 41 compares the measured and predicted gust harmonic amplitude spectra at four spanwise locations of the bypass stator at 66% design rpm. The predicted gust harmonic amplitude spectra at all the spanwise locations are in very good agreement with the data. In order to evaluate the spanwise extent of influence of the tip vortex on the gust harmonic spectra, computations were performed by suppressing the tip vortex calculations. Figure 42 compares the measured and predicted gust harmonic spectra

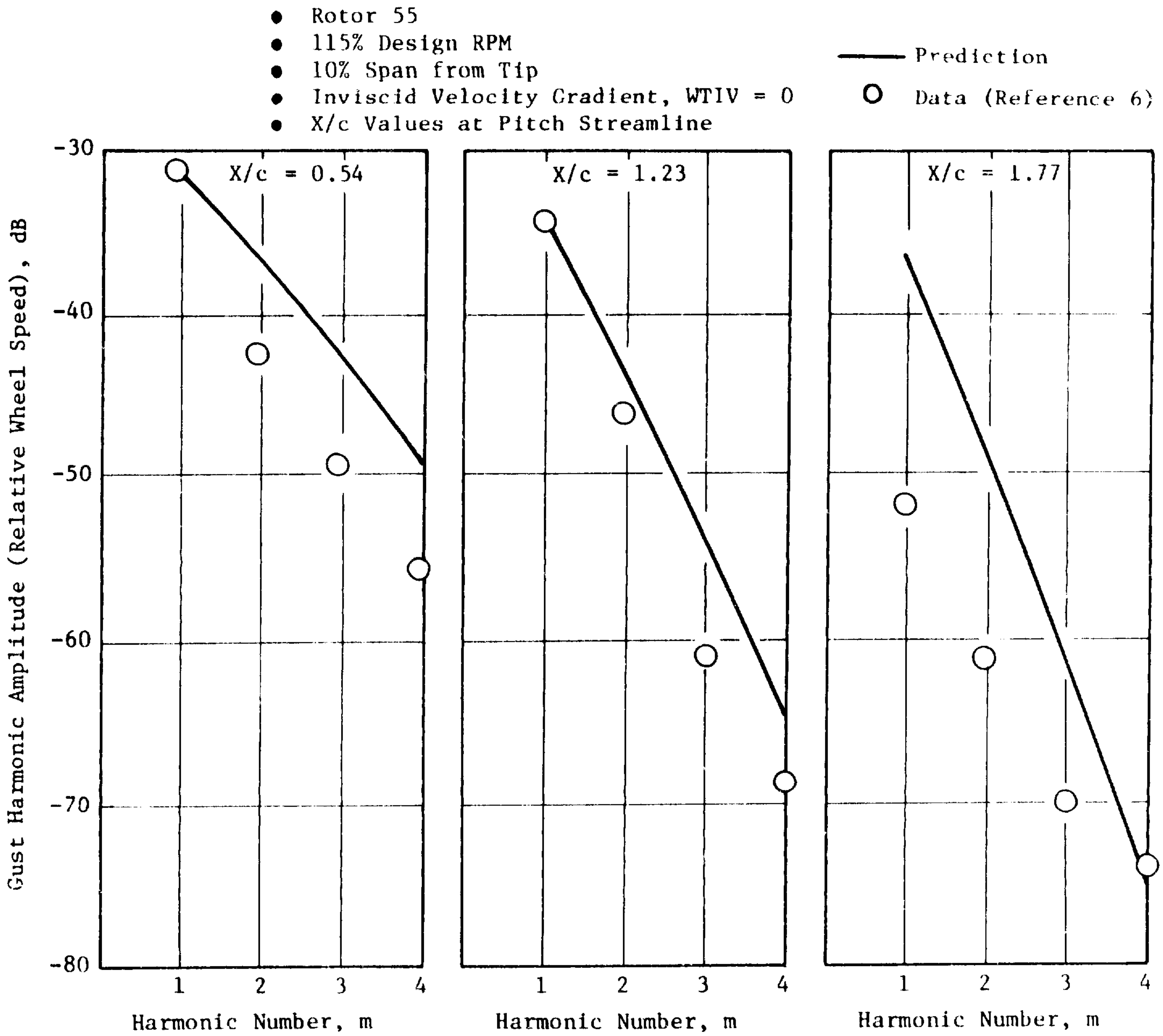

Figure 38. Comparison of Measured and Predicted Gust Harmonic Amplitude Spectrum at Three Rotor/Stator Spacings.

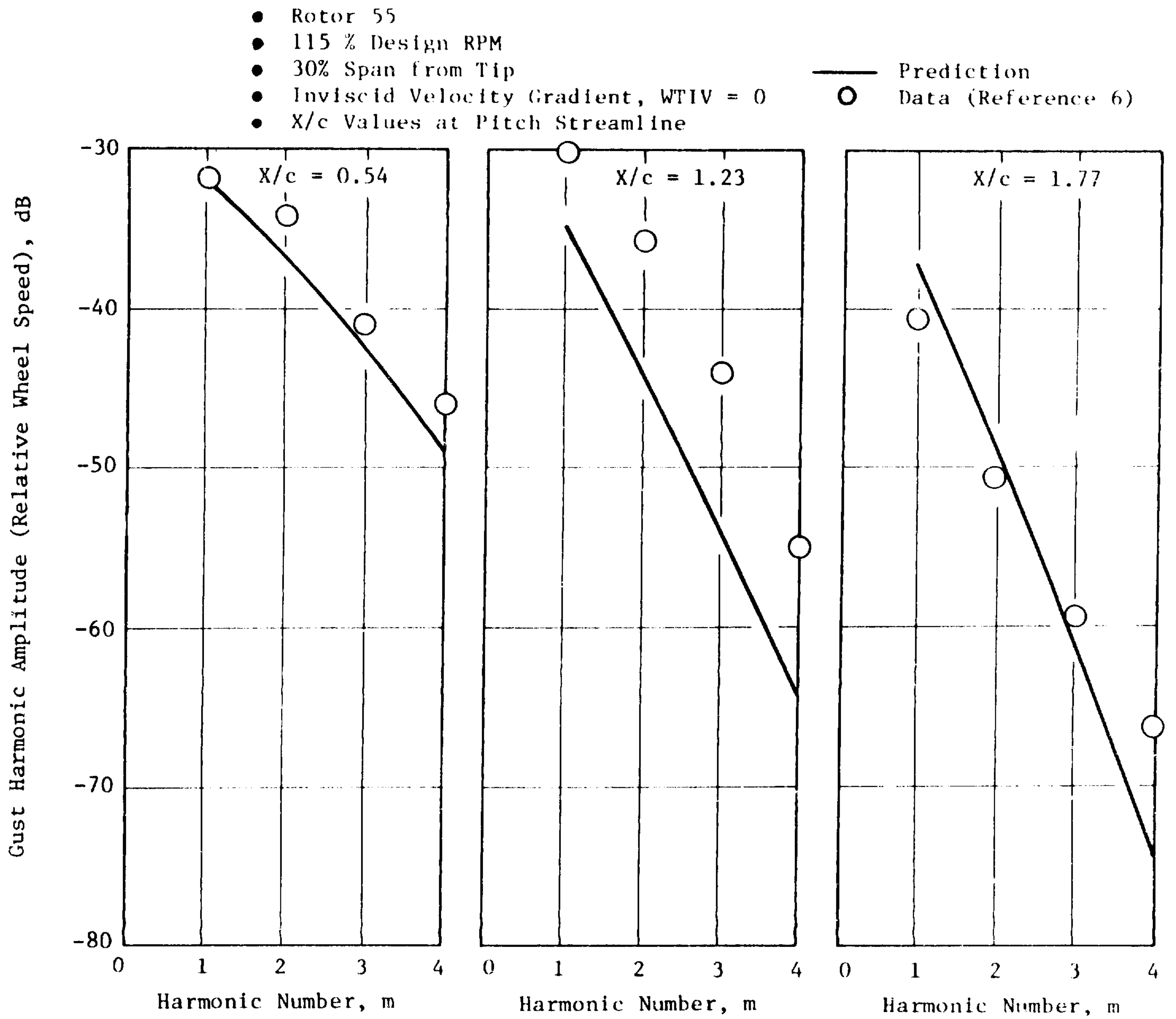

Figure 39. Comparison of Measured and Predicted Gust Harmonic Amplitude Spectrum at Three Rotor/Stator Spacings.

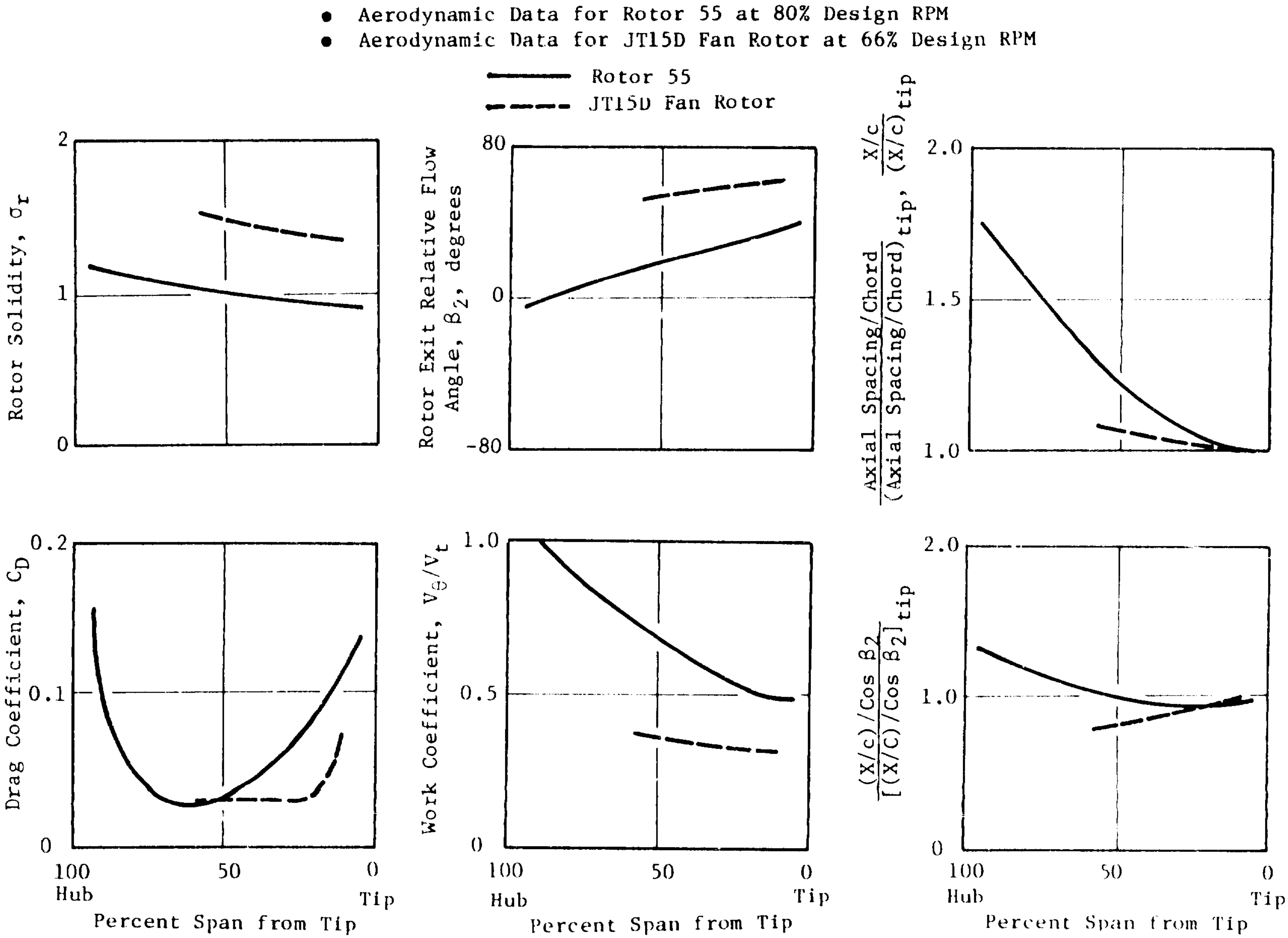

Figure 40. Comparison of Certain Key Geometric and Aerodynamic Parameters of Rotor 55 and JT15D Fan Rotor.

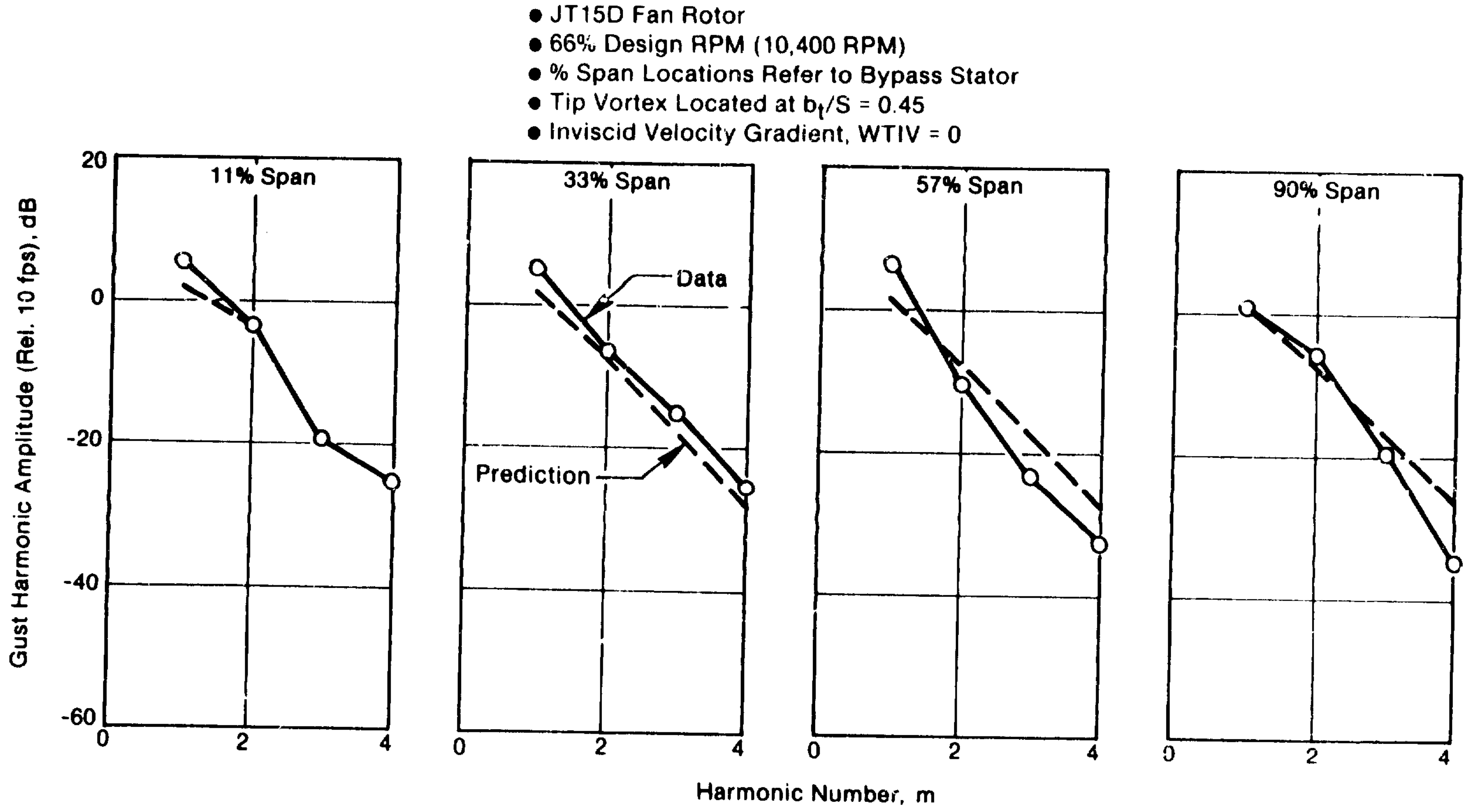

Figure 41. Comparison of Data and Predictions of the Gust Harmonic Amplitude Spectra at Four Spanwise Locations.

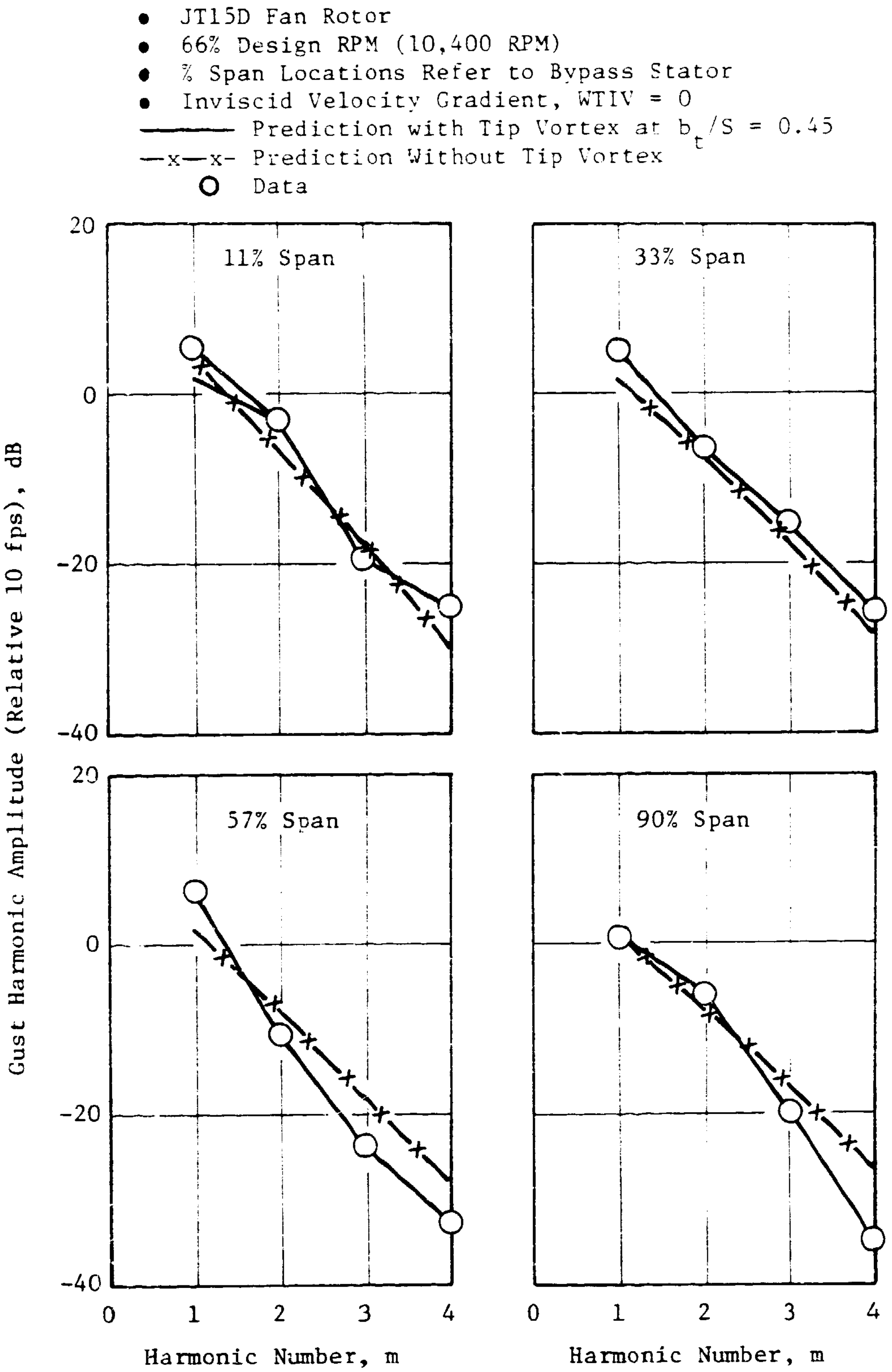

Figure 42. Comparison of Measurement and Predictions With and Without Tip Vortex of Gust Harmonic Amplitude Spectra at Four Spanwise Locations.

with and without tip vortex computations at the four spanwise locations for the 66% design rpm case. The axial spacing between the rotor and the bypass stator of JT15D fan, normalized by the rotor aerodynamic chord, is approximately 0.70 (Reference 36). For the above rotor-stator spacing, we note from Figure 42 that the tip vortex influences only the 11% span location from the tip and has no influence at the other spanwise locations.

Figures 43, 44, and 45 compare the data and predictions of the gust harmonic amplitude spectra for 61%, 54%, and 43% design rpm's respectively. For all these calculations, the tangential location of tip vortex is the same as that for the 66% design rpm case, namely, $b_t/S = 0.45$. The data and predictions agree very well at all the spanwise locations at 61% design rpm (Figure 43). The agreement between data and predictions for the 54% design rpm case at 11%, 57%, and 90% span of the bypass stator is excellent (Figure 44). Data and predictions at the 33% span locations disagree on absolute levels, but show similar fall-off rates. For the case of 43% design rpm, the data at the tip streamline (11% span) show a more pronounced tip vortex contribution than is predicted by the model. The agreement can be improved by adjusting the tangential location of the tip vortex. But, owing to the excellent agreement between data and predictions at three out of four speeds, the tip vortex location was maintained at $b_t/S = 0.45$ for this speed also. The data and predictions agree well at the 57% and 90% span locations, and show similar fall-off rates at the 33% span location.

In summary, the agreement between the predicted and measured gust harmonic amplitude spectra for the JT15D fan rotor at various span locations for various rpms along the engine operating line has been found to be excellent.

5.1.3 Rotor 67 Data-Theory Comparisons

Rotor wake measurements made on Rotor 67 at NASA Lewis using a Laser Doppler Velocimeter were supplied to us (Reference 36). This formed the third data set for evaluating the empirical wake model. The rotor wake measurements supplied were at the peak efficiency point, and essentially included blade passage averaged relative velocity wake profile data at various spanwise and axial stations. Rotor 67 is a two-stage fan having low-aspect-ratio first stage blading. The rotor wake measurements supplied were for the first stage rotor. These rotor wake measurements were obtained with the first stage rotor-alone configuration. The geometric and aerodynamic data for Rotor 67 were obtained from Reference 37. As in the case of Rotor 55, the section drag coefficients were computed from the measured profile loss coefficients.

Wake centerline defect normalized by the free stream velocity and semi-wake width normalized by the blade-to-blade spacing data were extracted from the wake profiles of the relative velocity data at the peak efficiency point (100% design rpm). At this operating point, a considerable portion of the first stage rotor has supersonic wheel speeds. Measurements revealed that for about 50% of span from the tip, the shock loss coefficient is equal to or greater than the profile loss coefficient, implying that more than half the span of the rotor blade has supersonic flow over it (Reference 37). Only the

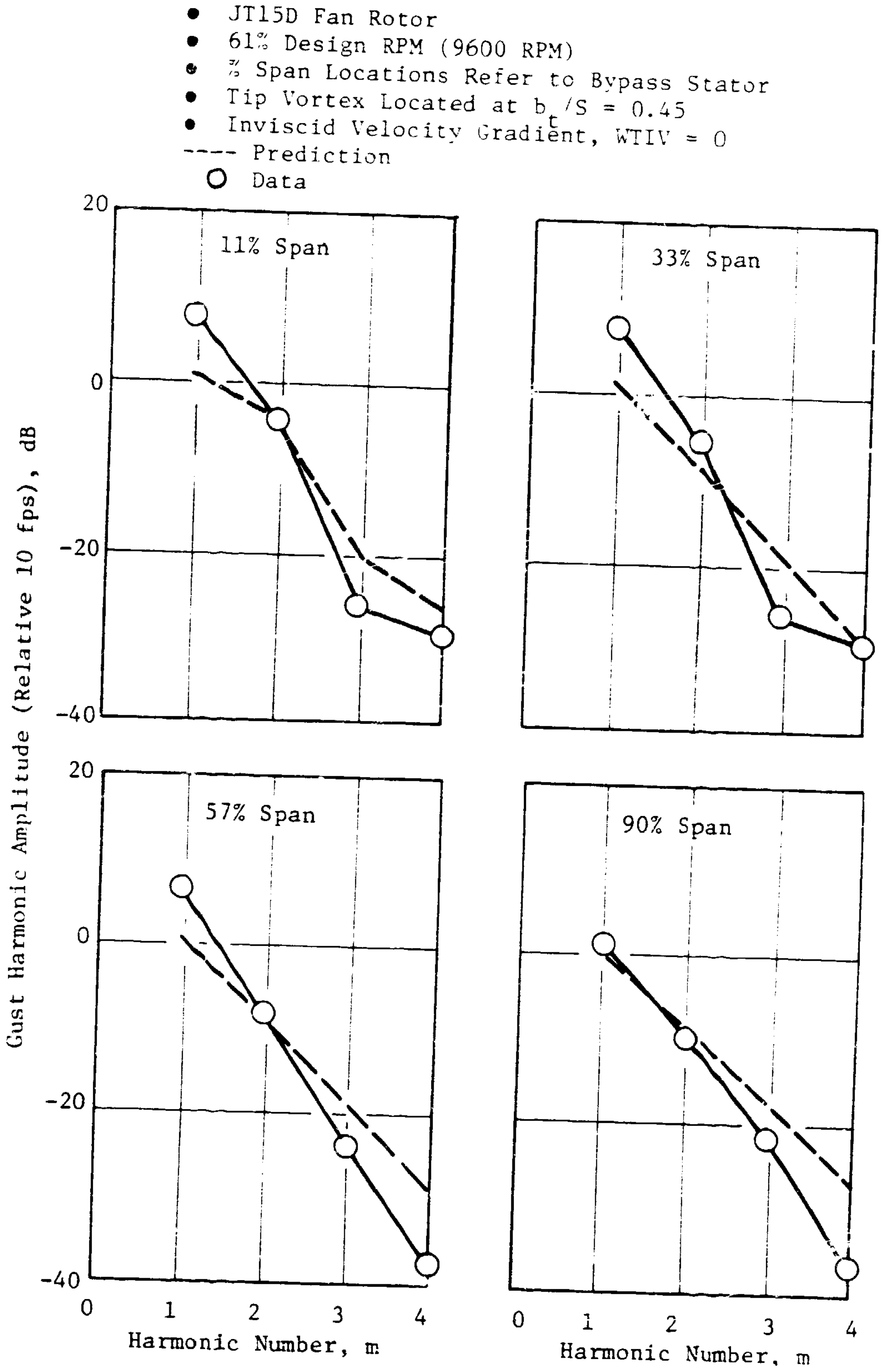

Figure 43. Comparison of Data and Predictions of the Gust Harmonic Amplitude Spectra at Four Spanwise Locations.

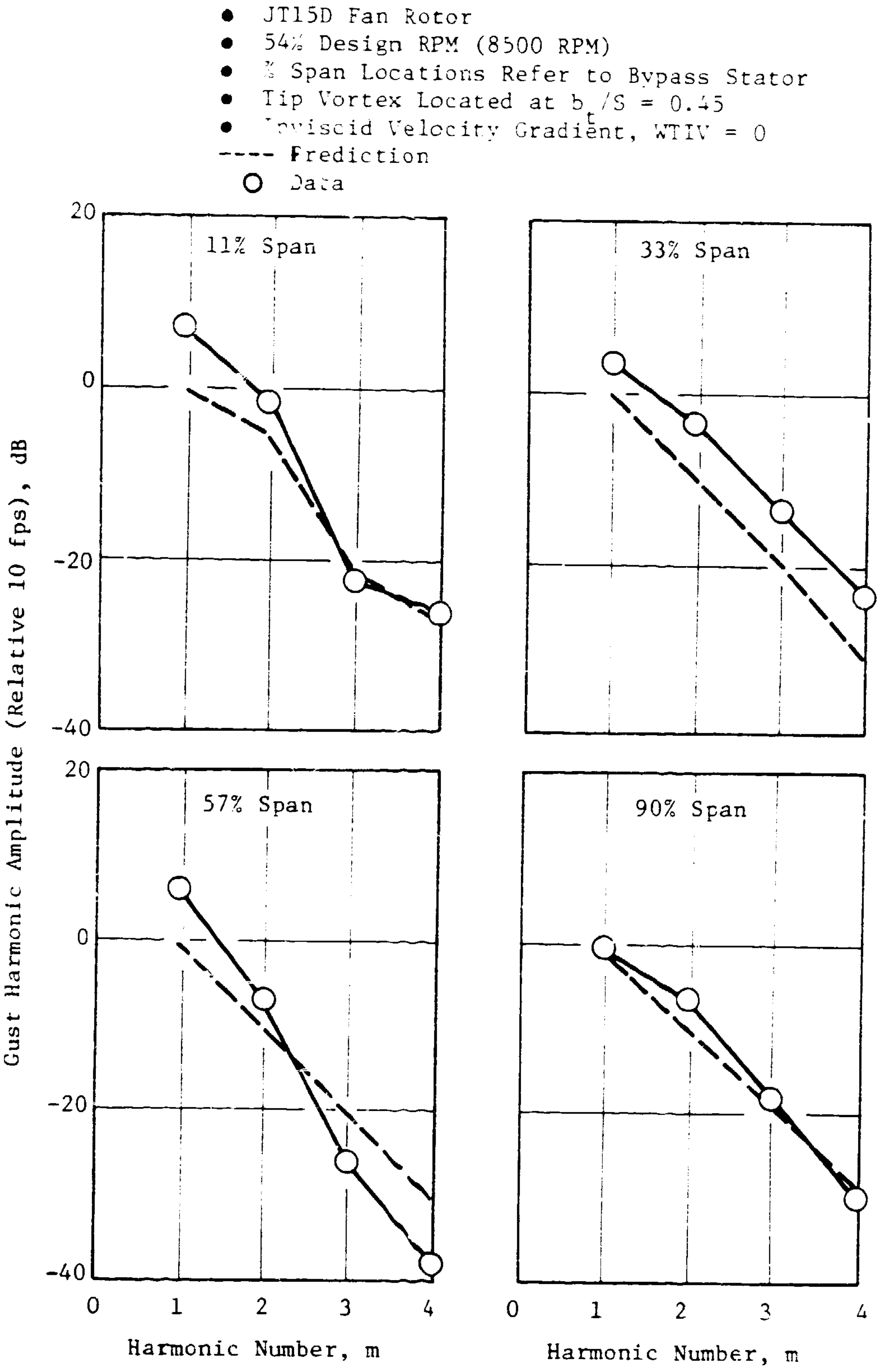

Figure 44. Comparison of Data and Predictions of the Gust Harmonic Amplitude Spectra at Four Spanwise Locations.

- JT15D Fan Rotor
- 43% Design RPM (6750 RPM)
- % Span Locations Refer to Bypass Stator
- Tip Vortex Located at $b_t/S = 0.45$
- Inviscid Velocity Gradient, WTIV = 0

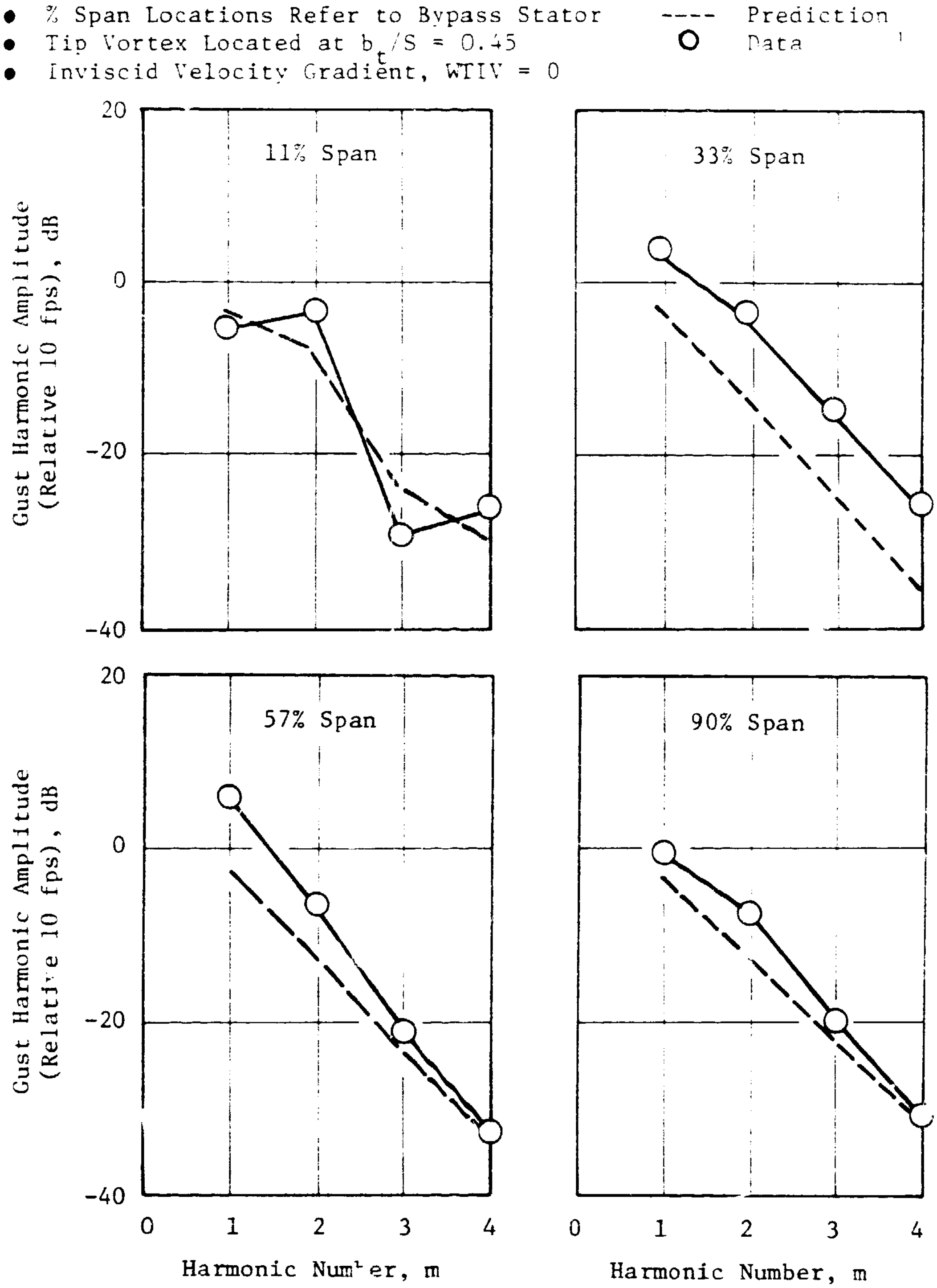

Figure 45. Comparison of Data and Predictions of the Gust Harmonic Amplitude Spectra at Four Spanwise Locations.

profile loss coefficient was considered in computing the section drag coefficient. Using the above information, rotor wake predictions were made.

Figure 46 compares the measured and predicted wake centerline defect and semiwake width axial variation at 50% span from the tip. The agreement between the predicted and measured semiwake width axial variation is very good. However, the measured centerline wake defect does not agree with the predictions for $X/c < 0.4$ Rotor 67 has a significant amount of supersonic flow over the blades, and as such may have strong shock-boundary layer interaction which could complicate the flow character at the rotor blade trailing edge. This in turn could result in a wake decay which is quite different from the wake decay of the low speed rotors used in developing the prediction model. Thus, the measured wake centerline defect does not agree with the predictions at distances close to the trailing edge. However, for $X/c > 0.4$, the measurements and predictions agree well, presumably because the complex flow character present at the trailing edge has dissipated and the wake displays the typical characteristics of wakes of subsonic tip speed rotors.

Figure 47 shows a comparison of the measured and predicted wake centerline defect and semiwake width axial variation at 10% span from the tip. As in the case of 50% span from the tip, the predicted wake centerline defect agrees with the measured wake centerline defect for $X/c > 0.4$. However, the semiwake width predictions do not agree well with the data. At 10% span from the tip location, the tip vortex significantly affects the rotor wake shape, and as such the measured wake at this spanwise location is highly complex in shape. Hence, extracting semiwake width data from such complex wake shapes involves a considerable amount of uncertainty. The experimental data of semiwake width at this spanwise location show almost no variation in the semiwake width over the range of axial stations. This is ascribed to the tip vortex interactions with the rotor wake.

In summary, the predicted and measured wake centerline defect in the midspan location for Stage 1 of Rotor 67 are in reasonable agreement for $X/c > 0.4$. The agreement for the semiwake width in the midspan location is good. The predictions and data of the wake centerline defect do not agree close to the rotor trailing edge.

5.2 PARAMETRIC STUDIES

The reasonably good agreement between the theoretical predictions and the experimental data shown in Section 5.1 for three rotors gives credence to the developed rotor wake and vortex model. The next step in the evaluation of the model is to perform parametric studies to determine the influence of various geometric and aerodynamic parameters on the rotor wake and vortex characteristics. The parametric studies included the following:

1. Influence of rotor-stator spacing on the rotor wake characteristics and the stator upwash gust harmonic spectrum.

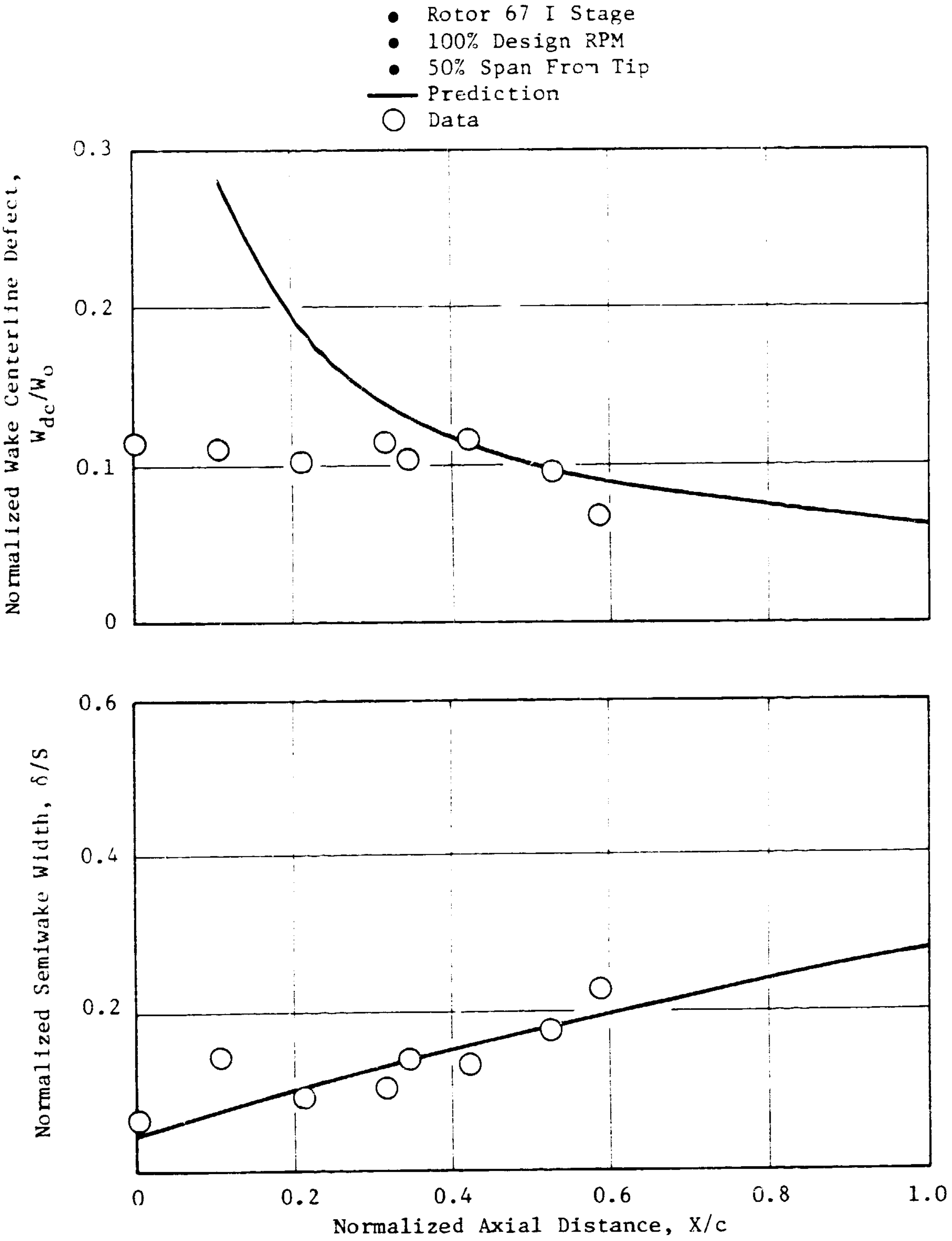

Figure 46. Comparison of the Measured and Predicted Wake Centerline Defect and Semiwake Width Variation at Midspan.

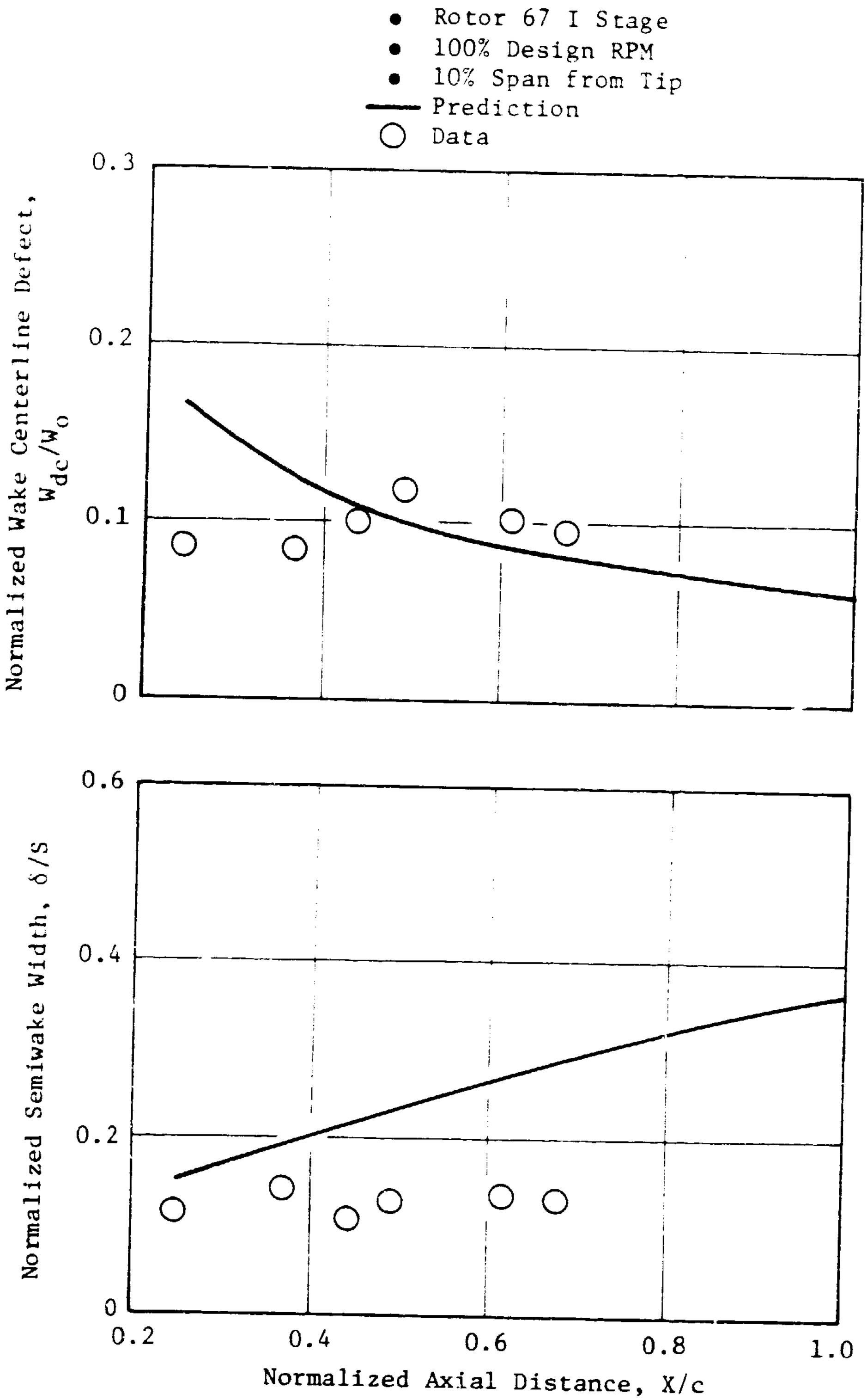

Figure 47. Comparison of the Measured and Predicted Wake Centerline Defect and Semiwake Width Variation.

2. Spanwise variation of rotor characteristics and their influence on the wake characteristics and the stator upwash gust harmonic spectrum.

3. Influence of rotor solidity on the rotor wake characteristics and the stator upwash gust harmonic spectrum.

4. Influence of section drag coefficient on the rotor wake characteristics and the stator upwash gust harmonic spectrum.

5. Influence of rotor loading at constant tip speed on the rotor wake characteristics and the stator upwash gust harmonic spectrum.

6. Influence of the inviscid velocity gradient on the rotor wake characteristics and the stator upwash gust harmonic spectrum.

7. Influence of the tip vortex parameters (tip clearance and tangential location of the tip vortex) on the stator upwash gust harmonic spectrum.

8. Influence of the axial and transverse velocity and length scales on the broadband turbulent velocity spectrum.

5.2.1 Influence of Rotor-Stator Spacing

Rotor-stator spacing is an important parameter in the rotor-stator interaction studies. As the rotor-stator spacing increases, the rotor wake dissipates, reducing the fluctuating lift force component on the stator and thus lowering rotor-stator interaction noise.

Figure 48 shows the influence of axial spacing on the normalized wake centerline defect and the semiwake width. The computations performed refer to the 10% streamline of Rotor 55 at 80% design rpm. The pertinent aerodynamic and geometric parameters were taken from Reference 35. The wake centerline defect is about 6% of the free stream velocity at X/c = 0.5 and decreases to about 4.5% at X/c = 5.0. The normalized semiwake width (w/S) reaches the asymptotic value of 0.5 for X/c = 2.25, indicating that the wakes from the adjacent blades are merged for X/c > 2.25.

Figure 49 shows the influence of the rotor-stator spacing on the gust harmonic amplitude spectra. Tip vortex is not included in the computation of the spectra. The BPF level (m=1) is the highest for X/c = 0.5 and reduces monotonically as X/c increases. The BPF level for X/c = 5 is about 13dB lower compared to the BPF level for X/c = 0.5. Since the wake width at X/c = 0.5 is the lowest, the fall-off rate of the spectra is the lowest for X/c = 0.5. As X/c increases, the wake width increases and the wake shape within a blade passage resembles a sinusoidal function with a period equal to the blade-to-blade spacing. Hence, the contribution from the higher harmonics is less. There is a distinct change in the spectra as the semiwake width reaches the asymptotic

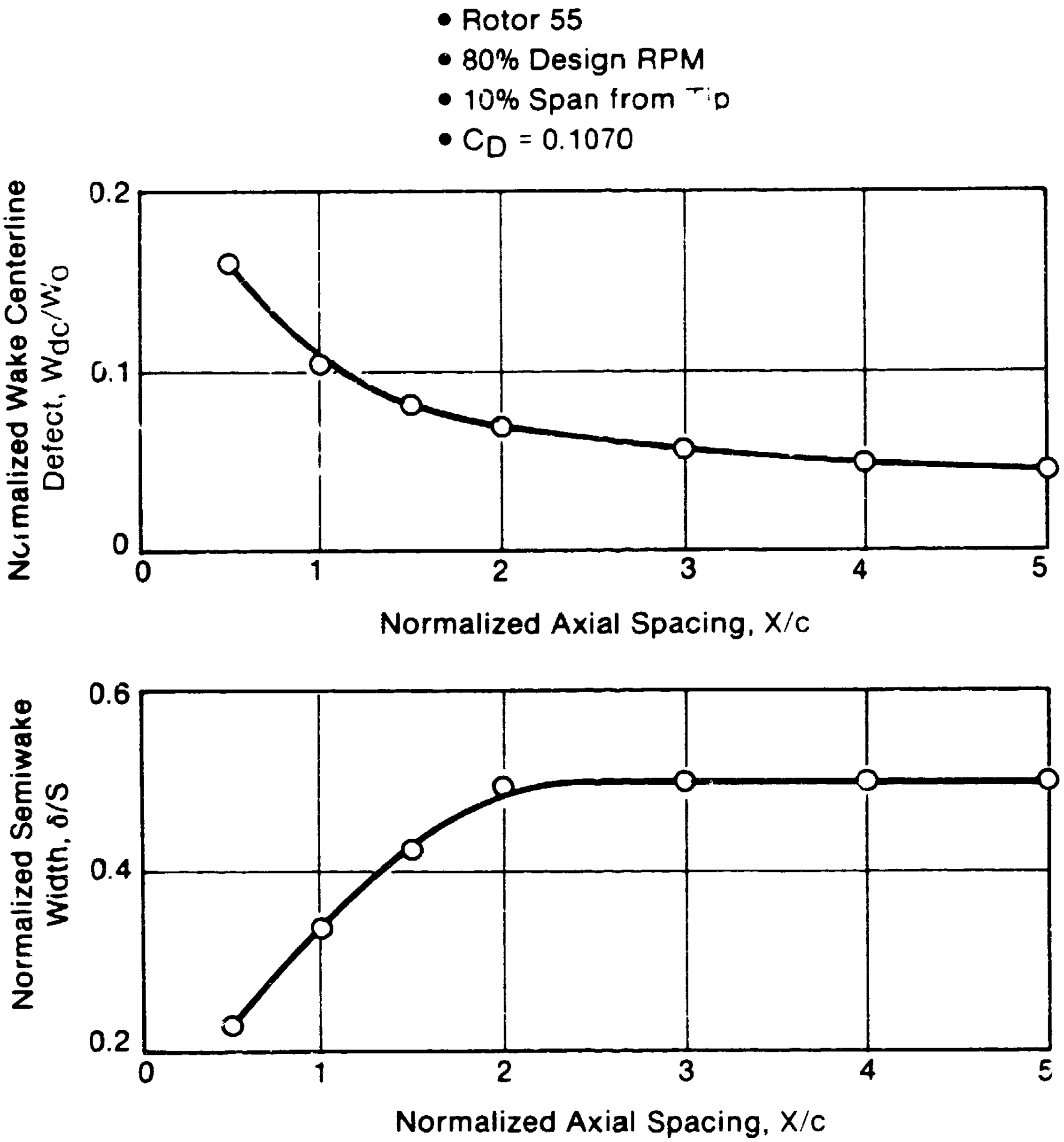

Figure 48. Axial Variation of Predicted Wake Centerline Defect and Semiwake Width.

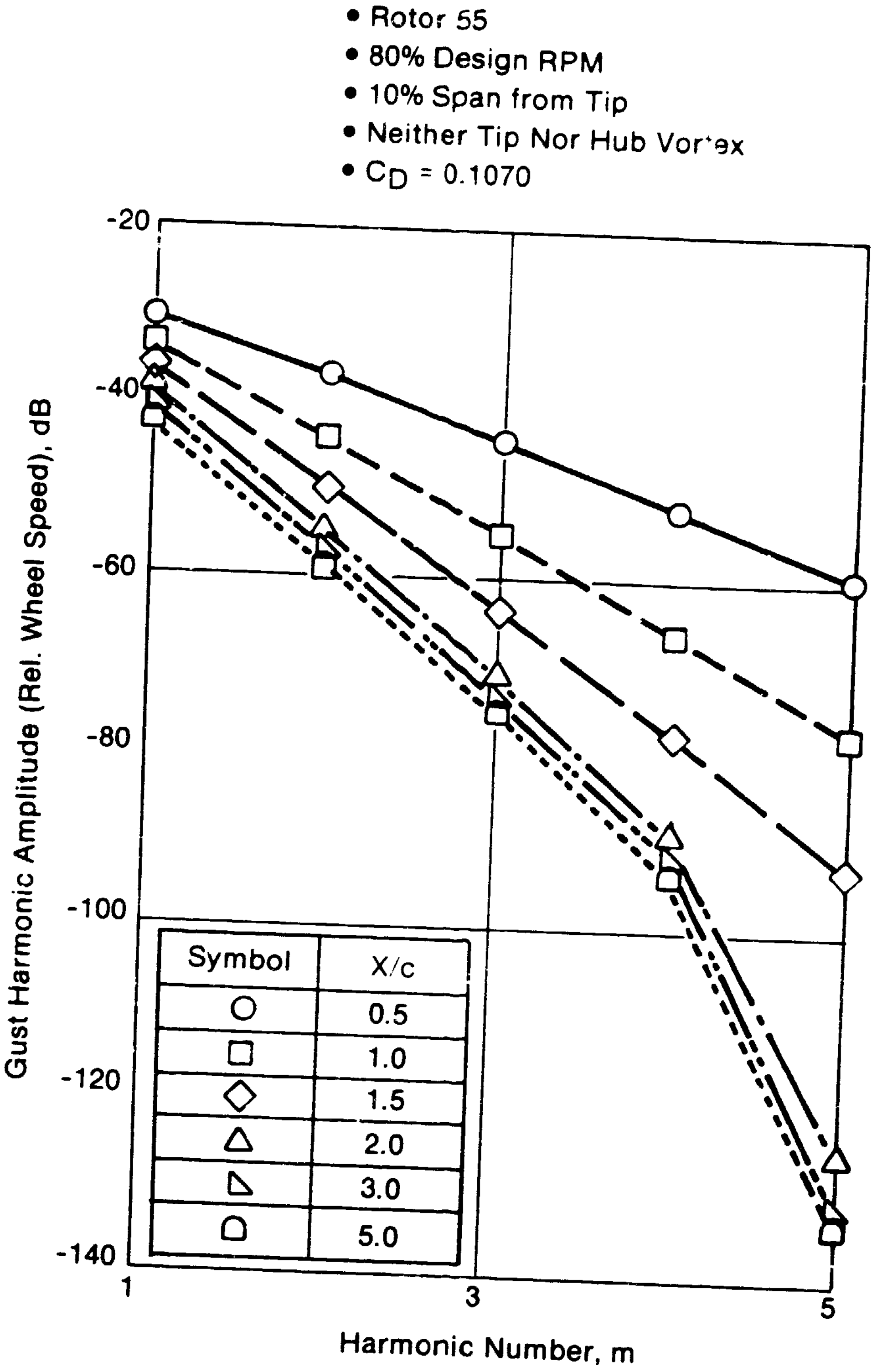

Figure 49. Predicted Gust Harmonic Amplitude Spectra at Various Rotor/Stator Spacings.

value of $\delta/S = 0.5$ for $X/c > 2$). This change in character is due to the merging of wakes from the adjacent blades. Also note that once the wakes merge, the spectral shape does not change as X/c increases above 2. The slight reductions in the levels seen are due to a decrease in the centerline wake defect. Thus, increasing the rotor-stator spacing above a value at which the wakes from adjacent blades merge does not appreciably reduce the fluctuating lift component. This can be used as a design guide in the selection of the rotor-stator spacing, from the point of reducing the rotor wake interaction with the stator.

5.2.2 Spanwise Variation in Rotor Wake Characteristics

This section deals with the influence of the spanwise variation of the geometric and aerodynamic parameters of the rotor on the rotor wake characteristics. Computations are done for Rotor 55 at 80% design rpm (see Reference 35 for all the pertinent geometric and aerodynamic parameters). The gust harmonic amplitude spectra are computed with and without the tip vortex in order to study the influence of the tip vortex at different spanwise locations and downstream locations.

Figure 50 shows the spanwise variation of rotor solidity (σ_r), normalized axial spacing (X/c) and the rotor stagger angle (γ_R). The rotor-stator axial spacing shown in Figure 50 refers to the smallest spacing at which the rotor wake data were measured by Shaw and Balombin (Reference 6); it equals 0.54c at 50% span. Figure 51 shows the spanwise variation of the work coefficient (V_θ/V_T), drag coefficient (C_D), and rotor exit relative flow angle (β_2) at three rotor speeds (80%, 96%, and 115% design rpm). Note that only the drag coefficient near the tip shows some variation with the rotor speed. The drag coefficient is lowest for the 96% design rpm case and increases on either side of this rpm, which is close to the design rpm.

Figure 52 shows the predicted axial variation of the wake centerline defect (W_{dc}/W_o), normalized streamwise distance (s/c) and the semiwake width (δ/S), at three spanwise locations. The combination of the axial spacing (X/c) and rotor exit relative flow angle (β_2) at the three spanwise locations is such that the normalized streamwise distances at the three spanwise locations are about the same. Thus, the wake centerline defect and the semiwake width are essentially dependent on the drag coefficient at these spanwise locations. Since the drag coefficient is lowest at the midspan location (50% span from tip), the normalized wake centerline defect and the semiwake width are minimum at this spanwise location. The wake centerline defects at 10% and 90% span locations are about the same. The normalized semiwake width for the case of 90% span from tip is slightly higher than for the case of 10% span from tip. This is due to slightly higher streamwise distance and a slightly higher drag coefficient near the hub.

Figure 53 shows the predicted gust harmonic spectra at the three spanwise stations (10%, 50%, and 90% span from tip) at three axial spacings without a tip vortex. The three axial spacings (X/c = 0.54, 1.23, and 1.77) refer to the rotor-stator spacings at midspan at which rotor wake data were measured by

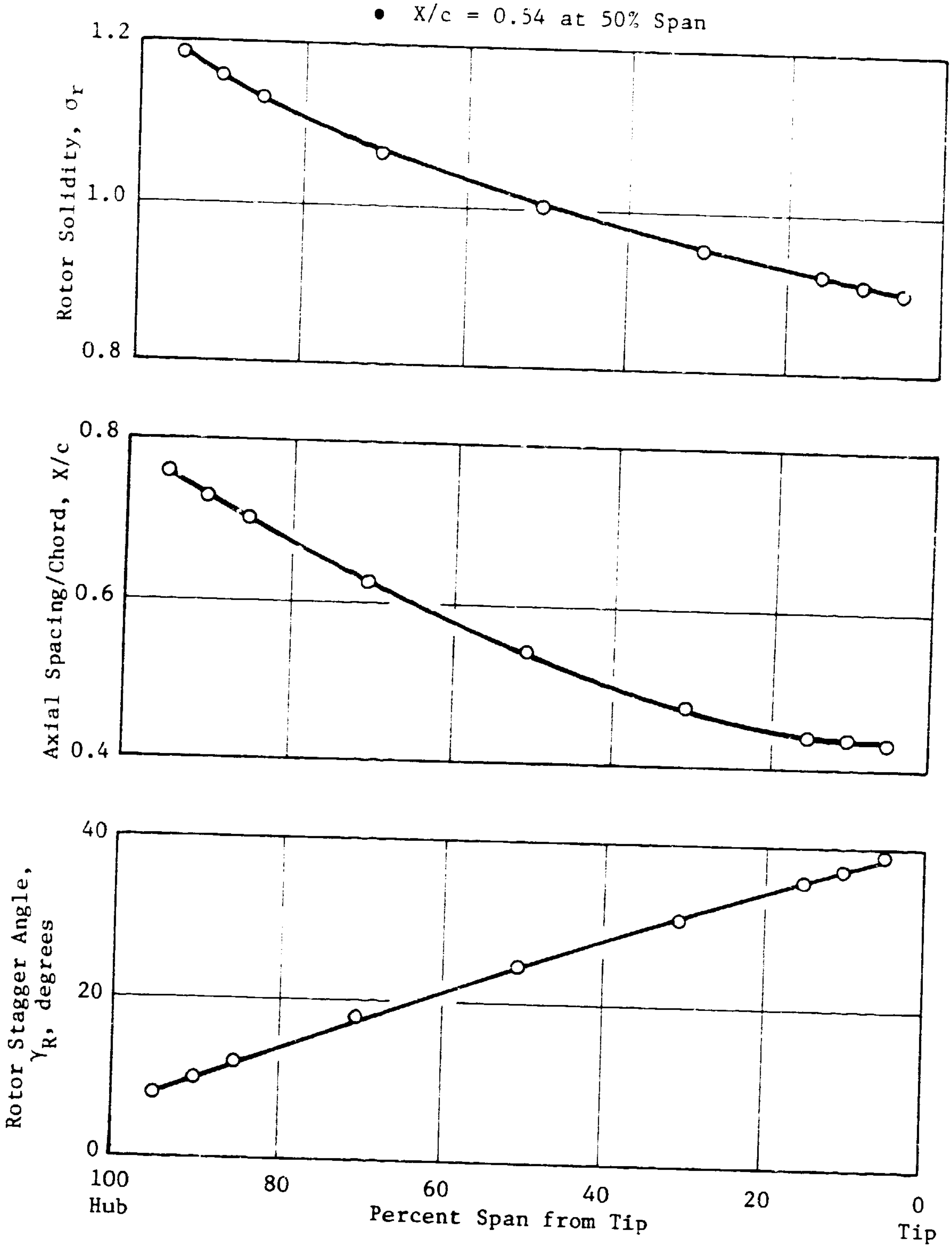

Figure 50. Spanwise Variation of Rotor Solidity, Rotor/Stator Axial Spacing, and Rotor Stagger Angle for Rotor 55.

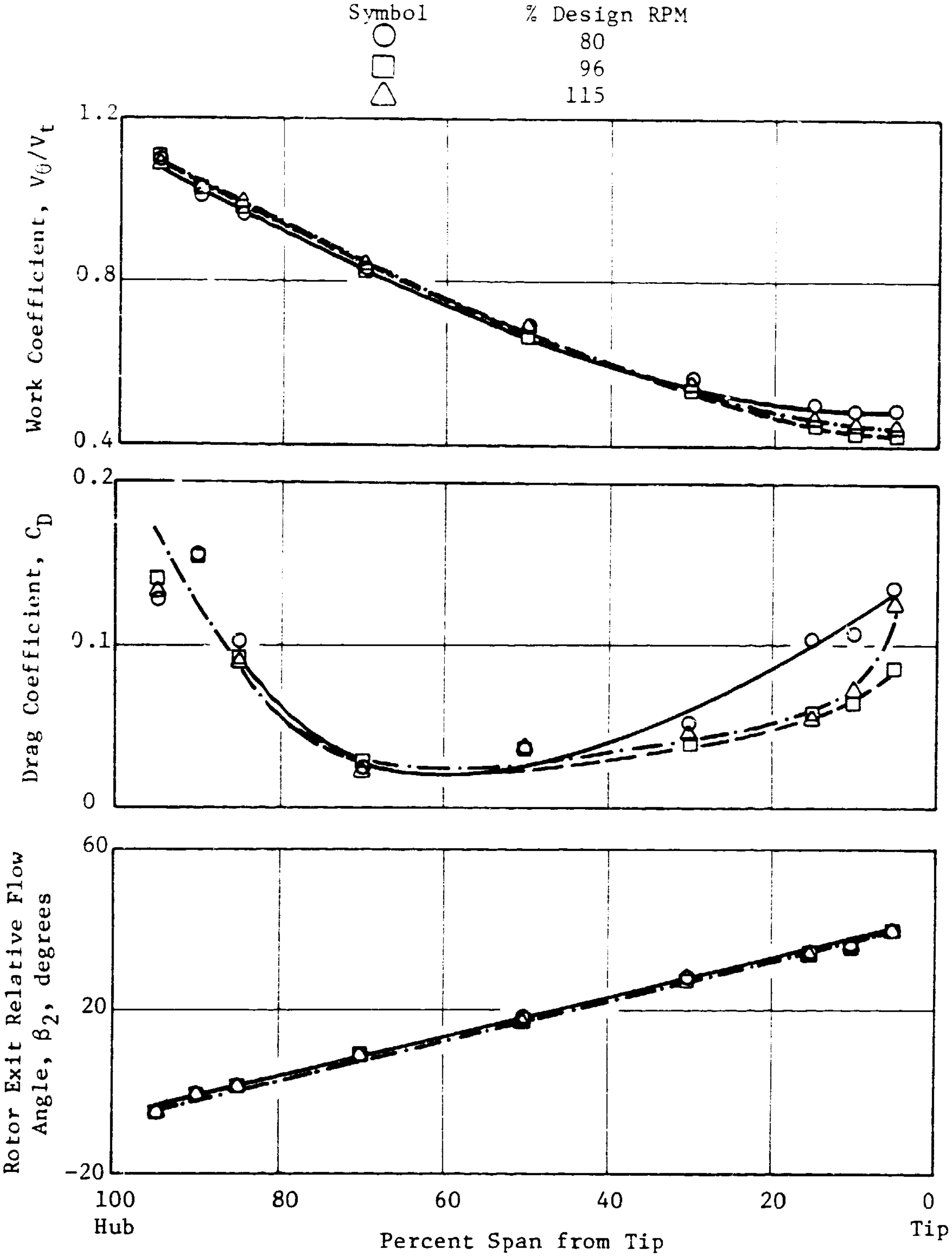

Figure 51. Spanwise Variation of Work Coefficient, Drag Coefficient, and Rotor Exit Relative Flow Angle at Three Rotor Speeds for Rotor 55.

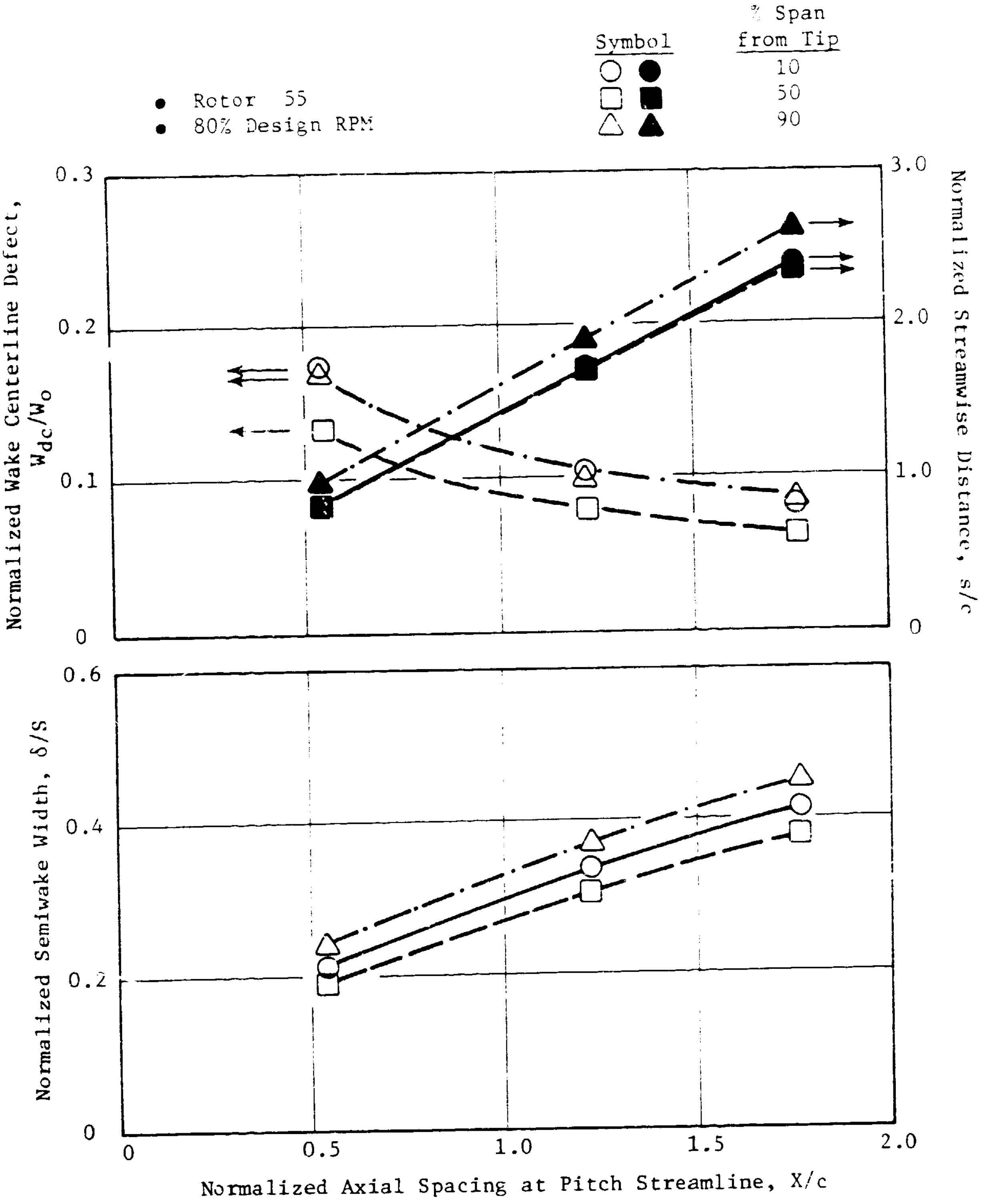

Figure 52. Predicted Axial Variation of Wake Centerline Defect, Streamwise Distance and Semiwake Width at Three Spanwise Locations.

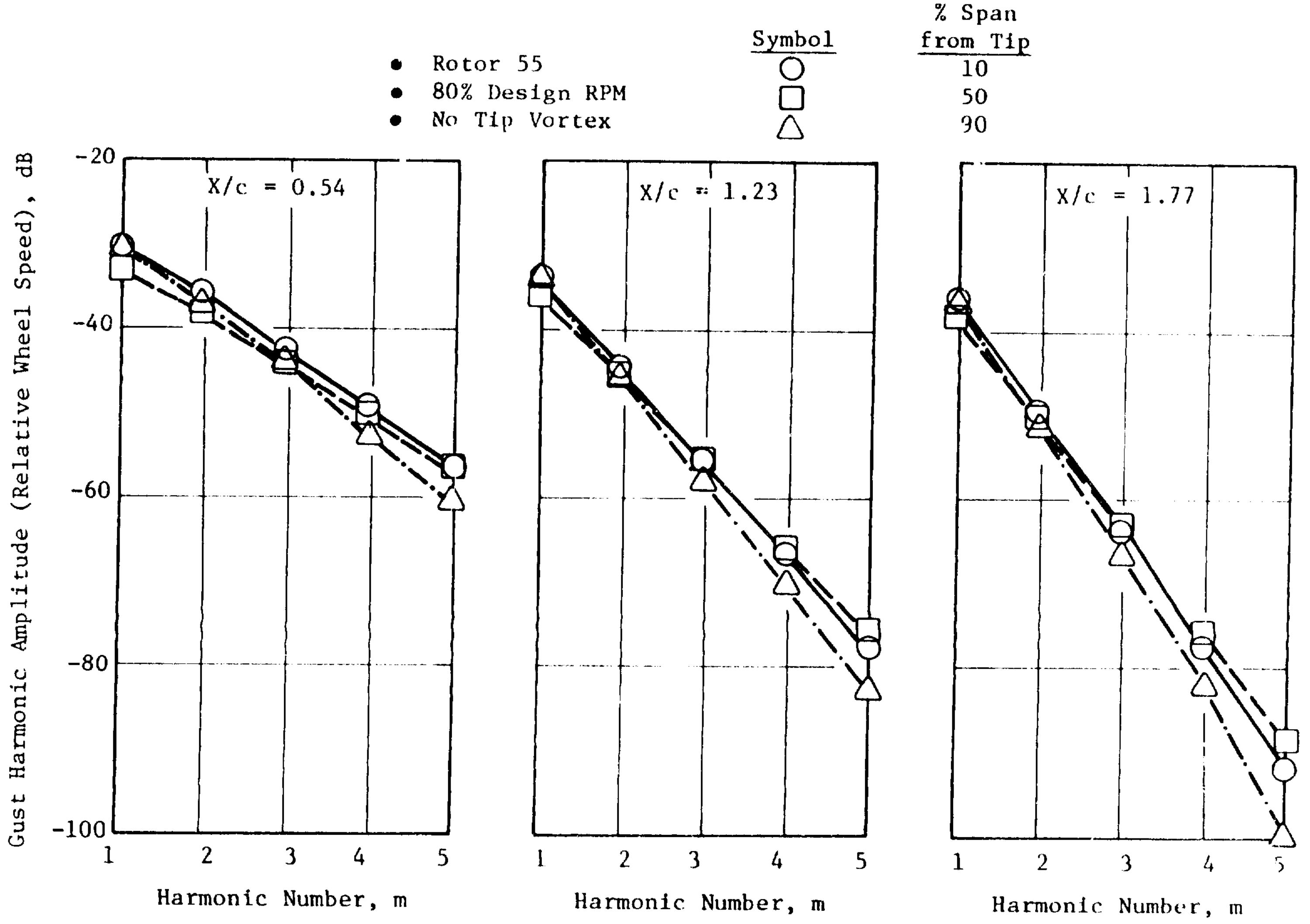

Figure 53. Predicted Gust Harmonic Spectra at Three Spanwise Stations for Three Rotor/Stator Spacings.

Shaw and Balombin (Reference 6). As X/c increases, the fall-off rate of the gust harmonic amplitude increases because of the growth of semiwake width. The fall-off rate for the 90% span from tip case is highest since its wake width is the highest. Note the reduction in BPF level as X/c increases at all three spanwise stations, because of the reduction in wake centerline defect. Also, at each axial location, the BPF level for the 50% span from tip location is lowest since the wake centerline defect is lowest for this spanwise location.

Figure 54 shows the predicted gust harmonic spectra at the same axial and spanwise locations as above, but including the tip vortex. The tangential location of the tip vortex is set at $b_t/S = 0.42$, as in the case of data-theory comparison for Rotor 55 (see Subsection 5.1.1). Note there are distinct changes in the spectral content for 10% span from the tip location (Figures 53 and 54) at all three axial stations. The 2xBPF levels are higher than the BPF level for this spanwise location and the fall-off rate is reduced due to the contribution from the tip vortex. The spectra at 50% and 90% span from tip are not influenced by the tip vortex, since they are sufficiently far away from the tip vortex center.

As shown in Subsection 3.3.1, the twist of the rotor blade from hub to tip results in a time delay (or phase lag) in the wake from hub portion impinging on the stator relative to the wake from the tip portion impinging on the stator. Figure 55 shows the predicted spanwise variation of the relative phase lag normalized by the angular spacing of the rotor for three rotor-stator spacings for Rotor 55 at 80% design rpm. Suppose that at $t = 0$, the wake from the tip region of a particular rotor blade "A" impinges on the stator. For the case of $X/c = 1.77$ (see Figure 55), by the time the wake from the hub region (95% span from tip) from the same rotor blade "A" impinges on the stator, approximately 4.6 rotor blade passages would have gone past the stator. Thus, in Figure 55 we see that as X/c increases, the phase lag increases. The extent of spanwise variation of the phase lag depends on the amount of twist in the rotor blade: the larger the twist, the more the phase lag.

5.2.3 Influence of Rotor Solidity

Rotor 55 at 80% design rpm is again chosen to study the influence of rotor solidity. The streamline at 10% span from tip is considered so that influence of rotor solidity on the stator upwash gust harmonic spectra can be studied with and without tip vortex. The solidity for Rotor 55 at 10% span from tip equals 0.905. The range of variation in the solidity studied is ±33% of the nominal valve of 0.905. The rotor solidity is varied by changing the rotor aerodynamic chord while keeping the same blade-to-blade spacing. The wake/vortex computations are performed at the same axial distance from the rotor trailing edge for these parametric studies. The X-locations correspond to the locations where Shaw and Balombin measured the wake data (Reference 6). As solidity increases, the rotor aerodynamic chord increases. As the rotor aerodynamic chord increases, X/c decreases for constant X values.

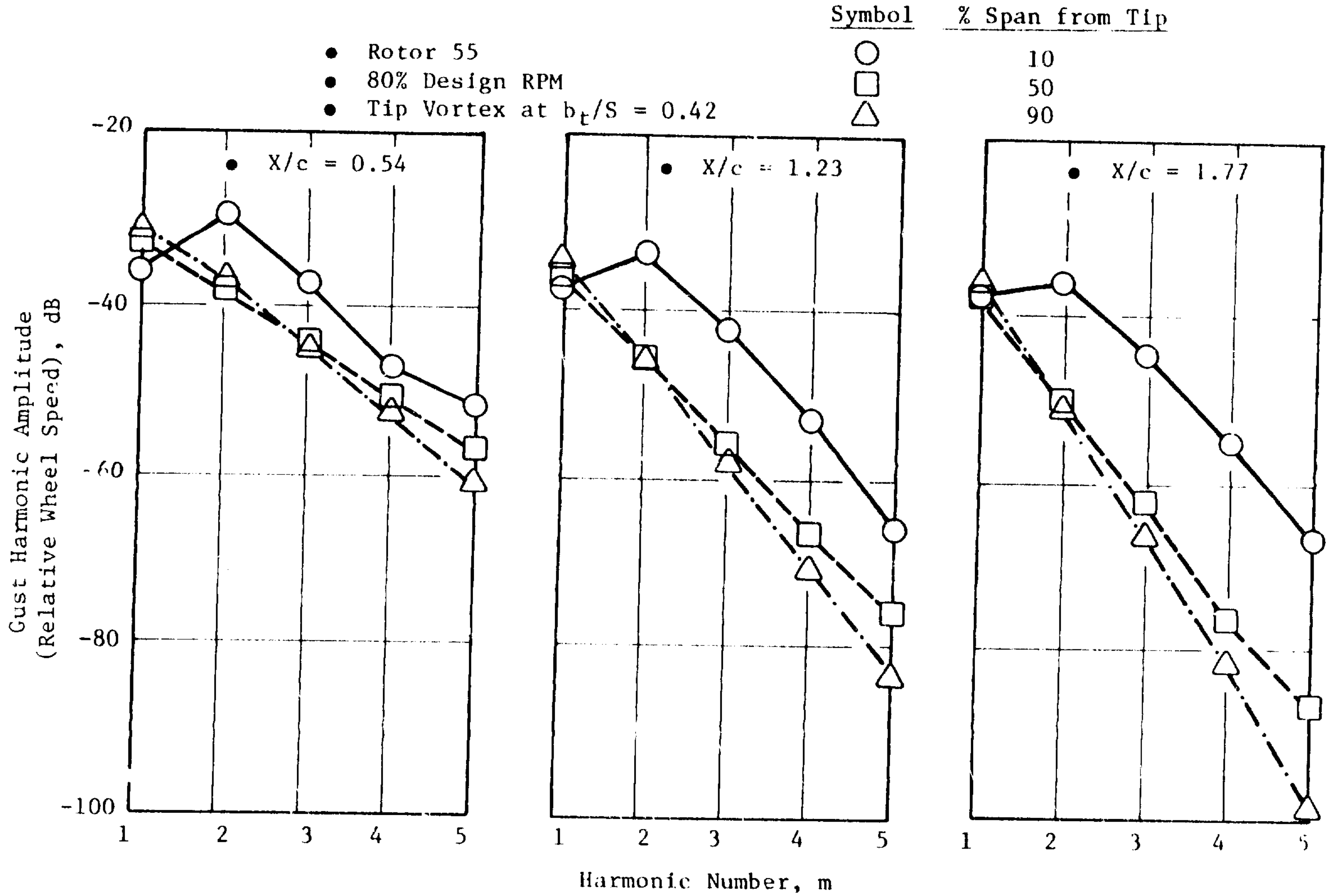

Figure 54. Predicted Gust Harmonic Spectra at Three Spanwise Stations for Three Rotor/Stator Spacings (Tip Vortex Included).

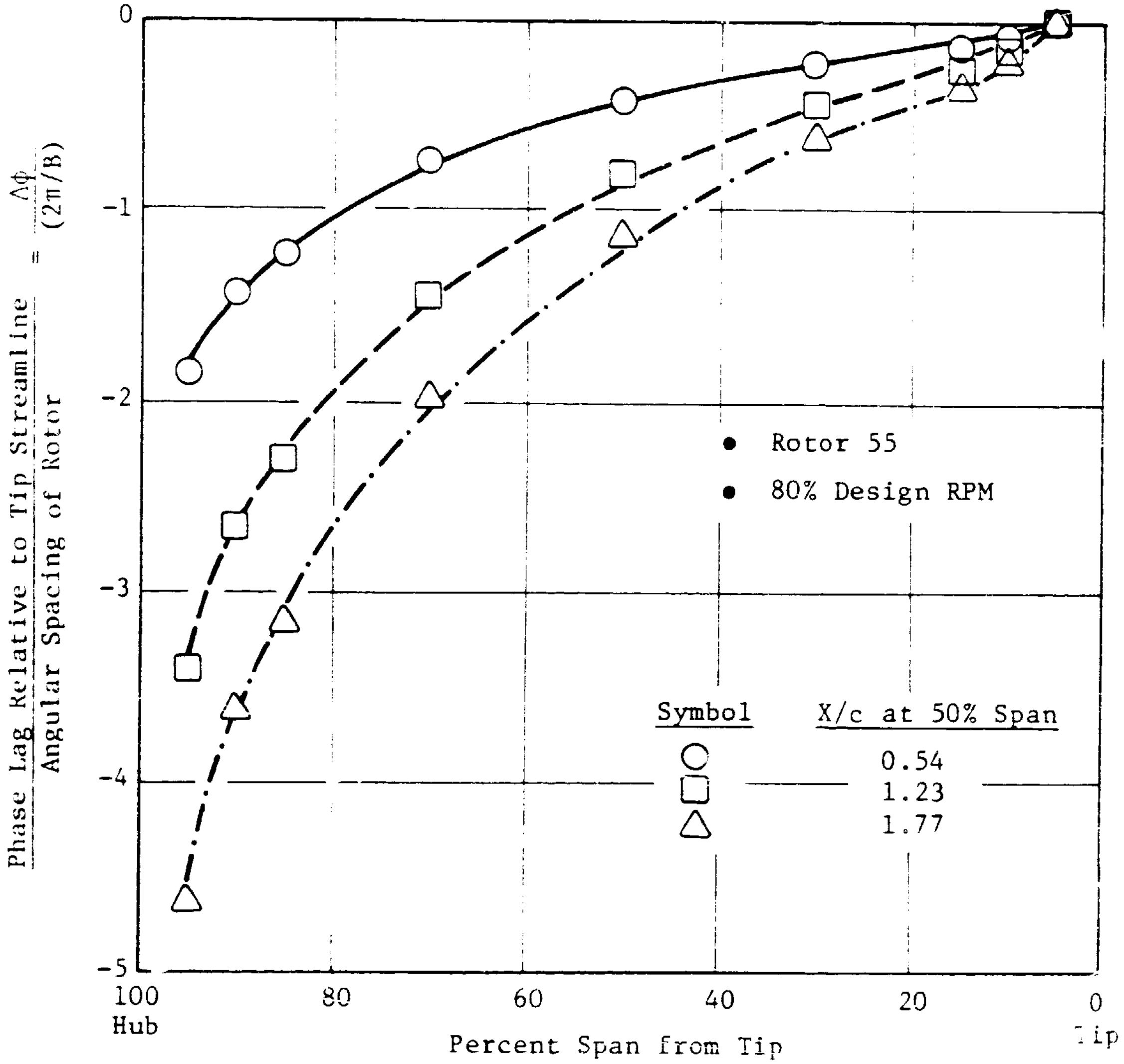

Figure 55. Predicted Spanwise Variation of Relative Phase Lag Normalized by Angular Spacing of Rotor for Three Rotor/Stator Spacings.

Figure 56 shows the influence of rotor solidity on the axial variation of the wake centerline defect and the semiwake width. As the rotor solidity increases, the wake centerline defect increases, and the semiwake width decreases at the same X-location due to reduced X/c value. Thus, the semiwake width reaches the limiting value of 0.5S for lower solidity case at a smaller axial distance from the rotor trailing edge, compared to the higher solidity case.

Figure 57 shows the predicted influence of rotor solidity on the gust harmonic spectra at three axial locations from the rotor trailing edge without the tip vortex. Since the case of the highest rotor solidity has the highest value of wake centerline defect at $X/r_{ann} = 0.18$, the BPF level for it is highest. Also, since the semiwake width is lowest for this case, the fall-off rate is also the lowest of the three solidity cases. The same trend is noticed at $X/r_{ann} = 0.71$. For $X/r_{ann} = 1.43$, the semiwake width has reached its limiting value of 0.5S for all three rotor solidities. Thus, the gust harmonic spectra for all three rotor solidities are almost identical. The slight differences are due to differences in the wake centerline defect for them at this X-location.

Figure 58 shows the predicted influence of rotor solidity on the gust harmonic spectra at these same three axial locations, but this time including the tip vortex. The tangential location of the tip vortex for this study is set at $b_t/S = 0.5$. Note that the significantly different character in the spectra for this streamline is due to the tip vortex. At $X/R_{ann} = 0.18$, the 2xBPF and 4xBPF levels are significantly higher than the BPF and 3xBPF levels, respectively. Since the tip vortex is exactly in the midpassage, the streamwise defects due to the wake and the tip vortex (in the relative frame of reference) yield two well-defined defects within one blade-to-blade spacing. This increases the contribution of even harmonics of BPF and lowers the contribution of odd harmonics of BPF. The tip vortex dominates the spectra at this spanwise location. A clear trend with rotor solidity cannot be extracted in the presence of tip vortex at streamlines close to the tip. As X/r_{ann} increases, the tip vortex decays and the relative dominance of 4xBPF over 3xBPF is not seen. However, 2xBPF levels are still higher than BPF levels, even at the $X/r_{ann} = 1.43$.

5.2.4 Influence of Section Drag Coefficient

A parametric variation of the section drag coefficient (C_D) and its influence on the wake centerline defect, semiwake width, and the stator upwash gust harmonic spectra are discussed in this subsection. As in Subsection 5.2.3, the streamline at 10% span from tip for Rotor 55 at 80% design rpm is considered. The nominal value of C_D computed from the measured profile loss coefficient equals 0.1070. C_D was varied ±50% from this nominal value and its influence was studied.

Figure 59 shows the axial variation of the predicted wake centerline defect and semiwake width for the three values of C_D. The influence of C_D on the wake centerline defect and semiwake width, in particular, is seen to

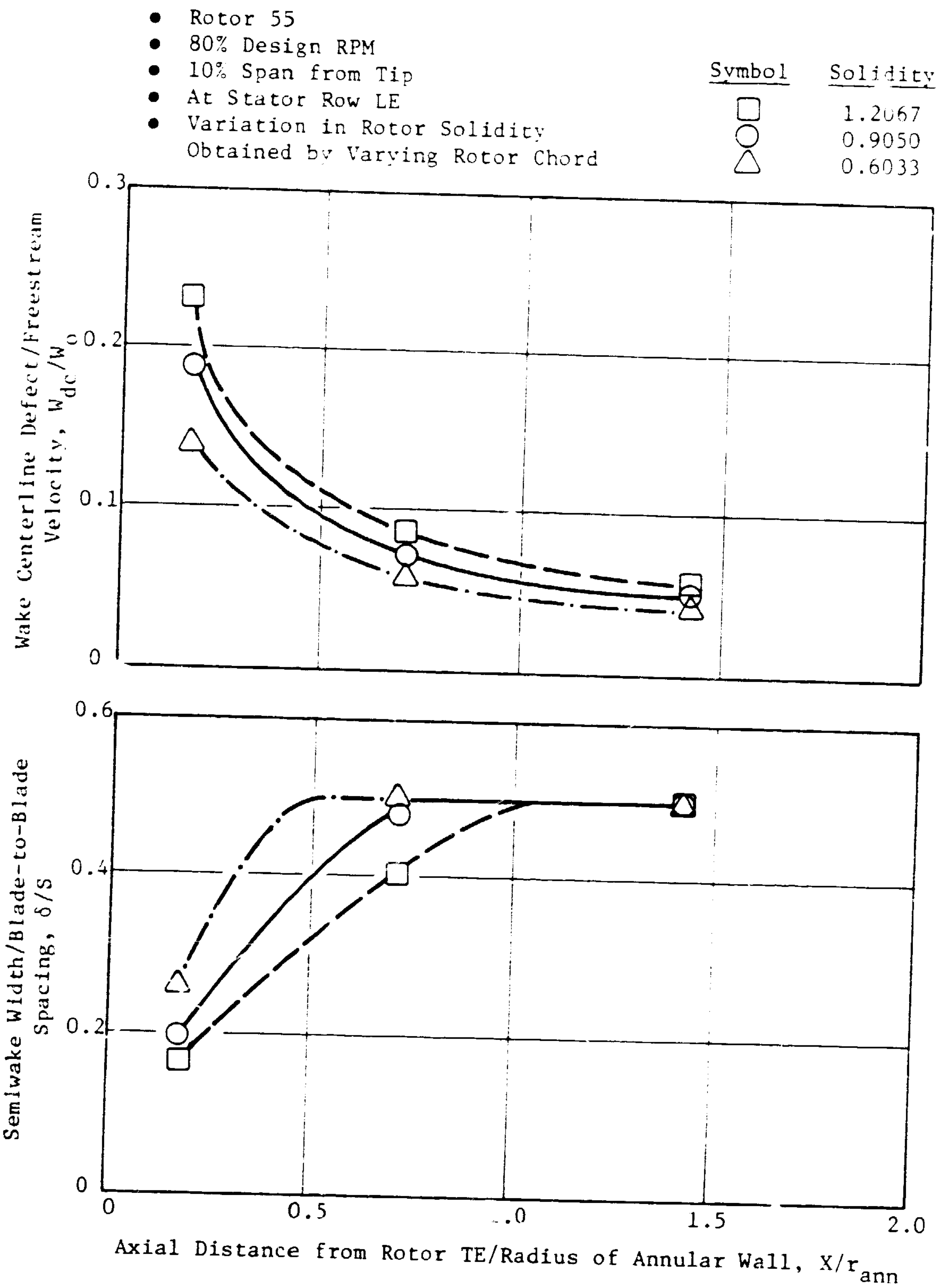

Figure 56. Predicted Influence of Rotor Solidity on Axial Variation of Wake Centerline Defect and Semiwake Width.

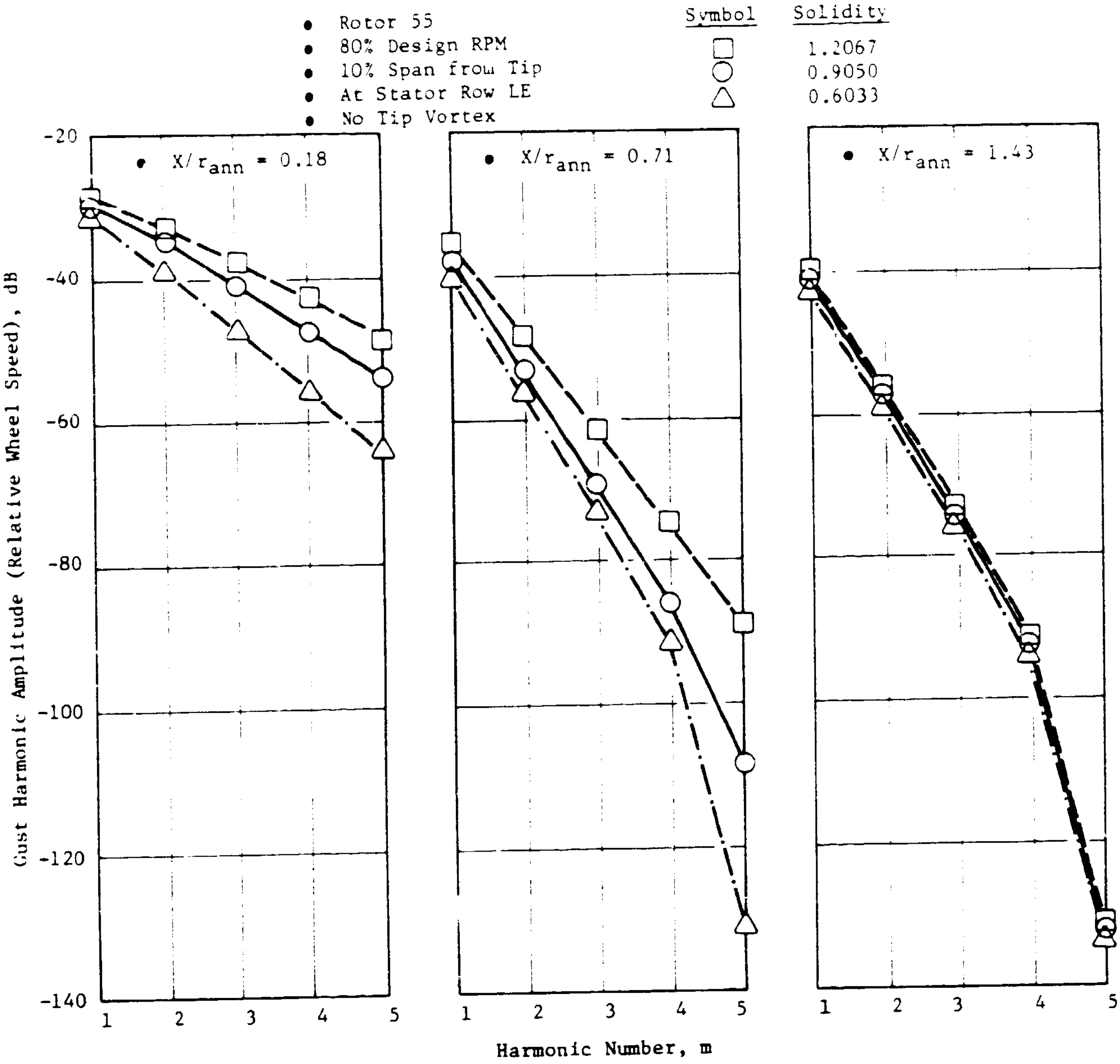

Figure 57. Predicted Influence of Rotor Solidity on Gust Harmonic Spectra at Three Axial Locations from Rotor Trailing Edge.

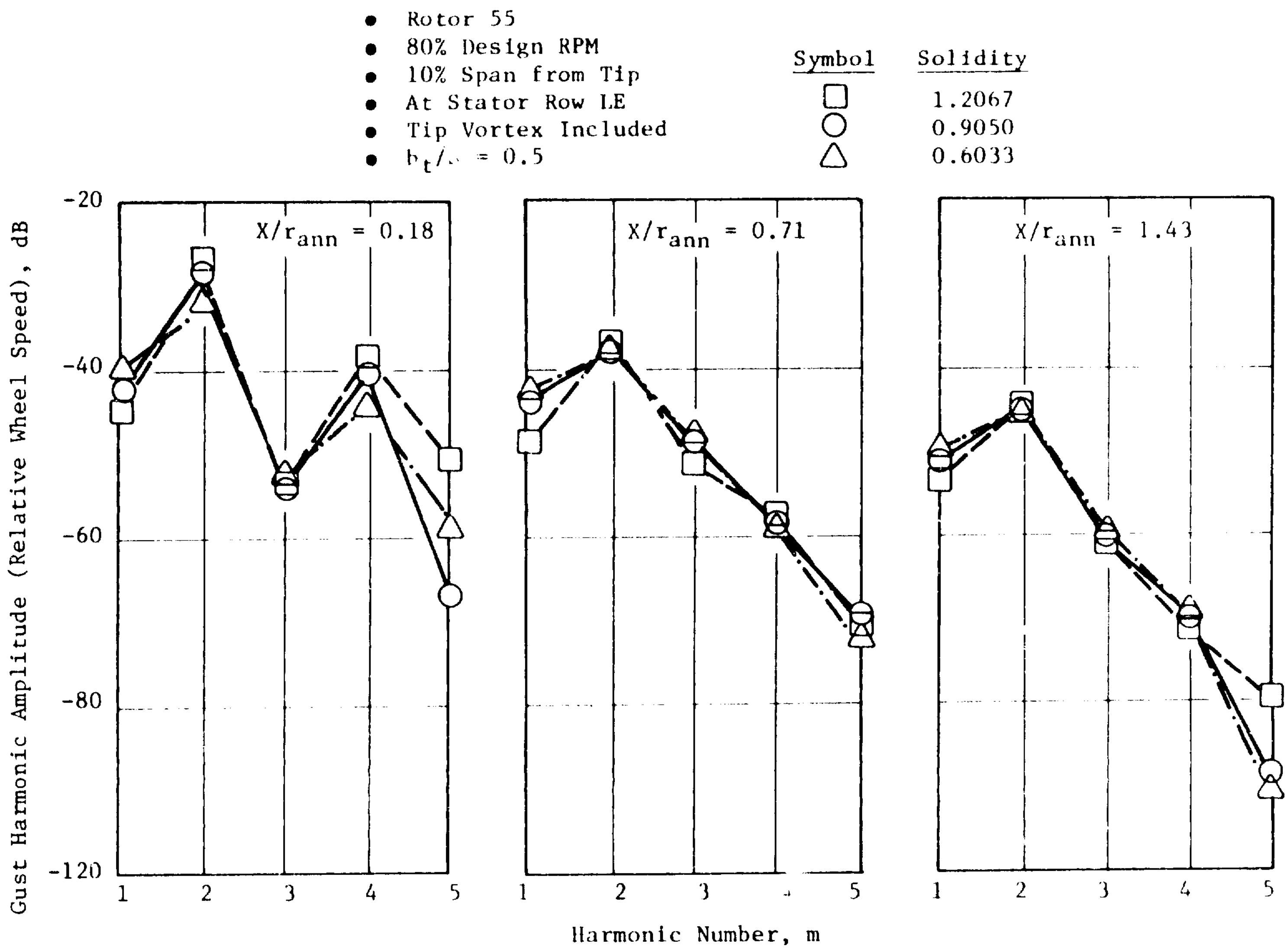

Figure 58. Predicted Influence of Rotor Solidity on Gust Harmonic Spectra at Three Axial Locations from Rotor Trailing Edge (Tip Vortex Included).

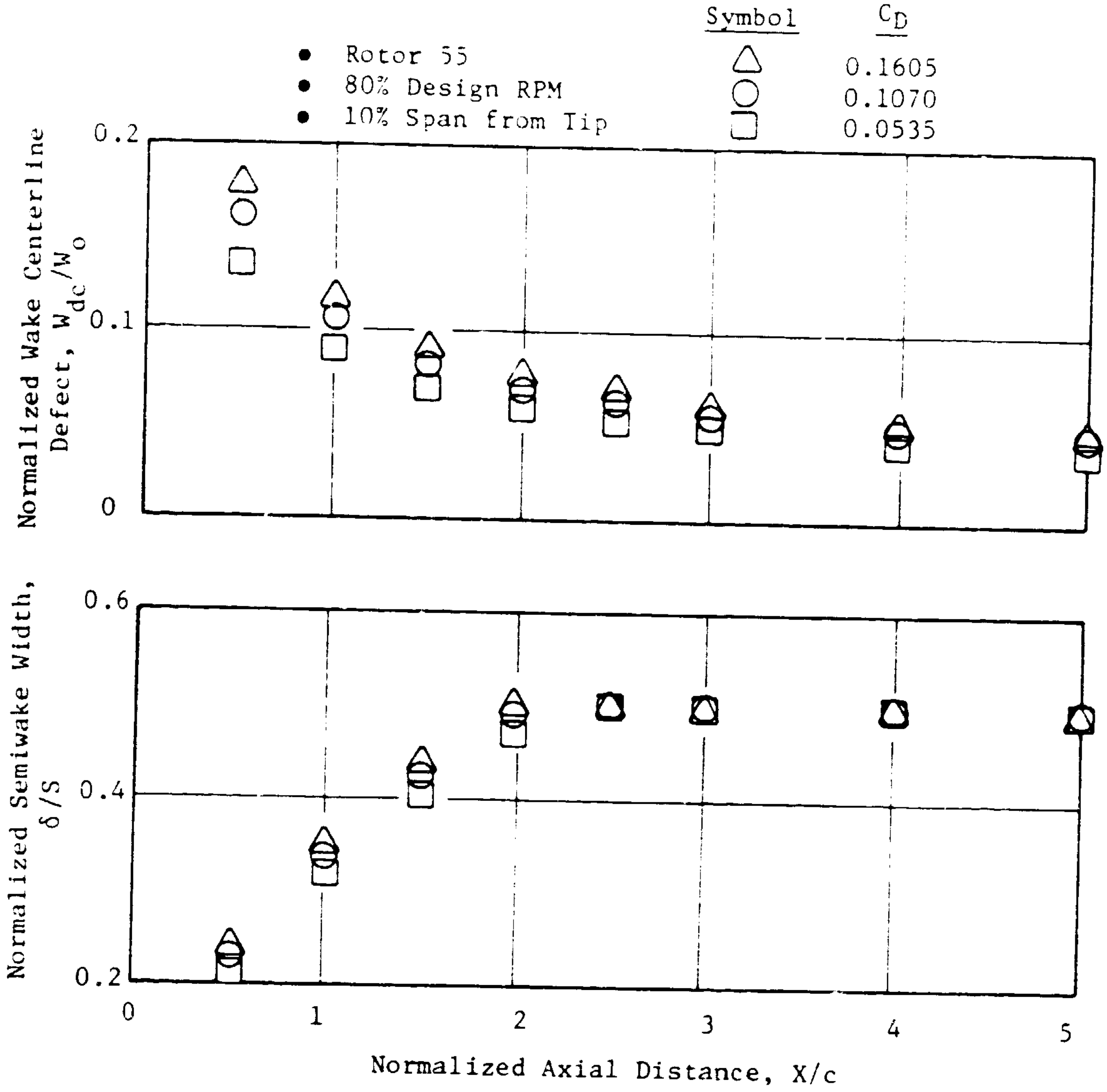

Figure 59. Axial Variation of Predicted Wake Centerline Defect and Semiwake Width for Three Values of C_D.

be small. For the case of the highest value of C_D, the wake centerline defect and the semiwake width are the highest. At large axial distances, these slight differences disappear for the wake centerline defect. Once the semiwake width reaches its limiting value of 0.5S, C_D has no effect. This lack of sensitivity of wake defect and semiwake width to the section drag coefficient is confirmed by the various data sources reviewed (see Subsection 3.1.1).

Figure 60 shows the predicted influence of section drag coefficient on gust harmonic spectra at these axial locations without tip vortex. The gust harmonic spectra are not sensitive to the section drag coefficient since neither wake centerline defect nor semiwake width is sensitive to the section drag coefficient.

5.2.5 Influence of Rotor Loading at Constant Tip Speed

The pressure ratio of a rotor is the indicator of rotor loading. For a single stage rotor, such as Rotor 55, the rotor loading does not vary noticeably along a constant speed line (see Reference 35). This is not the case for multistage rotors. To study the effect of rotor loading at constant tip speed, the second stage of Rotor 67 at 100% design rpm was chosen (see Reference 37), since it exhibited significant variation in rotor pressure ratio.

Figure 61 shows the variation of the work coefficient, lift coefficient at the tip, and section drag coefficient with the rotor total pressure ratio for Stage 2 of Rotor 67 at 10% span from tip, at 100% design rpm. The needed geometric and aerodynamic data were taken from Reference 37. The tip lift coefficient and the work coefficient are seen to increase rapidly with the rotor total pressure ratio. The drag coefficient is fairly flat. One would anticipate an increase in drag coefficient with increase in rotor total pressure ratio. An examination of the performance map of the second stage of Rotor 67 (Reference 37) indicates that the adiabatic efficiency of the rotor decreases rather sharply with decrease in rotor total pressure ratio. This has resulted in a fairly flat C_D variation with the rotor total pressure ratio. Figure 62 shows the variation of the section drag coefficient (again), wake centerline defect, and semiwake width with the rotor total pressure ratio. The wake centerline defect and the semiwake width are computed at the 1/4 chord point of the Stage 2 stator. Since the section drag coefficient shows little variation with the rotor total pressure ratio, the normalized wake centerline defect and the semiwake width also show little variation with the rotor total pressure ratio. Figure 63 shows the predicted influence of rotor total pressure ratio at 100% design rpm on the gust harmonic spectra, with and without the tip vortex. Because the wake centerline defect and the semiwake width are almost constant over the range of the rotor total pressure ratio considered, the gust harmonic spectra for the case of no tip vortex show negligible variation with the rotor total pressure ratio. However, the situation is quite different when tip vortex is included in the computation of gust harmonic spectra. In the case of the highest rotor total pressure ratio (P_r = 1.518), the influence of the tip vortex is noticeably strong in the sense that the 2xBPF level is higher than the BPF level. As the rotor total pressure ratio decreases, the influence of tip vortex is observed to decrease. The

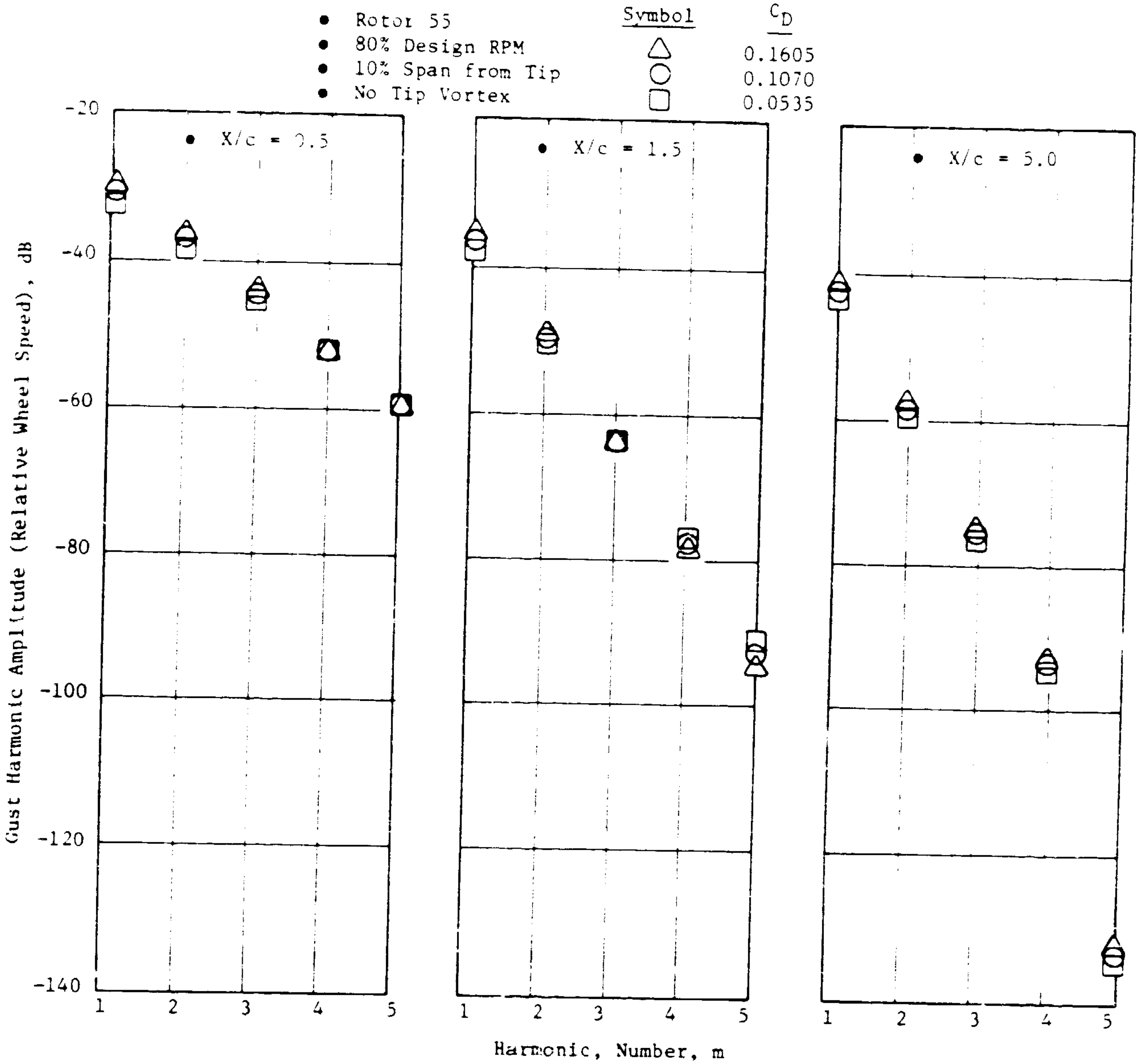

Figure 60. Predicted Influence of Section Drag Coefficient on Gust Harmonic Spectra at Three Rotor/Stator Spacings.

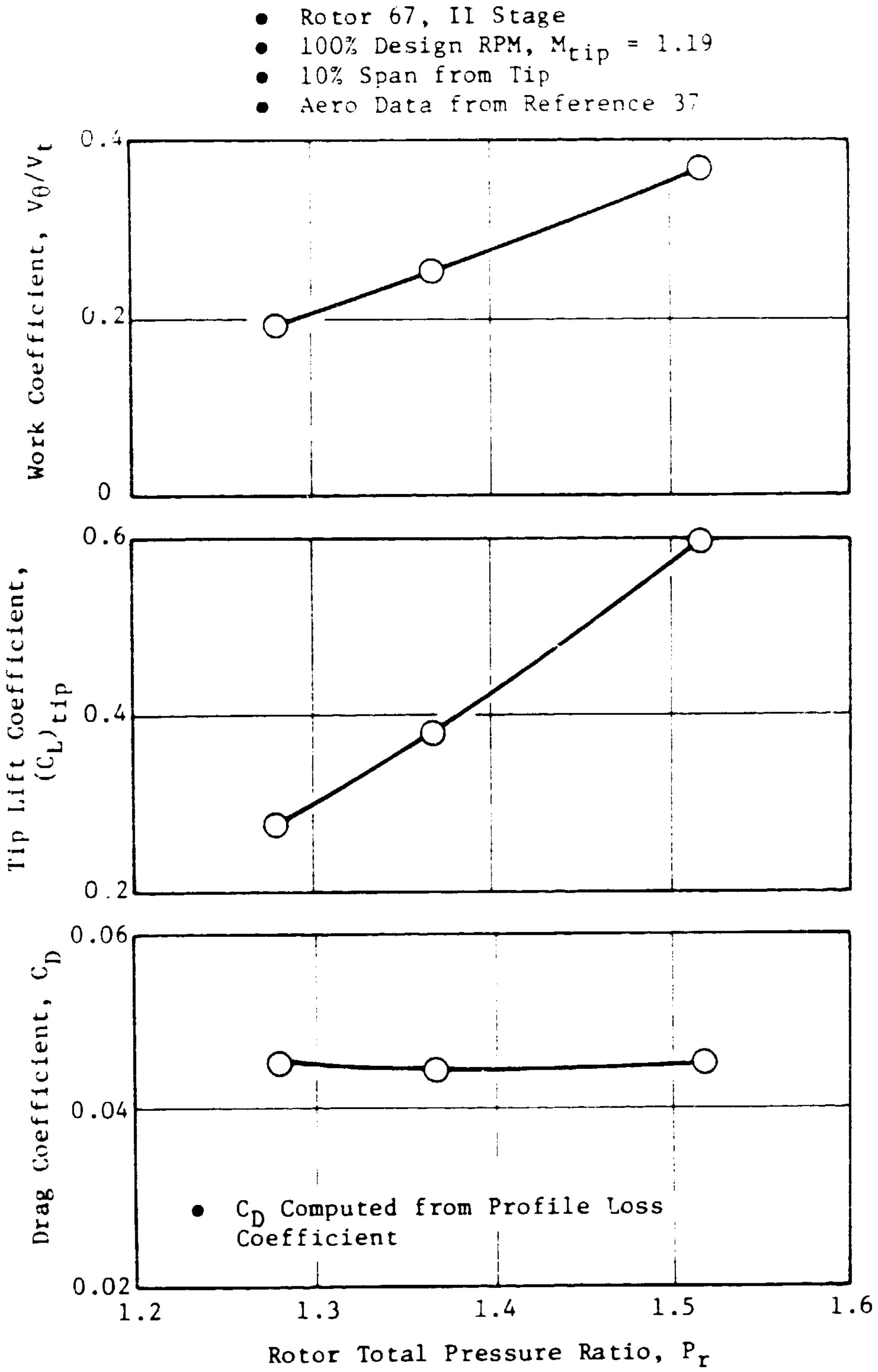

Figure 61. Variation of Work Coefficient, Tip Lift Coefficient, and Drag Coefficient with Rotor Total Pressure Ratio.

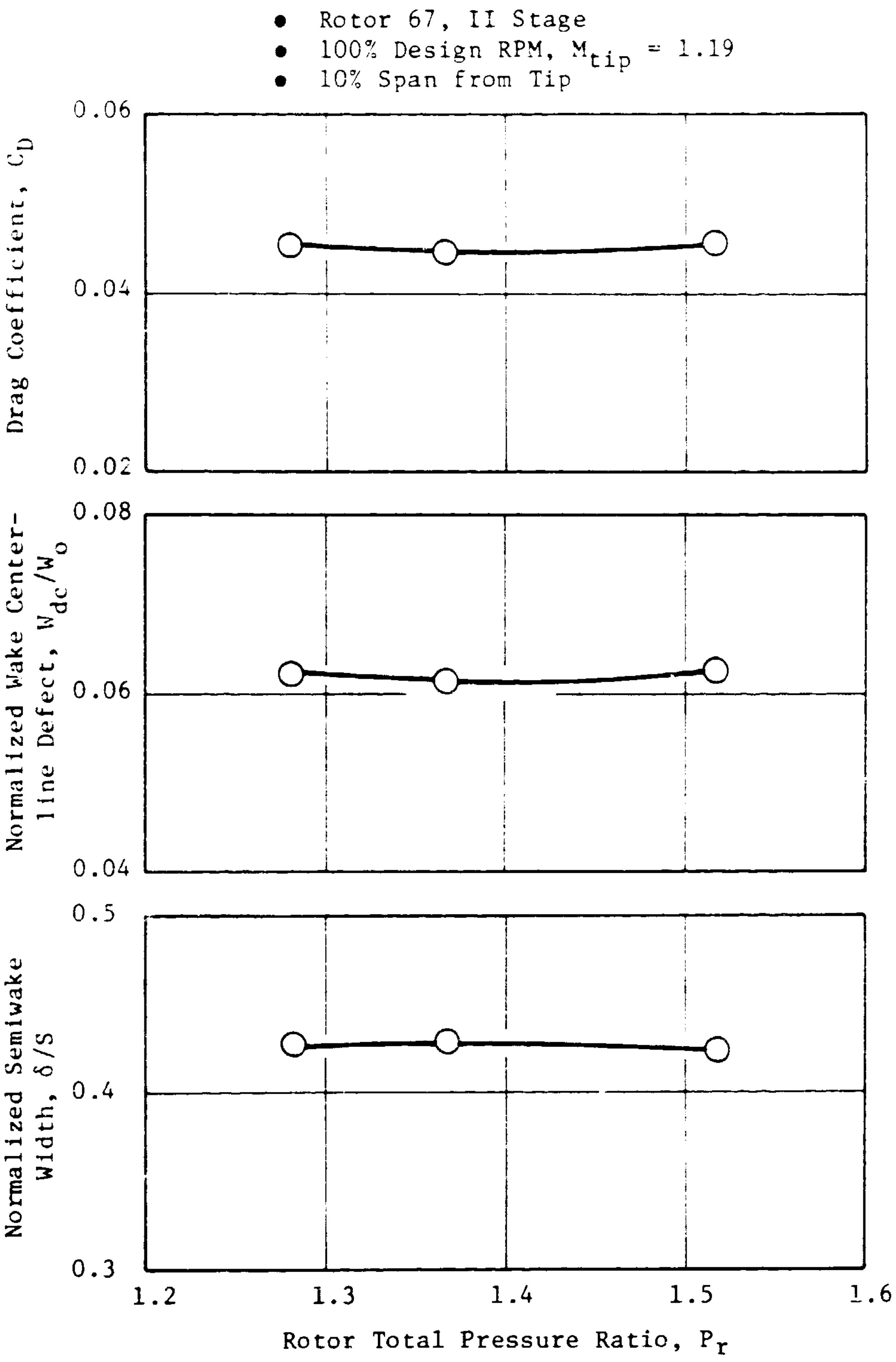

Figure 62. Variation of Drag Coefficient, Wake Centerline Defect, and Semiwake Width with Rotor Total Pressure Ratio.

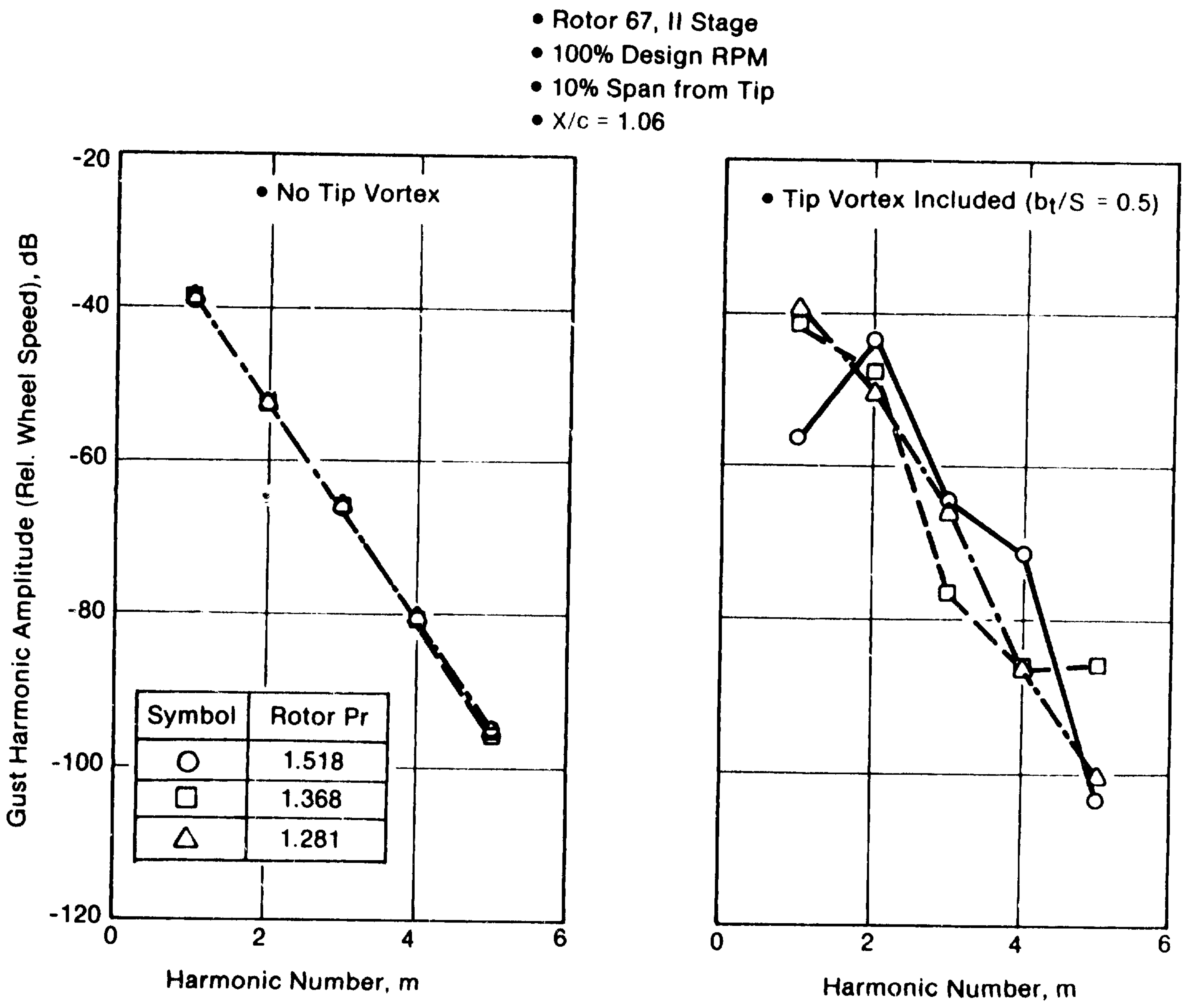

Figure 63. Predicted Influence of Rotor Loading at Constant Rotor Speed on Gust Harmonic Spectra With and Without Tip Vortex.

gust harmonic spectrum for $P_r = 1.281$ with and without the tip vortex is not significantly different. The reason for the above behavior is that the lift coefficient at the tip increases with the rotor loading. Therefore, for the same fraction of lift lost to the tip vortex, $(k)_{tip}$, the circulation of the tip vortex increases (see Subsection 3.2.1) and the influence of tip vortex on the stator upwash velocity and the corresponding gust harmonic spectrum increases.

5.2.6 Influence of Inviscid Velocity Gradient

The influence of the wake asymmetry in terms of a prescribed velocity gradient on the rotor wake and vortex characteristics was studied in this section. For the sign convention adopted for rotor wakes (see Figure 1), a negative value for the inviscid velocity gradient typically represents the fan rotor wakes (see Figure 15) because in such a case the relative velocities on the pressure side are lower than on the suction side.

The streamline at 10% span from the tip of Rotor 55 at 80% design rpm was chosen for this study. Figure 64 shows the predicted influence of three values for the inviscid velocity gradient (WTIV = -1.0, 0.0 and +1.0) on the tangential distribution of the relative velocity normalized by wheel speed, over one blade passage, at three values of rotor-stator spacings. The tip vortex is not included in these predictions. The extent of asymmetry decreases as X/c increases. Note the excessive asymmetry in the relative velocity at X/c = 0.5. The tangential profile for the relative velocity for WTIV = -1.0 is a mirror image of the profile for WTIV = +1.0 for all X/c locations about the wake centerline.

Figure 65 shows the influence of inviscid velocity gradient (WTIV = -1.0, 0.0 and +1.0) on the tangential distribution of the normal perturbation velocity (that is, gust velocity) with and without the tip vortex at X/c = 0.5. The tangential distribution of the gust velocity is shown for the case of a tip vortex at $b_t/S = 0.5$ and 0.42, as well as for the case of no tip vortex. In the case of no tip vortex, the tangential profile of the gust velocity for WTIV = -1.0 is a mirror image of the profile for WTIV = +1.0 about the wake centerline. The tip vortex modifies considerably the tangential distribution of the gust velocity. For the case of the tip vortex located at $b_t/S = 0.5$, the tangential profile of the gust velocity for WTIV = -1.0 is still seen to be an almost mirror image of the profile for WTIV = +1.0. This happens because the tip vortex is exactly at the midpassage. However, when the tip vortex is located at $b_t/S = -0.42$, the tangential profile of the gust velocity for WTIV = -1.0 no longer resembles the profile for WTIV = +1.0. Also, there was a dip in the gust velocity at the tangential location of the tip vortex for all three values of WTIV. Thus, it is seen that the inviscid velocity gradient in combination with the tip vortex can yield complex tangential profiles of the gust velocity.

Figures 66 through 68 show the influence of the inviscid velocity gradients and tip vortex on the gust harmonic amplitude spectra at three values of rotor/stator spacing. Figure 66 shows the influence of the inviscid velocity

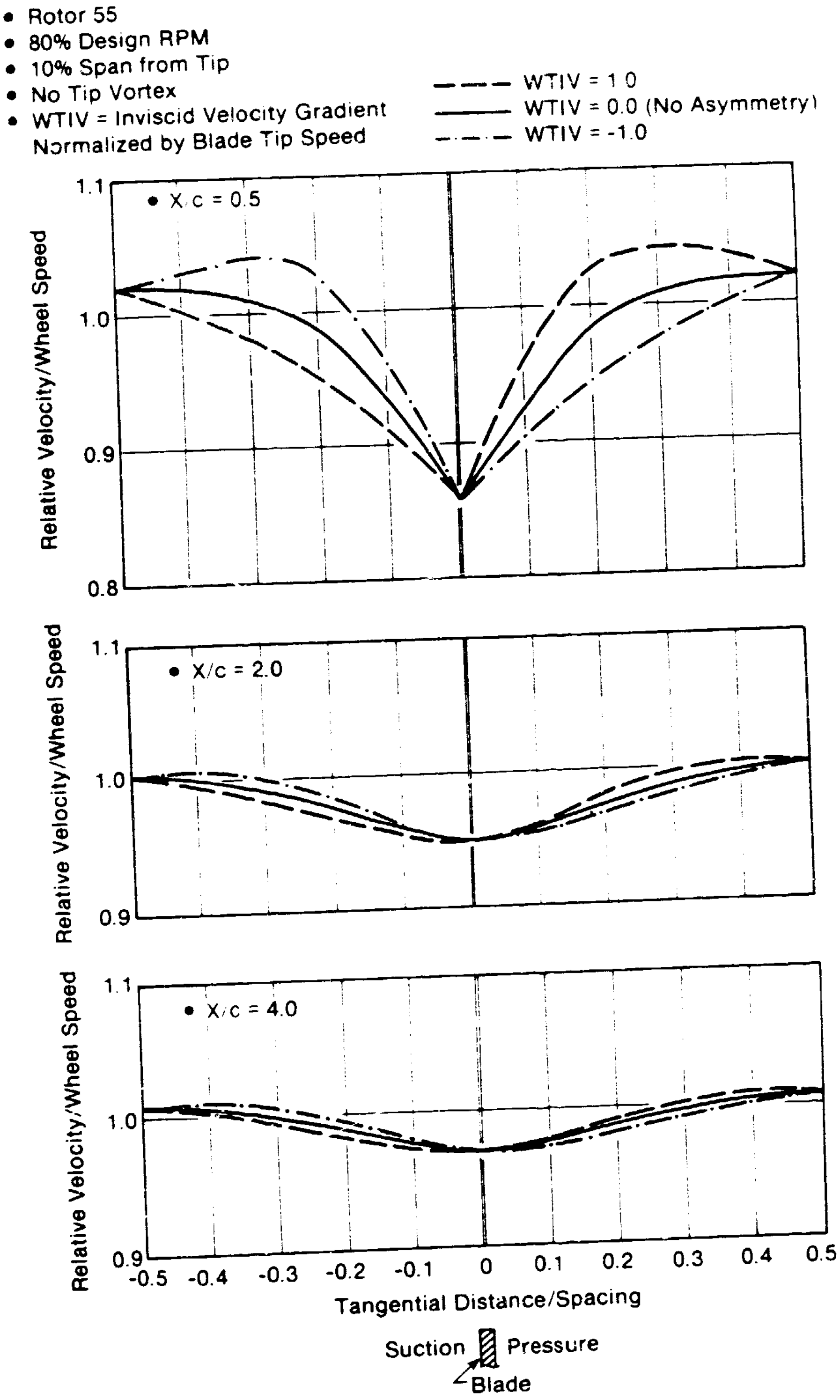

Figure 64. Predicted Influence of the Inviscid Velocity Gradient on Wake Asymmetry at Three Rotor/Stator Spacings.

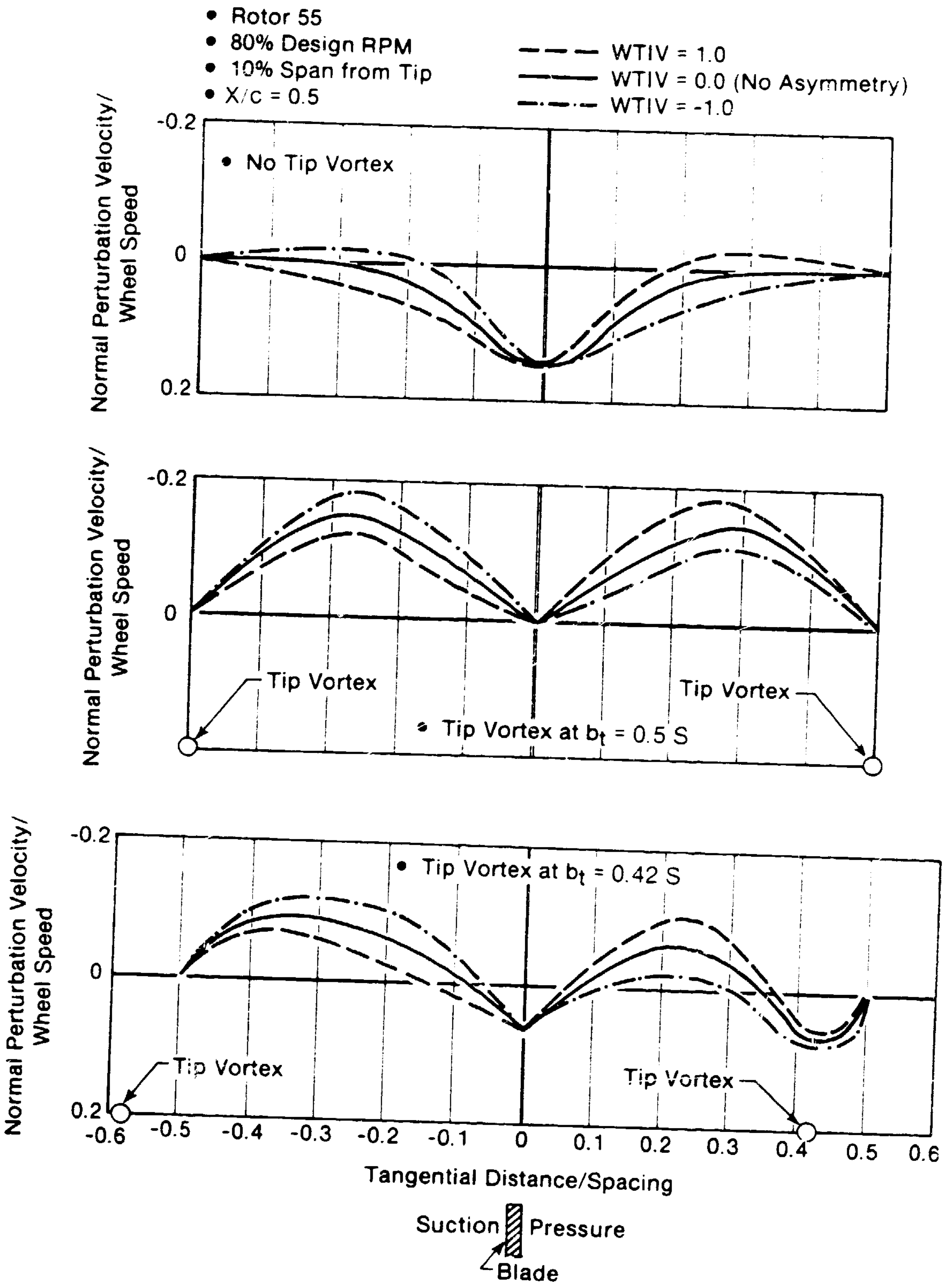

Figure 65. Predicted Influence of the Inviscid Velocity Gradient (WTIV) and Tip Vortex on the Tangential Distribution of Normal Perturbation Velocity.

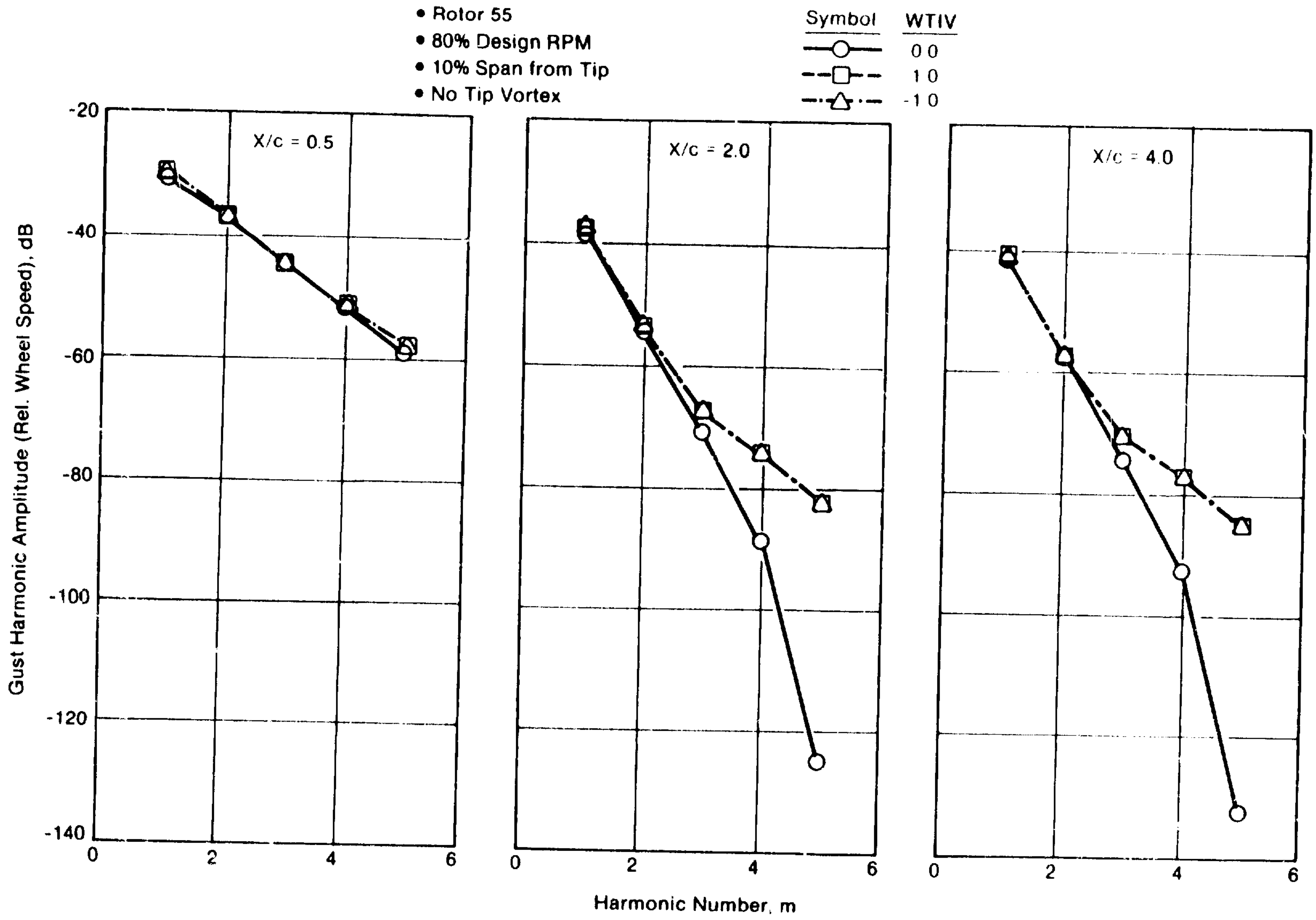

Figure 66. Predicted Influence of the Inviscid Velocity Gradient (Wake Asymmetry Parameter) on Gust Harmonic Amplitude Spectra at Three Rotor/Stator Spacings.

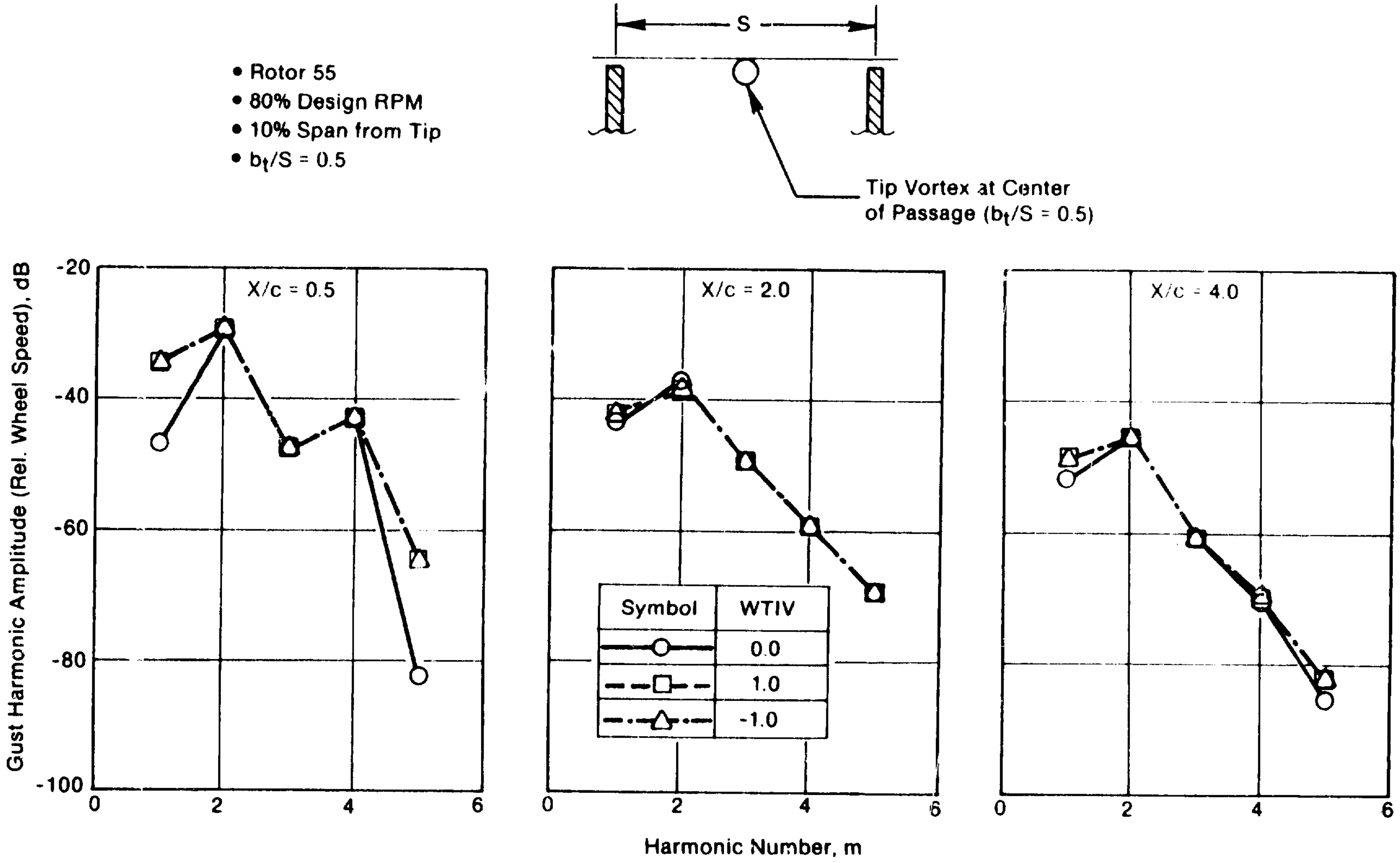

Figure 67. Predicted Influence of the Inviscid Velocity Gradient (Wake Asymmetry Parameter) and Tip Vortex on Gust Harmonic Amplitude Spectra at Three Rotor/Stator Spacings.

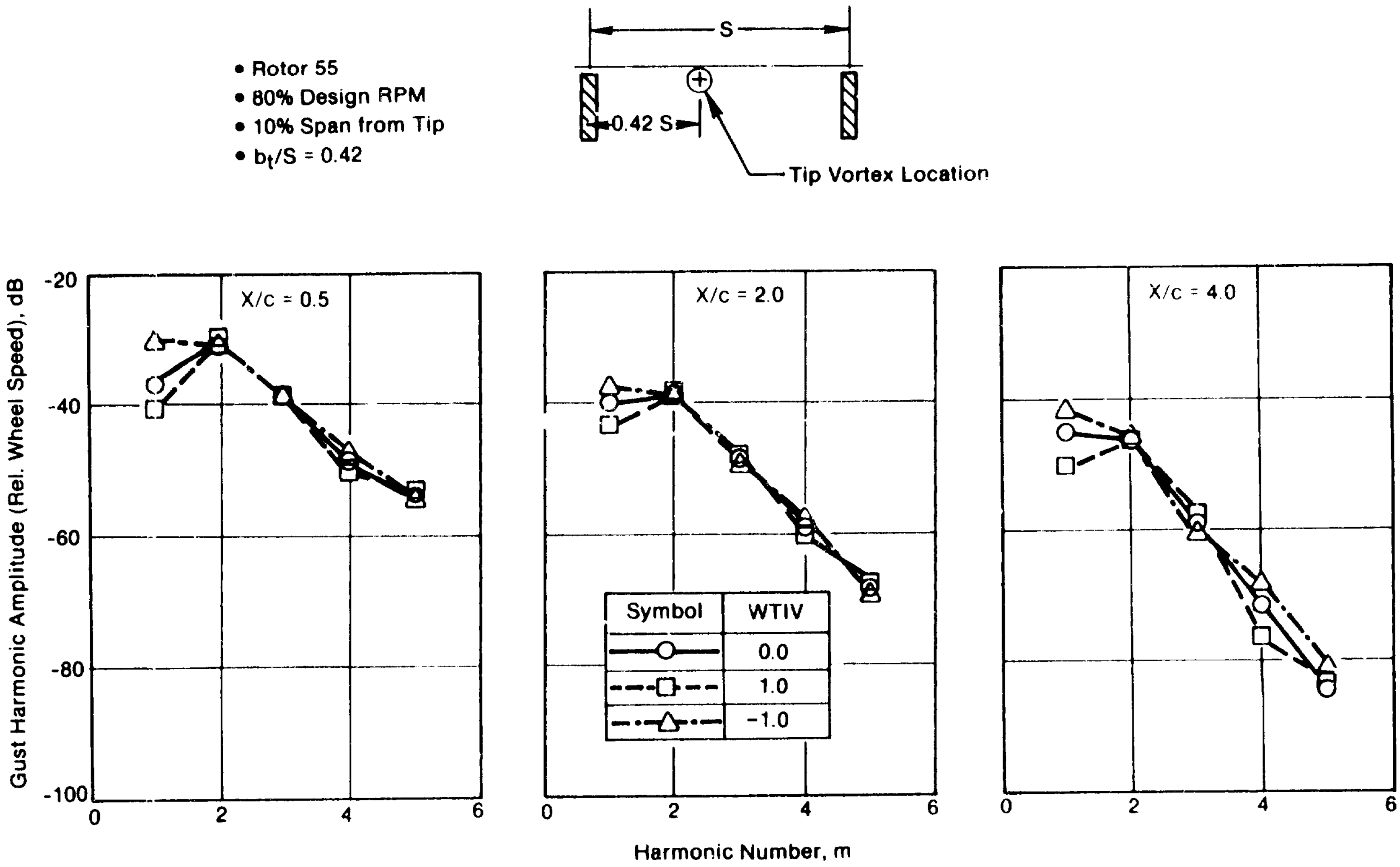

Figure 68. Predicted Influence of the Inviscid Velocity Gradient (Wake Asymmetry Parameter) and Tip Vortex on Gust Harmonic Amplitude Spectra at Three Rotor/Stator Spacings.

gradient on the gust harmonic amplitude spectra at three values of rotor/stator spacing for the case of no tip vortex. Since the tangential profiles of the gust velocity for WTIV = +1.0 and -1.0 are mirror images about the wake centerline, their Fourier decomposition yields the same Fourier coefficients and identical spectra. For the case of WTIV = 0.0 (no asymmetry), the higher harmonics fall off more rapidly than in the case of asymmetry. Figure 67 shows the influence of the inviscid velocity gradient on the gust harmonic amplitude spectra at three values of rotor/stator spacing for the case of tip vortex located at $b_t/S = 0.5$. Since the tangential profiles of the gust velocity for WTIV = +1.0 and -1.0 are almost mirror images of each other, the spectra for WTIV = +1.0 and WTIV = -1.0 are identical. We also notice significant dominance of the tip vortex at $X/c = 0.5$ for all three values of WTIV. Figure 68 shows the influence of the inviscid velocity gradient on the gust harmonic amplitude spectra at three values of rotor-stator spacing for the case of tip vortex located at $b_t/S = 0.42$. The inviscid velocity gradient influences the BPF levels more than the harmonics of BPF at all three rotor/stator spacings. At $X/c = 0.5$ and 2.0, the 2xBPF levels are higher than the BPF levels for WTIV = 0.0 and +1.0, whereas for WTIV = -1.0, the BPF level is slightly higher than the 2xBPF level. This indicates that the negative inviscid velocity gradient (WTIV = -1.0) can offset the influence of tip vortex by pushing the 2xBPF level below the BPF level. Thus, a combination of wake asymmetry and tip vortex can yield complex shapes for the gust velocity spectra.

5.2.7 Influence of Tip Clearance and Tangential Location of Tip Vortex

It has been shown in the previous subsections that the tip vortex can have a significant effect on the stator upwash velocity spectrum. This subsection deals with the influence of two parameters of the tip vortex (tip clearance and tangential location of tip vortex) on certain parameters of the vortex structure and on the stator upwash gust harmonic spectra. The streamline located at 10% span from tip for Rotor 55 at 80% design rpm is chosen for this parametric study.

Figure 69 shows the predicted variation of normalized radius of vortex core, streamwise velocity defect of vortex core, and circulation of vortex with rotor-stator spacing for five values of tip clearances. The mathematical modeling of these parameters is described in Subsection 3.2.1. The nominal value representing the tip clearance of Rotor 55 is $/(c)_{tip} = 0.009$. Tip clearance has been varied around this nominal value. The tip vortex radius increases with tip clearance, as well as with rotor-stator spacing. The vortex radius is modeled to increase as $(s/c + 1)^{0.5}$. The streamwise velocity deficit of the vortex core increases with the radius of vortex core, which in turn increases with tip clearance. The streamwise velocity deficit of the vortex core is modeled to decay as $1/(s/c+1)$ (see Subsection 3.2.1). Figure 69 also shows the decay of the circulation of the tip vortex with axial distance for the five values of the tip clearances.

Previous sections have demonstrated that the presence of a tip vortex at the mid blade passage yields another defect in the tangential profile of relative velocity in addition to that of the rotor wake within one blade passage.

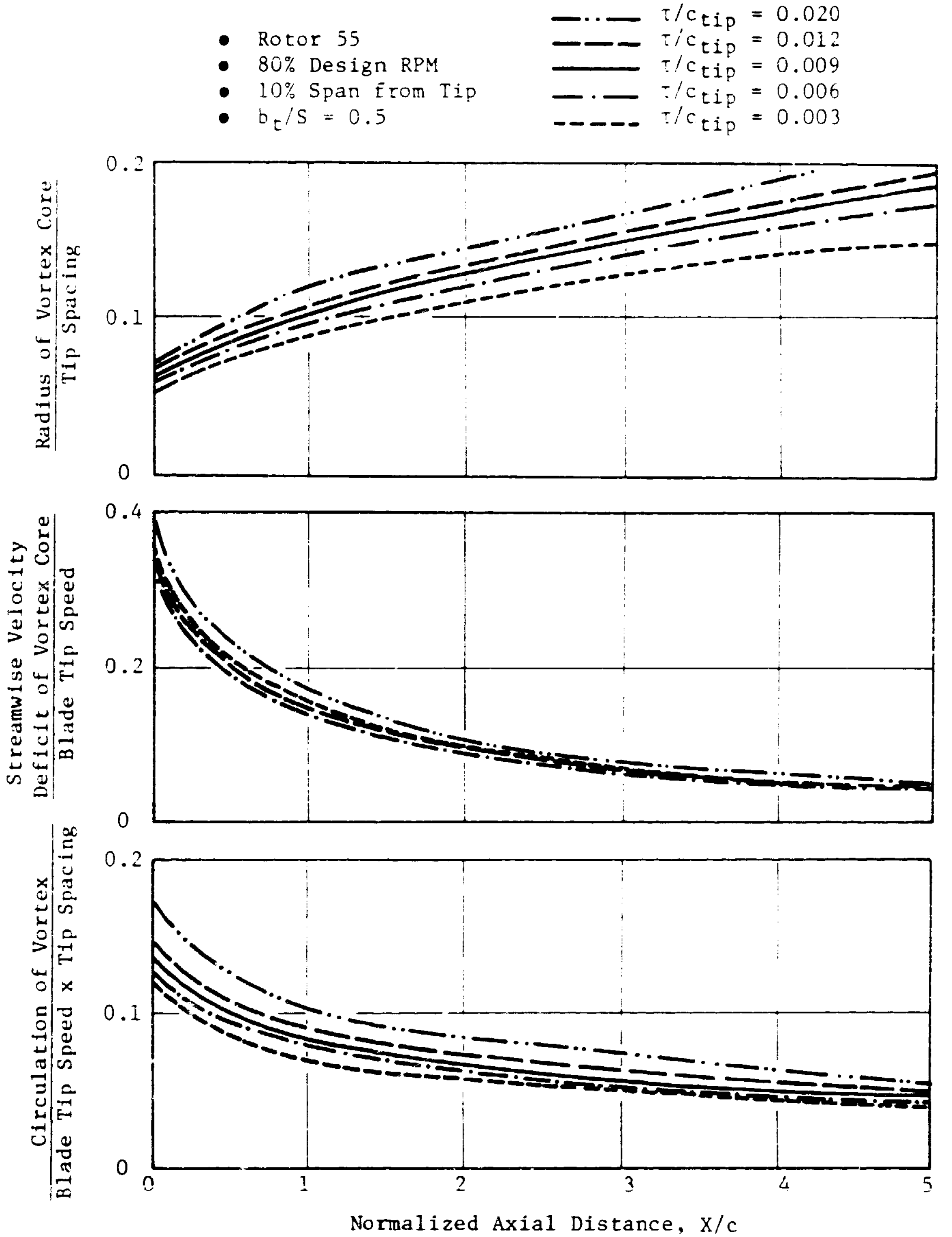

Figure 69. Predicted Variation of Tip Vortex Parameters with Rotor/ Stator Spacing for Five Values of Tip Clearance.

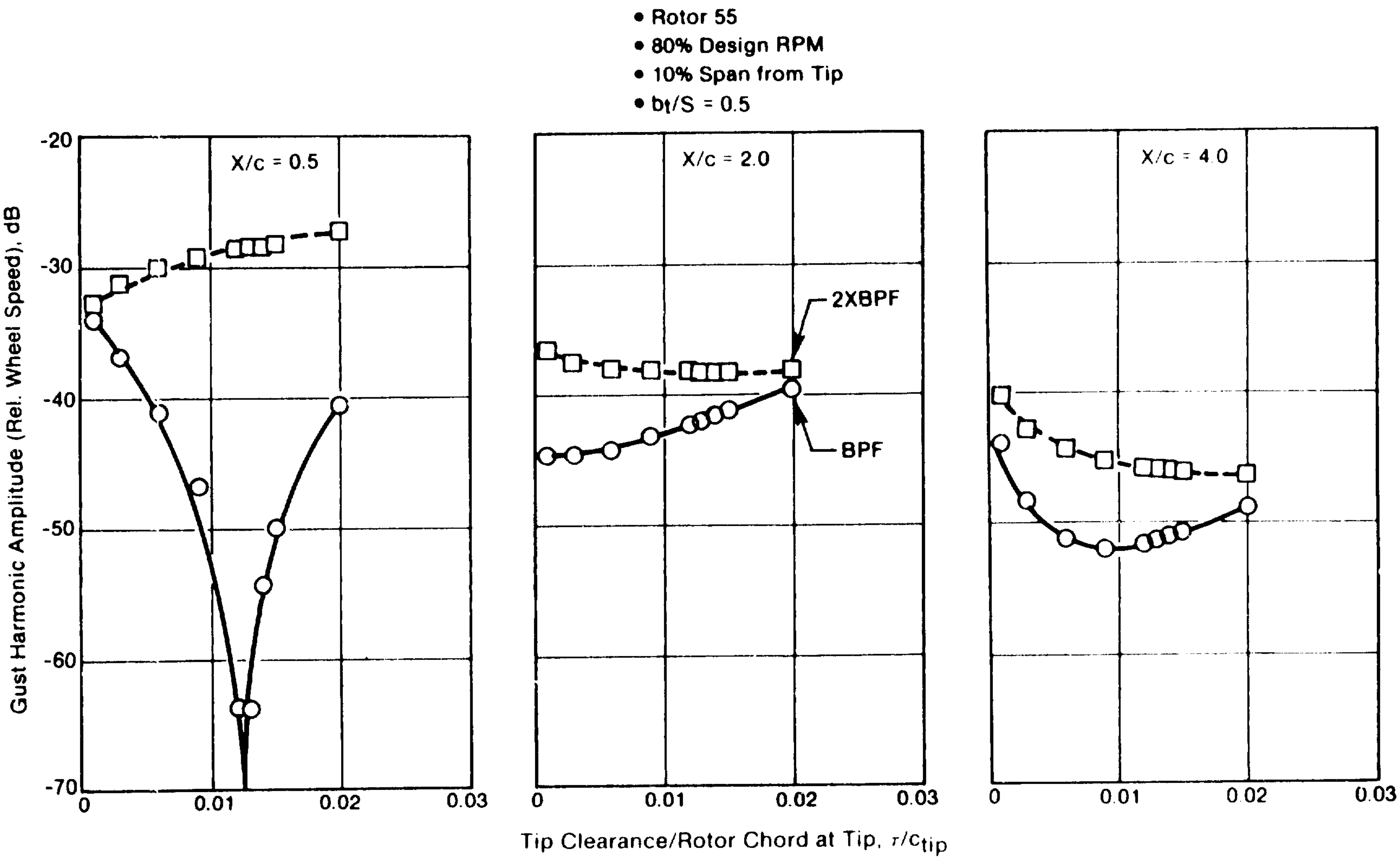

Figure 70. Predicted Influence of Tip Clearance on the Gust Harmonic Amplitude of BPF and 2XBPF Tones at Three Rotor/Stator Spacings.

Hence, 2xBPF levels of the gust velocity harmonic spectra have tended to be higher than the BPF levels. A more detailed study of this phenomenon is reviewed here. Figure 70 shows the predicted influence of tip clearance on the gust harmonic amplitude of BPF and 2xBPF tones at three rotor-stator spacings for the streamline at 10% span from the tip for Rotor 55 at 80% design rpm. The tangential location of the tip vortex for these computations is set at $b_t/S = 0.5$. The 2xBPF levels are larger than the BPF levels at all three rotor-stator spacings. For $X/c = 2$ and 4, the ΔdB between 2xBPF and BPF levels decreases, indicating decay of the vortex at these distances. Also, we notice sharp reduction in BPF level in the vicinity of $\tau/(c)_{tip} = 0.012$, at $X/c = 0.5$. For values of $\tau/(c)_{tip}$ on either side, the ΔdB between 2xBPF and BPF levels decreases. This behavior can be explained by examining the tangential distribution of the gust upwash velocity (Figure 71). Figure 71 shows the tangential distribution of the gust upwash velocity over two blade passages for $\tau/(c)_{tip} = 0.003$, 0.012, and 0.02, at $X/c = 0.5$. As the tip clearance increases, the peak defect due to the tip vortex (that is, defect at $x/S = 0.5$ or 1.5) increases compared to the rotor wake (that is, defect at $x/S = 0.0$ or 1.0 or 2.0). At $\tau/(c)_{tip} = 0.012$, the peak defect created by the tip vortex is almost identical to that due to the rotor wake. Thus, for $\tau/(c)_{tip} = 0.012$, the gust upwash velocity tangential distribution shows two almost identical waveforms within one blade passage. Hence, the Fourier analysis of such a waveform shows a negligible contribution from the BPF harmonic amplitude relative to the 2xBPF amplitude. On either side of this tip clearance, the peak defects due to tip vortex and rotor wake are not identical, even though there are two waveforms within one blade passage; thus, the ΔdB between 2xBPF and BPF levels decreases. This is the reason why the BPF level tends to approach 2xBPF tone level for increasing tip clearances at other axial locations.

Figure 72 shows the predicted influence of tip clearance on the gust harmonic amplitude of BPF and 2xBPF at three rotor-stator spacings for the case of $b_t/S = 0.45$, for the streamline at 10% span from tip for Rotor 55 at 80% design rpm. Since the tip vortex is not exactly at the middle of the blade passage, there is not a sharp fall in the BPF level at $X/c = 0.5$, as was noticed in Figure 70, where the tip vortex was exactly in the middle of the blade passage. Figure 73 compares the predicted tangential distribution of the gust upwash velocity for $b_t/S = 0.5$ and 0.45, for $\tau/(c)_{tip} = 0.012$. For $\tau/(c)_{tip} = 0.012$ and $b_t/S = 0.5$, almost two identical waveforms exist within one blade passage. When the tip vortex is at $b_t/S = 0.45$, there are no two identical waveforms within one passage, even though the peak defects due to rotor wake and tip vortex are almost the same. The relative variation between 2xBPF and BPF amplitudes at $X/c = 2$ and 4 as a function of tip clearance for $b_t/S = 0.45$ follows that of $b_t/S = 0.5$ (Figures 70 and 72). Thus, one notes that the behavior of the upwash velocity spectrum near the tip region is very sensitive to the tip clearance and tangential location of the tip vortex.

Figure 74 shows the predicted influence of the tangential location of tip vortex on the gust upwash harmonic amplitude spectra at three rotor-stator spacings for the streamline at 10% span from tip for Rotor 55 at 80% design rpm. The gust upwash harmonic amplitude spectrum for the case of no tip vortex is also included for the sake of reference. At all three rotor-stator

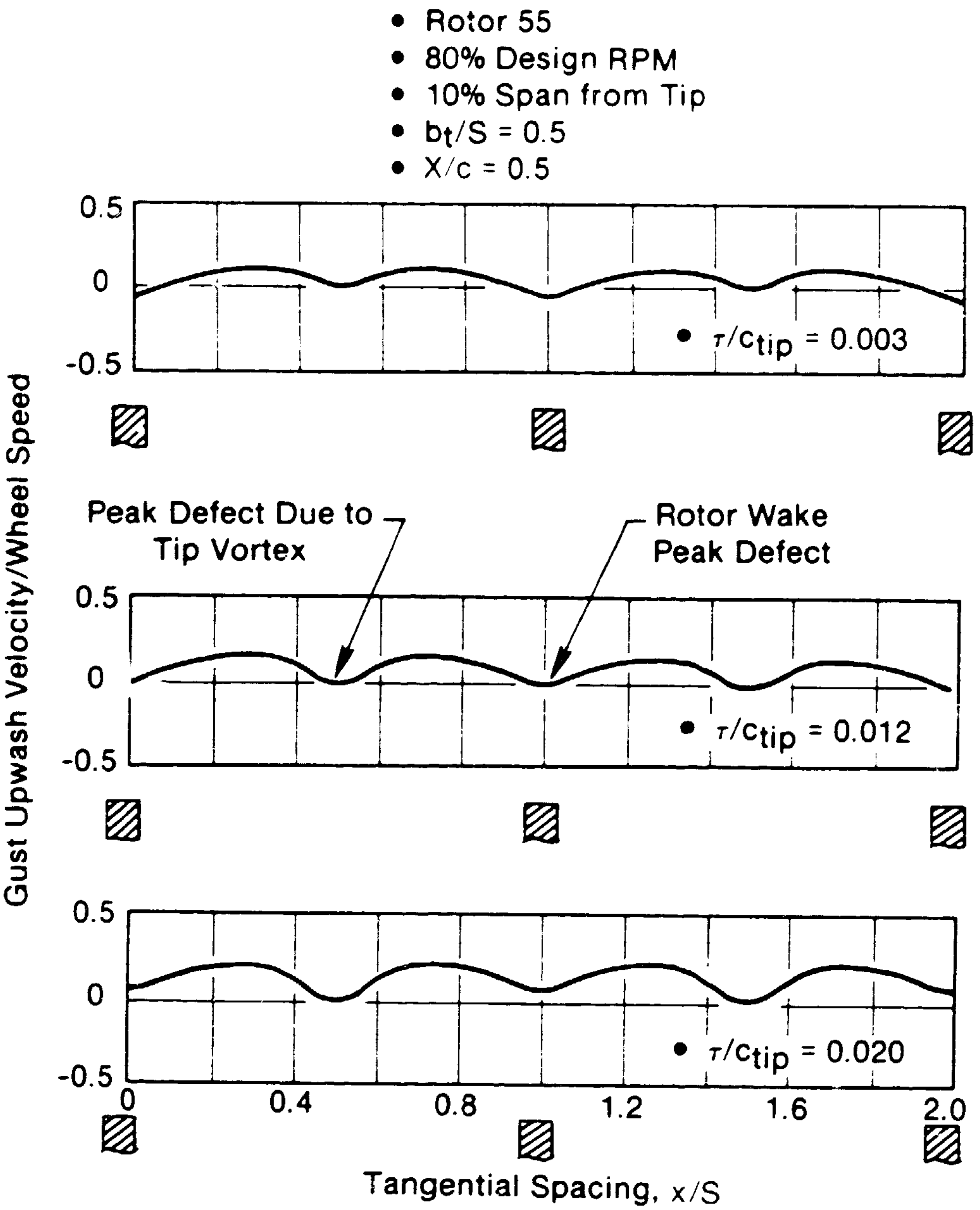

Figure 71. Predicted Tangential Distribution of the Gust Upwash Velocity for Three Values of Tip Clearance.

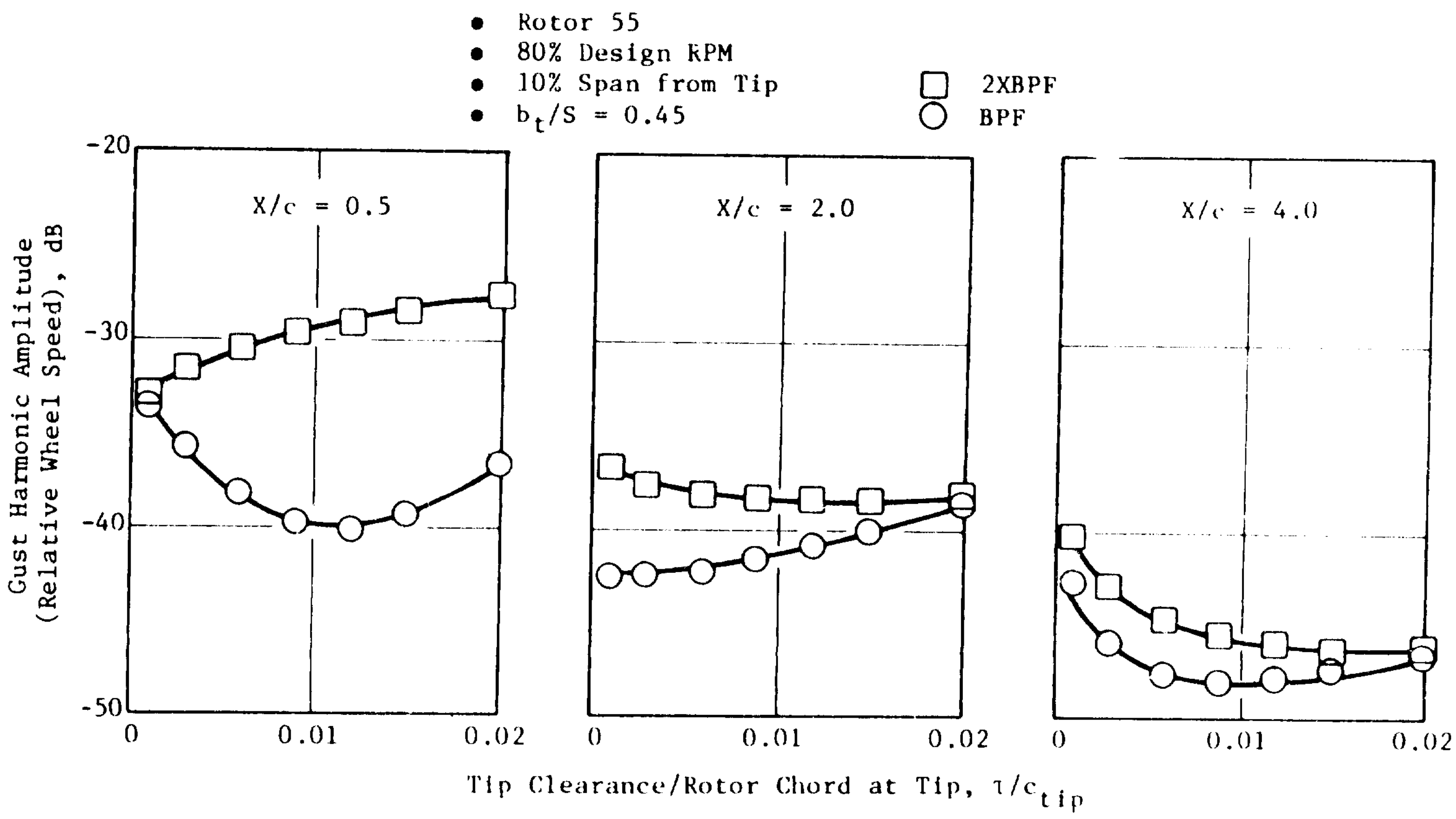

Figure 72. Predicted Influence of Tip Clearance on the Gust Harmonic Amplitude of BPF and 2XBPF Tones at Three Rotor/Stator Spacings.

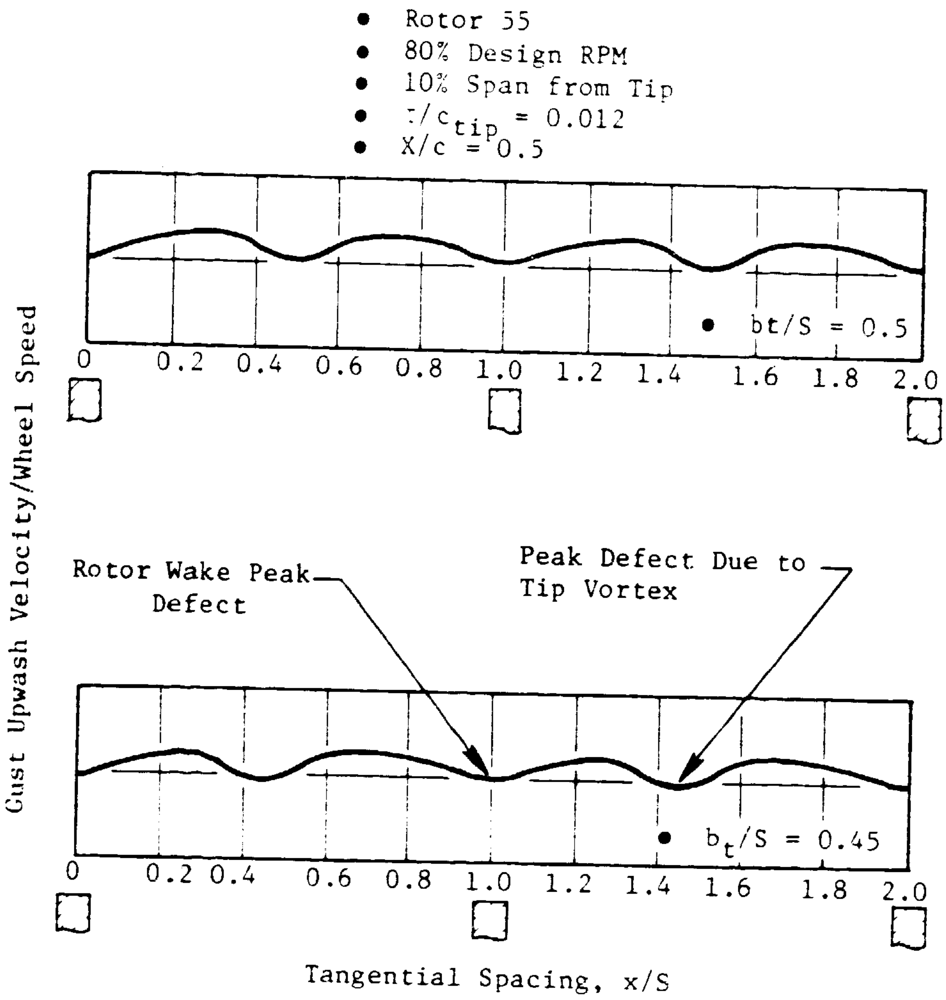

Figure 73. Predicted Tangential Distribution of the Gust Upwash Velocity for Two Tangential Locations of the Tip Vortex.

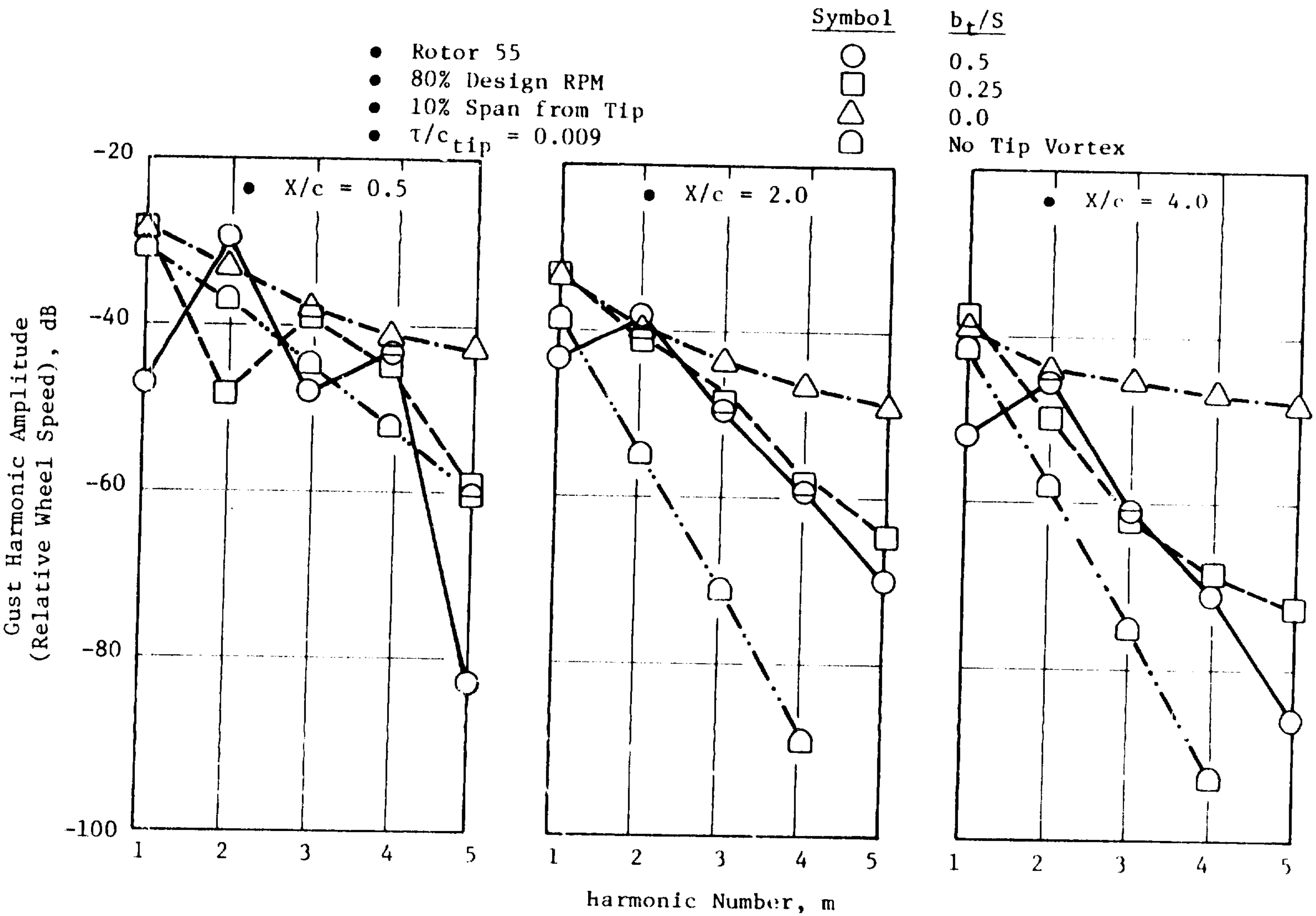

Figure 74. Predicted Influence of Tangential Location of Tip Vortex on the Gust Harmonic Amplitude Spectra at Three Rotor/Stator Spacings.

spacings, the 2xBPF levels are higher than the BPF level when the tip vortex is located at $b_t/S = 0.5$. In fact, at $X/c = 0.5$, the 4xBPF level is higher than the 3xBPF level, for $b_t/S = 0.5$. As the tip vortex is moved away from the blade midpassage to $b_t/S = 0.25$, the 2xBPF level is no longer higher. In fact, the odd multiples of BPF are higher than the subsequent even multiples of BPF. When the tip vortex is located right at the wake centerline of $b_t/S = 0.0$, the fall-off rate of the harmonics is very slow. For the case of no tip vortex, the spectrum shows monotonic fall-off with harmonic number. At $X/c = 2$ and 4, the fall off rate is quite high, indicating sufficiently large semiwake widths, so that the wake profile within one blade passage resembles a sinusoidal wave with blade passage as its period. Also, at large spacings ($X/c = 2$ and 4), there is a significant difference between the no tip vortex case and cases with a tip vortex at any tangential spacing. This implies that, for streamlines close to the tip, no matter what the tangential location of a tip vortex, it can significantly modify the gust upwash velocity spectrum.

Figure 75 shows the predicted influence of the tangential location of the tip vortex on BPF and 2xBPF levels at three rotor-stator spacings in order to highlight some of the features presented in Figure 74. We note that at $X/c = 0.5$, the 2xBPF level is higher than the BPF if $0.36 \leq b_t/S \leq 0.5$. At $X/c = 2.0$, the 2xBPF level is higher than BPF if $0.41 \leq b_t/S \leq 0.5$. For $X/c = 4.0$, the 2xBPF level is higher than BPF if $0.44 \leq b_t/S \leq 0.5$. This indicates that as X/c increases, the existence of two similar waveforms within one blade passage (one due to rotor wake and another due to tip vortex) is restricted to narrower regions about the blade midpassage where the tip vortex ought to exist. This happens because the tip vortex and the rotor wake decay at different rates. At $X/c = 0.5$, there is a sharp drop in the 2xBPF level when $b_t/S = 0.25$. As shown in Figure 74, odd multiples of BPF are predominant at this location. An explanation for this and other features observed in Figure 74 can be found by examining the tangential distribution of the gust upwash velocity (see Figure 76). Figure 76 shows the predicted tangential distribution of the gust upwash velocity for three tangential locations of the tip vortex ($b_t/S = 0.5$, 0.25, and 0.0) and for the case of no tip vortex, for $X/c = 0.5$. For $b_t/S = 0.5$, there are almost two identical waveforms within one passage. Therefore, even multiples of BPF show higher levels than the preceding odd multiples of BPF (see Figures 74 and 75). For $b_t/S = 0.25$, the defects due to tip vortex and rotor wake interact, and the resulting waveform is not symmetric as it was for $b_t/S = 0.5$. This causes the odd multiples of BPF to increase more than succeeding even multiples of BPF. When $b_t/S = 0.0$, the defects due to wake and vortex yield a sharp upwash velocity profile at the blade centerline, similar to a step function. The Fourier transformation of an impulse function is a constant (that is, a step function can be constructed by summing infinite harmonics of constant amplitude). The gust upwash harmonic amplitude spectrum for $b_t/S = 0.0$ indeed shows the lowest fall-off rate with the harmonic number. In the case of no tip vortex, the gust upwash velocity profile shows one defect due to the wake, and thus the higher harmonics fall monotonically with the harmonic number.

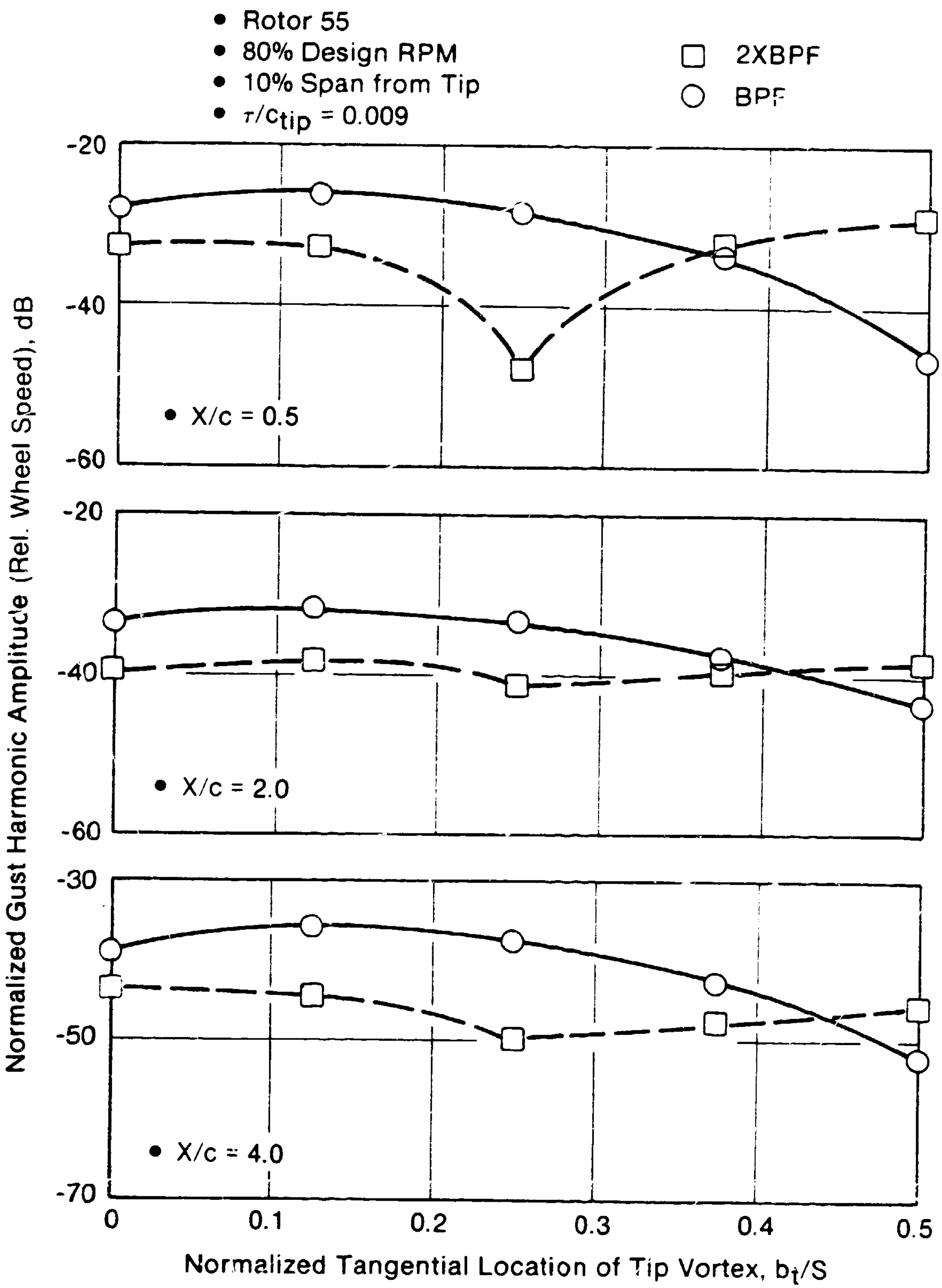

Figure 75. Predicted Influence of Tangential Location of Tip Vortex on BPF and Its Harmonic Tone Levels at Three Rotor/Stator Spacings.

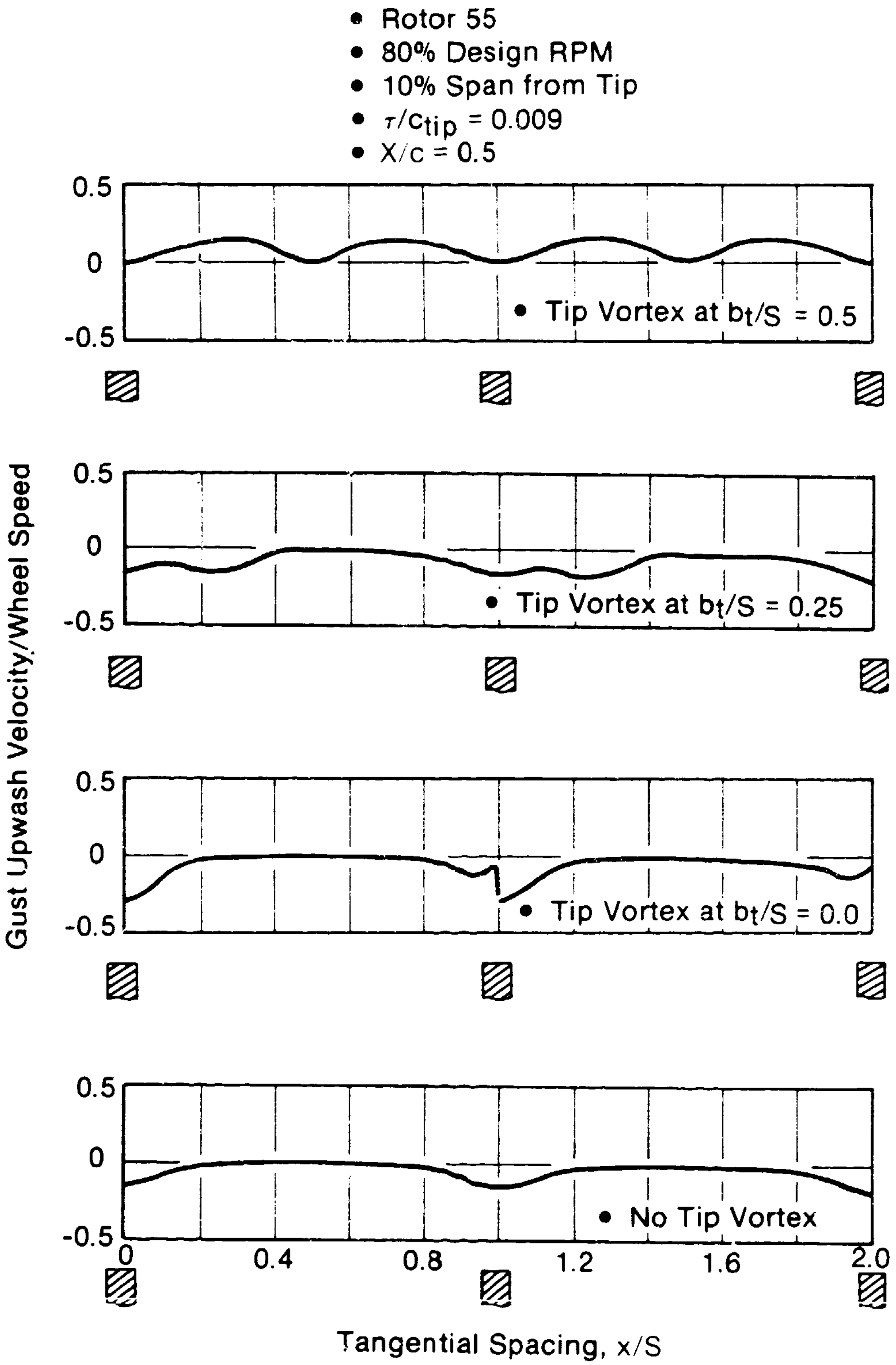

Figure 76. Predicted Tangential Distribution of the Gust Upwash Velocity for Three Tangential Locations of the Tip Vortex and for the Case of No Tip Vortex.

5.2.8 Influence of Velocity and Length Scales on Turbulence Spectrum

This subsection deals with the influence of axial and transverse velocity and length scales on the axisymmetric turbulent velocity spectrum model, which was described briefly in Subsection 3.3.2.

The streamline at 10% span from the tip of Rotor 55, operating at 80% design rpm, was chosen for this parametric study. The predicted axial and tangential turbulence velocities at $X/c = 0.54$ at midspan equal $0.0333 \times V_{wheel}$, and the predicted radial turbulence velocity equals $0.0394 \times V_{wheel}$. Since there is not enough information available on axial and transverse length scales, they are assumed to be equal, and are prescribed as fractions and multiples of the semiwake width. The above velocity and length scales yield a value of 1.8 for the turbulence asymmetry parameters, ϵ (see Subsection 3.3.2).

Figure 77 shows the predicted influence of varying the axial and transverse velocity scales while holding the axial and transverse length scale constant at $L_a/\delta = L_t/\delta = 0.5$, and also the predicted influence of varying the axial and transverse length scales while holding the axial and transverse velocities constant at the nominal values of $u'/V_{wheel} = 0.0333$ and $w'/V_{wheel} = 0.0394$. The bandwidth for these predictions equals 0.5 BPF. The axial and transverse velocity and length scales are varied so that ϵ is constant at a value of 1.8. We notice that doubling the velocity scales increases the broadband levels by about 6 dB and the shape of the broadband spectrum is not altered. However, varying the length scale alters the levels and the shape of the broadband turbulence spectrum. At smaller length scales, the broadband levels fall more slowly with increasing frequency.

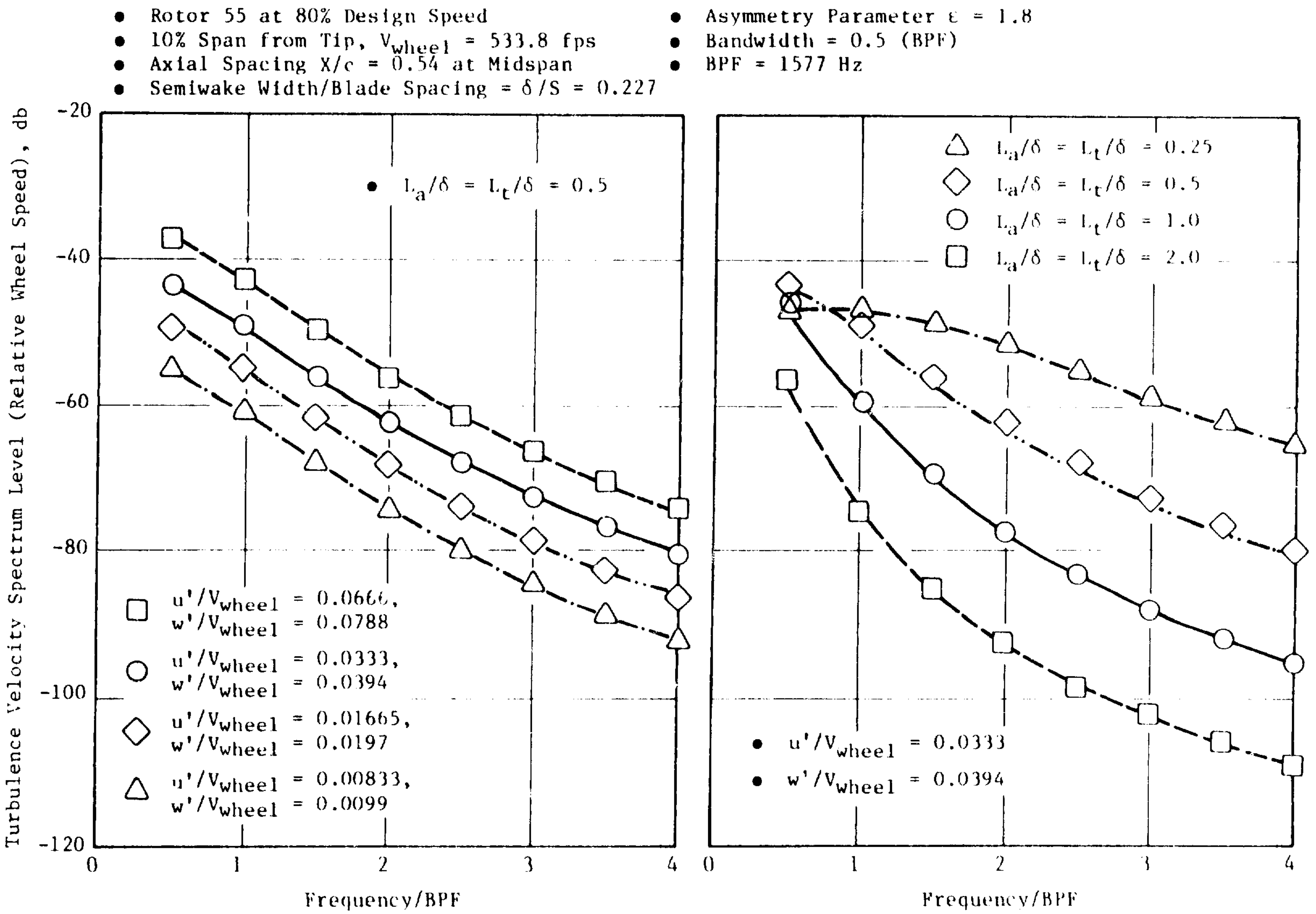

Figure 77. Predicted Influence of Axial and Transverse Velocity and Length Scales on Axisymmetric Turbulent Velocity Spectrum.

6.0 CONCLUSIONS AND RECOMMENDATIONS

The principal objective of this research program was to establish a verified rotor wake and vortex model for specific application to fan and compressor rotor-stator interaction and resulting noise generation. The program called for the development of an empirical model for rotor wake and tip vortex characteristics, along with a turbulence spectrum model to predict the broadband spectrum of the stator gust upwash.

6.1 CONCLUSIONS

Certain empirical rotor wake and turbulence relationships were developed using the low speed rotor wake data of the Pennsylvania State University rotors. A tip vortex model was developed by replacing the annulus wall with a row of image vortices. An axisymmetric turbulence spectrum model, developed in the context of rotor inflow turbulence, was adapted for predicting the turbulence spectrum of the stator gust upwash. An interesting conclusion, arrived at while correlating the tangential distribution of turbulent velocities, is that the tangential profile of turbulent velocities is fairly flat, whereas the tangential profile of the turbulent intensity is Gaussian.

The principal conclusions drawn from the data-theory comparisons performed in this research program are as follows:

- The agreement between the predicted and measured gust harmonic amplitude spectra for the JT15D fan rotor at various span locations for four rpm's along the engine operating line is excellent.

- The empirical rotor wake and vortex model has been shown to predict very well the observed trends both in the gust harmonic spectra and the turbulence spectra for Rotor 55 at three speeds.

- The predicted and measured wake centerline defect and semiwake width for Rotor 67 are in reasonable agreement for axial distance greater than about 0.4 chord, but do not agree close to the rotor trailing edge. The reason for the disagreement is believed to be the shock boundary layer interaction over the rotor blades of this high speed rotor, which significantly modifies the wake flow close to the trailing edge. The prediction model has been developed using low speed rotors which do not exhibit the shock boundary layer interaction.

- The table below gives the range of certain key parameters of the data base employed to develop the empirical relations for the prediction model and the range over which the prediction model has been verified to yield reasonable data-theory comparisons.

Parameter	Range of Parameter in the Data Base	Range of Parameter Over Which the Model is Verified
Axial Spacing at Midspan (X/c)	0.01 to 1.664	0.4 to 1.8
Tip Speed	95 fps to 168 fps	560 fps to 1000 fps
Rotor Solidities	0.68 to 1.28	0.9 to 1.772

A significant portion of this effort was devoted to parametric studies of the verified rotor wake and vortex prediction model. Some of the interesting conclusions of these parametric studies are given below:

- Increasing the rotor-stator spacing above a value at which the merging of wakes from the adjacent rotor blades takes place does not yield any appreciable reduction in the fluctuating lift component. This can be used as a design guide in the selection of rotor-stator spacing from the point of view of reducing the rotor wake interaction with the stator.

- Tip vortex yields a streamwise defect just like the wake from the rotor blade, and also induces a significant amount of azimuthal and spanwise velocity components. By virtue of this, the tip vortex can significantly influence the gust spectrum, particularly near the tip region. The presence of a tip vortex typically results in higher levels for 2*BPF compared to BPF, which is essentially due to the presence of two defects within one blade passage.

- The tip clearance is a critical parameter in determining the strength of the tip vortex, in that the higher the tip clearance, the higher is the fraction of lift lost to the tip vortex. At a certain value of the tip clearance, the streamwise defect caused by the tip vortex equals that caused by the rotor wake. If the tip vortex were to be located at exactly the midpassage in such a case, the rotor exit flow has two identical defects within one blade passage, which results in a gust harmonic spectra dominated by even harmonics of BPF.

- The tangential location of the tip vortex has an important bearing on the gust harmonic spectra. If the tip vortex is exactly in the blade midpassage, even harmonics of BPF dominate the gust spectra; if the tip vortex is exactly at 1/4 blade passage, odd harmonics of BPF dominate. If the tip vortex is right at the wake centerline, the combination of the wake and vortex defects yields a narrow defect which results in increased contribution to the gust harmonic spectra by all harmonics of the BPF.

- Rotor loading (rotor pressure ratio) causes asymmetry of rotor wakes on the pressure and suction sides of the rotor blades. A simple model of the rotor wake asymmetry in terms of a prescribed inviscid velocity gradient was developed to study this aspect. Wake asymmetry by itself did not have much effect on the gust harmonic spectra even at small rotor/stator spacings. However, a combination of asymmetric wake and tip vortex results in complex gust harmonic spectra.

- The section drag coefficient is normally minimum at the midspan location of a rotor blade, so the wake defect and the semiwake width are lowest in the midspan location.

- The section drag coefficient is normally minimum at the design rpm, so the wake defect and the semiwake width are lowest at the design rpm.

- Higher rotor solidity (obtained by increasing the rotor chord and keeping the same blade-to-blade spacing), results in larger wake defects and smaller semiwake widths at a prescribed distance from the rotor trailing edge. Hence, the stator upwash spectra (without tip vortex) shows higher absolute level and lower fall-off rate with the harmonic number with higher solidity, as long as the wakes from the adjacent blades have not merged. Once the wakes from the adjacent blades merge, the rotor solidity has very little influence on the stator upwash spectral fall-off rate with the harmonic number. A clear trend with rotor solidity cannot be extracted in the presence of a tip vortex at streamlines close to the tip because the tip vortex dominates the stator upwash spectra at these streamlines.

In summary, this research program has established and verified a rotor wake and vortex model. The parametric studies have given a valuable insight into the influence of various geometric and aerodynamic parameters on the stator upwash gust harmonic spectra. The computer program requires about 10 seconds of CPU time per case on the GE Honeywell-6000 system and thus is ideally suited for extensive parametric and preliminary design studies.

6.2 RECOMMENDATIONS

There are several possible improvements for the above developed rotor wake and vortex model. Some of the salient improvements recommended are discussed as follows.

- In recent times, the counterrotating propeller concept has been shown to be a very attractive way to reduce specific fuel consumption. It is anticipated that there will be strong rotor-to-rotor interactions because of the small axial spacings between the two counterrotating propellers, possibly introducing high noise levels and/or forced vibrations. The rotor-stator wake and tip vortex interaction model developed here could be generalized to the case of the counterrotating propellers to aid in the understanding and prediction of the rotor-rotor interaction noise mechanisms. It is recommended that such a study be undertaken.

- The tangential location of the tip vortex could not be pinned down by correlating the existing experimental data of the wave forms of the upwash component in the tip region, and hence it is prescribed as an input parameter. At present this parameter is somewhat arbitrary in the sense that we have to adjust this parameter to get reasonable agreement between data and theory. The detailed parametric studies show the sensitivity of the gust harmonic spectra to this parameter. A detailed experimental survey of the tip region waveforms of the upwash component at several axial stations for various rotors at different operating speeds is recommended. A correlation for predicting the tangential location of the tip vortex in terms of tip clearance, rotor speed, rotor loading at the tip, etc., can then be developed.

- The rotor wake momentum integral analysis (Section 4.2) offers the ability to predict rotor wake structure, accounting for many more influential parameters with much less empiricism than the current correlation approach (Section 3.1). The choice of blade spacing, instead of rotor aerodynamic chord, as the normalizing dimension for the semiwake width, is reasonable for the high solidity rotors being considered in the current correlation approach. However, for low solidity rotors, rotor aerodynamic chord presumably is the correct normalizing dimension. The rotor wake momentum integral analysis will clarify this issue and will aid in the proper choice of the characteristic dimension for rotor wakes of widely varying solidities.

- As the parametric studies have indicated, the stator upwash harmonic spectrum is influenced significantly by the combined presence of the tip vortex and the inviscid velocity gradient (that is, rotor loading). At the present time, the inviscid velocity gradient is a prescribed input and is not correlated with rotor loading. A cascade flow analysis is recommended so that the inviscid velocity gradient can be correlated with the rotor loading.

- Though the prediction model can handle both tip and hub vortices, the rotor data surveyed did not give any quantitative information useful in developing empirical relations to compute the hub vortex strength and radius. It is recommended that, if and when such data become available, the empirical relations for hub vortex strength and radius be finalized.

7.0 REFERENCES

1. Magliozzi, B., Hanson, D.B., Johnson, B.V., and Metzger, F.B., "Noise and Wake Structure Measurements in a Subsonic Tip Speed Fan," NASA CR-2323, November 1973.

2. Reynolds, B. and Lakshminarayana, B., "Characteristics of Lightly Loaded Fan Rotor Blade Wakes," NASA CR-3188, October 1979.

3. Ravindranath, A. and Laksminarayana, B., "Three Dimensional Mean Flow and Turbulence Characteristics of the Near Wake of a Compressor Rotor Blade," NASA CR-159518, June 1980.

4. Lakshminarayana, B., Govindan, T.R., and Reynolds, B., "Effects of Blade Loading and Rotation on Compressor Rotor Wake in End Wall Regions," AIAA Paper No. 82-0193, Jan. 1982.

5. Dring, R.P., Joslyn, H.D., and Hardin, L.W., "An Investigation of Axial Compressor Rotor Aerodynamics," ASME J. Engineering for Power, Transactions of the ASME, Volume 104, Jan. 1982, pp. 84-96.

6. Shaw, L.M., and Balombin, J.R., "Rotor Wake Characteristics Relevant to Rotor-Stator Interaction Noise Generation," NASA TM-82703, Oct. 1981.

7. Kool, P., DeRuyck, J., and Hirsch, Ch., "The Three-Dimensional Flow and Blade Wake in an Axial Plane Downstream of an Axial Compressor Rotor," ASME Paper No. 78-GT-66, April 1978.

8. Fleeter, S., Jay, R.L., and Bennett, W.A., "The Effect of Rotor-Stator Axial Spacing on the Time-Variant Aerodynamic Response of a Compressor Stator," DDA Report No. EDR 9379, AFSC Contract No. F49620-77-C-0024, December 1977.

9. Larguier, R. and Desievers, A., "Methodes De Measures Instationnaires dans Les Turbomachines," (in French), Presented at AAAF 10th Colloquium Applied Aerodynamics, Lille, France, November 1973.

10. Schlichting, H., Boundary Layer Theory, McGraw Hill, New York, 1960 (4th Ed.).

11. Johnsen, I.A. et al., ed., "Aerodynamic Design of Axial Flow Compressors," NASA SP-36, 1965.

12. Lakshminarayana, B., "Methods of Predicting the Tip Clearance Effects in Axial Flow Turbomachinery," ASME Journal of Basic Engineering, Vol. 92, Series D, pp. 467-482, September 1970.

13. Adkins, G.G. and Smith, L.H., Jr., "Spanwise Mixing in Axial Flow Turbomachines," ASME Paper 81-GT-57, March 1981.

14. Davino, R.M., "Rotor Viscous Exit Flow Model Development as Applied to Rotor/Stator Interaction Noise," General Electric Aeroacoustic Design Methods Memorandum No. 81-03, August 1981.

15. Rains, D.A., "Tip Clearance Flow in Axial Flow Compressors and Pumps," California Institute of Technology, Mechanical Engineering Lab Report 5, 1954.

16. Lamb, H., Hydrodynamics, 6th Edition, Dover Publications, p. 224, New York, 1945.

17. Dosanjh, D.S., Gasparek, E.P., and Eskinazi, S., "Decay of a Viscous Trailing Vortex," The Aeronautical Quarterly, May 1962.

18. Neuman, B.G., "Flow in a Viscous Trailing Vortex," Aeronautical Quarterly, May 1959.

19. Shaw, L.M. and Glaser, F.W., "Mean Rotor Wake Characteristics of an Aerodynamically Loaded 0.5 m Diameter Fan," NASA TM 81657, January 1981.

20. Selby, S.M. (Ed), "CRC Standard Mathematical Tables," 17th Edition, pp. 14, 1969.

21. Mani, R., "Noise Due to Interaction of Inlet Turbulence with Isolated Stators and Rotors," Journal of Sound and Vibration, Vol. 17, No. 2, 1971, pp. 251-260.

22. Kerschen, E.J. and Gliebe, P.R., "Noise Caused by the Interaction of a Rotor with Anisotropic Turbulence," AIAA Journal, Vol. 19, No. 6, June 1981, pp. 717.

23. Gliebe, P.R., "Analytical Study of the Effects of Wind Tunnel Turbulence on Turbofan Rotor Noise," AIAA Paper No. 80-1022, June 1980.

24. Hah, C., Private Communication, May 1984.

25. Raj, R. and Lakshminarayana, B., "Three Dimensional Characteristics of Turbulent Wakes Behind Turbomachinery Rotors," Journal of Engineering for Power, Vol. 98, No. 2, pp. 218-228, April 1976.

26. Lakshminarayana, B., "Nature of Flow Distortions Caused by Rotor Wakes," Proc. of the NATO-AGARD Symposium on Unsteady Phenomena in Turbomachinery, AGARD CP-177, pp. 4-1 to 4-13, April 1976.

27. Kool, P. and Hirsch, Ch., "A Prediction Scheme for the Decay of a Turbomachine Blade Wake," ASME Paper 82-GT-273, 1982.

28. Hah, C. and Lakshminarayana, B., "Numerical Analysis and Fortran Program for Computation of the Turbulent Wakes of Turbomachinery Rotor Blades, Isolated Airfoils and Cascades," NASA Contractor Report 3509, February 1982.

29. Raj, R. and Lakshminarayana, B., "On the Investigation of Cascade and Turbomachinery Rotor Wake Characteristics," NASA CR-134680, 188 pp., February 1974.

30. Anand, A.K. and Lakshminarayana, B., "An Experimental and Theoretical Investigation of Three Dimensional Turbulent Boundary Layer Inside an Axial Flow Inducer," NASA CR-2888, pp. 1-209, August 1977.

31. Coustieux, J. and Aupoix, B., "An Integral Method for Calculating a Three Dimensional Wake," Fiche Technique No. 2, 1983, ONERA, Toulouse, June 1983.

32. Schlichting, H., Boundary Layer Theory, McGraw Hill, Sixth Edition, 1968.

33. Mager, A., "Generalization of Boundary Layer Momentum Integral Equations to Three Dimensional Flow Including Those of Rotating System," NACA Rep. 1067, 1952.

34. Head, M.R., "Entrainment in Turbulent Boundary Layers," British ARC R&M 3152, September 1958.

35. Lewis, G.W., Jr. and Tysl, E.R., "Overall and Blade-Element Performance of a 1.2-Pressure-Ratio Fan Stage at Design Blade Setting Angle," NASA TM X-3101, September 1974.

36. Homyak, L., NASA Lewis, Private Communication.

37. Urasek, D.C., Gorrell, W.T., and Cunnan, W.S., "Performance of Two-Stage Fan Having Low-Aspect-Ratio, First Stage Rotor Blading," NASA TP 1493, August 1979.

8.0 NOMENCLATURE

a	Radius of the vortex core
AR	Aspect ratio (span/chord)
B	Number of rotor blades
b	Tangential distance of the center of the vortex core from the wake centerline (see Figure 26)
BPF	Blade Passing Frequency
c	Rotor aerodynamic chord
c_o	Ambient speed of sound
C_D	Drag coefficient
C_L	Lift coefficient
c_m	m-th Complex Fourier coefficient of the gust upwash velocity component
DoD	Department of Defense
DTIC	Defense Technical Information Center
GE	General Electric Company, USA
h	Rotor blade span
i	$\sqrt{-1}$
IGV	Inlet Guide Vane
k	Fraction of suction lift lost to the vortex
$\underline{K}$ $(k_{\bar{x}}, k_{\bar{y}}, k_{\bar{z}})$	Wave number vector
L	Turbulence length scale
l	Characteristic length scale
La	Axial turbulence length scale
L_p, L_s	Semiwake width at half the depth on the pressure and suction sides of the wake, respectively

L_t	Transverse turbulence length scale
m	Harmonic number $m = 1$ BPF $m = 2$ 2 x BPF, etc.
M_a	Axial Flow Mach No.
M,N,p	Parameters associated with vortex (see Equations 27 through 29 and Figure 26)
n	Normal to the streamwise coordinate (in the tangential direction)
NACA	National Advisory Committee for Aeronautics
NASA	National Aeronautics and Space Administration
O(#)	Order of magnitude
P	Static Pressure
P_r	Pressure ratio
R	Domain of the vortex core (see Figure 26)
r	Radial distance
R_s, RN	Reynolds Number
r'	Distance from the vortex center
R/S	Rotor-stator
S	Blade-to-blade spacing
s	Streamwise distance from the rotor trailing edge
U	Axial velocity (see Figure 30)
(u', v', w')	Axial, tangential, and radial component of turbulent (rms) velocity
u_c	Velocity defect at centerline
u_d	Axial component of wake velocity defect
u_{dc}	Axial component of the wake centerline velocity defect
$\overline{u_a^2}$, $\overline{u_t^2}$	Axial and transverse components of turbulence intensity

V	Normal velocity component (see Figure 31)
$\bar{V}$	Velocity vector in the stationary frame of reference
$\bar{v}'$	Perturbation velocity vector in the stationary frame of reference
v'_n	Upwash component of the perturbation velocity
v'_s	Streamwise component of the perturbation velocity
V_{ref}	Reference velocity used in evaluating dB level for upwash velocity harmonic content
V_t	Tip speed
V_{wheel}	Wheel speed at a given radial location
V_y	Tangential velocity (see Figure 30)
V_θ	Tangential component of the flow velocity at rotor exit (assuring no swirl at rotor inlet)
$\bar{W}$	Velocity vector in the rotating frame of reference
W	Total velocity in the rotating frame of reference
W_{dv}	Maximum defect in the streamwise velocity of the vortex core in the rotating frame of reference
$W_d(\gamma')$	Velocity defect in the streamwise component of velocity at a distance γ' from the vortex center in the rotating frame of reference
W_m	Mean flow velocity through the blade passage in the rotating frame of reference
W_1	Main stream flow velocity at the rotor inlet in the rotating frame of reference
W_θ	Work coefficient
$W_t \big\|_{(\ )}$	Tangential velocity induced by the ( ) vortex in the rotating frame of reference
$W_r \big\|_{(\ )}$	Radial velocity induced by the ( ) vortex in the rotating frame of reference

WTIV	Inviscid velocity gradient normalized by wheel speed
X	Axial distance from the rotor trailing edge
x, y	Coordinates of the unwrapped annulus (see Figure 26)
$(\bar{x}, \bar{y})$	Cascade plane (see Figure 30, Section 3.3.2)
$(\bar{x}_o, \bar{y}_o, \bar{z}_o)$	Fluid fixed coordinates (see Section 3.3.2)
ΔX	Axial distance between rotor trailing edge and 1/4 chord point of stator as a point at which the gust velocity is being evaluated

GREEK SYMBOLS

α	Flow angle of the absolute velocity vector to the axial direction
β	Flow angle of the rotor relative velocity vector to the axial direction
$\beta 1$	Rotor relative inlet flow angle
$\beta 2$	Rotor relative exit flow angle
Γ	Circulation
γR	Rotor stagger angle
γS	Stator stagger angle
δ	Semiwake width
δij	Kronecker's delta, $\delta_{ij} = 1$ if $i = j$ $= 0$ if $i \neq j$
η	Normalized tangential distance $[\eta = x/(\delta/2)]$
θ	Momentum thickness in a two-dimensional boundary layer
λ_r, λ_s	Rotor or stator stagger angles, used in Section 4.2
μ	Turbulence velocity scale (see Equation 104)
ν	Kinematic viscosity (laminar)
ν_T	Eddy viscosity

ν_t	Turbulent equivalent kinematic viscosity
ρ	Density (fluid density)
σ_r	Rotor solidity (rotor aerodynamic chord/blade-to-blade spacing)
τ	Tip clearance
τ_{rn}, τ_{sn}	Shear stresses in radial and streamwise directions
τ_t	Turbulent shear stress
τ_x	Axial component of turbulent intensity
$\tau_{x,\,o}$	Axial component of turbulent intensity in the free stream
$(\tau_x)_c$	Axial component of turbulent intensity at the wake centerline
ϕ	Angle from the rotor blade stacking axis to the 1/4 chord point of stator or a point at which the gust velocity is being evaluated
ϕ_m	Phase of the complex m-th order Fourier coefficient, c_m
ϕ_{nn}	Turbulence upwash velocity spectrum
ϕ_o	Angle from the rotor blade stacking axis to the trailing edge of the rotor
$\Delta\phi$	$\phi - \phi_o$
χ	Turbulence wavenumber (see Equation 79)
Ω	Angular velocity of the rotor
ω	Angular velocity of the vortex
$\bar{\omega}$	Turbulence spectrum frequency

Subscripts

a	Refers to axial/tangential turbulent length scales
ann	Refers to annulus wall
c	Refers to centerline
d	Refers to wake defect

dc	Refers to defect at the wake centerline
e	Refers to edge
h, hub	Refers to hub
$(\ _{hub})_{vtx}$	Refers to hub vortex (particularly for circulation)
n	Refers to normal to the streamwise direction (in the tangential direction)
o	Refers to free stream condition
ps	Refers to pressure side of rotor blade
s	Refers to the streamwise direction
ss	Refers to suction side of rotor blade
t	Refers to transverse (radial) turbulent length scale
t, tip	Refers to tip
$(\ _{tip})_{vtx}$	Refers to tip vortex (particularly for circulation)

1 Report No NASA CR-174849	2 Government Accession No	3 Recipient's Catalog No

4 Title and Subtitle Development of a Rotor Wake/Vortex Model Volume I - Final Technical Report	5 Report Date June 1984 6 Performing Organization Code
7 Author(s) Majjigi, R.K. and Gliebe, P.R.	8 Performing Organization Report No 10 Work Unit No
9 Performing Organization Name and Address General Electric Company Aircraft Engine Business Group Cincinnati, Ohio 45215	11 Contract or Grant No NAS3-23681 13 Type of Report and Period Covered Final Report
12 Sponsoring Agency Name and Address National Aeronautics and Space Administration Washington, D.C. 20546	14 Sponsoring Agency Code

15 Supplementary Notes

Project Manager: L. Homyak/J. Groeneweg
NASA-Lewis Research Center
21000 Brookpark Road
Cleveland, Ohio 44135

16 Abstract The principal objective of this research program was to establish a verified rotor wake/vortex model for specific application to fan and compressor rotor-stator interaction and resulting noise generation. Certain empirical rotor wake and turbulence relationships were developed using existing low speed rotor wake data. A tip vortex model was developed by replacing the annulus wall with a row of image vortices. An axisymmetric turbulence spectrum model, developed in the context of rotor inflow turbulence, was adapted to predicting the turbulence spectrum of the stator gust upwash. Volume II of this contractor report (NASA CR-174850) provides a detailed description of the computer program.

The significant conclusions of this investigation are:

- The agreement between the measured and predicted rotor wake characteristics, stator gust harmonic amplitude, and turbulence spectra for three high-speed rotors has been found to be good.
- Increasing the rotor-stator spacing above a value at which the merging of wakes from the adjacent rotor blades takes place does not yield any appreciable reduction in the stator upwash harmonic spectral levels. This can be used as a design guide in the selection of rotor-stator spacing from the point of reducing the rotor wake interaction with the stator.
- The tip vortex can significantly influence the stator upwash spectrum, particularly near the tip region. The presence of a tip vortex typically results in higher levels of twice the Blade Passing Frequency (BPF) compared to the BPF essentially due to the presence of two defects, one due to the wake and the other due to the tip vortex, within one blade passage. Tip clearance and the tangential location of the tip vortex are the two most important parameters governing the contribution of the tip vortex to the stator upwash harmonic spectrum.
- Wake asymmetry due to the rotor loading did not have much impact on the gust harmonic spectrum even at small rotor-stator spacings. However, a combination of an asymmetric wake and a tip vortex results in a complex gust harmonic spectrum.
- The influence of rotor blade section drag coefficient on the wake defect and wake width was found to be smaller compared to the case of the wake of a two dimensional airfoil.

17 Key Words (Suggested by Author(s)) Rotor Wake, Tip Vortex, Rotor-Stator Interaction, Turbomachinery Noise, Wake Turbulence, Forced Vibration.	18 Distribution Statement Unclassified - Unlimited

19 Security Classif (of this report) Unclassified	20 Security Classif (of this page) Unclassified	21 No of Pages 156	22 Price*

* For sale by the National Technical Information Service Springfield Virginia 22161

END

DATE

FILMED

JUL 25 1985